



Fakultät für Physik
Physics of Energy Conversion and Storage

**Methodological Aspects of In-Depth
Electrochemical Characterization of Metal and
Metal Oxide Electrocatalysts**

Sebastian Anselm Watzele

Vollständiger Abdruck der von der Fakultät für Physik der Technischen Universität
München zur Erlangung des akademischen Grades eines
Doktors der Naturwissenschaften
genehmigten Dissertation.

Vorsitzender: Prof. Dr. Alejandro Ibarra

Prüfer der Dissertation:

1. Prof. Dr. Aliaksandr S. Bandarenka
2. Prof. Dr. Ifan E. L. Stephens

Die Dissertation wurde am 20.01.2020 bei der Technischen Universität München
eingereicht und durch die Fakultät für Physik am 21.02.2020 angenommen.

Abstract

Efficient energy storage attains increased importance for today's society due to a gradual change of energy provision towards "renewables". A promising way to store excess electrical energy is to store it in the form of hydrogen obtained electrochemically by water electrolysis. The efficiency of associated electrolyzers and fuel cells is strongly related to the performance of the applied electrocatalysts. Therefore, the development of highly active electrocatalysts and their optimization is of great importance to make aforementioned devices cost effective. In turn, the rational design of electrocatalysts requires a distinct fundamental knowledge of the catalyzed electrochemical reaction and its reaction mechanism(s). However, even for the reactions, which are considered to be simple, such as the hydrogen evolution reaction (HER), there is a serious lack of knowledge of the dominating reaction mechanisms. In this work, a method has been developed to estimate the relative contribution of Volmer-Heyrovsky and Volmer-Tafel mechanisms. It is based on electrochemical probing of the frequency dependent impedance of Pt microelectrodes. Analysis using a model developed in this work indeed allowed to differentiate both mechanisms. This contributes to a better understanding but at the same time somewhat questions the validity of the classical approaches to analyze reaction mechanisms.

After the theoretical identification of promising electrocatalysts, their performance is usually benchmarked before their application in real devices. However, the significance of results from pre-testing of the catalysts under laboratory conditions can be questionable as the conditions in real applications are often strongly different. For this purpose, a novel approach was elaborated to benchmark electrocatalysts using industrial relevant conditions such as operation at high current densities and at elevated temperatures and in concentrated electrolytes. Especially the benchmarking at high current densities was facilitated by the use of microelectrodes, which allow quasi iR -free measurements and suppresses the

formation of a gaseous phase at the electrode. This is supposed to greatly reduce the probability for wrong predictions of activities under such conditions.

Another fact is that the comparison of electrochemical activities is not meaningful without consideration of the electrochemically active surface area (ECSA) of a catalyst. However, this is especially a problem for transition metal oxides and perovskites that are commonly used as OER catalysts, and in most cases no ideal method exists to determine their ECSA. This problem was addressed by the development of a new method for the determination of ECSA of OER electrocatalysts using electrochemical impedance spectroscopy measurements. The application of this method was demonstrated using several examples. It is shown that the main advantages of this approach are its accuracy, the short measuring time and the possibility to perform it in-situ. It can be assumed that it will have significant impact on future studies of oxide electrocatalysts.

Zusammenfassung

Effiziente Energiespeicherung gewinnt für die heutige Gesellschaft zunehmend an Bedeutung, da die Energieerzeugung allmählich auf erneuerbare Energien umgestellt wird. Ein vielversprechender Weg, überschüssige elektrische Energie zu speichern, ist die Speicherung in Form von Wasserstoff, der elektrochemisch durch Wasserelektrolyse gewonnen wird. Dabei hängt der Wirkungsgrad von Brennstoffzellen und Elektrolyseuren stark von dem eingesetzten Elektrokatalysators ab. Daher ist die Entwicklung hochaktiver Elektrokatalysatoren und deren Optimierung von großer Bedeutung, um die oben genannten Geräte kosteneffizient zu machen. Das rationelle Design von Elektrokatalysatoren wiederum erfordert ein ausgeprägtes fundamentales Wissen über die jeweilig katalysierte elektrochemische Reaktion und deren Reaktionsmechanismen. Jedoch besteht sogar bei als einfach angesehenen Reaktionen, wie beispielsweise der Wasserstoffevolutionsreaktion (HER), ein gravierender Mangel an Wissen über deren dominierenden Reaktionsmechanismus. Daher wurde eine Methode entwickelt, um den Beitrag von Volmer-Heyrovsky und Volmer-Tafel Mechanismus zu identifizieren. Sie basiert auf der elektrochemischen Untersuchung der frequenzabhängigen Impedanz von Mikroelektroden. Die Analyse mit einem neuartigen Modell ermöglichte es tatsächlich, beide Mechanismen zu unterscheiden. Dies trägt zu einem besseren Verständnis bei und hinterfragt auch die Validität der klassischen Ansätze zur Analyse von Reaktionsmechanismen.

Nach der theoretischen Identifizierung vielversprechender Elektrokatalysatoren wird deren Leistung in der Regel vor ihrer Anwendung in realen Geräten überprüft. Die Bedeutung der Ergebnisse aus der Vorprüfung von Katalysatoren unter Laborbedingungen kann jedoch fragwürdig sein, da die Bedingungen in der realen Anwendung oft stark unterschiedlich sind. Zu diesem Zweck wurde ein neuartiger Ansatz zum Testen von Elektrokatalysatoren unter industriell relevanten Bedingungen entwickelt, wie z.B. dem

Betrieb bei hohen Stromdichten und bei erhöhten Temperaturen sowie in konzentrierten Elektrolyten. Die Messung bei hohen Stromdichten wurde durch den Einsatz von Mikroelektroden erleichtert, welche quasi iR -freie Messungen ermöglichen und die Bildung einer Gasphase an der Elektrode unterdrücken. Dies reduziert die Wahrscheinlichkeit für Aktivitätsfehlprognosen maßgeblich.

Eine weitere Tatsache ist, dass der Vergleich elektrochemischer Aktivitäten ohne Berücksichtigung der elektrochemisch aktiven Oberfläche (ECSA) eines Katalysators nicht sinnvoll ist. Dies ist jedoch besonders problematisch für Übergangsmetalloxide und Perowskiten, die häufig als OER-Katalysator verwendet werden, da in den meisten Fällen keine ideale Methode zur Bestimmung deren ECSA existiert. Dieses Problem wurde durch die Entwicklung einer universellen Methode zur Bestimmung von OER-Elektrokatalysatoren gelöst. Die Anwendung dieser neuartigen Methode wurde an mehreren realistischen Beispielen demonstriert. Die Hauptvorteile sind ihre Genauigkeit, die kurze Messdauer und die Möglichkeit, sie in-situ durchzuführen. Es ist davon auszugehen, dass diese Methode einen signifikanten Einfluss auf zukünftige Studien zu OER-Elektrokatalysatoren haben wird.

Content

Abstract	3
Zusammenfassung	5
Acknowledgement	11
1 Introduction	13
1.1 Renewable energy.....	13
1.2 Energy storage.....	14
1.3 Hydrogen.....	15
1.4 Methodological challenges.....	16
1.5 Aim of this work.....	17
2 Theory	19
2.1 Electrocatalysis.....	19
2.2 Reaction kinetics.....	22
2.3 Nernst equation.....	24
2.4 Water electrolysis.....	25
2.5 The PEM electrolyzer.....	27
2.6 Alkaline water electrolysis.....	29
2.7 High temperature electrolysis.....	30
3 Experimental Part	31
3.1 Experimental setup.....	31
3.1.1 Rotating (ring) disk electrode.....	32
3.1.2 Microelectrodes.....	35
3.1.3 Electrode preparation.....	38

3.1.4 Equipment	44
3.1.5 Materials	45
3.1.6 Chemicals.....	46
3.1.7 Software	47
3.2 Experimental techniques	48
3.2.1 Electrochemical techniques	48
3.2.2 X-Ray photoelectron spectroscopy	53
3.2.3 Atomic force microscopy.....	55
4 Results and Discussion.....	57
4.1 Determination of electroactive surface area of oxide materials.....	57
4.1.1 Motivation.....	57
4.1.2 Definition of the problem.....	58
4.1.3 State-of-the-art approaches	59
4.1.4 Principles of the developed method.....	62
4.1.5 Explanation of the EEC	66
4.1.6 Calibration.....	69
4.1.7 Application.....	83
4.2 Evaluation of the intrinsic activity of electrocatalysts under industrially relevant conditions.....	93
4.2.1 Benchmarking of conventional OER/ HER electrocatalysts	95
4.2.2 Benchmarking the OER performance of novel MOF-based electrocatalysts.	104
4.3 On the dominating mechanism of the HER	112
4.3.1 HER mechanisms.....	113
4.3.2 Analysis of polarization curves.....	118
4.3.3 Analysis of the EIS spectra	120
5 Conclusions and an Outlook	129

6 Appendix	132
6.1 Figures.....	132
6.2 Symbols and abbreviations	133
6.3 Related publications.....	137
6.4 Other publications	174
6.5 Conference presentations	175
6.6 References.....	176

Acknowledgement

The completion of this thesis would not have been possible without the contribution and support of many people. Therefore, I would like to thank...

... my supervisor **Prof. Dr. Aliksandr S. Bandarenka** for giving me the opportunity to work in his group on various interesting topics and his guidance and support throughout my thesis.

... **Dr. Frédéric Maillard** for hosting me at the “Laboratoire d’Electrochimie et de Physico chimie des Matériaux et des Interfaces” at Grenoble and for extensive collaborations related to synthesis and characterization of nanoparticles. Additionally, I am grateful for the hospitality also of the other group members of LEPMI, especially I want to mention **Fabien Claudel** and **Laetitia Dubau** for acquiring TEM images.

... **Dr. Ifan E. L. Stephens** for hosting me at the “Imperial College London”. I am grateful for the hospitality and fruitful discussions. Moreover, I want to thank his group members **Daisy Thornton, Rose Oates, James Murawski, Ricardo Paz Moldes Duarte, Xuyang Shen, Yang Ming**, and especially mentioning **Shuaihang Yin**, who allowed me to analyze and utilize her recorded EIS spectra of IrO_x for this work. Additionally, I want to thank **Stefano Mezzavilla** for collaboration and provision of his laboratory equipment.

... **Prof. Dr. Roland A. Fischer** and **Dr. Weijin Li** for collaborations related to the development of SURMOFDs as highly active electrocatalysts. The synthesis and characterization of these catalysts were mainly done by **Dr. Weijin Li**. I also want to thank other collaborators of this project: **Dr. Hany A. El-Sayed, Gregor Kieslich, Katia Rodewald** and **Bernhard Rieger** (My contribution on this project was mainly the activity measurements using microelectrodes and analysis of the film *via* XPS).

... **Prof. Dr. Hubert A. Gasteiger, Dr. Jan Schwämmlein** and **Paulette Loichet** for their collaboration in the joint project “ActiveElectroCat” and interesting discussions.

... all former and current members of the ECS who made my daily work more enjoyable: **Manuela Ritter, Susanne Tillich, Dr. Batyr Garlyyev, Jeongsik Yun, Song Xue, Philipp Marzak, Johannes Fichtner, Jarek Peter Sabawa, Xing Ding, Tim Lochner,**

Regina Kluge, Shujin Hou, Leon Katzenmeier, Richard Haid, Siegfried Schreier, Michael Stanglmeir, Theophilus Kobina Sarpey, Xaver Lamprecht, Xiaohan Sun, Simon Helmer, Leif Carstensen, Peter Schneider, Muhamad Hilmi Afa, Eleftherios Psaltis, Thorsten Schmidt, Dr. Viktor Colic, Dr. Marcus Pohl, Dr. Yunchang Liang, Dr. Daniel Scieszka, Dr. Jonas Pfisterer, Bianca Paulitsch, Albrecht Dorsel, David Reinisch, Florian Schiegg, Lakshmi Swaroopa Ganti, Franz Dinkelacker, Michael Obermaier, Christian Sohr, Christoph Csoklich, David McLaughlin, Radu Bors, Lukas Spanier, Alexander Wieczorek, Paul Scheibenbogen, Marc Kosiahn, Namitha Rajendran, Pascal Hauenstein, Angus Laurenson, Stefan Oswald, Andreas Oberbauer, Enggar Pramanto Wibowo, Philipp Moser, Jongho Kim, Maximilian Schart, Armin Lang, Fiona Treber, Mike Dao, Mathias Rehm, Felix Haimerl, Simon Lechner, Johannes Figueiredo, Leonardo Stamerra, Caspar Galen, Adrian Callies, and Johanna Schönecker. It was a big pleasure to work with you!

Especially I want to mention...

...**Siegfried Schreier** who always had advice for technical problems and was open for many and long discussions for innovative solutions.

...**Johannes Fichtner** for his support with the polarization curves of microelectrodes in acidic environment and very pleasant collaboration in many joint projects, fruitful discussions and other support.

... **Song Xue** for the measurement of an urgently needed EIS spectra of a Pt(pc) disk electrode in 0.1 M HClO₄ and many fruitful collaborations.

...**Dr. Batyr Garlyyev** for interesting discussions and both scientific and non-scientific support.

... **Pascal Hauenstein** for measuring numerous EIS spectra of metal oxides.

...**Yunchang Liang** and **Daniel Scieszka** for measuring AFM and XPS, respectively.

... **Philipp Marzak** for many interesting discussion and mental support during writing.

Further, I wish to express my deepest gratitude to **my parents** and **my brother** for all the support and encouragement I received.

Finally, I would like to thank my partner, **Kirsten**, for all her support, understanding, and patience.

1 Introduction

1.1 Renewable energy

With the steady increase in the usage of carbon-based energy in the last century, today's society is facing unprecedented problems, like the human made climate change and dwindling resources^{1,2,3,4}. The global annual consumption of electric energy increased by 4% compared to the previous year and reaches a new record of ~23 PWh⁵. Currently, energy produced from coal and gas are ~39% and ~22% of total energy, respectively⁶. Nuclear power can be seen as the special case, as it does not significantly contribute to the emission of CO₂, though the Uranium/Plutonium is limited, and the disposal of the nuclear waste is an unsolved issue^{7,8,9}. The share of "renewables" with ~25%¹⁰ is a small, but the fastest increasing energy source^{11,12}. A change of energy production towards the renewables might be the way for sustainable energy production to fight against man made climate change and to preserve our planet for future generations^{12,13,14,15}.

The recent attempts to increase the share of renewables, however, revealed several weaknesses: their higher prices and their intermittent production^{16,17,18}. In contrast to plants run by fossil fuels, the energy output of photovoltaic and wind plants can't be adjusted to the need, and their daily production rate heavily depends on environmental influences^{19,20}. This leads to various situations, such as the need for energy production by conventional power plants, or regenerative power plants, which need to be shut down to prevent power grid overloads^{21,22}.

1.2 Energy storage

Improvement of the power grids and gas power plants, able to start-up rapidly to compensate energy supply shortages, can relieve this situation to a certain degree²³, however, efficient energy storage is an unavoidable need to compensate supply fluctuations and energy production/demand mismatches, especially when the percentage of renewables should be further increased^{24,25,26}. This short-term fluctuations are typically equalized *via* supercapacitors²⁷ or *via* superconducting magnetic energy storage equalizers²⁸, as they can operate with high efficiencies (> 95%) and have good power density. However, they are inappropriate to compensate larger intermittencies due to their limited energy densities^{29,30}. Mountainous regions often provide the geographical conditions to use dams and create water reservoirs at different levels and utilize the hydroelectricity as operational reserve for the power grids. In case of surplus energy, this electric energy can be converted to gravitational potential energy by pumping water from the lower to the higher basin³¹. This can be the most cost-effective technique and reaches efficiencies up to 60-80%³². Though, this often requires flooding of inhabited mountain valleys meaning forced relocation of the residents³³.

In special cases a thermal energy storage, *e.g. via* the molten salt technology is viable when, for instance, solar collectors are used as the energy source^{34,35}. Chemical and electrochemical storage of electric energy represents a promising solution for intermittent supply of solar and wind energy sources^{36,37}. Lithium-ion batteries for instance, which are already used in electric cars, have a good efficiency (80-90%³⁸) and a high power and energy density³⁹. Low abundance and uneven distribution⁴⁰ of the needed materials lead to various problems. For example, lithium is mainly mined in Chile, Australia, Argentina, and China resulting in an economical dependency, which can be abused as political leverage^{41,42}. Moreover, cobalt, which is used on a large scale for electrode materials⁴³ is mainly mined in the Democratic Republic of Kongo, also by the use of child-labor and bad working conditions. This is an often-forgotten truth, when speaking about “clean” electric cars.⁴⁴ Alternatives are other types of batteries, using more (earth) abundant alkali metal cations or (vanadium) redox flow batteries^{45,46}. However, the required resourced and capital costs of 176 \$/kWh (2018)⁴⁷ limit the widespread application of such batteries⁴⁸.

1.3 Hydrogen

Energy storage *via* the production of hydrogen can be a reasonable approach to the aforementioned problems. Hydrogen produced *via* electrolysis of water can be stored in *e.g.* high-pressure tanks, and it can be converted back to electricity by fuel cells (as shown in **Figure 1**)^{49,50}. The advantage is, that in order to scale up the energy capacity of the system, solely the amount of gas tanks at a relatively low current cost of 14.19 \$/kWh⁵¹ needs to be increased. The costs for electrolyzers can be as low as 450 \$/kW in the case of alkaline electrolyzers⁵². Furthermore, hydrogen is by itself a valuable resource and starting material for many industrial applications like the synthesis of ammonia, methanol and metal refining⁵³. Interestingly, for more than 50 years, Iceland used some of its excess electric energy from its hydroelectric plants to produce hydrogen (2000 tons per year) *via* electrolysis for ammonia production showing the principle feasibility of the whole approach.^{54,55}

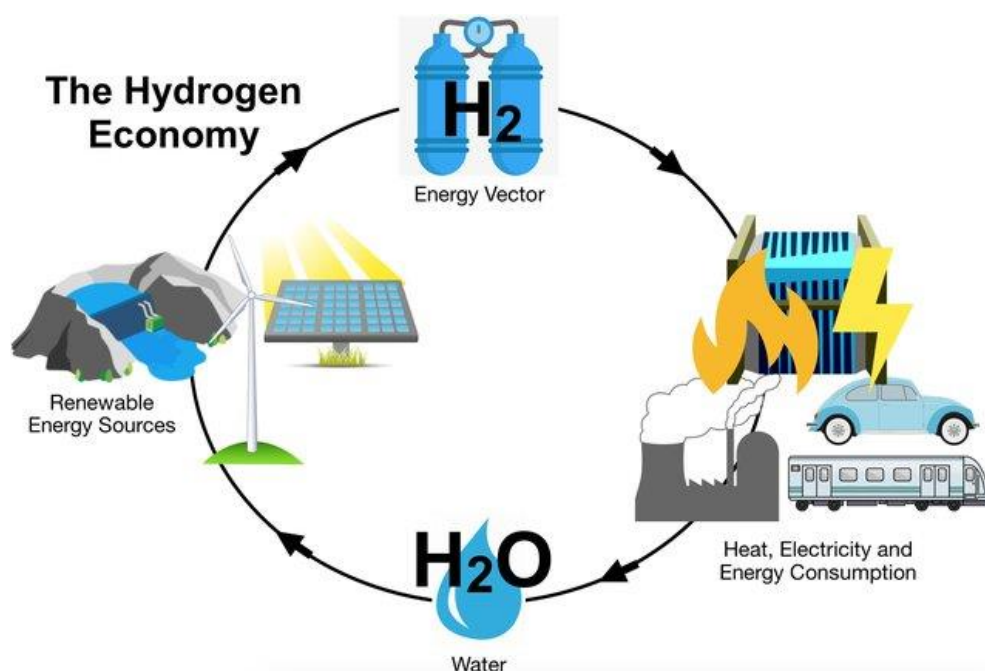


Figure 1. Schematic overview of a hydrogen-based energy economy. Adapted from ref. [56] (open access, permission of unrestricted use).

Currently, hydrogen is mainly produced *via* steam reforming, gasification of oil, coal, and petroleum coke, and just ~4% of total hydrogen is produced *via* water electrolysis, which

means that there is an enormous potential for cutting the amount of CO₂ emission, as each ton of hydrogen produced from *e.g.* natural gas results in 9-12 tons of CO₂^{57,58}. Although the efficiency of the state-of-the-art electrolyzers has been improved significantly up to ~70% within the last decades, there is still a potential for further optimizations^{59,60}. The increasing lifetime and decreasing cell voltage at a constant production rate would lead to an increased cell efficiency and is highly desirable for making electrolyzers economically more viable^{61,62}.

Increasing the cell efficiency of a polymer electrolyte membrane (PEM) electrolyzer requires certain technical optimizations of *e.g.* the bipolar plates, gas diffusion layers and membrane materials^{63,64}. On the other hand, the choice and optimization of the catalysts has also a major impact on the device's performance^{63,65,66}.

1.4 Methodological challenges

In-situ testing of all catalyst materials in a PEM device would be very expensive, meaning that a good electrocatalyst prescreening methodology is required. Computational techniques, like the calculations of binding energies using for example density function theory, can suggest various materials^{67,68,69,70}. These calculations typically make several simplifications, *e.g.* neglecting effects of the electrolyte, which, however, have shown significant influence on experimental results^{71,72,73,74}. To make reliable forecasts, a complete understanding of the reaction mechanism on different catalyst surfaces is mandatory. However, even for the hydrogen evolution reaction (HER) on platinum surfaces, which is considered as one of the simplest reactions in the field of electrocatalysis, is not fully understood.^{75,76,77,78} It is known to have two parallel reaction mechanisms; but even their contribution to the overall reaction rate is unknown. Multi-step reactions like the oxygen evolution reaction (OER) on non-model surfaces of metal oxides and perovskites are even more complex⁷⁹. Therefore, the predictions made by computational techniques still need to be validated experimentally by electrochemical measurements^{80,81}.

Lack in the comparability of measurement protocols from different research groups examining the same type of catalyst materials is a common problem for identifying the most active catalysts^{82,83}. Furthermore, these protocols are often neglecting various important factors. The electrochemically active surface area (ECSA) for instance, is typically not determined accurately,^{84,85,86} and in some cases is even misunderstood as the geometric surface area,⁸⁷ which distorts the results for the electrochemical activity^{88,89,90}. This is especially true for metal oxide catalysts, which are used as anode catalysts in alkaline electrolyzers. The determination of their ECSA is currently very complex and just a few methods exist, like *e.g.* mercury underpotential deposition on iridium oxide⁹¹. Other methods such as the evaluation of double layer capacitance are not accurate^{91,92}.

Another issue is related to experimental conditions: typical laboratory conditions differ significantly from the conditions in real devices. While catalysts are typically benchmarked under laboratory conditions, such as at room temperature, low concentration of electrolytes and low current densities ($\sim \text{mA cm}^{-2}$), the working conditions relevant for practical applications in industry are different. For instance, alkaline electrolyzers operate at elevated temperatures $\sim 80\text{ }^\circ\text{C}$, at considerably higher current densities of $\sim \text{A cm}^{-2}$ and utilize concentrated electrolytes^{93,94}. Therefore, trends of activity determined in laboratories do not necessarily prove true in real applications.

1.5 Aim of this work

This work aims to address several aspects of the aforementioned problems.

A method for the determination of electroactive surface area for oxide and perovskite materials has been developed. It enables a non-destructive in-situ examination of the electrocatalyst ECSA with good accuracy, which can be performed within a few minutes.

A method to benchmark electrocatalysts for electrolyzers at more realistic laboratory conditions has been established. As a promising approach, the idea shown by A. Gannassin *et al.*⁹⁵ to use microelectrodes for benchmarking catalysts at high current densities was further elaborated. This requires identification of a suitable microelectrode, which shows high durability in harsh alkaline environments⁹⁶. This is required as they serve as substrate

for the catalyst films and benchmarking process should be expanded to achieve conditions, which can be found in alkaline electrolyzers. The method was applied on state-of-the-art OER and HER catalysts to investigate the necessity to analyze at such conditions and to determine benchmark activities. The same approach was then used to benchmark a new type of highly active OER catalyst derived from a metal organic frameworks (MOFs).

Finally, the HER reaction mechanism on Pt(pc) surfaces in acidic environment was studied utilizing microelectrodes. More precisely, the contribution of Volmer-Heyrovsky and Volmer-Tafel mechanism towards the total catalytic activity has been investigated under the influence of applied potential and electrolyte pH values. The question was if one of the mechanisms becomes dominating and rate determining at certain conditions.

2 Theory

This chapter gives an overview of electrocatalysis in a historic context. Then some additional fundamentals, which will be elaborated in later chapters are briefly discussed, before the focus is put on the electrolysis of water. Derivations of fundamental equations are not shown but can be found in standard electrochemistry books.

2.1 Electrocatalysis

By definition, a catalyst is a substance, that accelerates a reaction but remains unchanged after the reaction. This was reported already in 1836 by J. J. Berzelius who was one of the first scientists addressing the topic of catalysis.⁹⁷ F.W. Ostwald further specified that catalysts change the rate but not the thermodynamic equilibrium of a chemical reaction.⁹⁸ Three properties are of paramount importance for catalysts: activity, selectivity and stability. The activity is often measured as the turnover frequency, which describes the number of catalytic cycles per time and per active site. The catalyst selectivity, the property of directing a reaction towards a specific product, is also crucial, as the amount of produced undesired side products can be reduced. The catalyst stability is obviously also essential; as fast deactivation or other degradation of the catalyst can make its use impractical.

The field of catalysis can be divided into the so-called homogeneous catalysis, where the catalyst and reactants exist in the same aggregate state, and the heterogeneous catalysis, where they have different states.⁹⁹ Electrocatalysis, is a sub-field of heterogeneous catalysis and involves an electron transfer between the catalyst and the reactants. *Via* the so-called electrode potential, the reaction itself and the reaction path can be influenced.¹⁰⁰ Importantly, electrocatalysis requires adsorption of reactants at the catalyst surface.

Sabatier described in 1902 that the catalytic surface should bind atoms and molecules neither too strong, nor too weak.¹⁰¹ A certain binding strength is required that the reactants get adsorbed and activated. If, however, the binding is too strong, the surface gets blocked for a long time as the desorption of products is hindered.

This Sabatier Principle is one basic trait of heterogeneous catalysis, but it gives only a qualitative idea and does neither suggest ideal binding energy, nor does it allow speculation about maximum activity.¹⁰² Further, the question arose, where on the surface the reaction actually takes place. In 1922, Langmuir claimed that adsorption energies can vary for different surface sites, which are not homogeneously distributed at the atomic level. The idea of active sites was further shaped by Taylor, who observed in 1925 that surface sites can have different catalytic activity.¹⁰³ These specific surface sites are available for adsorption and largely contribute to the catalytic activity. Active sites depend on the chemical reaction and can be a single atom or consist of several atoms or a structural motive. One can distinguish between two groups of reactions: (i) structure-sensitive and (ii) structure-insensitive. The former requires specific sites, where the reaction takes place, which suggests a relatively strong interaction between the reactants and the surface. The latter show typically rather weak interactions of reactants with the surface and appear to be independent of such structural motives.

An important step for fundamental understanding of catalytic activity was made by A. A. Balandin, when he introduced so-called volcano plots in 1969¹⁰⁴. They correlate the activity of a catalyst to a so-called “descriptor”, which is typically the heat of adsorption of reaction intermediates or a related property¹⁰⁵. The applicability of volcano plots for the purpose of electrocatalysis was proven three years later by S. Trasatti¹⁰⁶. As can be seen in **Figure 2.1** the activities of several different electrocatalysts are compared and the volcano shape trend is eponymous for this representation. This concept allows to evaluate whether a catalyst’s binding strength is too strong or too weak. For instance, it can be seen that Pt is almost at the tip of the volcano for the HER, but its binding energy is slightly too strong. This can have some predictive power, *e.g.* for the development of novel catalysts. In case of a single adsorbed intermediate, the binding energy for this intermediate can be relatively easily optimized. However, typical reactions involve several adsorbed species and an optimal catalyst should have ideal binding energies for each intermediate. Though, these binding

energies often scale with each other, making their independent optimization very difficult.¹⁰⁷ These so-called scaling relations can be represented as¹⁰⁸:

$$\Delta E_1 = \gamma \Delta E_2 + \xi \quad (2.1)$$

Where ΔE_1 and ΔE_2 are the adsorption energies of both species, while γ and ξ are constants depending on the nature of the adsorbate and the surface facet.

Nowadays, the Sabatier principle and the volcano plots are indispensable for developing optimized electrocatalysts. Thanks to increasing computational power, more complex calculations based on density function theory allow to derive binding energies for various catalysts and surface sites.¹⁰⁹ To date, even several attempts were successful to break the scaling relations.^{110,111,112,113,114}

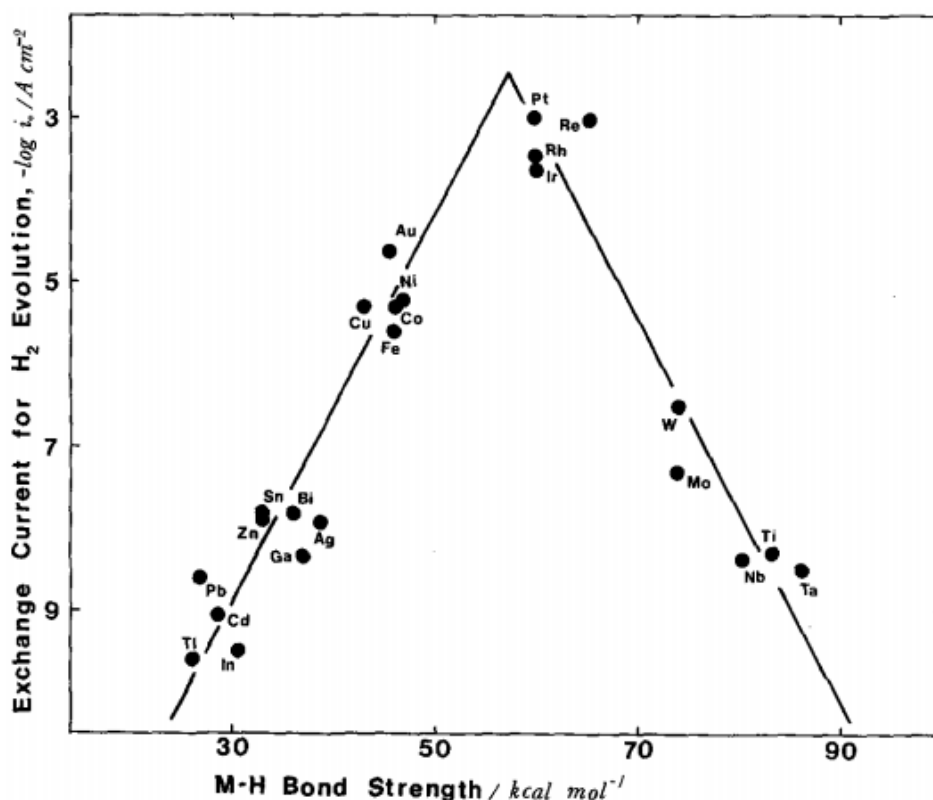


Figure 2.1. Exemplary volcano plot for the hydrogen evolution reaction. S. Trasatti related the measured exchange current densities of different electrocatalysts to their hydrogen adsorption strength. As can be seen, the activity shows a linear dependence on the binding energy. Adapted from reference [106] with permission. Copyright © 1972 Published by Elsevier B.V.

2.2 Reaction kinetics

Faradaic processes are considered as electrochemical reactions, where charge is transferred across an electrified interface. In the simplest case, just one electron is transferred in one step¹¹⁵.



The forward and backward reaction rate between the oxidized O and reduced species R are described *via* the rate constants k_f and k_b , respectively. Arrhenius showed that these rate constants are dependent on the temperature T , the gas constant R , the activation energy ΔG^\ddagger , and the preexponential factor A' , which is normally a constant¹¹⁵.

$$k = A' \exp\left[-\Delta G^\ddagger/RT\right] \quad (2.3)$$

Considering the influence of a potential on the standard free energy of activation, and assuming parabolic shaped profiles of free energy, the so-called Butler-Volmer reaction can be derived¹¹⁵:

$$j = Fk_0 \left[c_O^*(0, t) e^{\alpha z F (E - E^0)/RT} - c_R^*(0, t) e^{(1-\alpha) z F (E - E^0)/RT} \right] \quad (2.4)$$

Here, k_0 is the standard rate constant, $c_{O,R}^*$ are the concentrations of oxidized and reduced species at the electrode, α is a symmetry factor, z is the amount of electrons transferred through the interface, and E^0 is the equilibrium potential.

With the definition of the overpotential $\eta = E - E^0$ and by introducing the exchange current density j_0

$$j_0 = Fk_0 c_O^{*1-\alpha} c_R^{*\alpha}, \quad (2.5)$$

the Butler-Volmer equation condenses to¹¹⁵:

$$j = j_0 \left(e^{\frac{\alpha z F \eta}{RT}} - e^{-\frac{(1-\alpha) z F \eta}{RT}} \right) \quad (2.6)$$

This dependence is sketched in **Figure 2.2 (A)**. This equation further simplifies for large overpotentials to the so-called Tafel equation¹¹⁵:

$$\eta = \frac{RT}{\alpha z F} \ln \left(\frac{j}{j_0} \right) \quad (2.7)$$

Noteworthy, although this describes the reaction kinetics, the overall reaction rate is typically limited by mass transport and resistances, especially at larger overpotentials. In a Tafel plot, the overpotential is plotted versus the logarithm of the current (density) as displayed in **Figure 2.2 (B)**.

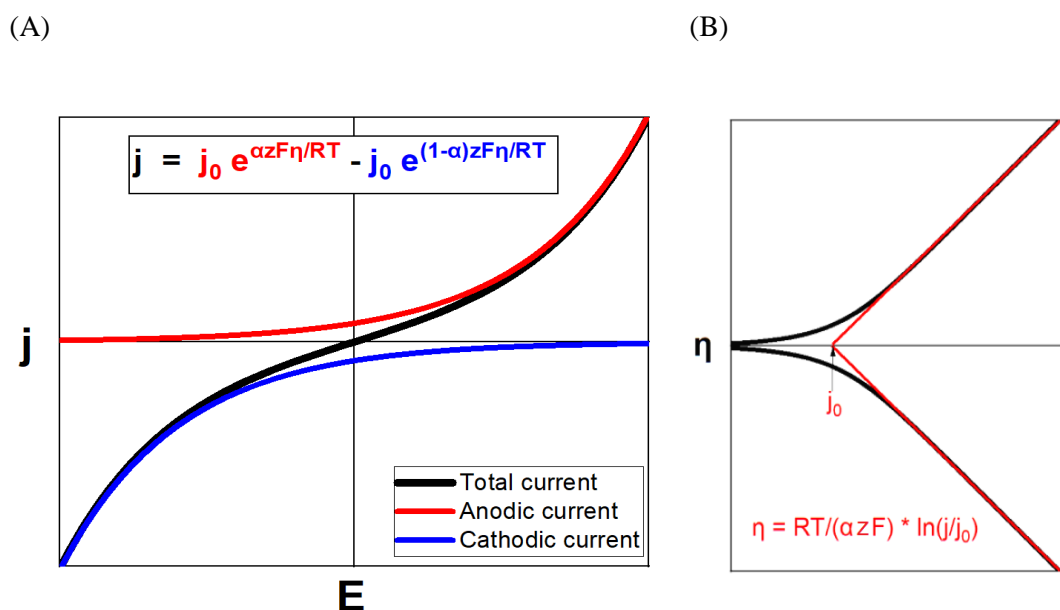


Figure 2.2. Reaction kinetics. (A) The kinetic current (—) as predicted by the Butler-Volmer equation is the sum of the anodic (—) and cathodic (—) current. At high overpotentials, the current can be approximated by just the anodic/cathodic current resulting in the Tafel equation. (B) Approximation of the kinetic current (—) from the Tafel equation (—).

2.3 Nernst equation

The Nernst equation describes the (reduction) potential of an electrode as a function of the activities of the reacting species, which are being oxidized/reduced during electrochemical reactions¹¹⁵.

$$E_{red} = E_{red}^0 - \frac{RT}{zF} \ln \prod_i a_i v^i \quad (2.8)$$

Here, E_{red}^0 is the standard reduction potential, R - the gas constant, T - the temperature in Kelvin, z is the number of transferred electrons, F is the Faraday constant, a_i is the activity and v^i - the stoichiometric coefficient of species i . Noteworthy, v^i is negative for reactants and positive for products. The activities are dependent on the concentrations c_i and partial pressures p_i ¹¹⁵:

$$a_i = \gamma_i \frac{p_i}{p_0} \quad (2.9)$$

$$a_i = \gamma_i \frac{c_i}{c_0} \quad (2.10)$$

Here $p_0 = 1$ bar, $c_0 = 1$ M, and γ is typically 1 for relative diluted electrolytes. Thus, the activity can often simply be replaced by the concentrations.

The Nernst equation originates from thermodynamics and can be derived considering the change of Gibbs energy due to the transfer of electrons and the change of entropy. Though, this potential (E_{red}) also corresponds to the potential, where the net reaction rate of the redox reaction according to Butler-Volmer equation is $j = 0$.

2.4 Water electrolysis

The electrolysis of water is already known since the first documented discovery by the English scientists William Nicholson and Anthony Carlisle in 1800¹¹⁶. In the same year the German scientist Johann Wilhelm Ritter developed the first water electrolyzer that was able to collect and measure the so produced oxygen and hydrogen¹¹⁷, as shown in the **Figure 2.3**. With the first direct current electrical generator by Antonio Pacinotti in 1860 and the Gramme Machine, the electrolysis of water became nearer to a practical realization^{118,119}. In 1939, the first large scale electrolyzer with 10,000 m³ (H₂) / h was finally built.¹²⁰

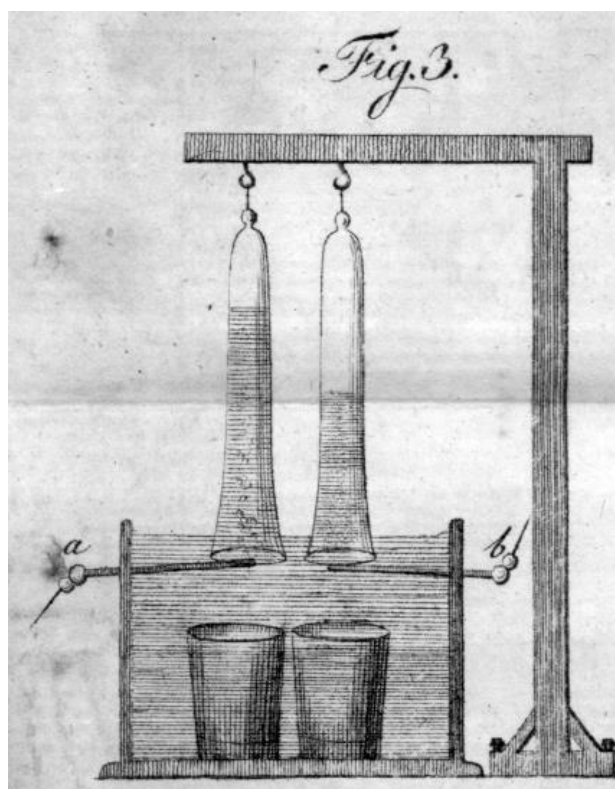
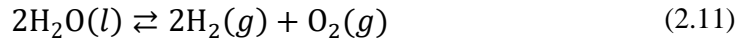


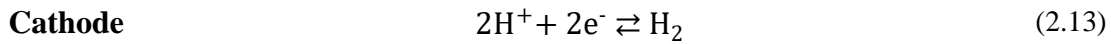
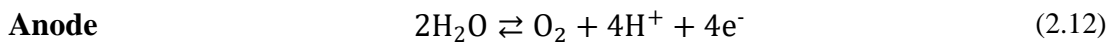
Figure 2.3. Schematic of the electrolyzer developed by Johann Wilhelm Ritter. The gases, oxygen and hydrogen produced at anode (left) and cathode (right), respectively, are collected in two separate vessels. Adapted from ref [117] (open access, CCO)

The overall water splitting reaction is as follows¹¹⁵:

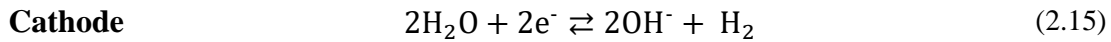
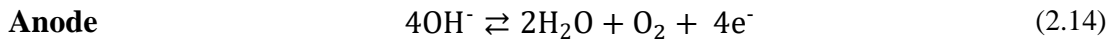


Hereby, the oxygen evolution reaction (OER) and the hydrogen evolution reaction (HER) take place simultaneously at the anode and the cathode, respectively. The half-cell reactions depend on the electrolyte¹¹⁵.

In acidic media:



In alkaline media:



Generally, the OER has slower kinetics compared to HER resulting in higher overpotentials on the anode side. The equilibrium cell voltage for water electrolysis is ~1.23 V at 25 °C, however, in practice, significantly higher voltages are typically required, especially due to the OER kinetics.

Today, there are various types of water electrolyzers. The focus of the discussion will be first on the commonly used polymer electrolyte membrane (PEM) electrolyzers describing their basic principle and properties. Afterwards, other types of electrolyzers are compared.

2.5 The PEM electrolyzer

PEM electrolyzers are typically operated at a temperature of 50-80°C, pressures below 30 bar and a cell voltage between 1.75 V and 2.2 V. They reach current densities from 0.6 A cm⁻² up to 2 A cm⁻² and a voltage efficiency of 57% to 70%.¹²¹ Notably, efforts are being made to increase the pressure of the produced hydrogen up to 200 bar, so that no further external compressor is required¹²².

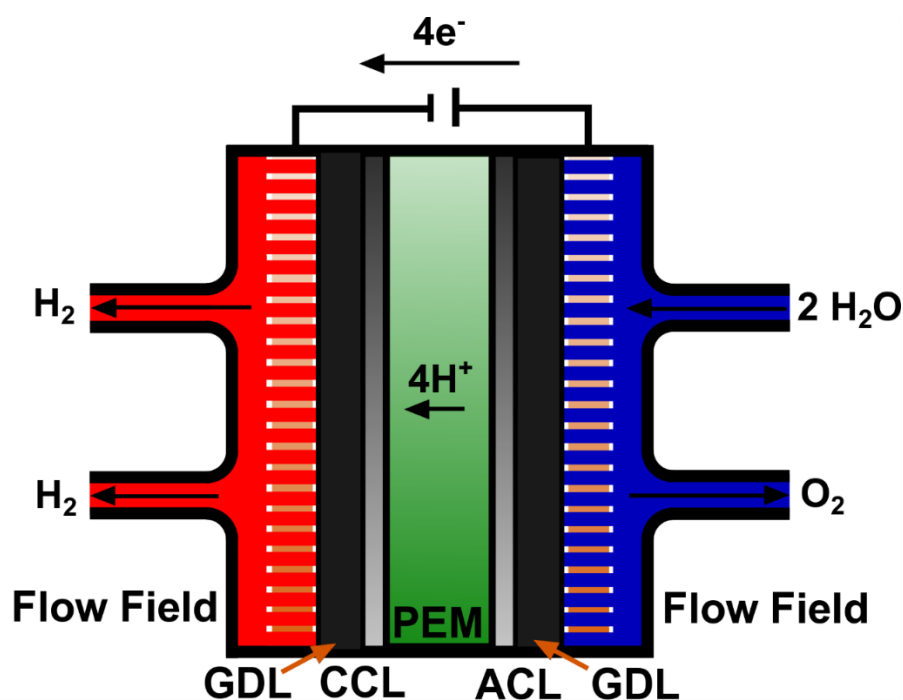


Figure 2.4. Sketch of a PEM electrolyzer. The core part of an acidic PEM electrolyzer is its name-giving polymer membrane, which is proton conducting. The membrane is in contact with the CCL and ACL, which catalyze the HER and OER, respectively. This is sandwiched between GDLs and flow field plates to ensure electrical contact, water supply from the anode side, as well as collection and removal of reaction products.

A schematic view of a PEM membrane electrode assembly (MEA) is shown in **Figure 2.4**. The core element of a PEM electrolyzer is a proton conducting membrane (*e.g.* Nafion) acting as the electrolyte and inhibiting crossover of the gaseous reaction product towards the opposite electrode. This membrane is coated on both sides by a catalyst layer. The cathode catalyst layer (CCL) typically consists of platinum nanoparticles supported by larger carbon nanoparticles. For the anode catalyst layer (ACL), iridium oxide particles are used either unsupported or supported on titanium oxide. Carbon is not suitable due to its

relatively quick corrosion, which would significantly increase the degradation rate of the ACL. To effectively remove the gases produced at the catalyst layers and ensure electrical contact, the so-called gas diffusion layer (GDL) is utilized. The GDLs on the cathode typically consist of a carbon sheet or mesh, which is treated with a hydrophobic coating (e.g. Polytetrafluoroethylene PTFE) to hinder the blockage of the pores of the GDL with water. For the same reason as for the ACL, the anode GDL often consists of a sintered titanium body or titanium mesh instead of a carbon sheet to hinder the corrosion. In contrast to the cathode GDL, the anode GDL has also the function to enable water transport towards the ACL, where it is consumed. The transfer of water prohibits a high degree of hydrophobic coating. The flow field plates consist of titanium, often additionally coated with Au or Pt. They collect the gasses and enable electrical contact to the GDL.^{123,124,125,126,127,128}

The current-voltage characteristic curves (I-V curves) of different state-of-the-art PEM electrolyzers are compared in **Figure 2.5**. Note, that some of these results were only achieved under laboratory conditions, and that these products are not commercially available yet.

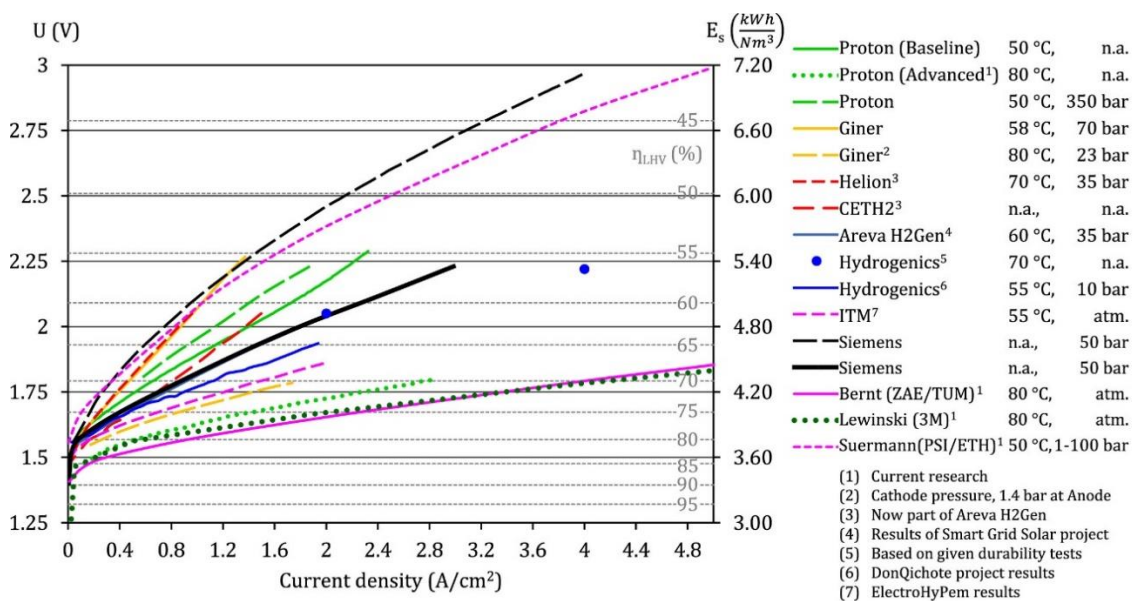


Figure 2.5. Comparison of I-V curves of state-of-the-art PEM electrolyzers. The approximated electrical efficiencies are additionally displayed, although the energy for compression was neglected. Adapted with permission from ref. [129]. Copyright © 2017 Elsevier Ltd. All rights reserved.

2.6 Alkaline water electrolysis

Alkaline water electrolyzers utilize an alkaline electrolyte, usually concentrated aqueous KOH solutions. The operation range is well comparable with the one in acidic PEM electrolyzers. The cell temperature is between 60 and 80°C and the stack pressure is also typically below 30 bar. However, the cell voltages are slightly higher (from 1.8 V to 2.4 V) leading to a lower efficiency of 52% to 60% at current densities of just 0.2 A cm⁻² to 0.4 A cm⁻². Nevertheless, these devices do not necessarily need platinum group metals (PGMs) and can utilize more abundant catalysts, such as nickel-based materials. Furthermore, the lifetime of these electrolyzers is usually higher, as the electrolyte can simply be exchanged.^{130,131,132}

Figure 2.6 compares state-of-the-art alkaline electrolyzers. As can be seen, the biggest difference compared to PEM electrolyzers is the significantly lower current density.

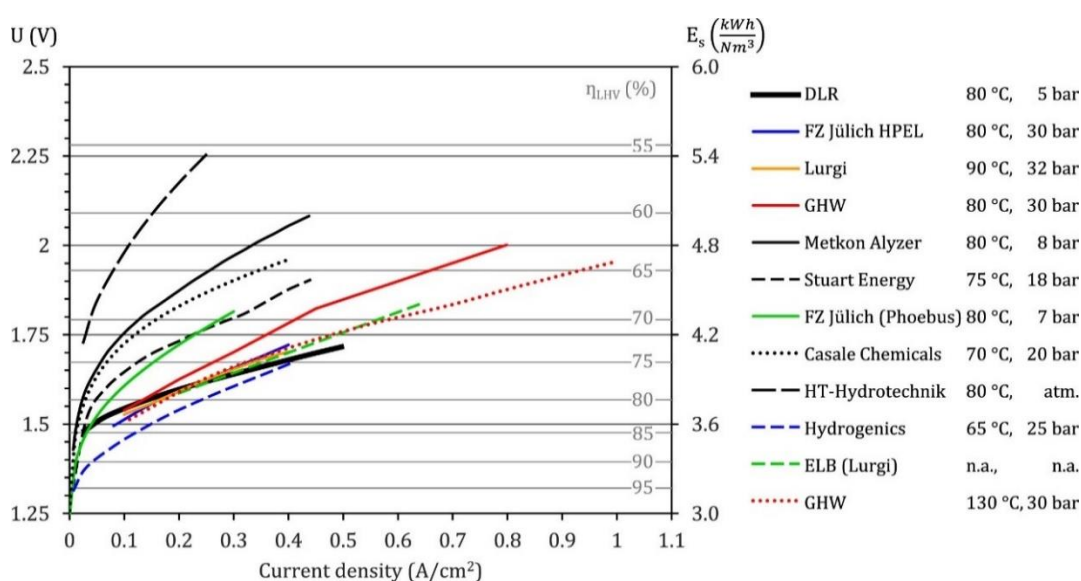


Figure 2.6. Comparison of I-V curves of some state-of-the-art alkaline electrolyzers. The approximated electrical efficiencies are additionally displayed; however, the energy for compression was neglected. Adapted with permission from ref. [129]. Copyright © 2017 Elsevier Ltd. All rights reserved.

Remarkably, the state-of-the-art research succeeded on the development of highly conductive anion exchange membranes AEM, allowing to combine the advantages of both, the acidic PEM electrolyzer and the flexibility of the choice of catalyst. This enables a compact cell design.^{131,133}

2.7 High temperature electrolysis

The splitting of water is thermodynamically more favorable at high temperatures and would happen spontaneously at 2500 °C. However, such temperatures are not very practical. High temperature electrolysis (HTE) typically utilizes a solid O²⁻ conducting electrolyte, *e.g.* yttrium stabilized zirconia and operates at temperatures between 100 °C and 900 °C. The main advantage is that the reaction is partially driven by heat, and less electrical energy is required. As can be seen in **Figure 2.7** it allows the electric efficiencies well above 100%. This is, however, only reasonable if the heat energy is very cheap, like exhausts from gas power plants. Though, an electrolyzer powered by renewables, which is itself dependent on exhaust heat produced by a gas power plant next by, might not be the most reasonable solution, as the gas could be directly steam reformed into hydrogen with higher efficiency. Of course, in other scenarios, such as in combination with concentrated solar thermal systems, a meaningful application can be conceivable. Moreover, at the price of efficiency, HTEs can be also operated in exothermic conditions, where no external heating is required.^{134,135,136}

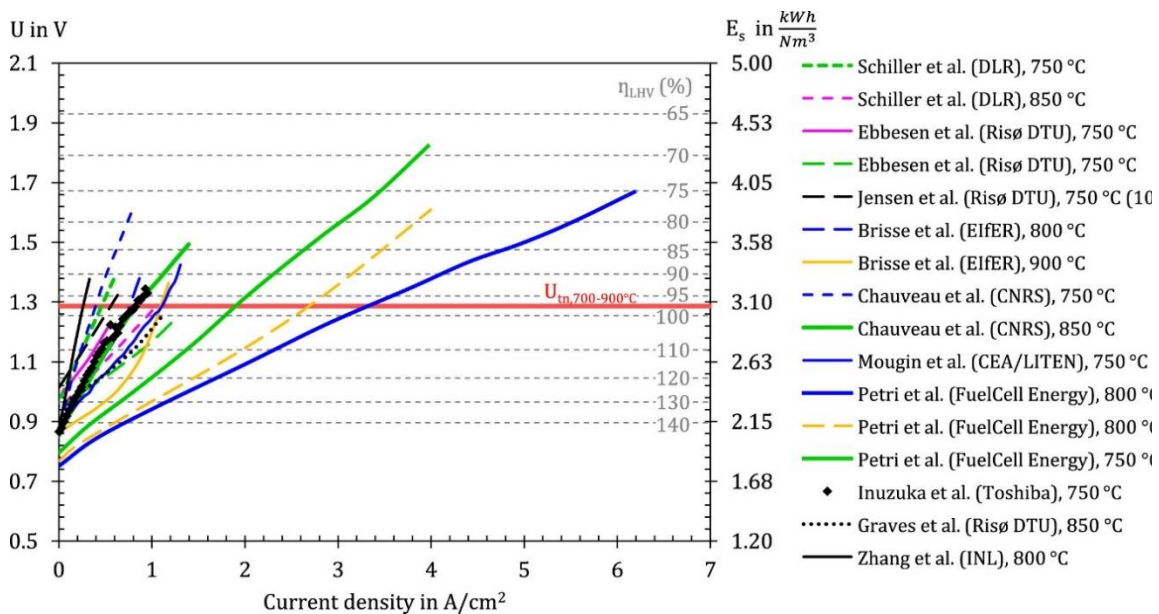


Figure 2.7. Comparison of I-V curves of state-of-the-art high temperature electrolyzers. The approximated electrical efficiencies are additionally displayed. Adapted with permission from ref. [129]. Copyright © 2017 Elsevier Ltd. All rights reserved.

3 Experimental part

3.1 Experimental setup

Prior to experiments, all glassware was cleaned using peroxymonosulfuric acid, which was freshly prepared by mixing H_2SO_4 , and H_2O_2 , in a ratio of 2:1. After rinsing with ultrapure water, the glassware was boiled with ultrapure water to remove any contaminants, filled up with water and sealed using Parafilm until usage. The electrochemical experiments were performed using a 3-electrode configuration. All electrochemical potentials in this work are referred to reversible hydrogen electrode RHE scale, but in practice silver/silver chloride SSC (Schott, Germany), mercury/mercury sulfate MMS (Schott, Germany) and a HydroFlex (Gaskatel, Germany) were utilized as reference electrodes. A platinum wire/mesh (Goodfellow, Germany) served as counter electrode while various disk electrodes and microelectrodes were applied as working electrode. For all experiments, the same type of glass cell was utilized, which allowed for temperature control using a thermostat. The potentials were controlled using a VSP-300 potentiostat (Biologic, France) and an Autolab PGSTAT302N potentiostat (Metrohm, France). In the following section, the different cell configurations and their (dis)advantages will be explained in more detail.

3.1.1 Rotating (ring) disk electrode

A rotating disk electrode (RDE) typically consists of a flat disk-shaped electrode, which is electrically connected from the back side while the front side is immersed into the electrolyte of the electrochemical cell. The sides of these electrodes are often coated with an inert non-conducting material, such as Teflon or PEEK, to define the surface exposed to the electrolyte. During electrochemical measurements, this electrode is rotated with a constant rotation speed to establish a forced convection flow of electrolyte. As depicted by **Figure 3.1**, the electrolyte close to the electrode is accelerated in rotation direction of the electrode and, due to centrifugal force, away from the center of the electrode.

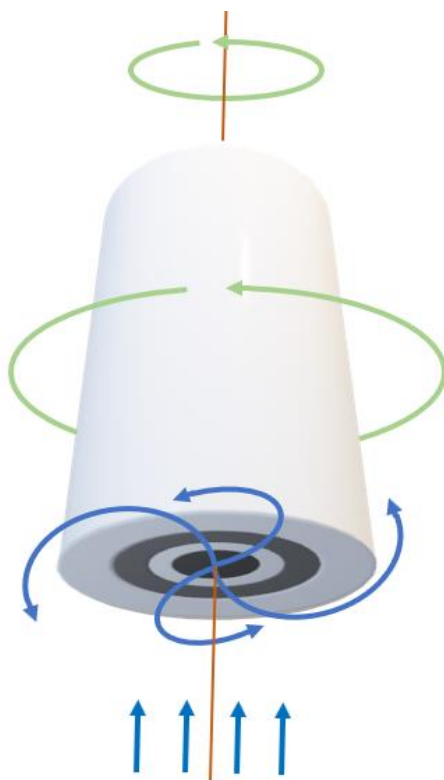


Figure 3.1. Sketch of an R(R)DE electrode. The disk and ring are contacted separately, and their potentials/currents can be controlled and measured independently. The green arrows show the rotation direction and the blue arrows indicate the flow direction of the electrolyte.

According to Bernoulli's principle, this decreases the local pressure close to the electrode resulting in a suction effect and a steady stream of electrolyte towards the disk as long as the electrode is rotated with a constant speed.

The maximum current density, denoted as limiting current density j_{lim} [A cm⁻²] of a reaction, assuming that all species approaching the disk react and each exchanges n electrons, can be calculated by the Levich-equation¹¹⁵:

$$j_{lim} = 0.201 n F D^{2/3} \nu^{-1/6} \omega^{1/2} c_0 \quad (3.1)$$

Here, F is the Faraday constant, D - the diffusion coefficient [cm² s⁻¹], ν - the kinetic viscosity [cm² s⁻¹], ω is the frequency in revolutions per minute [rpm], and c_0 [mol cm⁻³] is the concentration of the species. Due to the enhanced and well-controllable mass transport properties compared to a motionless electrode, this technique is typically preferred for the benchmarking of electrocatalysts for the reactions like the ORR, OER, and HOR. As one can see from the Levich equation, another advantage of the RDE is that j_{lim} is independent of the diameter of the electrode, which implies that also the mass flux is homogeneous towards the electrode, which is not necessarily the case if no rotation is applied. This method, of course, has also its limitations. If the electrode is not perfectly balanced, the holder and the electrode start to vibrate heavily at higher rotational speeds, which can introduce noise to the measurement. Moreover, manufacturers of the electrode tips usually advise not to exceed 4000 rpm as this could cause damages. Therefore, the maximum achievable limiting current is ultimately confined by the rotation speed. Another drawback for the gas evolving reactions is that at higher current densities ~ 10 mA cm⁻² the electrode usually tends to get partially blocked by bubbles from evolving gasses making accurate electrochemical measurements impossible.

Noteworthy, there is a modification of the RDE, which includes a separate ring around the disk which typically consist of Pt. The potential and the current of this ring can be adjusted and measured independently. This so-called rotating ring disk electrode (RRDE) configuration can be utilized to investigate the reaction products from the disk. These products flow towards the ring, where they can get oxidized or reduced depending on the applied potential, which results in a measurable current for the ring.

For this work, the RDE technique was used for calibrating the method to determine the ECSA of oxide materials. In this case, the applied currents were relatively small, and the highest priority was to create homogeneous catalyst films with a well measurable surface

area. Moreover, an RRDE was utilized to determine the onset of the OER of a novel catalyst.

Figure 3.2 displays the cell configuration used for R(R)DE: The disk-shaped working electrode is placed in the center of the electrochemical cell and mounted onto a rotator (Pine, USA), which rotates the electrode. For this study, in most cases, a polycrystalline Pt disk (Mateck, Germany) was utilized as a substrate to grow catalyst films on; but also glassy carbon (homemade at LEPMI, France) and iridium (111) single crystal disks (Mateck, Germany) have been utilized as substrate. Counter and reference electrodes are as stated in **Chapter 3.1**.

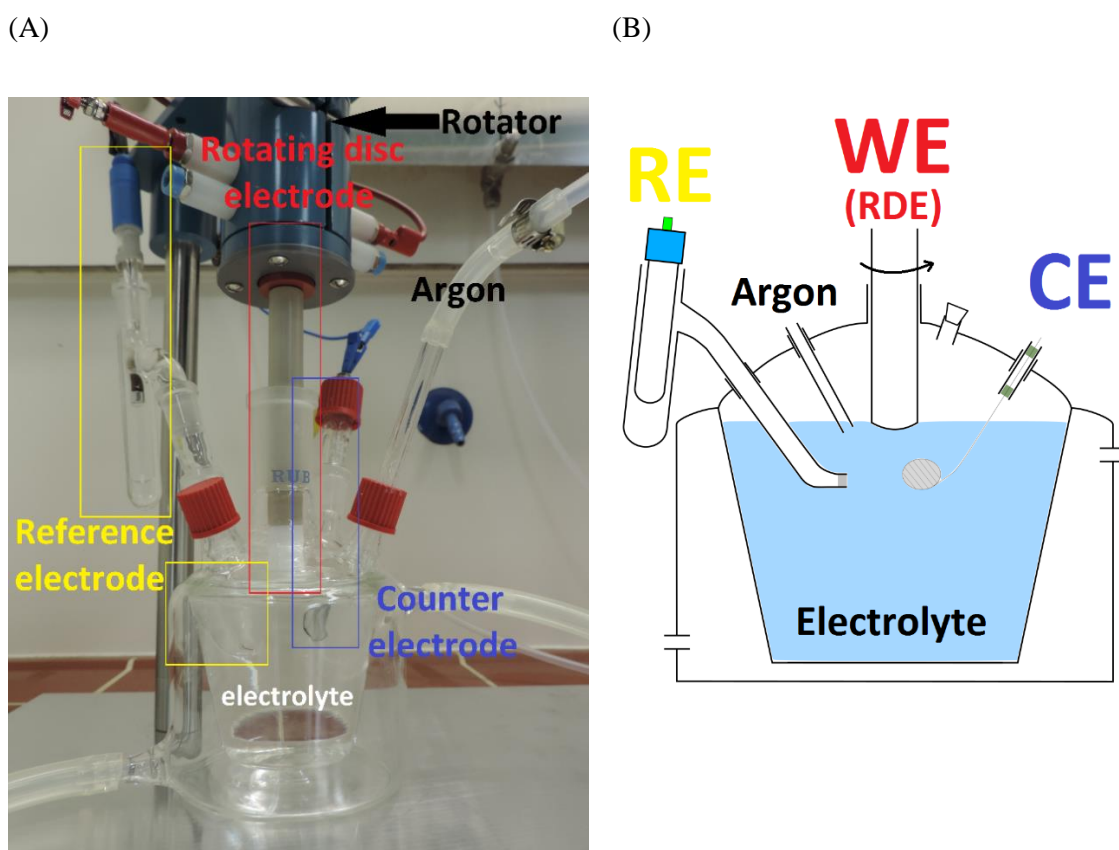


Figure 3.2. Photography (A) and schematic (B) of the R(R)DE cell configuration. A double-walled glass cell was used. The mantle allows temperature control. The reference electrode (RE) is connected to the main cell *via* a Luggin-capillary, while the counter electrode (CE) is directly immersed into the electrolyte. (B) Adapted with permission from ref [90].

3.1.2 Microelectrodes

Microelectrodes have tips at a micrometer scale. The focus in the following section will be set on disk shaped electrodes. These electrodes typically consist of a wire with a small diameter that is embedded into an inert and insulating material such as glass. The tip is usually polished until the wire is exposed and exhibits a flat surface.

There are several advantages of microelectrodes. Due to their relatively small dimensions, the electrolyte shows an almost spherical diffusion profile already close to the electrode associated with greatly enhanced mass transport. The time dependent j_{lim} can be approximated by a spherical diffusion profile, as follows¹¹⁵.

$$j_{lim} = n F D c_0 \left(\frac{1}{(\pi D t)^{1/2}} + \frac{1}{r} \right) \quad (3.2)$$

Here t is the time since applying the current, while only diffusion is the driving force and r is the radius of the microelectrode. Obviously, if no perturbation is applied, the limiting current correlates inversely to r . If, however, an additional forced convection is applied, j_{lim} could be further increased. This could be achieved by *e.g.* rotating the electrode or intermixing the electrolyte by purging continuously.

Another important aspect is the ohmic drop caused by the electrolyte. Assuming the simplified case that the cell is very large in comparison to the dimension of the (disk shaped) working electrode and a remote CE and RE, the ohmic (uncompensated) resistance R_U can be approximated by¹³⁷:

$$R_U = \frac{1}{4r\kappa}, \quad (3.3)$$

where κ is the conductivity of the electrolyte. The voltage drop for a certain current density j can then be derived:

$$\Delta E_U = \frac{1}{4r\kappa} \cdot jr^2\pi = r \cdot \frac{j \cdot \pi}{4 \cdot \kappa} \quad (3.4)$$

The voltage drop correlates linearly with the applied current density and the radius of the electrode, which reveals another advantage of the microelectrode: the ohmic drop compensation, which is not always very accurate, can become unnecessary because ΔE_U is often negligible *e.g.* a microelectrode with $r_{micro} = 12.5 \mu\text{m}$ has a 200 fold smaller ohmic drop compared to the commonly used disk electrode with $r_{disk} = 2.5 \text{ mm}$.

Additionally, for gas evolving reactions, the formation of gas bubbles at the electrode is often a disturbing factor. When these bubbles are attached to the electrode, they can block certain parts of the catalyst and decrease its ECSA. Even if they can be removed *e.g.* by rotation of the electrode, this temporal blockage introduces noise and complicates accurate measurements. Further, gas bubbles in the electrolyte increase the resistance of the electrolyte according to Bruggeman equation¹³⁸:

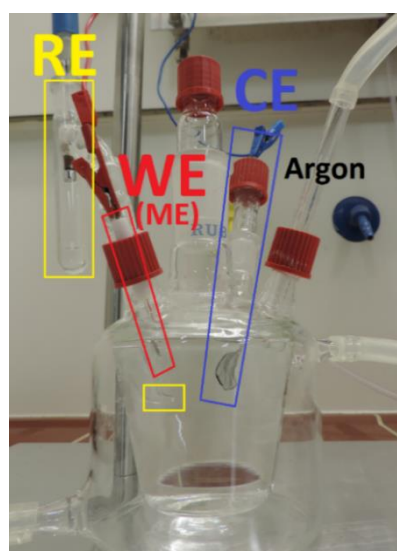
$$R_b = R_e(1 - \varepsilon)^{-3/2}, \quad (3.5)$$

where R_b is the resistance with bubbles, R_e is the resistance without bubbles and ε the fraction of gas. It is therefore desirable to avoid the formation of gas bubbles. This is the reason why catalysts for *e.g.* the OER are often compared at current densities of 10 mA cm^{-2} or less. The reaction products are initially dissolved in the electrolyte. If, however, the production rate is faster than the mass transport of the dissolved gas, then the concentration increases in the vicinity of the electrode. At a certain degree of oversaturation, the dissolved products randomly form very small gas bubbles. Depending on their size, these nuclei are often unstable and might collapse due to their high surface energy (per volume), which makes them energetically unfavorable. Exceeding a certain size, so-called critical radius calculated by Ward et al¹³⁹ in 1970, the probability that these nuclei grow and form larger bubbles increases. Under ideal conditions a local oversaturation up to a factor of ~ 100 can be reached until bubbles are formed. However, due to surface defects on the electrode such as pits and scratches¹⁴⁰, which act as nucleation centers, such high oversaturation is hardly achieved.^{141, 142, 143} A motivation to utilize a microelectrode was to suppress the formation of such gas bubbles. These oxygen/hydrogen bubbles are limited by the radius of the electrode, as the degree of oversaturation drops significantly around the active disk. This allows to achieve a higher level of oversaturation before energetically stable bubbles can form. The relatively quick mass transport decreases the concentration of reaction products

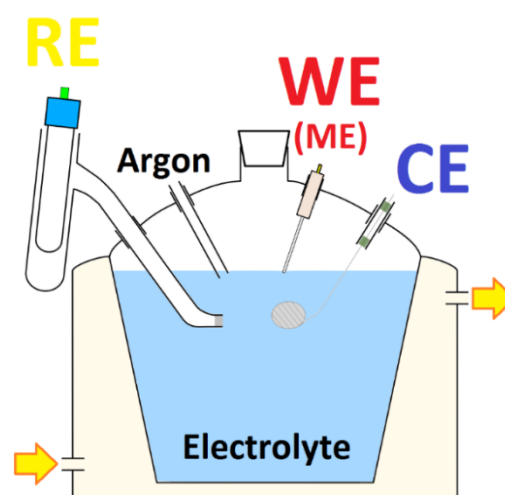
(dissolved oxygen/hydrogen) and impedes the formation of gas bubbles, which allows to perform electrochemical measurements at higher current densities.

However, there are also certain limitations. These microelectrodes tend to be very fragile, especially when tips for scanning electrochemical microscopy are used. Moreover, due to the size of the microelectrode and its bulky glass holder, it was not possible to put it into certain devices for characterization such as XPS and AFM. Therefore, they were not suitable for all parts of this work.

(A)



(B)



(C)

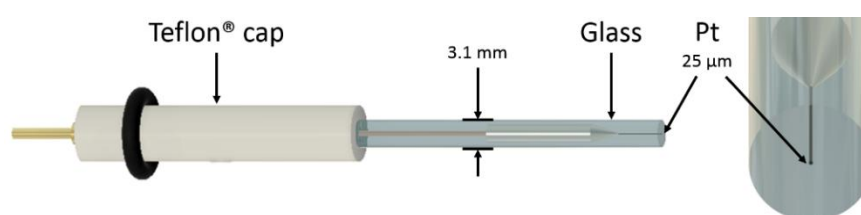


Figure 3.3. Experimental setup for the measurements using microelectrodes. (A) Picture of the electrochemical cell. (B) Sketch of the electrochemical cell. The electrochemical cell is the same double walled cell, as used for measurements in the R(R)DE configuration, however, the RDE is replaced with a microelectrode. (C) Sketch of the microelectrode. It consists of a Pt wire, which is insulated and mechanically stabilized by glass. The microelectrode possesses an additional Teflon® cap which prevents agglutination with the glass of the electrochemical cell. This electrode was mounted into the cell, which was sealed using a sealing ring. Adapted with permission from ref. [144].

The setup for electrochemical measurements using a microelectrode and a scheme of the microelectrode is shown in **Figure 3.3**. The microelectrode was inserted into the double-walled cell (described in the general section) and the tip was immersed into the electrolyte. Note that different types of microelectrodes have been tested and **Figure 3.3 (C)** shows the most suitable microelectrode (Ch. Instruments, USA). In comparison to microelectrodes produced for scanning electrochemical microscopes, it is relatively sturdy, as the Pt wire is embedded in a thick (3.1 mm) glass rod and its tip could even be re-polished. During the experiments the electrolyte was heavily purged to ensure a constant gas saturation of the bulk electrolyte and to introduce additional convection which increases the mass transfer according to **Equation 3.2**.

3.1.3 Electrode preparation

Electrode cleaning

A prerequisite for preparing homogeneous catalyst films is, that the substrate itself is clean and not covered by residual films from subsequent experiments or other contaminations. Therefore, the electrodes/substrates were always electrochemically and/or mechanically cleaned.

Mechanical cleaning:

The electrodes were initially washed with ultrapure water (18.2 M Ω cm) to remove residues from electrolyte and unstable and soluble contaminants. Electrodes coated with catalyst inks were afterwards cleaned by washing them with ethanol and then wiped with a disposable tissue (Kimberley-Clark, Germany).

Glassy carbon electrodes (Pine, USA) were always polished subsequently three times, using aluminum oxide slurry (Buehler, Germany) with particle diameters of 3 μ m, 1 μ m, and 0.05 μ m. As the slurry was water based, rinsing with water and wiping again with the tissue was sufficient to remove it from the electrode.

Electrochemical cleaning:

After mechanical cleaning, the electrodes were electrochemically cleaned. The electrode was mounted into an electrochemical cell filled with acidic electrolyteⁱ. Cyclic voltammetry (scan rate: 100 mV s⁻¹ or 50 mV s⁻¹) was then applied to polarize the electrode alternatingly cathodically and anodically. The potential window and number of cycles were adjusted to the sturdiness of the residual catalyst films. For instance, NiFeO_x films were more difficult to remove and several hundred cleaning cycles were required.

Oxy-hydroxide films

In principle, there are many methods to create thin films such as electrochemical vapor deposition, epitaxial growth or pulsed laser beam deposition on the substrate. For this work electrochemical deposition were selected and protocols known to create non-porous thin films were chosen and further optimized for our requirements.

Depending on the requirements of the electrode for subsequent measurements, a Pt(pc) disk (Mateck, Germany, d = 5 mm), a Pt(pc) microelectrode (Ch. Instruments, USA, d = 25 μm) and quasi-Au(111) (Arrandee, Germany) were selected as substrates for the oxy-hydroxide films.

Thin films of NiO_x and CoO_x were formed *via* anodic deposition and potential cycling, as described in detail by Tench and Warren.¹⁴⁵ A cathodic deposition technique, which was adapted from McCrory et al.⁹² was applied to form NiCoO_x, NiFeO_x, and CoFeO_x films (**Table 3.1**). However, due to availability and safety concerns, NH₄ClO₄ was replaced by (NH₄)₂SO₄.ⁱⁱ

ⁱ Depending on availability, 1 M H₂SO₄, 0.1 M H₂SO₄, and 0.1 M HClO₄ were utilized

ⁱⁱ The successful deposition was verified by X-Ray Photon Spectroscopy.

Table 3.1 Solution composition and conditions for the metal oxy-hydroxide films deposition. Note that the specified rotation speeds were only applied to the macroscopic disk electrodes, but not to the microelectrodes. Adapted with permission from ref. [90].

Catalyst	Solution composition	pH	Deposition Condition
NiO_x	0.13 M NiSO ₄ · 6 H ₂ O 0.13 M NaOAc 0.10 M Na ₂ SO ₄	6.94	Anodic deposition, potential cycle between 0.97 and 1.83 V vs RHE at 50 mVs ⁻¹ , 400 rpm
CoO_x	0.10 M CoSO ₄ · 7 H ₂ O 0.10 M NaOAc 0.10 M Na ₂ SO ₄	7.43	Anodic deposition, potential cycle between 1.30 and 1.70 V vs RHE at 50 mVs ⁻¹ , 400 rpm
NiFeO_x	9.0 mM NiSO ₄ · 6 H ₂ O 9.0 mM FeSO ₄ · 7 H ₂ O 7.3 mM (NH ₄) ₂ SO ₄	2.32	Cathodic deposition, constant current of 50 mA cm ⁻² for 40 s, 1200 rpm
CoFeO_x	0.4 mM CoSO ₄ · 7 H ₂ O 0.36 mM FeSO ₄ · 7 H ₂ O 1.35 mM (NH ₄) ₂ SO ₄	5.4	Cathodic deposition, constant current of 125 mA cm ⁻² for 30 s, 1200 rpm
NiCoO_x	10 mM NiSO ₄ · 6 H ₂ O 10 mM CoSO ₄ · 7 H ₂ O 20 mM Na ₂ SO ₄ 20 mM H ₃ BO ₃	4.72	Cathodic deposition, constant current of 50 mA cm ⁻² for 180 s, 400 rpm
IrO_x	Ir (111) crystal 0.1 M HClO ₄	1.04	Potential cycling between 0.7 and 1.575 V vs RHE at 50 mV s ⁻¹ , 400 rpm
PtO_x	Pt (pc) crystal 0.1 M HClO ₄	1.04	Constant potential 1.1 V vs RHE, 400 rpm
PtNi “UPD”	Pt (pc) microelectrode 0.10 M H ₂ SO ₄ 2.5 mM NiSO ₄	0.70	Constant potential 0.051 V vs RHE (220 s)
PtNi “OPD”	Pt (pc) microelectrode 0.10 M H ₂ SO ₄ 2.5 mM NiSO ₄	0.70	Constant potential 0.051 V vs RHE (220 s) Followed by constant potential -0.031 vs RHE (25 s)

For the PtO_x and the IrO_x films, the surface of a Pt(pc) and an Ir(111) crystal were oxidized. For PtO_x this was achieved by holding the potential at 1.2 V *vs* RHE for 1 minute. The surface of the Ir(111) crystal was oxidized as described by Ganassin *et al.*⁹⁵. This was realized by the potential cycling (scan rate: 50 mV s⁻¹) in 0.1 M HClO₄ electrolyte within a potential window from 0.7 V to 1.575 V *vs* RHE until the CVs were stabilized.

For the sake of clarity, the (deposition) solution compositions and the deposition conditions are summarized in **Table 3.1**.

Nickel islands on Pt

Pt decorated with small Ni(OH)₂ islands is a promising catalyst for the HER¹⁴⁶ and one aim of this thesis was to investigate its performance at electrolyzer conditions. To prepare such an electrode, a Pt microelectrode was immersed into an electrolyte containing 0.1 M H₂SO₄ (96% Suprapure, Merck, Germany) and 2.5 mM NiSO₄ (Sigma-Aldrich, Germany). Nickel hydroxide was then underpotentially deposited^{147,148} by applying a potential of 0.051 V *vs* RHE. After 220 s the electrode was extracted (still under potential control) to achieve a partial Ni-coverage.

For a higher Ni-coverage, a similar procedure is used, however, after the underpotential deposition (UPD) the potential was decreased to -0.031 V *vs* RHE for 25 s before the electrode was pulled out. This second electrode should have a higher coverage of Ni. Details about this protocol can be found in **Table 3.1**.

Nanoparticles

Porous catalyst layers were required to validate the applicability of our new method to determine the ECSA of oxide materials (presented in **Chapter 4.1**). For this purpose, commercial catalysts were utilized to prepare an ink, which was then drop casted on an RDE tip and dried. For preparing the porous PtO_x/C catalyst layer an ink was mixed using 10 mg Pt/C (20 wt. %, Tanaka Kikinzo, Japan), 54 µl Nafion solution (5 wt. %, DuPont, USA), 1.446 ml isopropanol (96%, Sigma Aldrich, Germany) followed by applying ultrasonication (10 min, 35 kHz, 40 W) with 3.6 ml H₂O to disperse the catalyst homogeneously. The ink was then drop casted on a preheated (80 °C) glassy carbon RDE tip (d = 5 mm), which was rotated (100 rpm) to ensure a uniform coverage. A heat gun (PHG 600-3, Bosch, Germany) was utilized to dry the ink quickly. The surface of the Pt nanoparticles was subsequently oxidized in the electrochemical cell. The IrO_x/C layer was produced similarly, using 10 mg Ir/C (20 wt.%, Premetek, USA) of the catalyst instead of Pt/C. The catalyst was oxidized by potential cycling (similar to the oxidation of the Ir(111) crystal). **Table 3.2** summarizes the ink composition and the drop casting procedure.

Table 3.2. Ink composition and conditions for the metal oxy-hydroxide films deposition. Adapted with permission from ref. [90].

Catalyst	Ink composition	Deposition Condition
PtO _x /C	10 mg Pt/C (20 wt. %), 54 µl Nafion solution (5 wt. %), 1.446 ml isopropanol, 3.6 ml H ₂ O	10 µl of the ink drop-casted on a pre-heated (80°C) glassy carbon electrode (100 rpm)
IrO _x /C	10 mg Ir/C (20 wt. %), 54 µl Nafion solution (5 wt. %), 1.446 ml isopropanol, 3.6 ml H ₂ O	10 µl of the ink drop-casted on a pre-heated (80°C) glassy carbon electrode (100 rpm)

Preparation of surface-mounted metal organic frameworks (SURMOFs)

A Pt microelectrode, which served as a substrate, was pretreated by immersion into a 20 μM 16-mercaptohexadecanoic acid (MHDA) in ethanol/acetic acid (5%) for 24 h. After a washing step with ethanol/acetic acid (10%), the substrate was exposed to 2% triethylamine (Et_3N)/ethanol solution for 5 min. On the resulting self-assembled organic monolayers (SAMs), the catalyst films were grown. Therefore, the electrode was first immersed into a metal containing solution (0.5 mM NiCl_2 and 0.5 mM CoCl_2 in ethanol/water ($v/v = 17:1$)) for 10 min. Then, the unstable metal ions were removed through a washing step with ethanol (2 min). Afterwards, exposure to the linker solution (H_2BDC (0.2 mM) in 0.3 mL Et_3N) for 10 minutes, followed by a washing step to remove unstable linkers, forms a layer of organic linkers. This allows to deposit an additional layer of metal ions, as displayed in **Figure 3.4**. Each step is self-limiting, which enables a very defined layer-by-layer growth. To automatize the deposition procedure, a homebuilt automated pump system was applied. During the film growth, the temperature was set to 60 $^\circ\text{C}$. More experimental details can be found in the publication, attached to this work.

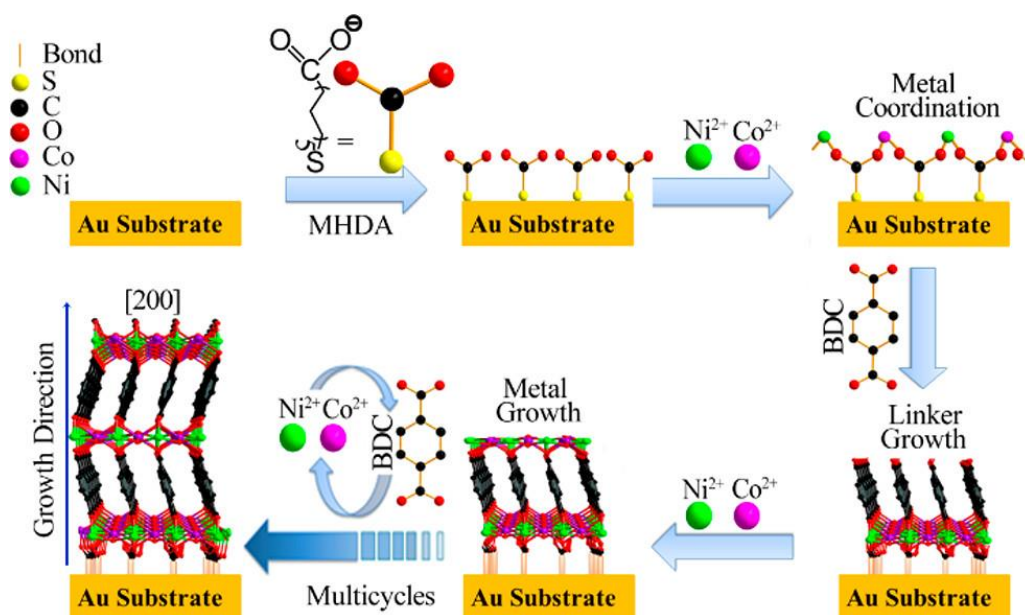


Figure 3.4. Approach used to synthesize the $[\text{M}(\text{BDC})]$ SURMOF directly on the electrode substrate. ($\text{M} = \text{Ni}^{2+}$, Co^{2+} ; BDC, 1,4-benzenedicarboxylate; MHDA, 16-mercaptohexadecanoic acid.) Initially, a SAMs was formed on the Au substrate, using MHDA. Subsequently, the electrode was alternately immersed in metal-salt and a linker solution, accompanied by washing steps. Each step is self-limiting, which allows a very defined layer-by-layer growth. Adapted with permission from ref. [149].

3.1.4 Equipment

For the sake of clarity all the equipment used in this work is listed in **Table 3.3**

Table 3.3. List of equipment.

<u>Device</u>	<u>Specifications</u>	<u>Company</u>
AFM	Multimode EC-STM/AFM instrument with a Nanoscope IIIA controller	Veeco Instruments, Germany
AFM tips	RTESP-300	Bruker, Germany
Heat gun	PHG 600-3	Bosch, Germany
Potentiostats	VSP-300	Bio-Logic, France
	Autolab PGSTAT302N	Metrohm, France
Pump systems		Homebuilt, TUM
Quartz crystal microbalance analyzer	Q-Sense E4 Auto	Biolin Scientific, Germany
RDE Rotator	MSR Rotator	Pine Research Instruments, USA
Reference electrodes	HydroFlex (RHE)	Gaskatel, Germany
	Hg/ Hg ₂ SO ₄ (0.6 M K ₂ SO ₄)	Schott, Germany
	Ag/AgCl (3 M KCl)	Schott, Germany
Thermostat	MA-26 Heating Circulator	Julabo, Germany
Water purification systems	Evoqua Ultra Clear 10 TWF 30 UV	Evoqua, Germany
XPS	X-ray source: XR 50, Al K-alpha anode (1486.61 eV)	Specs, Germany
	hemispherical energy analyzer PHOIBOS 150 (150 mm mean radius)	Specs, Germany

3.1.5 Materials

Important materials, which were used for this work are summarized in **Table 3.4**

Table 3.4. List of Materials.

<u>Material</u>	<u>Specifications</u>	<u>Company</u>
Argon	Ar – 5.0.	Air Liquide, Germany
Carbon monoxide	CO – 4.7	Air Liquide, France
Glassy Carbon Electrode	Diameter: 5mm	Pine Research Instruments, USA
	Diameter: 5mm (homemade)	LEPMI, France
Hydrogen	H ₂ – 5.0	Air Liquide, Germany
Ir/C	20 wt. %	Premetek, USA
Iridium crystal	Ir(111) 99.99%, Diameter: 5mm, oriented better than 0.1°	Mateck, Germany
Oxygen	O ₂ – 4.7	Linde, Germany
Platinum crystal	Pt(pc) - 99.99%, Diameter: 5mm. roughness: 30nm	Mateck, Germany
	Pt(111) Diameter: 10mm, oriented better than 0.1°	Icryst, Jülich Germany
Platinum microelectrode	Pt(pc), Diameter: 25 μm	Ch Instruments, USA
Platinum wire (CE)	Pt-wire – 99.99%, Diameter: 0.25 mm.	GoodFellow, Germany
Platinum mesh (CE)	Pt mesh – 99.99%	GoodFellow, Germany
Pt/C	TEC10 V20E, 20 wt. %	Tanaka Kikinzoku Kogyo, Japan
QCM substrate	Surface: Au(pc)	Biolin Scientific

3.1.6 Chemicals

All chemicals utilized in this work were used as received and are listed in the table below (Table 3.5).

Table 3.5. List of chemicals

<u>Chemical</u>	<u>Specifications</u>	<u>Company</u>
16-Mercaptohexadecanoic acid	HS(CH ₂) ₁₅ CO ₂ H (99%)	Sigma-Aldrich, Germany
Acetic acid	CH ₃ CO ₂ H (>99%)	Sigma-Aldrich, Germany
Ammonium sulfate	(NH ₄) ₂ SO ₄ (>99%)	Sigma-Aldrich, Germany
Cobalt chloride	CoCl ₂ ·6H ₂ O (98%)	ABCR, Germany
Cobalt sulfate	CoSO ₄ ·7H ₂ O (>99%),	Sigma-Aldrich, Germany
Ethanol	C ₂ H ₅ OH (99.8%)	VWR
Hydrogen peroxide	H ₂ O ₂ (30%, Suprapur)	Merck, Germany
Iron sulfate	FeSO ₄ ·7H ₂ O (>99%)	Sigma-Aldrich, Germany
Nafion solution	Nafion 117, 5 wt.% in lower aliphatic alcohols,	Sigma-Aldrich, Germany
Nickel chloride	NiCl ₂ ·6H ₂ O (99.3%)	Alfa Aesar, Germany
Nickel sulfate	NiSO ₄ ·6H ₂ O (>99%),	Sigma-Aldrich, Germany
Perchloric acid	HClO ₄ (Suprapur)	Merck, Germany
Potassium hydroxide	KOH (85%)	VWR, Germany
	KOH (85%)	Grüssing, Germany
Sodium acetate	NaOAc (>99%) anhydrous	Sigma-Aldrich, Germany
Sodium sulfate	Na ₂ SO ₄ (>99%), anhydrous	Sigma-Aldrich, Germany
Sulfuric acid	H ₂ SO ₄ (96%, Suprapur)	Merck, Germany
Terephthalic acid	C ₆ H ₄ -1,4-(COOH) ₂ (98%)	Sigma-Aldrich, Germany
Triethylamine	C ₆ H ₁₅ N (99%)	Acros (USA)

3.1.7 Software

The software utilized for data evaluation and controlling devices in this work are summarized in **Table 3.6**.

Table 3.6. List of Software

<u>Name</u>	<u>Type</u>	<u>Company</u>
Analysis of EIS data	EIS Data Analysis 1.3 ^{150,151}	Homemade, Prof. Dr. A. S. Bandarenka
AFM data acquisition	Nanoscope 5.31r1	Brucker, Germany
Routine data analysis	OriginPro 2018B	OriginLab, USA
Software for potentiostat (VSP-300)	EC-LAB Version 10.40 and 11.30	BioLogic, France
Software for potentiostat (Autolab)	Nova 2.0	Metrohm, Netherlands
XPS	SpecsLab Prodigy 4.8.3-r48573	SPECS, Germany

3.2 Experimental techniques

This section presents the main surface science techniques used in this work. X-Ray Photoelectron spectroscopy (XPS) and Atomic Force Microscopy (AFM) were utilized to investigate the elemental composition and morphology of the electrode surface, respectively. Electrochemical methods include galvanostatic methods, Cyclic Voltammetry (CV) and Electrochemical Impedance Spectroscopy (EIS).

3.2.1 Electrochemical techniques

3.2.1.1 Cyclic Voltammetry

Cyclic Voltammetry is a frequently used electrochemical technique to investigate electron transfer initiated processes. Although the technique itself is easily applicable, it can disclose valuable information about the electrochemical system. Beginning from a starting potential E_1 , the electrode potential is linearly ramped over time upwards (anodic scan) or downwards (cathodic scan) until the potential E_2 is reached. Subsequently, the scan direction is reversed until the potential is equivalent to the initial potential E_1 . This is typically repeated multiple times, while the current is measured as shown in **Figure 3.5 (A)**. In addition to the potential limits (E_1 and E_2), the scan rate [mV s^{-1}] is an important parameter, which needs to be considered. The current is typically plotted versus the applied potential; the graph is called a cyclic voltammogram.¹¹⁵ **Figure 3.5 (B)** shows a typical example: the cyclic voltammogram measured for a polycrystalline platinum electrode, which has been adapted from the literature¹⁵². Different regions can be identified according to the processes occurring at the catalyst surface. Between the potentials between ~ 0.05 V and ~ 1.50 V is the so-called “water window” for platinum, which means neither hydrogen nor oxygen is evolved at the working electrode.ⁱⁱⁱ Close to the cathodic limit is the hydrogen adsorption/desorption region. Scanning from the potentials of 0.3 V *vs* RHE in the cathodic direction results in an adsorption of protons on the platinum surface accompanied by a transfer of electrons. At the anodic scan, the layer of protons is then oxidized. At these

ⁱⁱⁱ The production rate is barely measurable.

potentials, it is energetically favorable for adsorbates to form a single monolayer. This is called underpotential deposition UPD and allows to estimate the electrochemically active surface area ECSA of platinum electrodes by integration of the charge of this peak. At slightly more anodic potentials there is no redox reaction ongoing, and the current results from the capacitive behavior of the electrode. The difference between anodic and cathodic current equals twice the change of electrochemical potential over time (scan rate) multiplied by the double layer capacitance C_{dl} . At even higher anodic potentials the platinum surface begins to oxidize, and an oxide layer is formed, which can subsequently be reduced at the cathodic scan. In comparison to the adsorption of protons, this oxidation/reduction of the platinum surface is less reversible, which means that the peaks are energetically shifted away from each other. The shape of a cyclic voltammogram can be very characteristic for certain catalysts surfaces. For instance, a Pt(111) surface can be easily distinguished from polycrystalline or stepped platinum surfaces by CV.

In this study, CV is used for different purposes, as will be reported in the following. The electrodes are cleaned from contaminations or residual catalyst films by cycling the electrodes in a relatively large potential window that exceeds the “water window” in acidic electrolytes. This alternating polarization leads to a quicker erosion of the surface layers than by applying an anodic potential only. To confirm the successful removal of *e.g.* an OER catalyst film from the substrate through cleaning, the cyclic voltammogram was compared to the one of a clean electrode. Furthermore, in case of the fresh OER catalysts, the activity towards the OER was compared. Further, for the deposition of certain catalyst films (NiO_x and CoO_x) on a substrate, the thin films were deposited anodically by cycling the electrodes in the deposition solution. Moreover, CVs were utilized to precondition films of the carbon supported platinum Pt/C and the carbon supported iridium Ir/C nanoparticles before further measurements. Last, cyclic voltammetry was utilized to investigate electrocatalytic activities of the different catalysts.

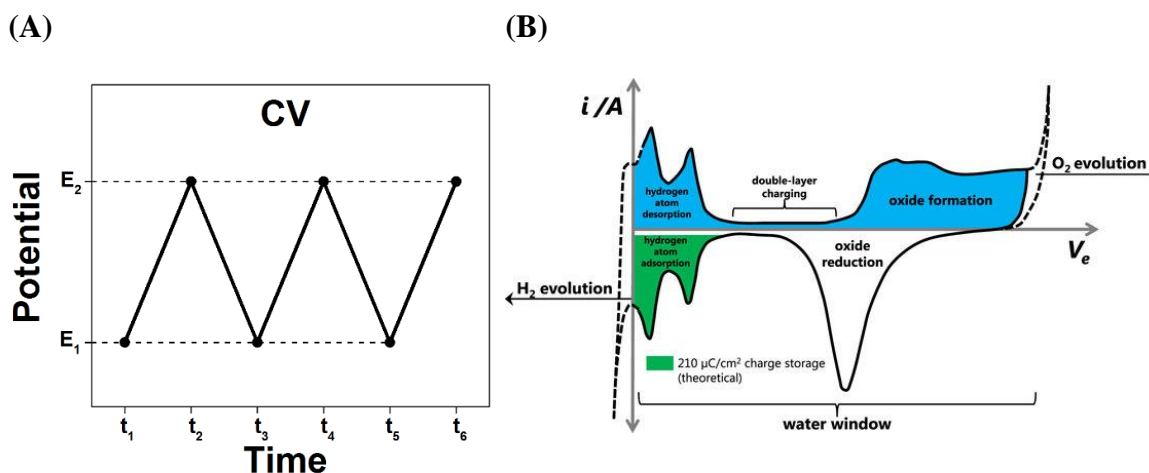


Figure 3.5. Cyclic voltammetry. (A) Time dependence of the applied potential during cyclic voltammetry. (B) A typical cyclic voltammogram recorded for a (poly)crystalline Pt electrode. This figure is adapted from ref. [152] (license: CC BY 3.0)

3.2.1.2 Electrochemical Impedance Spectroscopy

Electrochemical Impedance Spectroscopy (EIS) has been employed as another important electroanalytical technique in this thesis. EIS can provide information about reaction kinetics, electrode capacitance, as well as electrolyte and contact resistances. The interpretation of the obtained data, however, is often complex and requires initial assumptions. To probe the frequency dependent complex resistance (the so-called impedance Z), EIS is typically performed under quasi-stationary conditions at a fixed potential^{iv}. This means in practice that for potentiostatic EIS, a fixed potential E is applied and modulated with a small sinusoidal signal ΔE and frequency f , while the current I is measured. Typically, this is repeated for a broad range of frequencies. For industrial applications, such as *e.g.* fuel cells or electrolyzers, it is more practical to control the current while recording the potential (galvanostatic EIS). The response of an electrochemical system on a perturbation is in general non-linear. However, if the sine-shaped perturbation is sufficiently small, the response is quasi-linear, which means, that it also follows a sine-shape with the same frequency, but is phase shifted by $\Delta\phi$. Hence, independent if EIS is

^{iv} It must be noted that there are also nonstationary applications of EIS

performed in potentiostatic or galvanostatic mode, it is important that the amplitude of the applied potential/current is sufficiently small (which depends on the degree of local linearity of the electrochemical system at the chosen potential/current), but also large enough not to interfere with the background noise. According to common practice, amplitudes between 2 mV and 30 mV are typically chosen in the potentiostatic mode. The quality of the recorded EIS data can be examined using the Kramer-Kronigs (KK) transform test, which relates the frequency dependent real part $ReZ(f)$ with the imaginary part $ImZ(f)$ of the impedance. To clarify a widespread misconception: fulfilling the requirements of the KK relation is a necessity, but not sufficient to guarantee good impedance data. The impedance data are most commonly represented by relating $(-ImZ)$ vs ReZ in so-called Nyquist plot (see **Figure 3.6(A)**). This relatively comprehensible way of presenting the data is most popular, however, it lacks information about the frequency dependence. The Bode representation solves this problem by showing the absolute value $|Z|$ and $\Delta\varphi$ vs the frequency f , as shown in **Figure 3.6 (B)**.^{115,153}

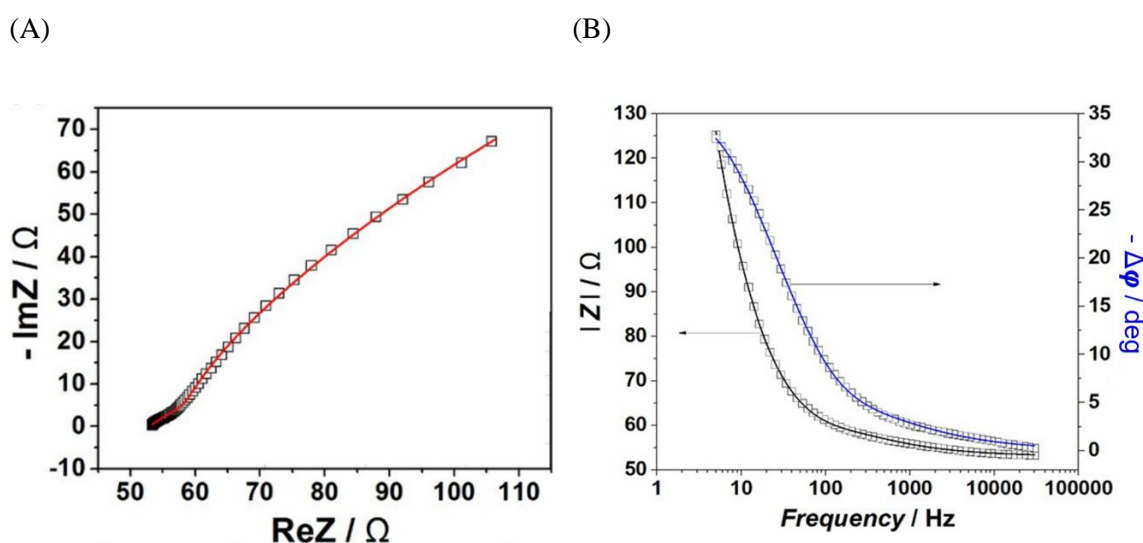


Figure 3.6. Exemplary EIS data (open symbols), (A) in Nyquist and (B) in Bode representation. Fitting these data (see solid lines) is required to extract important information about the system. Adapted with permission from ref. [89].

As described before, data analysis is typically complex and requires information about the electrochemical system and at least a rough background knowledge about possible reactions and their mechanism(s) occurring at the electrode (or system) under investigation. These assumptions can be used to formulate equations to describe the Faradaic and non-Faradaic current resulting from small perturbations. In turn, this can be used to derive an equation for the total impedance of the system. Often this equation is (if possible) represented in form of an equivalent electric circuit (EEC), which facilitates understanding. However, it has to be emphasized that the EECs in this work are not arbitrary but based on electrochemical phenomena and their influence on the impedance. Accordingly, the model can be applied to fit the recorded impedance data. In cases where the model cannot fit the impedance data sufficiently, or some parameters are not well defined (*e.g.* the case if a side reaction was accounted but does not contribute), the model needs to be readjusted. Once a good fitting is achieved, the model should be further validated and checked for plausibility. For instance, experimental conditions are varied, and the influence on the fitting parameters have to be carefully evaluated and compared with theoretical predictions.^{115,153}

An exemplary EEC which was also used in **Chapter 4.1** is shown in **Figure 3.7**.

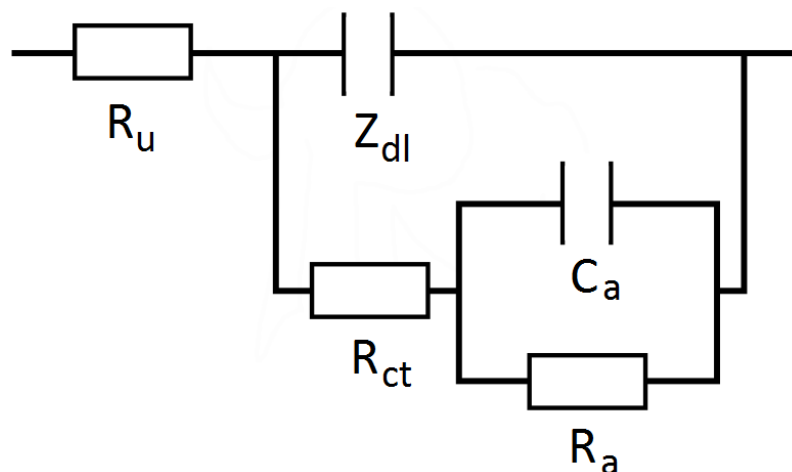


Figure 3.7. Proposed EEC for the fitting EIS data in OER regime. R_u , Z_{dl} , R_{ct} , C_a , and R_a correspond to the uncompensated resistance, double layer impedance, charge transfer resistance, adsorption capacitance and adsorption resistance, respectively.

3.2.2 X-Ray photoelectron spectroscopy

Several decades after the discovery of the photoelectric effect in 1887 and its explanation by Albert Einstein in 1905, the research group of Kai Siegbahn was the first to show the potential of photoelectron spectroscopy (XPS) by utilizing the photoelectric effect and record a high energy resolution XPS spectrum of an NaCl crystal in 1954.^{154,155}

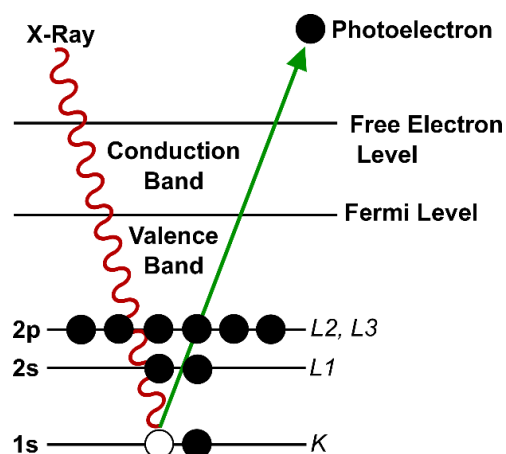
XPS is a highly surface sensitive technique allowing quantitative analysis of material surface composition. This non-destructive technique is able to detect elements with atomic number (Z) of 3 and larger. These devices usually operate under high vacuum (10^{-9} mbar) and use an X-ray beam, which is focused onto the sample surface. The photons eject electrons from the sample surface, which eventually hit the detector where their kinetic energy E_{kin} is determined. The principle is based on the photoelectric effect, as shown in **Figure 3.8 (A)**. The electromagnetic wave of a photon can interact with an electron by transferring its energy entirely on it, effectively vanishing the photon. This is only possible, when the energy of the photon $E_{photon} = \hbar\omega$ exceeds the binding energy of the electron. The exceeding energy of the photon results in kinetic energy of the electron E_{kin}' . However, a certain amount of the initial kinetic energy E_{kin}' is lost before the electrons reach the detector so that the energy of the detected electrons is $E_{kin} = E_{kin}' - \phi_w$, where ϕ_w is the so-called work function.¹⁵⁶

Hence, the binding energy E_{bind} of a detected electron can be determined by:

$$E_{bind} = \hbar\omega - (E_{kin} + \phi_w), \quad (3.6)$$

Each orbital of each element has a very characteristic binding energy, which is influenced *e.g.* by the chemical state of the element resulting in so-called chemical shift of the corresponding XPS spectrum. This allows the discrimination of different elements as well as the discrimination of different oxidation states and even a quantitative analysis of the surface species by comparing the peak integrals.

(A)



(B)

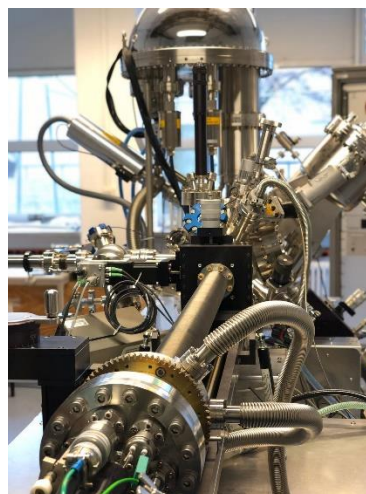


Figure 3.8. X-ray photoelectron spectroscopy. (A) The technique is based on the photoelectric effect: a photon interacts with a bound electron and transfers its energy completely to it. (B) Photograph of the XPS setup: at the top is the hemispherical analyzer which records the electron energy.

For this work, an XPS by SPECS, which operates at UHV and equipped with a SPECS PHOIBOS 150 hemispherical energy analyzer was utilized. As shown on **Figure 3.8 (B)**, this device has three chambers, the load lock, which is serving as an airlock, a preparation chamber (which also serves as additional protection to maintain the vacuum level) and the main chamber to which the X-ray source and the detector are connected. The X-rays are generated by accelerating electrons, which are released from a hot electron by a high voltage of 12 kV towards an Aluminum target. This target then emits the x-rays, which are subsequently filtered by a monochromator, resulting in a monochromatic x-ray beam of 1486.61 eV.

3.2.3 Atomic force microscopy

The first atomic force microscope (AFM) was developed by G. Binnig, C. F. Quate and C. Gerber in 1985.¹⁵⁷ This technique is a type of scanning probe microscopy and is based on short-ranged forces at the atomic scale as described below. This method often reaches atomic resolution and does not require conductive sample surfaces.

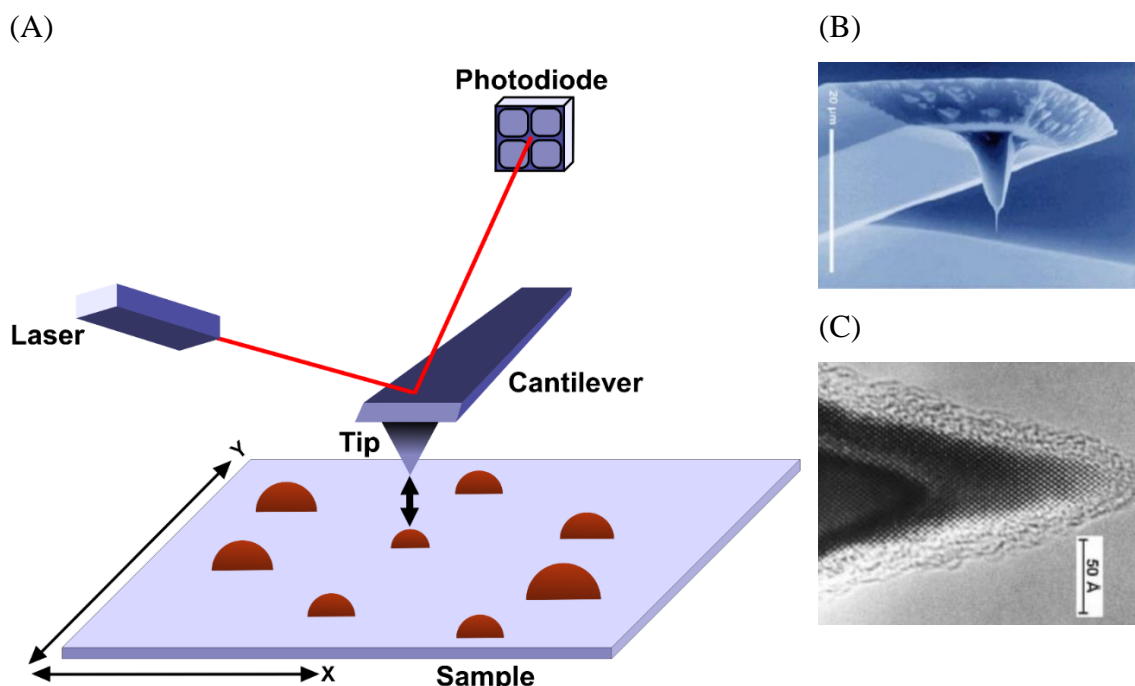


Figure 3.9. (A) Schematic of the working principle of an atomic force microscope. The tip mounted on a cantilever probes the samples surface, which interacts *via* attracting and repelling forces. The resulting deflection of the cantilever is monitored using a laser beam, which is reflected by the cantilever to a field of photodiodes. (B) Scanning electron microscope (SEM) image of the cantilever and (C) transmission electron microscope (TEM) image of the tip. In order to have an optimal resolution, the tip needs to be pointy, even at the atomic scale. (B) and (C) are adapted from refs. [158,159] with permission. Copyright AIP Publishing.

The principle of this technique is the following: As shown in **Figure 3.9** (A), a cantilever with a very sharp tip (B,C) is utilized to scan across the sample while the force between this tip and the sample is measured. The cantilever acts as a small spring and even small deflections of its position can be visualized by a laser, which is reflected at the cantilever towards a photodetector. This allows to measure the extremely small forces (10^{-18} N)^[157] of the sample atoms, which attract or repel the tip.

The forces acting on the tip can be estimated using the Lennard-Jones potential. A qualitative and simplified explanation for the shape of the potential is the following. If the atom at the tip comes to very close distance to the atoms at the sample surface, the electronic orbitals of these atoms start to overlap, which forces these electrons (according to Pauli's Principle) to occupy states of higher energy, which results in a relatively strong repulsive force as shown by **Figure 3.10**. However, at larger distances attracting forces like Van-der-Waal forces dominate.

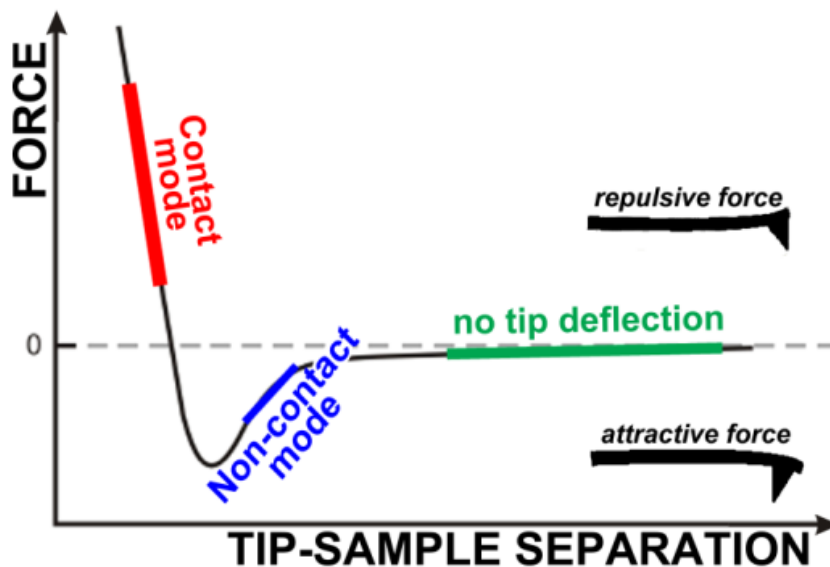


Figure 3.10. Schematic explanation of the Lennard-Jones potential. Depending on the selected distance between tip and sample, the tip is affected by an attractive or (and) repulsive force. Adapted from ref. [160] (open access, license: CC BY 3.0)

Three main operation modes for the AFM exist:

The non-contact mode, where the tip is kept at a distance where the attractive force dominates, the contact mode in repulsive regime and the tapping mode, where the tip oscillates between both regimes. In brief, the resolution improves with shorter distance to the sample but also the probability to scratch the sample's surface. For this work, the tapping mode was chosen, where the tip oscillates slightly above the resonance frequency. A constant (average) height level is ensured by a feedback-loop measuring the oscillation amplitude (20-100 nm) and readjusting and measuring the height.^{160,161}

4 Results and Discussion

4.1 Determination of electroactive surface area of oxide materials

This part of the dissertation deals with the up-to-date difficulties related to the experimental determination of a real electroactive surface area (ECSA) of oxide materials. A novel method addressing this issue has been developed and has been reported in two scientific articles^{89,90}. Those can be found in the Appendix. In this Chapter, the concept of the method is presented, firstly. Further, its validity is proven even for the non-trivial case of catalyst nanoparticles on a solid support. The results presented in this chapter were published in: “S. Watzele, A.S. Bandarenka. Quick determination of electroactive surface area of some oxide electrode materials. *Electroanalysis* 28 (2016) 2394-2399” and “S. Watzele, P. Hauenstein, Y. Liang, S. Xue, J. Fichtner, B. Garlyyev, D. Scieszka, F. Claudel, F. Maillard, A.S. Bandarenka. Determination of electroactive surface area of Ni-, Co-, Fe-, and Ir-based oxide electrocatalysts. *ACS Catalysis* 9 (2019) 9222-9230” (see **Chapter 6.3**)

4.1.1 Motivation

Concerning functional materials, transition metals and their oxides/perovskites are of high importance. Oxides show a remarkable variety of applications being used for medical purposes, in superconductors, supercapacitors, batteries or classical heterogeneous catalysts and electrocatalysts. However, compared to metals, there is a serious lack of their understanding. This lack of information is partially originated from the difficulties of the electroactive surface area (ECSA) determination. The ECSA is a crucial parameter not only

for fundamental studies but also for the optimizations in industrial applications. For example, current research in the field of electrocatalysis focusses on the synthesis of supported nanostructures to increase the active surface area. Furthermore, monitoring the ECSA over time can provide insight into aging behavior of these materials.

4.1.2 Definition of the problem

The determination of the ECSA using classical techniques can be more or less complicated depending on the structure and manufacturing process of the electrode. **Figure 4.1 (A)** and **(B)** sketch two different cases. The situation is relatively simple when the electrode consists of the catalyst material, or it is entirely covered by a non-porous catalyst layer (see **Figure 4.1 (A)**). However, often the presence (and amount) of pores in the catalyst film and their contribution to the ECSA is unclear.

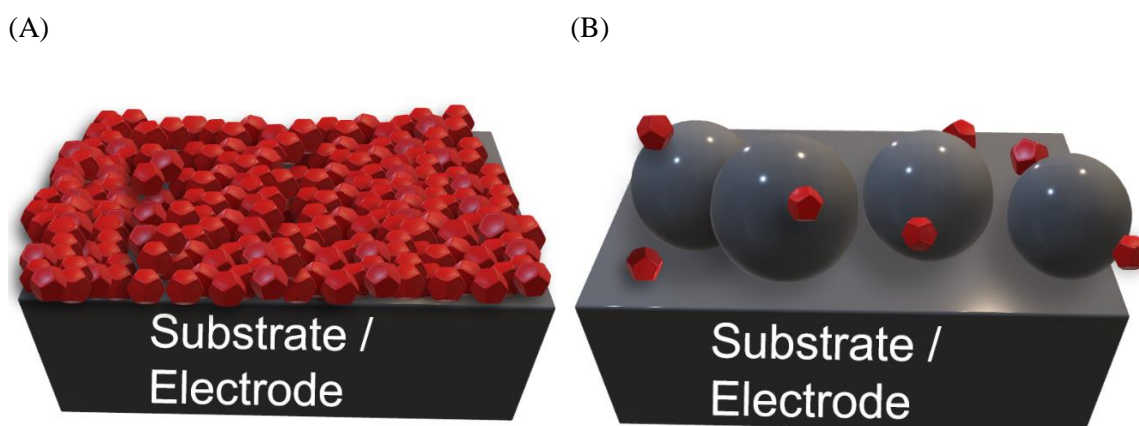


Figure 4.1. Scheme of different electrode coatings. The catalyst particles are represented with the red dodecahedra. In the simplest scenario (A), the particles cover the entire electrode and no substrate is exposed. In reality, the situation is often different as some part of the substrate is exposed. For instance, the catalyst might be supported by an inactive material (to prevent the agglomeration of the catalyst particles), which can also be exposed as shown in (B).

The general case is, however, much more challenging as schematized by **Figure 4.1 (B)**. Typically, the (active) catalyst does not cover the whole surface of an electrode. Furthermore, it often consists of nanoparticles, which decorate an inactive the support

material. This support is utilized to prevent agglomeration of the particles, which would decrease the ECSA. In such a case, the methods, which simply measure the samples surface area cannot be applied for the accurate ECSA determination.

4.1.3 State-of-the-art approaches

Before presenting the details of the newly developed method, it makes sense to take a look at state-of-the-art approaches used for the estimation of the electroactive area. The principles of the most common techniques are presented in the following and their advantages and disadvantages are summarized.

4.1.3.1 Brunauer-Emmett-Teller method

The principle of Brunauer-Emmett-Teller (BET) method utilizes a phenomenon of gas molecules adsorption on the surface of a solid material. Hereby, the surface area, especially of powders or porous materials can be determined. Unfortunately, the thereby measured surface area is only equivalent to the ECSA in very special cases. For instance, even for the case shown by **Figure 4.1 (A)**, nanopores which are accessibly by the gas atoms but not by electrolyte are erroneously accounted for the surface area. The situation sketched by **Figure 4.1 (B)** would be even worse, as the surface area would be a sum of the surface areas of the electrode, the support and the catalyst.^{91, 162}

4.1.3.2 Microscopic techniques

AFM (see **Chapter 3.2.3**) and scanning electron microscopy (SEM) can in principle map the morphology of a flat electrode with an atomic resolution. However, the resolution is decreased for very rough samples, and porous structures cannot be accurately measured. Obviously, it is not useful for the case shown by **Figure 4.1 (B)**. Transmission electrode microscopy (TEM) can image single particles and allows to assess their size and shape.

Metal based particles can be usually distinguished from nonmetallic support (*e.g.* carbon). Thus, it allows a rough estimation of the surface area of the catalyst, assuming the regarded particles are representative for the whole catalyst.^{163,164}

4.1.3.3 Double layer capacitance

This technique of the surface area determination of electrode materials is based on the Gouy-Chapman-Stern theory. During a measurement the capacitive behavior of an electrode is evaluated in a potential region, where only the electrical double layer contributes to this capacitance. This type of capacitance can be determined by CV or EIS. Due to the lack of alternatives, this method is commonly used to estimate the ECSA of oxide materials, although even for unsupported catalysts, it can show high inaccuracies (up to 700%)⁹². Evidently, this method is not meaningful for the situation of supported catalyst because similar to the BET method, as it does not distinguish between active (catalyst) and inactive material (support / electrode).^{165,166}

4.1.3.4 Techniques based on adsorption

A variety of techniques is based on the principle of species, which adsorb specifically on metal surfaces. In contrast to the before mentioned techniques, only the surface area of the active material is measured without the contribution of the surface area of the inactive support (**Figure 4.1 (B)**), which appears as an obvious advantage. Unfortunately, these methods are only applicable for certain metals and, with few exceptions, cannot be used for the analysis of oxide materials.⁹¹

Adsorption of hydrogen

Some transition metals adsorb hydrogen (atoms) at their surface already at potentials, which are more anodic compared to the onset of the HER. The associated charge can be measured *e.g.* by the CV. Therefore, the corresponding adsorption/desorption peaks are corrected for

the current originating from the charging of the double layer capacitance and then integrated. Thus, the charge per surface area for a “saturated coverage” depends on the crystal facet.^{167,168} Note that a full coverage is not reached due to entropic reasons, but this method can still be applied using empirical values for the surface specific charge.

For the case of polycrystalline Pt, a value of $210 \mu\text{C cm}^{-2}$ has been found.^{169,170} This method is well suitable for platinum catalysts but can be in principle extended to Ir and Rh.^{171,172} However, in the latter cases, only a fractional surface coverage might be reached causing inaccuracies. Another source of inaccuracies for Pt surfaces is the subtraction of the current originating from charging of the electrical double layer, as the adsorbed species can also influence the capacitive parameters of the phase boundary.⁹¹

Adsorption of oxygen

This technique can be utilized, similar to the previously shown technique. However, this applies for materials, which show the adsorption of a monoatomic layer of oxygen at potentials lower than the onset of the OER. This method is typically only used, when hydrogen adsorption is not applicable. For instance, surface specific adsorption charge values for Au are found in the literature.^{173,174} Note that this method is not applicable for materials where several layers get oxidized.

Underpotential deposition of metals

This method is similar to the one utilizing adsorption of hydrogen, but here a potential is applied, which only allows the adsorption of metal cations (from the electrolyte) to form one monolayer. Cu, Ag, or Pb are typically used as adatoms^{175,176}. This allows the determination of surface area of Pt but also of *e.g.* Cu, Ag, and Ru layers^{176,177} and is especially suitable in the case of supported catalysts. Remarkably, Hg underpotential deposition is one of the few state-of-the-art techniques, which allow to determine the ECSA of IrO_x catalysts.¹⁷⁸ However, a drawback of this method is that the measurement usually requires exchanging the electrolyte and can also contaminate the electrochemical cell with some residues.

Adsorption of carbon monoxide

Another possibility for an *in-situ* measurement of the ECSA is the adsorption of CO (carbon monoxide) on the electrode surface. This can be applied to *e.g.* for Pt or Ir surfaces.^{178,179} The electrode is immersed in a CO-containing electrolyte and a potential is applied, which allows the adsorption of (almost) one monolayer. The CO is then removed from the electrolyte (while keeping the potential). Subsequently, the potential is typically cycled towards more anodic potentials. Depending on the catalyst and surface facet the CO oxidizes at a certain potential to CO₂. The charge of this Faradaic current can be attributed to the ECSA. Similar approaches are reported for the adsorption of I₂ on *e.g.* Au surfaces.¹⁸⁰

4.1.4 Principles of the developed method

The principles of the new method is based, similar to the above-mentioned conventional methods, on specific adsorption. It takes advantage of the oxygen evolution reaction, which involves several specifically adsorbed reaction intermediates that can be reversibly adsorbed. This manifests itself in an adsorption capacitance C_a , which can be measured *via* electrochemical impedance spectroscopy^{89,90}. This capacitance correlates to the ECSA.

For the sake of clarity, in the further discussion the generally accepted simplified OER reaction pathway is used¹⁸¹:



This reaction is associated with three specifically adsorbed OER reaction intermediates: *OH, *O, and *OOH. Note that the asterisk (*) denotes a surface adsorption site.

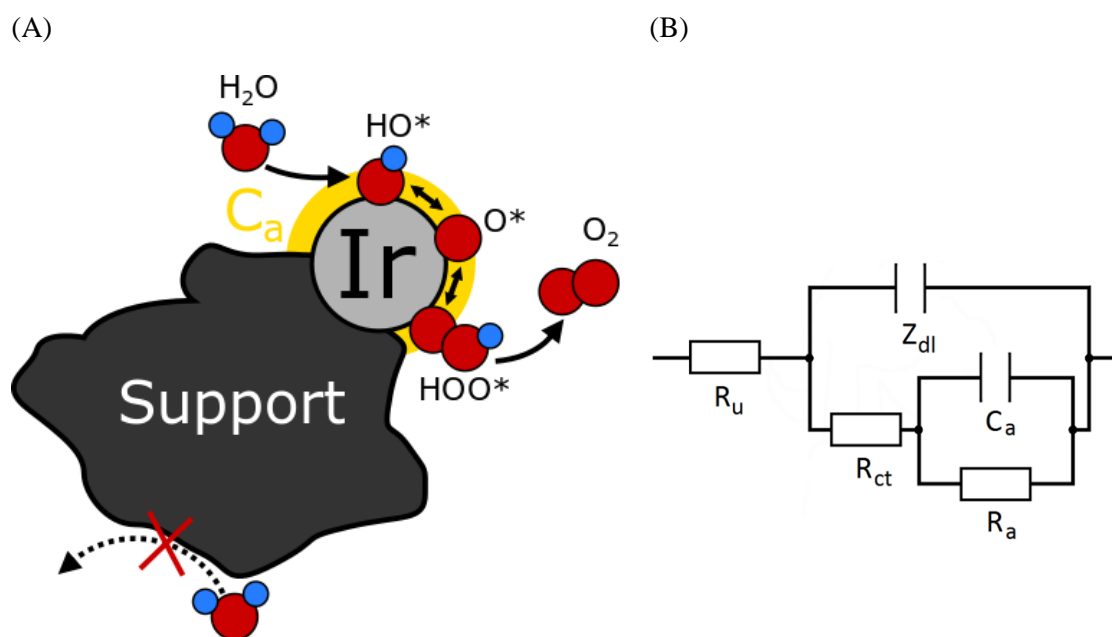


Figure 4.2. Specific adsorption of OER reaction intermediates as the origin of the adsorption capacitance C_a . (A) Schematic representation of a catalyst nanoparticle on an inactive support. The OER involves the reversible adsorption of reaction intermediates to the electroactive surfaces. This takes place only on the active oxide particle but not on the support. Therefore, solely the ECSA contributes to C_a . (B) EEC for the analysis of the EIS spectra, recorded at the onset of the OER. The derivation of this physical model is shown in **Chapter 4.1.5** R_u , Z_{dl} , R_{ct} , R_a , and C_a are the uncompensated resistance, the double layer impedance, the charge transfer resistance, the adsorption resistance, and adsorption capacitance, respectively. The latter two account for the specific and reversible adsorption of OER intermediates. Adapted with permission from ref. [90].

As sketched in **Figure 4.2** (OER on particle) adsorption of some intermediates can be reversible, and the adsorbate coverage at the active material depends on the electrode potential. In contrast, the material, which is inactive at the applied voltage shows either no or just irreversible adsorption of the intermediates. Though, the adsorption capacitance (as will be shown in the next section) can be defined as:

$$C_a = q \frac{\partial \theta}{\partial E} \quad (4.5)$$

where q is the charge of an adsorbate monolayer and $\partial\theta$ the alternation of fractional coverage due to an applied probing signal ∂E . Consequently, inactive materials with (locally) potential independent surface coverage $\frac{\partial\theta}{\partial E} \sim 0$ do not contribute to C_a , while active materials do, if their surface coverage is potential dependent $\frac{\partial\theta}{\partial E} \neq 0$. Therefore, potentials close to the onset of OER are applied, where the material, which is under investigation is active and its surface coverage with adsorbates increases with the potential $\frac{\partial\theta}{\partial E} > 0$. Thus, the surfaces of active materials do contribute to the adsorption capacitance, while inactive surfaces do not. This C_a can be measured *via* EIS using the EEC introduced in **Chapter 4.1.5** and should correlate with the ECSA. In other words, this method defines the ECSA as the area, which is accessible to the reversible adsorption of specifically adsorbed species of the OER (at the applied potential) and is similar to the area that can contribute to the OER. Further, this means, that parts of the catalyst, which are either not electrically connected to the electrode or blocked by *e.g.* oxygen bubbles do not account for the ECSA as shown in **Figure 4.3**. Therefore, this method can be also applied to investigate the blockage of the active surface area due to gas bubbles that typically accumulate when applying OER conditions over long time. Subsequent removal of those bubbles and re-measurement of EIS allow to determine the ECSA of the catalyst itself to detect possible aging processes such as particle detachment.

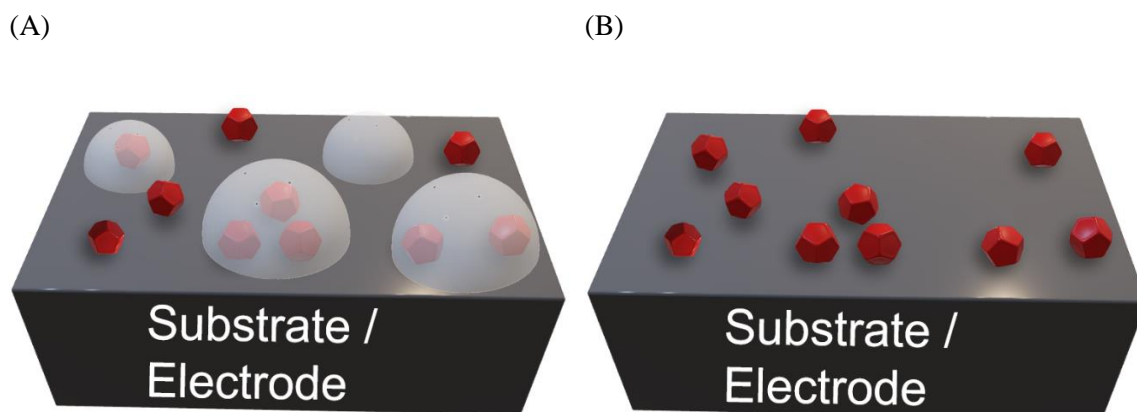


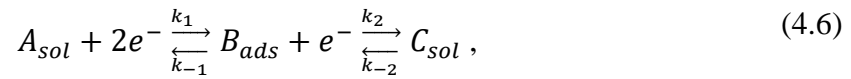
Figure 4.3. (A) Blockage of ECSA due to oxygen bubbles. After OER activity or stability benchmarking experiments gas bubbles are often found to cover fractions of the electrode surface. Their origin has been discussed in **Chapter 3.1.2**. The red particles represent catalyst nanoparticles, some of which are not accessible to the electrolyte due to a gaseous phase (represented by the semitransparent hemispheres) and do not contribute to the ECSA. However, after removal of the oxygen bubbles (B) they contribute again to the ECSA. An advantage of the presented method is that such effects can be investigated *in-situ*. No exchange of electrolyte, that could lead to the dissipation of the gaseous phase is required. This allows to examine both the ECSA directly after experiments and the ECSA after removal of the blocking gas phase.

4.1.5 Explanation of the EEC

This subchapter aims to introduce the EEC, which is used to analyze the EIS spectra and briefly assess its validity for the OER. The following discussion is based on ref. [182] and [183] and adopted from our recent publication.⁹⁰

The AC response of an electrochemical system usually splits up into a non-Faradaic and a Faradaic part. An ideally polarizable electrode could charge up like a capacitor and would be described by the capacitance C_{dl} with the resistance of the electrolyte R_u in series. In reality, however, the response of the electrochemical double layer needs to be represented by a constant phase element $Z_{dl} = \frac{1}{C_{dl}(j\omega)^n}$, where the exponent n accounts for the frequency dispersion of the double layer, while j is the imaginary unit, and ω stands for the angular frequency.

The response of Faradaic reactions manifests itself in a Faradaic impedance Z_f that is in parallel to Z_{dl} . For simplicity, it is assumed, that a reaction only involves one adsorbed reaction intermediate and a stepwise transfer of 2 electrons (e^-):



where $k_{(-)1}$ and $k_{(-)2}$ are the rate constants. Assuming a Langmuir adsorption isotherm, one can describe the reaction rates of both steps as:

$$v_1 = k_1^0 \Gamma_\infty C_A(0) (1 - \theta_B) \exp[-\alpha_1 f(E - E_1^0)] - k_{-1}^0 \Gamma_\infty \theta_B \exp[(1 - \alpha_1) f(E - E_1^0)] \quad (4.7)$$

$$v_2 = k_2^0 \Gamma_\infty \theta_B \exp[-\alpha_2 f(E - E_2^0)] - k_{-2}^0 \Gamma_\infty C_C(0) (1 - \theta_B) \exp[(1 - \alpha_2) f(E - E_2^0)] \quad (4.8)$$

Here $k_{1,2}^0$, Γ_∞ , and $C_{A,C}(0)$ are the rate constants, the total surface concentration of active sites, and the concentration of species A and C at the surface, respectively. Further, θ_B is the fractional coverage of the active centers and $\alpha_{1,2}$ are the transfer coefficients. Moreover, $f = F/RT$ and $E - E_{1,2}^0$ are the differences of applied potential E to the standard potentials

for both reactions $E_{1,2}^0$. F , R and T are the Faraday constant, the gas constant and the temperature, respectively. One can define an equilibrium potential, E_{eq} , where both net reaction rates become zero¹⁸²:

$$\exp[f(E_{eq} - E_1^0)] = \frac{k_1^0}{k_{-1}^0} C_A^* \frac{1 - \theta_B^*}{\theta_B^*} \quad (4.9)$$

$$\exp[f(E_{eq} - E_2^0)] = \frac{k_2^0}{k_{-2}^0} C_C^* \frac{\theta_B^*}{1 - \theta_B^*} \quad (4.10)$$

The equilibrium potential of the individual steps is of course dependent on the bulk concentration $C_{A,C}^*$ of species A and C as well as at the surface concentration of species B_{ads} in equilibrium θ_B^* . Introducing the overpotential, the difference $E - E_i^0$ can be transformed to $E - E_i^0 = E - E_{eq} + E_{eq} - E_i^0 = \eta + E_{eq} - E_i^0$. With the additional assumption, that the surface concentration is very similar to the bulk concentration, which is true for relatively low currents and high electrolyte concentrations, one can rewrite **Equations (4.7)** and **(4.8)** several times. For more detailed calculations, please refer to A. Lasia¹⁸²

The total current of both reaction steps is:

$$i = -F(v_1 + v_2) = -Fr_0 \quad (4.11)$$

Moreover, the change of surface coverage by species B_{ads} can be expressed as:

$$\frac{d\Gamma_B}{dt} = \Gamma_\infty \frac{d\theta_B}{dt} = \frac{\sigma_1}{F} \frac{d\theta_B}{dt} = r_1 = v_1 - v_2 = 0 \quad (4.12)$$

Where the charge of a monolayer corresponds to $\sigma_1 = F\Gamma_\infty$. Further, the term for the total current and for the surface coverage can be linearized and merged which allows to derive an equation for the complex admittance. The inverse of the admittance is the Faradaic impedance which can be transformed to:

$$Z_F = R_{ct} + \frac{1}{j\omega C_a + \frac{1}{R_a}} \quad (4.13)$$

Here, R_{ct} , C_a , and R_a are the so-called charge transfer resistance, adsorption capacitance and adsorption resistance, respectively. C_a is the derivative of the surface charge associated with the adsorption of species B by applied potential and is of course dependent on the adsorption isotherm.

The combination of Z_F with Z_{dl} and the uncompensated resistance of the electrolyte R_U allows to express the total impedance as:

$$Z_{total} = R_U + \frac{1}{C_{dl}(j\omega)^n + \frac{1}{R_{ct} + \frac{1}{j\omega C_a + \frac{1}{R_a}}}} \quad (4.14)$$

For easier understandability, this can be also represented as the EEC shown in **Figure 4.4**.

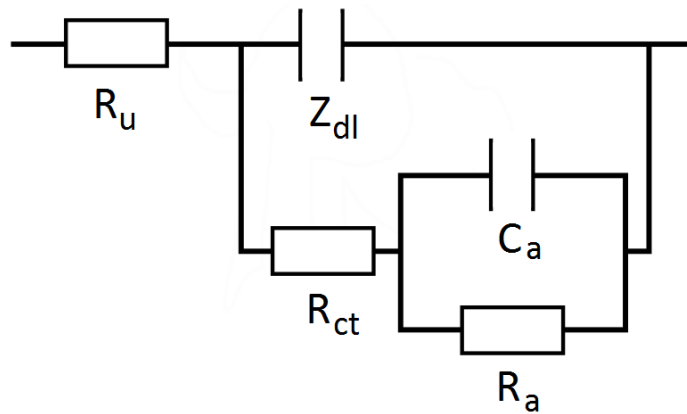


Figure 4.4. Equivalent electric circuit to analyze the impedance spectra recorded in OER regime. R_u , Z_{dl} , R_{ct} , C_a , and R_a are the uncompensated resistance of electrolyte, the impedance of the double layer, the charge transfer resistance, the adsorption capacitance, and adsorption resistance, respectively.

Note that for the derivation of the Faradaic impedance several simplifications were made. For instance, a Langmuir adsorption isotherm was assumed, which does not take any adsorbate-adsorbate interactions into account. In general, one could do similar calculations

using *e.g.* Frumkin adsorption isotherm, which could change the potential dependence of C_a . A more critical point is that the derivations were carried out on the basis of a Faradaic reaction involving one adsorbed species with subsequent desorption step, although the OER involves (at least) three adsorbed reaction intermediates (see **Chapter 4.1.4**). Accounting for two additional intermediates results in a far more complex system and a larger EEC with more branches. A justification to utilize this “simple” EEC could be, that at small overpotentials only one step is quasi-reversible. Therefore, the surface concentration of essentially just one specifically adsorbed species, which might be the *OH intermediate, varies with the applied potential. Furthermore, the recorded EIS spectra always feature two semicircles, which can be fully fit with this simplified EEC, as will be shown in the following chapters.

4.1.6 Calibration

The procedure for determining the electroactive surface area using conventional methods is relatively straightforward. For instance, in the case of adsorbed hydrogen, the integrated charge [μC] is divided by the specific charge (per surface area) [$\mu\text{C cm}^{-2}$], which can be taken from the literature. However, unlike for state-of-the-art techniques, no such literature values are known for the specific adsorption capacitance C_a' [$\mu\text{F cm}^{-2}$]. Therefore, the first step was to create such a database of the specific adsorption capacitances for each individual important catalyst and investigate their potential dependences.

This required measurements of C_a for the catalysts with the well-known ECSAs. Division of the adsorption capacitance C_a by the ECSA yields the specific adsorption capacitance C_a' :

$$C_a' = C_a / ECSA \quad (4.15)$$

Thus, thin catalyst films were deposited on flat substrates, which could be used as RDE and their thickness was optimized. To ensure, that the deposition was successful, XPS was utilized to investigate the films composition. For a more precise evaluation of the ECSA,

AFM was utilized to determine the electrodes roughness factor. The ECSA was then estimated from the geometric surface area of the electrode $A_{geometric}$ as:

$$ECSA \sim A_{geometric} \cdot \text{Roughness factor} \quad (4.16)$$

Afterwards, for each catalyst, EIS was measured in a potential window around the onset of the OER. To minimize statistical errors, this was repeated with freshly deposited films multiple times (up to 52 independent measurements). Adsorption capacitances were determined by fitting the impedance data utilizing the equivalent electric circuit deduced in the previous section and shown in **Figure 4.4**. In the following section each step of the calibration procedure is shown in more detail.

4.1.6.1 Thin film growth

There are various possibilities for creating catalyst films. For this work, we decided to utilize electrochemical deposition and adapted deposition protocols, which had been reported to result in non-porous thin films. The deposition conditions can be found in **Chapter 3.1.3**. Further, the thickness of the catalyst films was optimized such, that they became as thin as possible but, to keep the properties of bulk catalyst, without any influence of the support material. The idea was to subsequently decrease the surface roughness. Therefore, the electrocatalytic activity of catalyst films with different thickness were compared. The results for a NiO_x catalyst are presented below.

For the deposition of the NiO_x film, the electrode was immersed in the deposition solution and the potential was scanned between ~0.9 V and 1.9 V (as shown by the inset of **Figure 4.5**), which leads to a gradual growth of film thickness. Further, the film was optimized by correlating the films catalyst activity to the film thickness. The integrated charge was utilized as a parameter for the film thickness, as an exact measurement of thickness seemed to be impractical and not target oriented. Several films of different thickness were produced by stopping the deposition after different numbers of cycles (always at the anodic limit) and their catalytic activity (measured in 0.1 M KOH) was compared, as can be seen in **Figure 4.5**. The activity increased significantly within the first 5 mC cm⁻² and becomes

almost constant for films with an integrated charge of $\sim 10 \text{ mC cm}^{-2}$ and more. Though, we decided to utilize NiO_x films with an integrated charge of $\sim 20 \text{ mC cm}^{-2}$ to ensure high reproducibility. The other metal oxide films were optimized in a similar way and the resulting parameter of the most ideal deposition can be found in **Table 3.1** in **Chapter 3.1.3**.

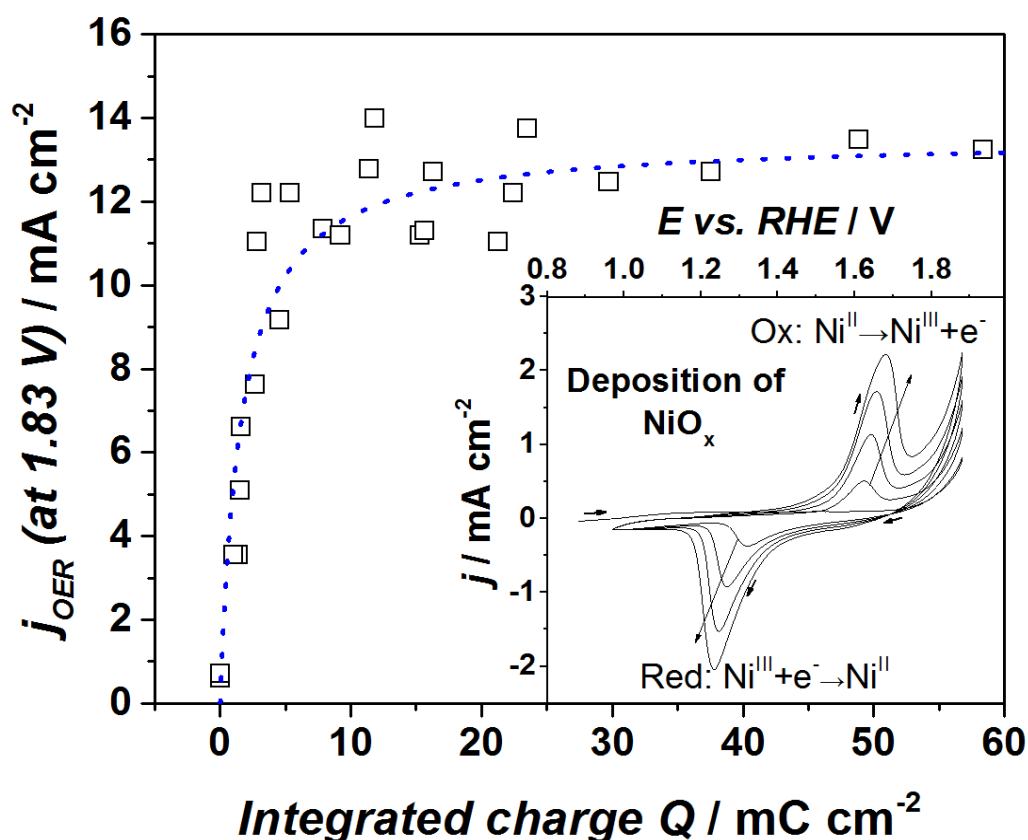
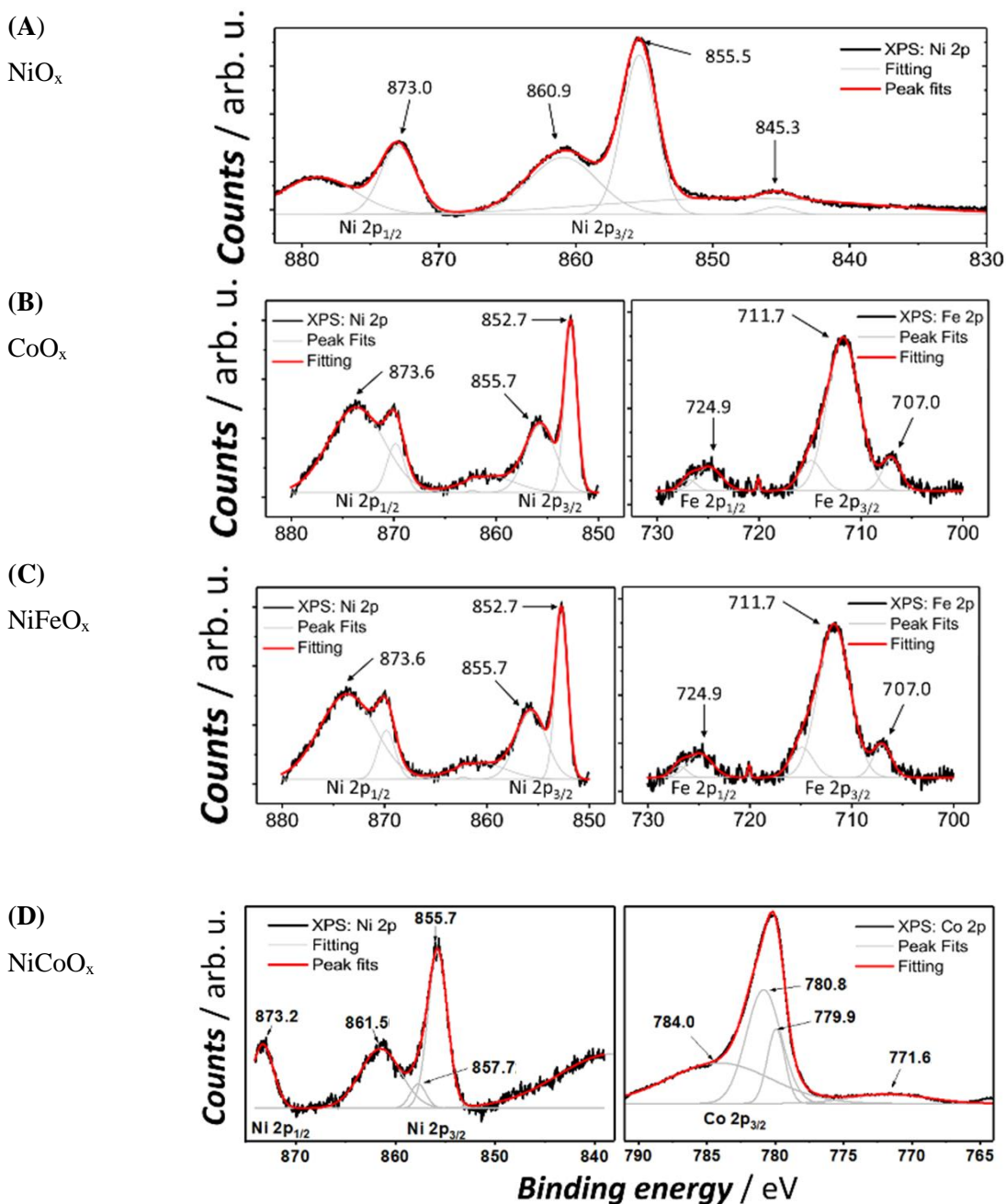


Figure 4.5. Optimization of the thickness of NiO_x films. As the inset shows, these films were deposited *via* potential cycling between $\sim 0.9 \text{ V}$ and $\sim 1.9 \text{ V}$ vs RHE. The depositions were stopped at the anodic limit and the total integrated charge was taken as a parameter for the film thickness. The anodic current densities (measured in 0.1 M KOH at 1.83 V vs RHE) are plotted vs the integrated charge, the blue dotted line shows an approximation curve. The activity increases significantly within the first 5 mC cm^{-2} and seems to reach a plateau at $\sim 10 \text{ mC cm}^{-2}$. Adapted with permission from ref. [89].

X-ray photoelectron spectroscopy was applied to the freshly prepared catalyst thin films to ensure, that the deposition procedures and the utilization of our chemicals resulted in the desired film composition.



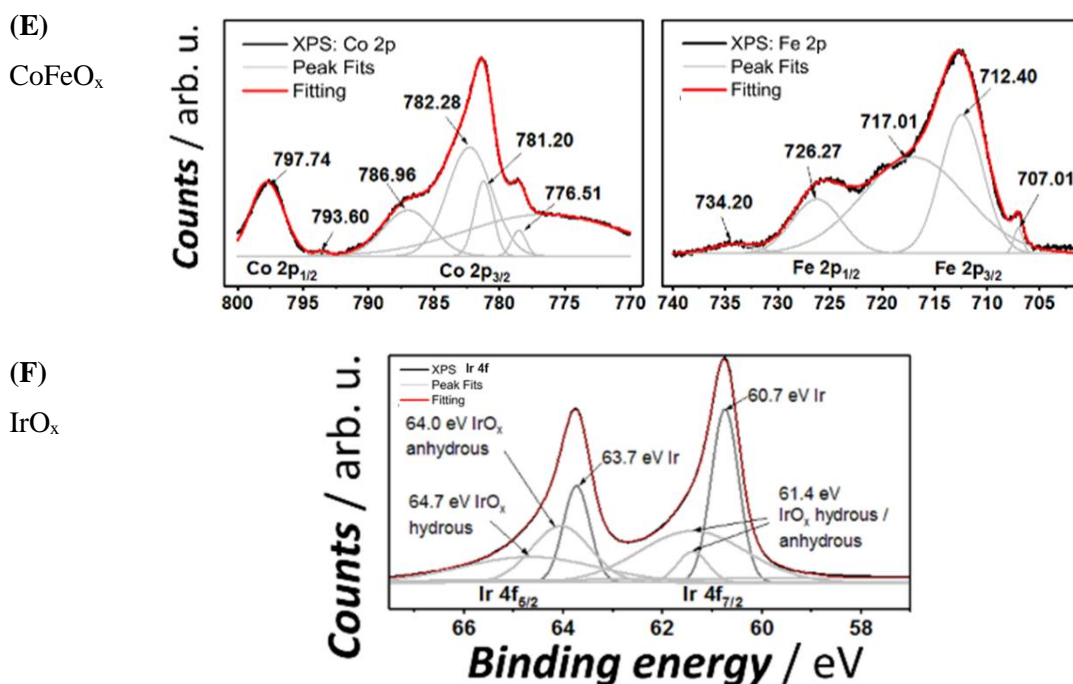


Figure 4.6. XPS spectra of (A) NiO_x, (B) CoO_x, (C) NiFeO_x, (D) CoNiO_x, (E) CoFeO_x, and (F) IrO_x. The spectra are shown in black, the fitting of the individual peaks and background are shown in grey, and the overall fitting is shown as a red line. Figures (A-C) are adapted with permission from ref. [144] and (D)-(F) are adapted with permission from ref. [90].

The corresponding XPS spectra of NiO_x, CoO_x, NiFeO_x, NiCoO_x, CoFeO_x, and IrO_x are presented in **Figure 4.6**. The NiO_x spectra show the main peak at 855.5 eV, which can be assigned to a superposition of the Ni 2p_{3/2} peaks of Ni(OH)₂ (855.2 eV) and of the NiOOH (855.8 eV) phase.¹⁸⁴ Division of the relative contribution of Ni²⁺ and Ni³⁺ turned out to be ambiguous and unnecessary, as the oxidation state changes, when applying different electrochemical potentials. In general, a shift towards the NiOOH phase is assumed at potentials >1.5 V vs RHE. Likewise, the film denoted as CoO_x consists also of more than a single phase. The spectra show (**Figure 4.6 (B)**) a distinct double 2p_{3/2} peak (780.4 and 782.8 eV) with an additional satellite peak (787.8 eV). Fitting this peaks by comparison with data from literature, the composition can be calculated to consist of ~17% Co(OH)₂, ~59% of CoOOH, and ~24% of a Co₃O₄ phase.¹⁸⁵ Looking at the XPS spectra (C) at binding energies between 880 eV and 850 eV (left spectra), there is a remarkable similarity with the spectra of NiO_x shown before, with the exception of one additional distinct peak at 852.7 eV. This additional peak can be attributed to a metallic nickel phase.¹⁸⁶ The Fe 2p spectra (right spectra) shows a pronounced peak at 711.7 eV. Due to the peak width, it is presumably an overlay of the 2p_{3/2} peaks of FeOOH, Fe₂O₃, and Fe₃O₄.^{187,188} Similar to the

case presented before, there are indications (peak at 707.0 eV) for a metallic (Fe) phase of the catalyst film.¹⁸⁹ Note, that these metallic phases are a result of the galvanic deposition method and can be assumed to oxidize during the first potential cycles reaching the OER regime. Integration of the Ni and Fe related peaks allowed to estimate (considering the atomic sensitivity factors) the Ni / Fe ratio as ~70% / ~30%. This is very close to the optimum reported in literature of ~75% / ~25%^{190,191}. The spectra of the film denoted as NiCoO_x (**Figure 4.6 (D)**) is well comparable to the previously investigated films of NiO_x (**Figure 4.6 (A)**) and CoO_x (**Figure 4.6 (B)**). A slight energy shift of ~0.2 eV might indicate an alloy phase. The atomic ratio Ni / Co was estimated as ~50% / ~50%. The spectra taken from CoFeO_x can be compared to the previously shown ones: the 2p Co peaks are very similar to those shown in the case of NiCoO_x and the 2p Fe spectra is comparable with the one taken for NiFeO_x. However, the 2p Co spectra features a small peak at ~777 eV indicating a metallic Co phase. Furthermore, Fe is present in a slightly higher oxidation state, which is *e.g.* visible at the increased intensities of the peaks corresponding to the Fe⁺³ phase. In the case of IrO_x, the binding energies were recorded in a range between 57 eV and 67 eV which corresponds to the 4f_{5/2} and 4f_{7/2} peak region. Analysis of these peaks suggests that a very thin (< 5 nm) oxide layer covers the iridium host crystal, as the signal of the metallic Ir peak is still predominant.^{192,193} Such a thin coverage is even beneficial, as metallic iridium has a better conductivity compared to its oxide phase.¹⁹³

To summarize, it has been shown that all these thin films have the almost perfectly desired composition.

4.1.6.2 Assessment of their ECSA

An essential requirement for the calibration of the new method is to start with electrodes with well-known ECSA. In principle, if the catalyst films would be perfectly flat (as it is the case *e.g.* for a single crystals), their ECSA could be approximated with the geometric surface area of the electrode. However, typically such oxide films are not 100% smooth, which results in a slightly larger ECSA compared to the geometric surface area. Therefore, roughness effects have to be taken into account. For this purpose, atomic force microscopy was applied, which allowed to assess the average roughness factor of the different catalyst thin films. The corresponding AFM images (see **Figure 4.7**) show the surface morphology of NiO_x, CoO_x, NiFeO_x, NiCoO_x, CoFeO_x, and IrO_x. While the surface of the of NiO_x, CoO_x, and IrO_x with the roughness factors of 1.15, 1.05 and 1.01, respectively, is quite smooth, the NiCoO_x NiFeO_x, and CoFeO_x with 1.45, 1.27, and 2.25, respectively, showed significantly larger roughness factors. Inserting these roughness factors and the geometric surface area of the disk electrode ($\sim 0.19635 \text{ cm}^2$) into **Equation 4.16** allowed to estimate the ECSA of the NiO_x-, CoO_x-, NiFeO_x-, CoFeO_x-, CoFeO_x-, and IrO_x-films as $\sim 0.226 \text{ cm}^2$, $\sim 0.202 \text{ cm}^2$, $\sim 0.249 \text{ cm}^2$, $\sim 0.285 \text{ cm}^2$, $\sim 0.442 \text{ cm}^2$, and $\sim 0.198 \text{ cm}^2$, respectively. In the case of Pt, the ECSA of the crystal was investigated *via* the adsorption of hydrogen (as explained in **Chapter 4.1.3.4**) prior to oxidizing its surface to PtO_x.

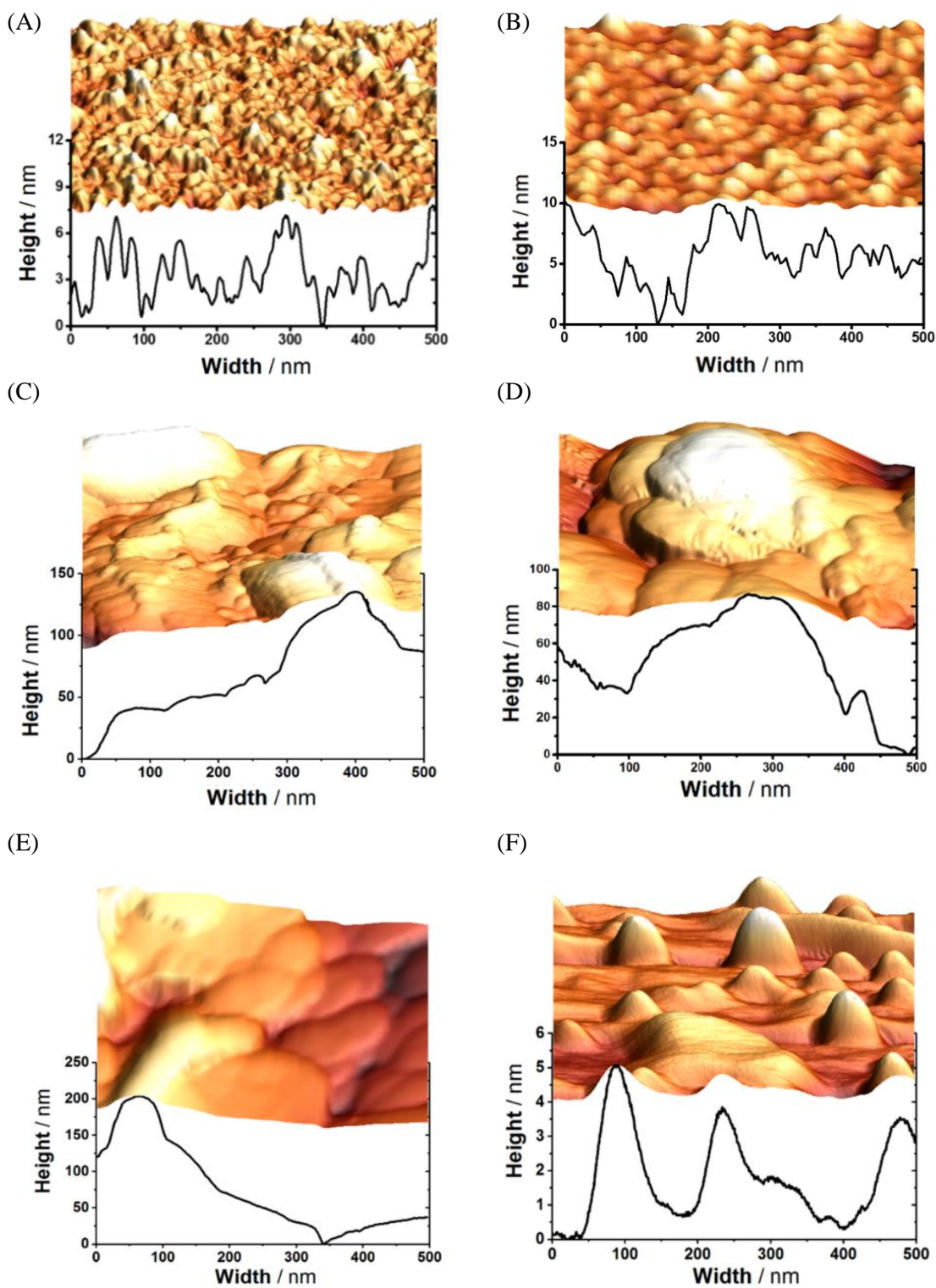


Figure 4.7. Surfaces profiles of (A) NiO_x, (B) CoO_x, (C) NiCoO_x, (D) NiFeO_x, (E) CoFeO_x, and (F) IrO_x thin films recorded with AFM. Note that, the y-axis are stretched compared to the x-axis for better visibility of the structure. (A), (B) and (D) are adapted with permission from ref.[144] and [90].

4.1.6.3 Determination of C_a'

The final step for the calibration procedure is to measure the specific adsorption capacitance and investigate its dependency on the applied potential. Therefore, for each catalyst material, a similar procedure was applied. Prior to the EIS measurement, the electrodes potential was cycled (50 mV s^{-1}) to activate the catalyst films. Afterwards, the potential was scanned slowly (1 mV s^{-1}) to the potential of the first EIS measurement. The intention of decreasing the scan rate was to ensure quasi-stationary conditions for the following measurements. Note that the electrolyte was constantly purged with Ar to maintain a low oxygen partial pressure in the bulk electrolyte in order to reduce the probability of O_2 bubble formation at the electrode. Additionally, the electrode was rotated (400 rpm). This activation procedure is depicted by **Figure 4.8** using the example of NiO_x . Three potential cycles between $\sim 0.93 \text{ V}$ and 1.73 V vs RHE were applied. After the third scan, which ended at 1.43 V , the potential is scanned linearly (1 mV s^{-1}) to 1.53 V , where the EIS measurements started^v. This procedure was similar for CoO_x , NiCoO_x , and PtO_x ; however, the cathodic limit was decreased to 1.63 V vs RHE in the case of CoFeO_x , NiFeO_x , and IrO_x , due to their higher activity that could have led to the formation of O_2 bubbles at higher current densities. The subsequent EIS spectra were recorded in 10 mV steps.

For each catalyst, a total number of 5 to 52 independent measurements were conducted. For reasons of clarity, **Figure 4.9** shows one representative EIS spectra for each catalyst at a potential close to the onset of the OER. Individual data points in the high frequency regime, which did not comply with KK-relation, were eliminated for further evaluation. All measurements around the onset of the OER have their “double semicircular” shape in common. The first imperfect semicircle at high frequencies is mainly determined by the double layer impedance and charge transfer resistance. It is typically smaller compared to the second semicircle, that is governed by the adsorption capacitance and the adsorption resistance. In case of NiCoO_x , IrO_x , and PtO_x , the first semicircle is barely visible due to the overlap of both semicircles. Therefore, it was important to ensure, that the fit followed the first one. The corresponding fitting curves are marked as red lines in each Nyquist plot, while the open squares represent the data points.

^v Note that a few measurements were extended to potentials below 1.53 eV .

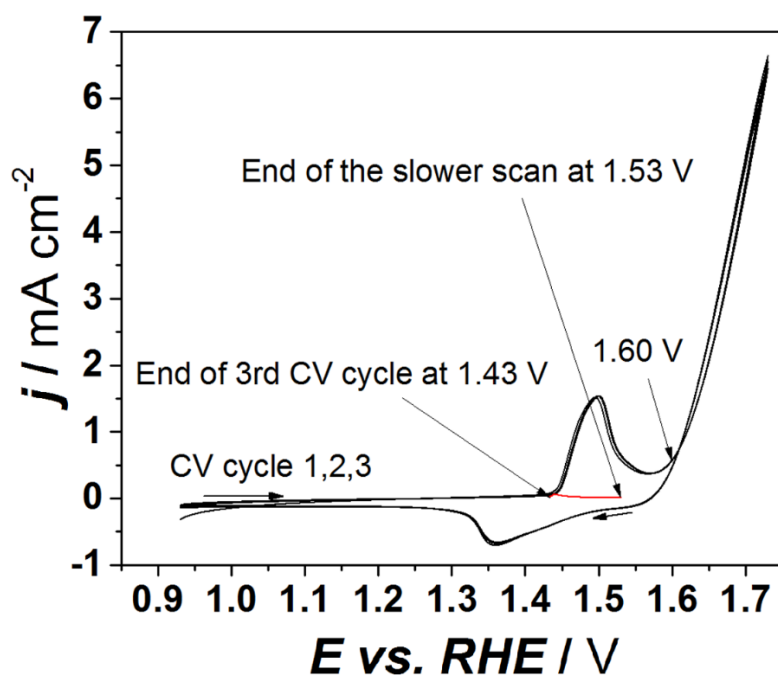


Figure 4.8. Preconditioning of the oxy-hydroxide films before the EIS measurement. The potential is cycled (scan rate 50 mV s^{-1}) in case of NiO_x thin films 3 times in order to fully activate them (\rightarrow). After the 3rd cycle, the scan rate was reduced to 1 mV s^{-1} (\rightarrow). Thereby, the film has time to oxidize and subsequent EIS measurements starting at 1.53 V can be performed in steady-state conditions. Adapted with permission from ref. [89].

The fitting using the EEC in **Figure 4.4** showed only low-mean-square deviations and the inaccuracy in the determination of the C_a' value was typically lower than $\sim 4 \%$. To investigate the dependency of the specific adsorption capacitance on the potential, C_a' values were estimated (from C_a) using **Equation 4.15** and plotted vs the applied potential, as can be seen in **Figure 4.10**. One can identify a general trend: at potentials far below the onset of the OER, C_a' is very low (or even zero) and starts to increase at a certain potential until it reaches a plateau. At this plateau, the C_a' value stagnates in a window, which can be between ca 30 mV (e.g. for NiFeO_x films) and ca 150 mV (NiO_x and CoO_x films). This behavior can be explained considering the definition of the adsorption capacitance ($C_a = q \frac{\partial \theta}{\partial E}$), as sketched in **Figure 4.11**: at lower potentials the surface coverage with adsorbate is quasi potential independent, while at a certain potential, close to the onset of OER, the coverage starts to increase gradually with the potential. We assume, that this increase in the first derivative of coverage can be attributed to an increase in the amount of electrocatalytic centers that successively activates and thereby facilitate adsorption on these

sites. At the “plateau” of C_a' , the majority of active centers have been activated and the surface coverage is linearly dependent on the applied potential. At even higher potentials, two phenomena can be expected: the ECSA becomes progressively fully covered, which means that $\frac{\partial\theta}{\partial E}$ and, therefore, also C_a' decreases. This behavior can be seen *e.g.* in the case of NiCoO_x, and IrO_x. Apart from that, one should not forget that oxygen is evolved at the electrode at these anodic potentials, which can lead to an occasionally fractional blockage of the electrode surface area by the gaseous phase. These fluctuating conditions impair the data quality of EIS spectra. This, in turn, impedes accurate fitting, leading to significant inaccuracies in the determined C_a' values at high anodic potentials. Thus, the optimum potential for evaluating the adsorption capacitance is found exactly at the point where the specific adsorption capacitance of the respective catalyst is “on the plateau” and locally potential independent. This optimum with the corresponding specific adsorption capacitance is highlighted in **Figure 4.10** and summarized in **Table 4.1**. Note, that the error bars are not a result of fitting accuracy. It originated from accounting multiple independent measurements for each of the catalysts. CoFeO_x can be considered as a special case, as no real plateau after an onset was detected. Presumably, such a plateau exists at potentials above 1.65 V. However, due to the strong noise caused by gas evolution, the data quality does not allow accurate determination of C_a' in this case. Hence, it makes sense to evaluate its spectra at 1.54 V, where the relative error of C_a' is the smallest.

These calibration values for C_a' form the basis for applying the newly developed method to real systems. In the following, the reliability of this method is shown in different relevant applications.

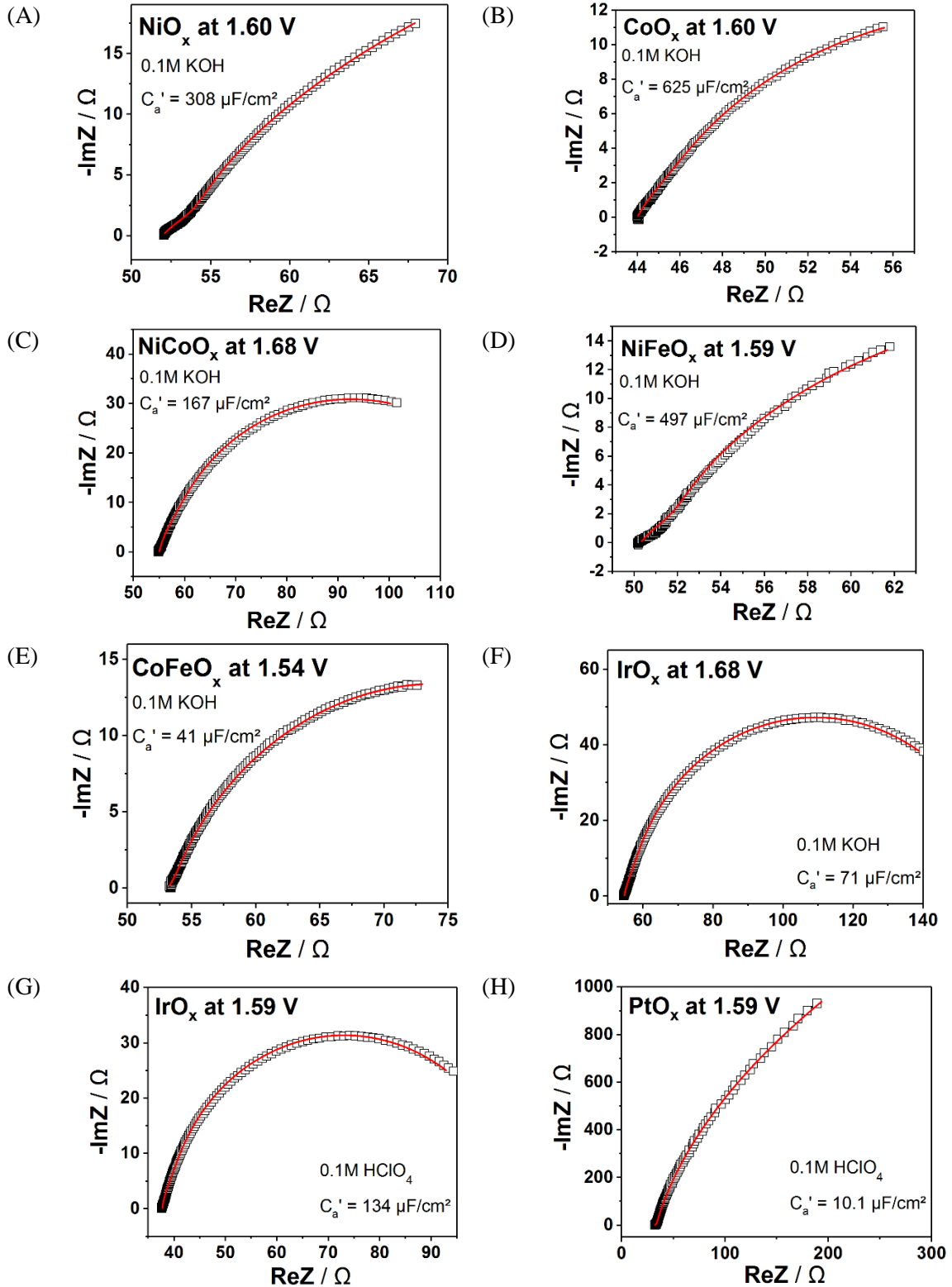


Figure 4.9. Nyquist plots of the different oxide materials recorded at the potentials indicated in **Table 4.1**. The fits (—) are based on the EEC shown in **Figure 4.4**. Note, that spectra (A)-(F) are recorded in Ar saturated 0.1 M KOH while spectra of (G) and (F) are recorded in Ar saturated 0.1 M HClO₄. Adapted with permission from ref. [90].

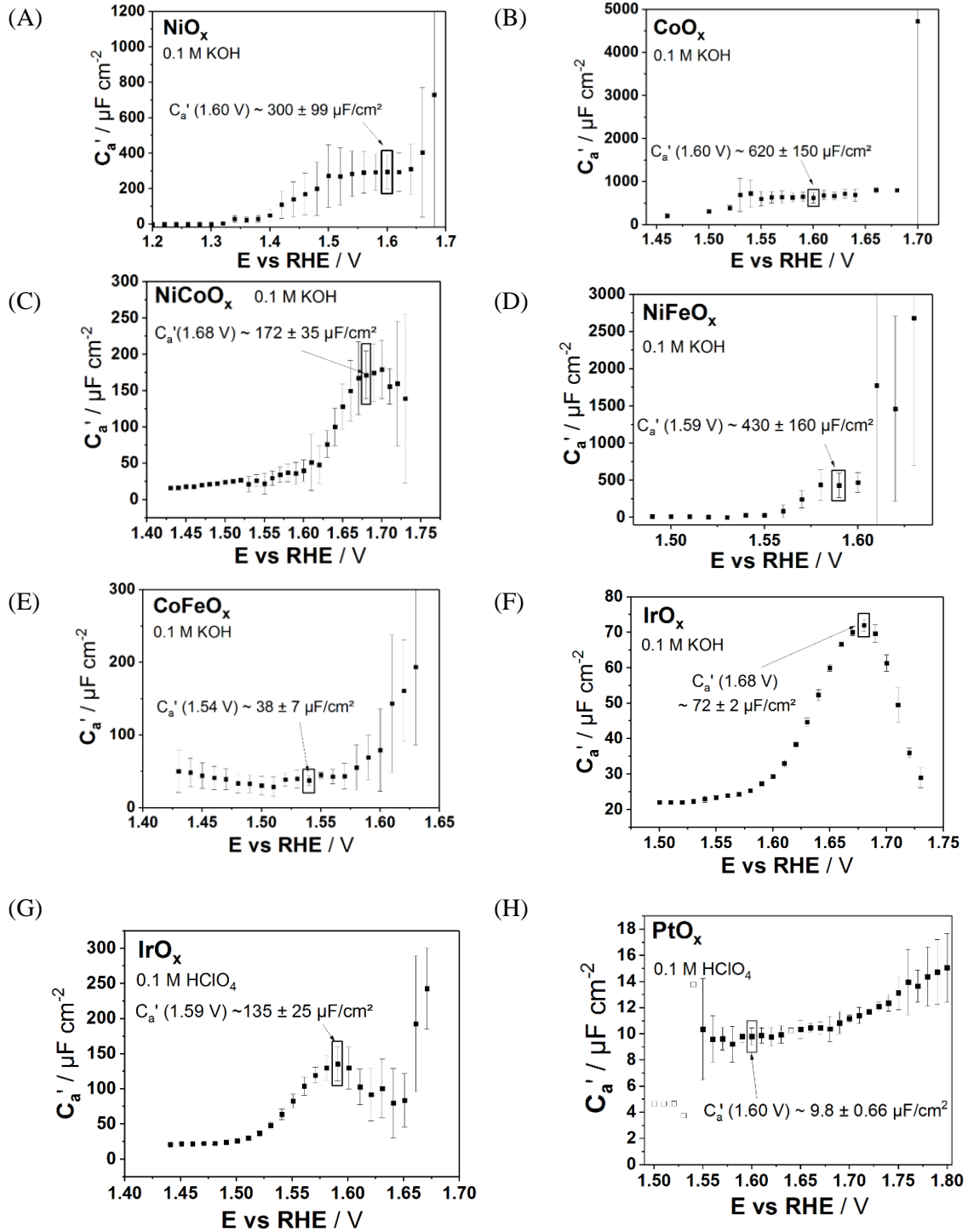


Figure 4.10. Specific adsorption capacitances as a function of the electrode potential recorded in 0.1 M KOH for (A) NiO_x, (B) CoO_x, (C) NiCoO_x, (D) NiFeO_x, (E) CoFeO_x, (F) IrO_x electrodes and in 0.1 M HClO₄ for (G) IrO_x and (H) PtO_x electrodes. The specific capacitances ($C'_a = C_a/\text{ECSA}$) were estimated by normalizing to the ECSA of the corresponding thin films. The ECSAs were determined, as described before. Error bars result from at least five independent experiments. Adapted with permission from ref. [90].

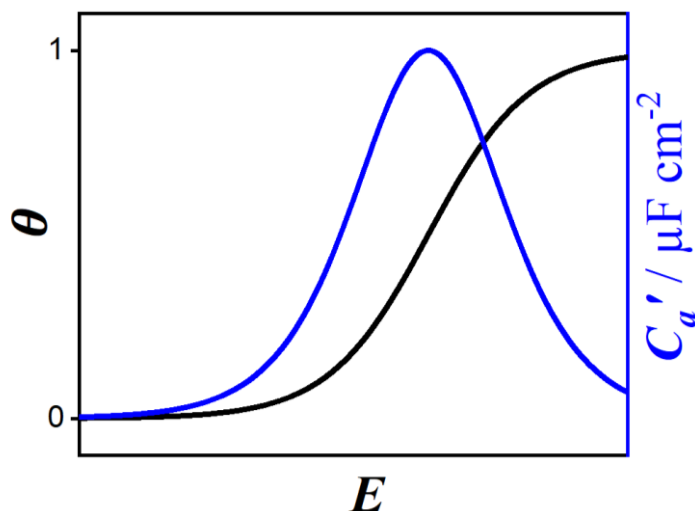


Figure 4.11. Schematic of an adsorption isotherm (—) and the related adsorption capacitance as a function of the potential (—). For simplicity, a Langmuir adsorption isotherm was used; however, it should be noted that adsorbate-adsorbate interactions modify the actual adsorption behavior¹⁹⁴. Moreover, it can be assumed, that a “complete” coverage might never be reached, as adsorbates are continuously “consumed” as the reaction proceeds. At low potentials the coverage is quasi potential independent, and C_a is therefore ~ 0 . The “plateau” in C_a' arises, when $\frac{\partial \theta}{\partial E}$ reaches a maximum.

Table 4.1. Specific adsorption capacitances of the oxide materials measured in 0.1 M KOH (NiO_x , CoO_x , NiFeO_x , NiCoO_x , IrO_x) and HClO_4 (IrO_x and PtO_x).

Catalyst	Potential (V vs RHE)	C'_a (μFcm^{-2})
NiO_x - KOH	1.60	300 ± 99
CoO_x - KOH	1.60	620 ± 150
NiFeO_x - KOH	1.59	430 ± 160
CoFeO_x - KOH	1.54	38 ± 7
NiCoO_x - KOH	1.68	172 ± 35
IrO_x - KOH	1.68	72 ± 2
IrO_x - HClO_4	1.59	135 ± 25
PtO_x - HClO_4	1.60	9.8 ± 0.66

4.1.7 Application

So far the principle of the new method and the calibration step has been discussed. However, the applicability and limitations of the method for real systems still needs to be investigated. Therefore, several different setups have been investigated starting with very fundamental experiments. First, the influence of the increase of the thickness of the NiO_x thin film on C_a is examined. Afterwards, the surface area of an unsupported (homemade) IrO_x catalyst is estimated *via* C_a and compared with the surface area determined *via* BET. Finally, the new method has been applied to a carbon supported catalyst: ECSA is assessed *via* C_a and compared to the surface area determined *via* conventional approaches.

Different thickness of NiO_x thin films

Variation of the catalyst film thickness was chosen as the first and very fundamental test for plausibility. The idea is that two almost identical catalyst films are deposited. However, one film has an increased thickness. A method sensitive to ECSA should show almost identical values for the surface area, if bulk properties do not significantly influence the method.

Therefore, one NiO_x film with an integrated charge of $Q_1 \sim 20 \text{ mC cm}^{-2}$ and a second one with $Q_2 \sim 21 \text{ mC cm}^{-2}$ were deposited and investigated *via* EIS. The corresponding Nyquist plots, measured at 1.60 V *vs* RHE, are shown in **Figure 4.12** The first curve, intersecting with the x-axis, at $\sim 54 \Omega$, corresponds to the thinner film. It has a comparable shape, but, differs in magnitude from the second curve with the thicker catalyst film. A shift in uncompensated resistance can be partially attributed to the larger film resistance due to the increased film thickness and the relatively low conductivity of the NiO_x. Fitting, using the EEC shown in **Figure 4.4** allowed to determine C_a as $63.1 \pm 1.2 \mu\text{F}$ and $63.7 \pm 1.2 \mu\text{F}$ for the thinner and thicker film, respectively. Hence, within the scope of measurement accuracy, these measured C_a values are identical, which was expected, as the ECSA should not significantly change. However, looking at the “double layer capacitance”, substantial difference was observed: the thicker film depicted with $C_{dl}(1.60 \text{ V}) = 2.71 \pm 0.01 \text{ mF s}^{-1}$ is approximately twice the double layer capacitance of the thinner film $C_{dl}(1.60 \text{ V}) = 1.36 \pm 0.01 \text{ mF s}^{-1}$. Normalizing C_a values by the estimated ECSA (accounting roughness factors) - obviously these specific adsorption capacitances ($\sim 279 \mu\text{F cm}^{-2}$ and

$\sim 282 \mu\text{F cm}^{-2}$) are very similar to those previously (during calibration) determined. To conclude, it can be seen as a first indication that there is a significantly better correlation between C_a and the ECSA, than between the latter one and C_{dl} .

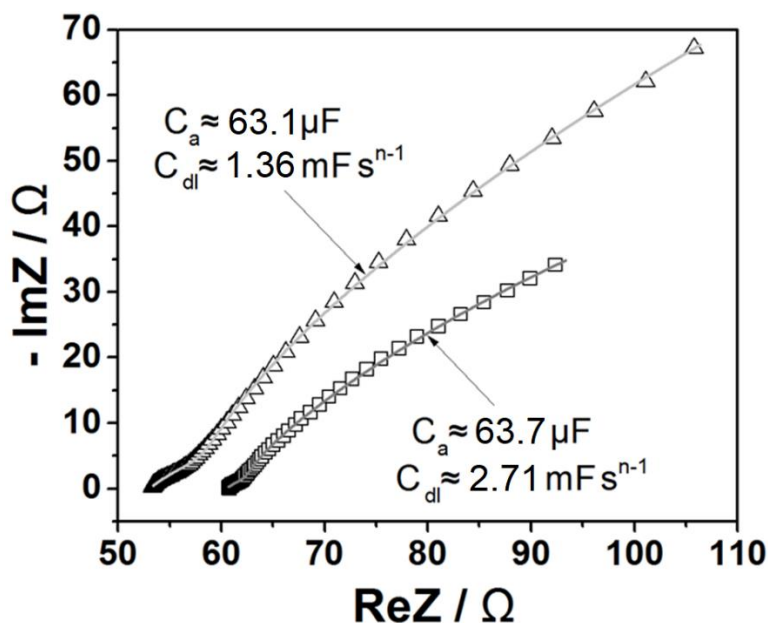


Figure 4.12. EIS spectra taken of two slightly different NiO_x films in Ar saturated 0.1 M KOH at 1.60 V. Open triangles and squares correspond to the thinner and thicker film, respectively. In both cases, the fitting shows only marginal deviation. Important fitting parameters (double layer (pseudo) capacitance and adsorption capacitance) are given for both fits. Obviously, C_a values are almost identical, while C_{dl} values are different by a factor of two for just a slightly different film. Adapted with permission from ref. [89].

Nanostructured IrO_x

In PEM electrolyzers, IrO_x is typically used as an anode electrocatalyst due to its decent activity and excellent long-term stability. Often, this catalyst is used without any support in order to increase long-term stability. In the following, the application of the new method to determine the ECSA of nanostructured catalysts with significantly larger surface area (larger than the geometric surface area of the electrodes) is investigated. The following investigation is based on the results of Ms. Yin's Master thesis (Prof. Ifan Stephens research group), including the synthesis and characterization of an IrO_x electrocatalyst. She assessed the surface area of the catalyst (powder) by BET. Subsequently, an ink of this catalyst was

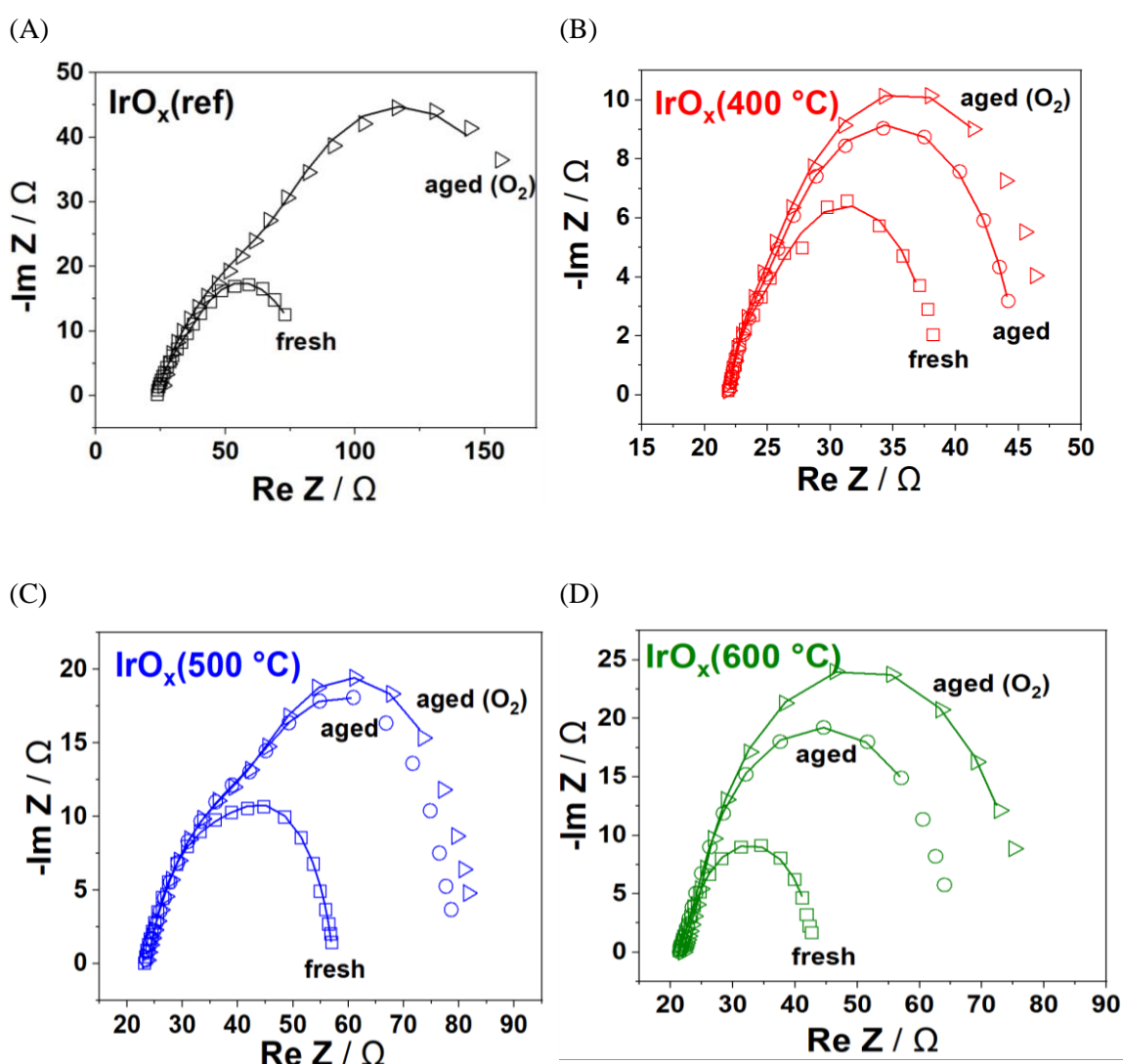
prepared and deposited on a (glassy carbon) RDE tip and electrochemical measurements were conducted using 0.1 M HClO₄. The measurement protocol included EIS measurements at 1.60 V, which were intended to be used to correct the ohmic resistance of the electrolyte. The synthesis procedure involved an annealing step that was varied (400 °C, 500 °C and 600 °C) resulting in three slightly different catalysts denoted as IrO_x(400 °C), IrO_x(500 °C), and IrO_x(600 °C). Additionally, a commercial catalyst (Ir black, Johnson Matthey, UK), which was oxidized (denoted as IrO_x(ref)) was examined. The (mass) specific surface areas (SSAs) were determined as ca 189 m² g⁻¹, ~167 m² g⁻¹, ~128 m² g⁻¹, and ~35.6 m² g⁻¹ *via* BET for IrO_x(400 °C), IrO_x(500 °C), IrO_x(600 °C), and IrO_x(ref), respectively. Note that, for technical reasons, the determination of surface area of IrO_x after deposition on the electrode using BET was not possible. For each catalyst, three different situations could be compared: first, the as-synthesized, fresh catalyst (denoted as “fresh”), directly after the preconditioning, second, after an accelerated degradation test, which involved 30000 potential cycles (1.3 V to 1.7 V *vs* RHE 500 mV s⁻¹) at 20 °C (denoted as “aged O₂”), and third, after removing the oxygen bubbles from the electrodes surface (denoted as “aged”). This is interesting in several respects, as it not only allows to compare the ECSA/mass with the SSA determined *via* BET, but also shows the great potential of this method to investigate the loss of ECSA due to aging and due to blockage by a non-conducting gas phase separately. **Figure 4.13** shows the Nyquist plots for each catalyst, at the beginning of life, after aging, and after the removal of oxygen bubbles. The corresponding fitting curves show normalized mean square deviations of less than 3% and low uncertainty of C_a values (< 7%). As expected, there is a small difference in the uncompensated resistance for the aged samples, which are partially blocked with the gaseous phase. The adsorption capacitances are summarized in **Table 4.1**. To determine the ECSA of these catalysts, these adsorption capacitances were divided by the specific adsorption capacitance measured at 1.60 V, $C_a'(1.60 \text{ V}) = 130 \mu\text{F cm}^{-2}$ (see **Figure 4.10**). Considering the targeted electrode loading of 3.92 μg (20 μg cm⁻²), the ECSA normalized to mass was estimated (see **Table 4.2**). As shown in **Figure 4.13**, ECSA/mass determined *via* EIS is well comparable to the BET determined SSA for each catalyst. However, the ECSA determined for IrO_x(400 °C), IrO_x(500 °C), and IrO_x(ref) is slightly increased compared to the BET determined surface area. This is not expected, as one can imagine, that some pores in the catalyst might be accessible to gas but not to electrolyte. Thus, one would assume, that the ECSA should rather be smaller than the BET surface area (as can

be seen in the case of IrO_x(600 °C)). However, one should not forget, that the deposition procedure involves drop casting of 10 µl of the ink onto an electrode. This ink consists of a dispersion of catalyst particles in water and isopropanol and has an imperfect distribution of these particles in the vessel, with typically more particles at the bottom. This results in a catalyst loading, which is dependent on the position of the pipette, when extracting the ink for deposition. Hence, one could hypothesize, that the ink was taken more from the bottom of the vessel resulting in an underestimation of catalyst mass deposited on the electrode. Nevertheless, a good agreement between both methods was found. Regarding the aged catalysts, one can observe a decrease in the ECSA by ~ 1/3 which can be explained with *e.g.* particle detachment or Ostwald ripening. Further, one can see, that a certain part (6 – 9 %) of the catalyst surface got temporarily blocked during the aging procedure. This partial blockage can lead to an accelerated aging behavior of the electrode, as previously shown by El-Sayed and co-workers.¹⁹⁵ In principle, this method would allow to make a vast study on the blockage of active catalysts surfaces, due to evolving gases. This could lead to an optimization of catalyst surfaces, which are less prone to get blocked.

Table 4.2. Adsorption capacitances and ECSAs (normalized to mass) of different IrO_x electrocatalysts. Values are shown before aging (“fresh”) and after 30000 potential cycles. After the aging, the electrode was partially blocked with small O₂ bubbles, which is denoted as “aged(O₂)”. To assess the ECSA without this fractional blockage, the visible bubbles were removed manually, and the electrode was kept at open circuit potential for at least 1h, allowing the microscopic bubbles to dissolve in the electrolyte, before C_a was re-measured. This is denoted as “aged”.

	IrO _x (ref)	IrO _x (400 °C)	IrO _x (500 °C)	IrO _x (600 °C)
fresh	214.5 µF	1014.2 µF	916.0 µF	531.4 µF
□	42.1 m ² g ⁻¹	199.0 m ² g ⁻¹	179.7 m ² g ⁻¹	104.3 m ² g ⁻¹
aged (O₂)	51.40 µF	574.2 µF	555.8 µF	361.2 µF
▷	10.1 m ² g ⁻¹	112.7 m ² g ⁻¹	109.1 m ² g ⁻¹	70.9 m ² g ⁻¹
aged	Not available	630.1 µF	609.2 µF	383.9 µF
○		123.7 m ² g ⁻¹	119.5 m ² g ⁻¹	75.3 m ² g ⁻¹

To conclude, these experiments demonstrated the accuracy, as well as the wide range of application for this in-situ measurement of ECSA. In this case, the surface area of an inactive material (with $\sim 0.196 \text{ cm}^2$), which was the glassy carbon electrode was relatively small compared to the ECSA of the catalyst (1.65 cm^2 to 7.8 cm^2). Hence, it makes sense, to investigate the contribution of inactive support on the measured C_a in additional experiments.



(E)

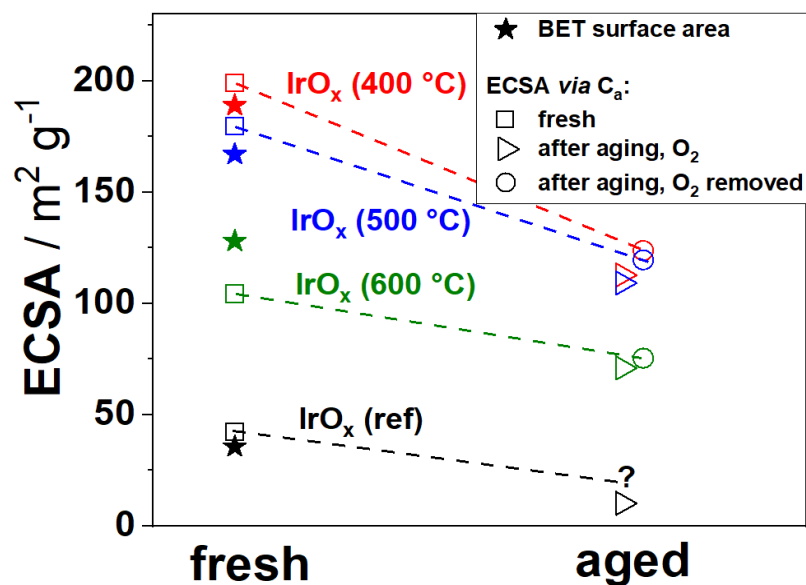


Figure 4.13. Analysis of EIS spectra measured at 1.60 V vs RHE in 0.1 M HClO₄. Four IrO_x catalysts, of which three are “homemade” (IrO_x(400 °C), IrO_x(500 °C), and IrO_x(500 °C)) at the Imperial College London and one commercial catalyst (here denoted as IrO_x(ref)) were investigated. The measurements on “fresh” catalysts are represented by squares, the aged catalysts partially blocked with oxygen bubbles (denoted as “aged (O₂)”) are represented with triangles and the measurements conducted using the aged catalyst after removal of the oxygen bubbles (denoted as “aged”) are represented with circles. The solid lines in (A)-(D) correspond to the fitting curves, which allowed to determine the adsorption capacitances and thereby the ECSA values presented in (E). The dashed lines in figure (E) between the ECSA of the “fresh” and the “aged” catalysts show the drop of the ECSA. Due to technical issues, there was no measurement performed for IrO_x(ref), after removal of the oxygen at the surface. Its expected ECSA is marked with a question mark. The stars in (E) represent the surface areas determined by BET.

Supported nanoparticles

The previous examples did not deal with the problem of inactive support. However, as discussed before, this method should be well applicable to determine the ECSA also in such cases, in contrast to most of the state-of-the-art techniques. Two commercial catalysts were selected: Pt and Ir nanoparticles, which were both supported on Vulcan XC72 carbon (BET

surface area: $\sim 250 \text{ m}^2 \text{ g}^{-1}$)¹⁹⁶. RDE tips were coated (see **Chapter 3.1.3**) with these catalysts and the surface of the catalysts were oxidized electrochemically. For convenience, they are denoted in the following as PtO_x/C and IrO_x/C. For verification, the ECSAs determined *via* C_a were compared to surface area determined by other, well-established methods.

PtO_x/C was chosen, as it shows a very small C_a' , which is beneficial to investigate possible effects of the support. In addition, the Pt surface area can be precisely determined *via* CO_{ads} stripping voltammetry. For the determination of ECSA of PtO_x, the calibration curve shown in **Figure 4.10 (H)** suggests evaluating C_a at $\sim 1.60 \text{ V vs RHE}$. During the measurements, which were performed using Ar saturated 0.1 M HClO₄, the electrode was rotated at 2500 rpm. The intention of introducing this forced convection was to reduce the surface blocking due to evolving oxygen, which is in principle more likely in this case of a porous catalyst layer. The Nyquist plot recorded at 1.60 V is presented in **Figure 4.14 (A)**. A good fitting quality was achieved, utilizing the same EEC as in the examples before. All fitting parameters, with the exception of the adsorption resistance, are well defined. R_a is very big in comparison to R_U and R_{ct} (~ 5 orders of magnitude), which is not surprising, as PtO_x is not good catalyst for the OER and not active at 1.60 V. In principle, in this special case, the branch with R_a in the EEC would not even be needed to achieve a decent fitting. The formation of *OOH, in contrast to the adsorption of *OH and *O, is energetically unfavorable, which hinders the OER¹⁹⁷. Though, the adsorption of *OH and *O manifests itself in a C_a of $\sim 31 \mu\text{F}$. The ECSA was estimated as $\sim 3.2 \text{ cm}^2$ by dividing C_a by $C_a' = 9.8 \mu\text{F}/\text{cm}^2$. The ECSA of the same sample was investigated by CO_{ads} stripping voltammetry. As shown in **Figure 4.14 (B)**, the associated integrated charge was determined as $\sim 1.31 \text{ mC}$, corresponding to an ECSA of $\sim 3.14 \text{ cm}^2$. Considering the uncertainty of the stripping method and probing C_a , one can state that both methods yield identical results within a deviation $< 2\%$ for the ECSA. This is an experimental validation that the inactive carbon support, which has a surface area of $\sim 40 \text{ cm}^2$, does not influence the C_a value. This is a great advantage, as this proves that the measurement only accounts for the active surface area at the applied potential. Additionally, C_a was evaluated in a wider potential range (1.56 to 1.80 V vs RHE). **Figure 4.14 (C)** compares the C_a' values of the PtO_x/C catalyst with the calibration values determined using the PtO_x thin film. Between ~ 1.575 and $\sim 1.625 \text{ V vs RHE}$ both curves are almost identical. However, at the potentials above 1.70 V they start to separate: while C_a' for the disk gradually starts to increase, it decreases for the case of

the PtO_x/C catalyst layer. This could be explained by the fact, that this porous structure might be more prone to get partially blocked by oxygen bubbles, which get trapped in this structure, thereby causing a temporary decrease of ECSA. This effect becomes more dominant at higher current densities achieved at large overpotentials.

IrO_x/C was chosen as an application related example since state-of-the-art electrolyzers often utilize IrO_x as the anode electrocatalyst. Even though the trend goes to the avoidance of carbon supports in order to increase long-term stability, there is usually a non-active material, such as carbon paper, titanium screen, or sintered titanium frit, that is at least partially in contact with the liquid electrolyte (or ionomer). The carbon support of the commercial Ir/C (Premetk) used here serves as an example for various inactive materials, which can be in contact with electrolyte. Apart from that, determining the ECSA of IrO_x/C is non-trivial and often problematic. As discussed in **Chapter 4.1.3**, it is possible to estimate the ECSA of Ir *e.g. via* hydrogen adsorption/desorption. However, when Ir is oxidized, then the situation becomes more complex and the ECSA is determined *e.g.* by Hg adsorption. This creates the risk, that the whole setup gets contaminated. Moreover, so-called pseudo-capacitance method^{91,198} is obviously not applicable. As the catalyst was taken from an earlier opened stock, it was unknown whether the surface of the Ir/C had been partially oxidized leading to inaccuracies when using hydrogen adsorption for ECSA determination. Therefore, a TEM based analysis was applied to estimate the ECSA and verify the results obtained from EIS. Durst et al.¹⁹⁹ showed, that such a TEM based study for nanostructured Ir catalysts yields similar results to those of *e.g.* hydrogen adsorption.

To assess the ECSA of the nanostructured IrO_x/C using the newly developed method, EIS data were recorded at 1.59 V vs RHE. Fitting these impedance data (see **Figure 4.14 (D)**) allowed to determine the adsorption capacitance as $C_a \sim 623 \mu\text{F}$. The active surface area was determined by dividing C_a by the C'_a ($135 \mu\text{F cm}^{-2}$) as $\sim 4.6 \text{ cm}^2$. TEM images of the catalyst shown in **Figure 4.14 (E)** and **(F)**, allowed to estimate the ECSA of the IrO_x/C catalyst. The ECSA of a comparable PtO_x/C catalyst with the same electrode loading is $A_{\text{PtO}_x/\text{C}} \sim 3.5 \text{ cm}^2$.

Assuming spherical particles and accounting for different particle diameter (averaged over mass) and densities, the ECSA of IrO_x/C ($A_{IrO_x/C}$) can be estimated⁹⁰:

$$\begin{aligned}
 A_{IrO_x/C} &\approx A_{PtO_x/C} \cdot \frac{\sqrt[3]{d_{PtO_x/C}^3}}{\sqrt[3]{d_{IrO_x/C}^3}} \cdot \frac{\rho_{Pt}}{\rho_{Ir}} \cdot (1 - \alpha) \\
 &= 3.5 \text{ cm}^2 \cdot \frac{2.75 \text{ nm}}{1.796 \text{ nm}} \cdot \frac{21.45 \text{ g cm}^{-3}}{22.40 \text{ g cm}^{-3}} \cdot (1 - \alpha) \\
 &\approx 5.131 \text{ cm}^2 \cdot (1 - \alpha)
 \end{aligned} \tag{4.17}$$

Here, ρ_{Pt} and ρ_{Ir} are the densities of Pt and Ir under the assumption that solely the surface of the nanoparticles is oxidized. $\sqrt[3]{d_{PtO_x/C}^3}$ and $\sqrt[3]{d_{IrO_x/C}^3}$ are the average diameters (by mass) of the nanoparticles and α ([0,1]) accounts for a reduction of the ECSA due to particle agglomeration. The reference catalyst showed almost no agglomerations. However, as can be seen in the TEM images (**Figure 4.14 (E), (F)**), IrO_x/C features several agglomerates, which could lead to an overestimation of the surface area determined by TEM. Remarkably, the ECSA resulted from both methods is differing by just ~10% (~4.6 cm² vs ~5.1 cm²). This, however, can be explained by agglomeration of the IrO_x nanoparticles. Moreover, this method allowed to determine the mass specific surface area (ECSA/mass) of the commercial IrO_x/C catalyst as ~117.6 m²/g_(IrO_x) for the first time with decent accuracy. To conclude, reasonable values for the ECSA were found and again no influence of the support material was detected. This demonstrates the applicability of the newly developed method especially for cases of active and inactive materials being in contact with the electrolyte.

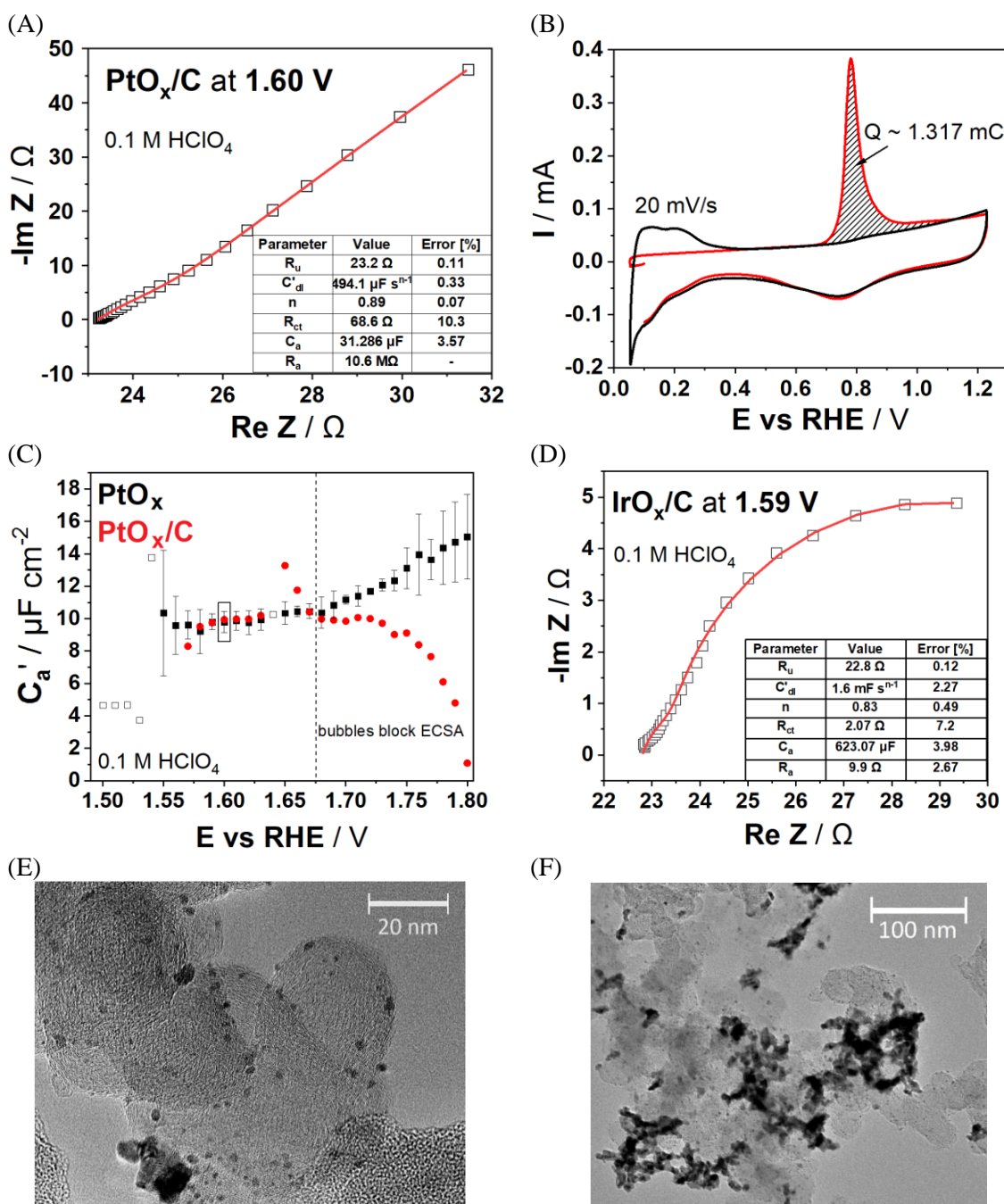


Figure 4.14. Surface area determination *via* the evaluation of the C_a and *via* control experiments. (A) EIS spectra of a PtO_x/C coated glassy carbon electrode, recorded at 1.60 V vs RHE (2500 rpm) in Ar saturated 0.1 M HClO₄. The data points are displayed as black squares, while the corresponding fit is represented with the red line. The fitting parameters are shown in the inset. The (B) CO_{ads} stripping voltammogram the same electrode in the same electrolyte recorded using a sweep rate of 20 mV s⁻¹. The red curve corresponds to the first scan, whereas the black curve relates to the following cycles to subtract the capacitive background. (C) C_a' as a function of applied potential of PtO_x/C (red circles) and a bulk Pt(pc) disk (black rectangles) electrode, is denoted as PtO_x. (D) Nyquist representation of EIS spectra recorded at 1.59 V using an IrO_x/C modified electrode. The fitting curve is represented with the red solid line and the fitting parameters can be found in the inset. (E) and (F) are TEM images of IrO_x/C. The grey larger particles are the support, while the smaller black particles are the IrO_x nanoparticles. Adapted with permission from ref [90].

4.2 Evaluation of the intrinsic activity of electrocatalysts under industrially relevant conditions

As discussed in the previous sections, determination of the real ECSA is one of the major problems for benchmarking the activity of typical electrocatalysts. Especially when performing lab scale activity evaluation, another serious problem has to be faced: actual operation conditions in energy conversion devices are often significantly differ from simulated test conditions. For instance, OER catalysts are often benchmarked at room temperature in relatively diluted electrolytes, such as *e.g.* 0.1 M KOH and at relatively small current densities (in the order of mA cm⁻²). Contrary, PEM and alkaline electrolyzers are operated at elevated temperatures (typically 60-80 °C) using solid or concentrated electrolytes and using significantly higher current densities (in the order of A cm⁻²). Benchmarking under such industrially relevant conditions would result in a strongly improved transferability of the results, as extrapolation of the performance from low to high overpotentials is often inaccurate. Moreover, the ohmic resistance of the electrolyte and the formation of a non-conducting phase due to evolving gases are typical obstacles for benchmarking at high current densities in the lab scale. Recently, Ganassin and co-workers⁹⁵ used homemade microelectrodes (STM tips) to partially overcoming these experimental issues. In detail, while benchmarking the OER activity of an CoO_x electrocatalyst, they were able to reach a realistic current density of ~550 mA cm⁻². Inspired by these results, we further extended this test protocol to mimic real industrial conditions by simply utilizing microelectrodes at elevated temperatures in the concentrated electrolyte (5.4 M KOH).

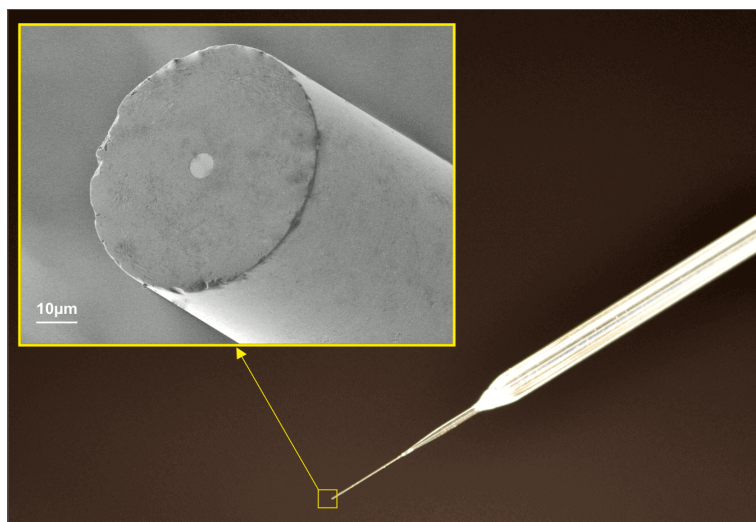


Figure 4.15. Typical SEM image of a tip of the microelectrode, as used for SEM. The inset shows the magnified fragile tip of this microelectrode. Reprinted with permission²⁰⁰. Copyright 2019 Thomas RECORDING GmbH.

Albeit several possible advantages of such a setup are noted, typical electrochemical cells are not designed for operation under such harsh conditions. In particular, glass corrosion in concentrated alkaline electrolytes is frequently reported in the literature,^{201,202} which could also account for other glass-made parts included. Moreover, temperature gradients within the glassware can cause strain, ultimately leading to fracture. Initially, this danger of fracture was underestimated and relatively fragile STM tip microelectrodes (Thomas Recording, Germany)^{203,204} were employed, similarly to the ones used by Ganassin and co-workers⁹⁵ (see **Figure 4.15**). Although, being well-suitable for the application at room temperature and mild environment, the fragile tip of such microelectrodes tends to break within few hours, when heated to 80°C. In replacement, resilient Pt microelectrodes (25 µm diameter) with relatively thick glass coating (~1.5 mm) were purchased from CH Instruments (see **Figure 3.3 (C)** in **Chapter 3.1.2**). However, in order to verify stability of these microelectrodes, examination of the corrosion behavior will be described in the following subsections.

In order to investigate the applicability of the aforementioned test protocol, benchmarking of different state-of-the-art OER and HER electrocatalysts under industrially relevant conditions will be discussed in this chapter.

It should be particularly emphasized, that the investigations were also extended towards novel thin film electrocatalysts based on metal-organic frameworks. These show exceptionally high activity and stability, even under highly corrosive test conditions. The large part of the results presented in this chapter was published: “S. Watzele, Y. Liang, A.S. Bandarenka. Intrinsic activity of some oxygen and hydrogen evolution reaction electrocatalysts under industrially relevant conditions. *ACS Applied Energy Materials* 1(2018) 4196–4202” and “W. Li, S. Watzele, H.A. El-Sayed, Y. Liang, G. Kieslich, A.S. Bandarenka, K. Rodewald, B. Rieger, R.A. Fischer. Unprecedented high oxygen evolution activity of electrocatalysts derived from surface-mounted metal-organic frameworks *J. American Chem. Soc.* 141 (2019) 5926–5933” (see **Chapter 6.3**)

4.2.1 Benchmarking of conventional OER/ HER electrocatalysts

To investigate the activity and durability of the state-of-the-art OER catalysts under industrially relevant conditions, NiO_x, CoO_x, and NiFeO_x were selected as model systems, mainly due to their particular relevance in electrolysis and the simple synthesis procedure. In favor of the specific test conditions, microelectrodes served as the substrates for electrocatalyst thin films. To ensure a film growth limited to the Pt microelectrode, excluding the surrounding glass frame, the films were deposited electrochemically. Experimental details on the deposition of such thin films are given in **Chapter 3.1.3** and **Chapter 4.1.6.1**.

To further examine the applicability towards the HER at similar conditions, Pt(pc) was benchmarked using the plain microelectrode. As reported in the literature, decorating the surface of Pt with single Ni islands can significantly improve its HER activity¹⁴⁶. Therefore, such electrodes were prepared by underpotential deposition of Ni on the microelectrode (for experimental details see **Chapter 3.1.3**) and were examined accordingly.

4.2.1.1 Determination of ECSA

Accurate assessment of a catalyst's electrocatalytic activity requires detailed knowledge of the ECSA. The roughness factor and the geometric area of the electrode were used to estimate the ECSA of the catalysts examined. As it was impossible to investigate the morphology of the film directly due to the small dimensions of the microelectrode, the film properties were determined after deposition on macroscopic Pt(pc) disk electrode (see **Chapter 4.1.5**). It has to be noted, that this procedure does not perfectly mimic the film morphology on the microelectrode. However, this can be considered more accurate than a typical normalization to the geometric surface area of the electrode. In the case of pure Pt and Ni-decorated Pt electrodes, the currents were normalized to the ECSA determined from H_{upd} , which turned out to be almost identical to the geometric area ($\sim 4.91 \cdot 10^{-6} \text{ cm}^2$). Moreover, the Ni islands were not easily visible on the macroscopic Pt(pc) disk and did not change the roughness factor.

4.2.1.2 Activity evaluation under industrially relevant conditions

Initial benchmarking of aforementioned electrocatalysts (NiO_x , CoO_x , and NiFeO_x) was performed in 0.1 M KOH solutions at room temperature in order to ensure reproducibility with previously published results. In a next step, the concentration of the electrolyte was increased to 5.4 M KOH (corresponding to $\sim 30 \text{ wt.}\%$), being similar to typical concentrations used in the alkaline water electrolyzers. In addition, the temperature was increased stepwise from 25 °C to 80 °C. As depicted in **Figure 4.16**, the higher electrolyte concentration results in an increase of the measured activity at 25°C. This effect is very pronounced in the case of NiFeO_x and NiO_x , where the enhancement of the current density is already visible at “low” current densities (*e.g.* at 10 mA cm^{-2}). This observation suggests, that in case of these two catalysts, there might be an interaction of cations as so-called spectator species, which improves the reaction kinetics. Similar influence of the spectator cations on the reaction rate was reported for various electrocatalytic reactions on different model surfaces.^{74,205} For instance, Garcia and co-workers recently showed, that the activity of nickel-oxyhydroxide indeed depends on the nature of cations present in the electrolyte.²⁰⁶ Coinciding with the results of this thesis, we assume that this relation not

only applies to the cation species, but also to the concentration. Surprisingly, in the case of CoO_x , this effect on the activity is slightly reversed at the onset of OER. Conversely, at higher current densities (*i.e.* $>100 \text{ mA cm}^{-2}$), the system with concentrated electrolyte outperforms the one with 0.1 M KOH, which can be at least partially attributed to the better conductivity of the highly concentrated electrolyte.

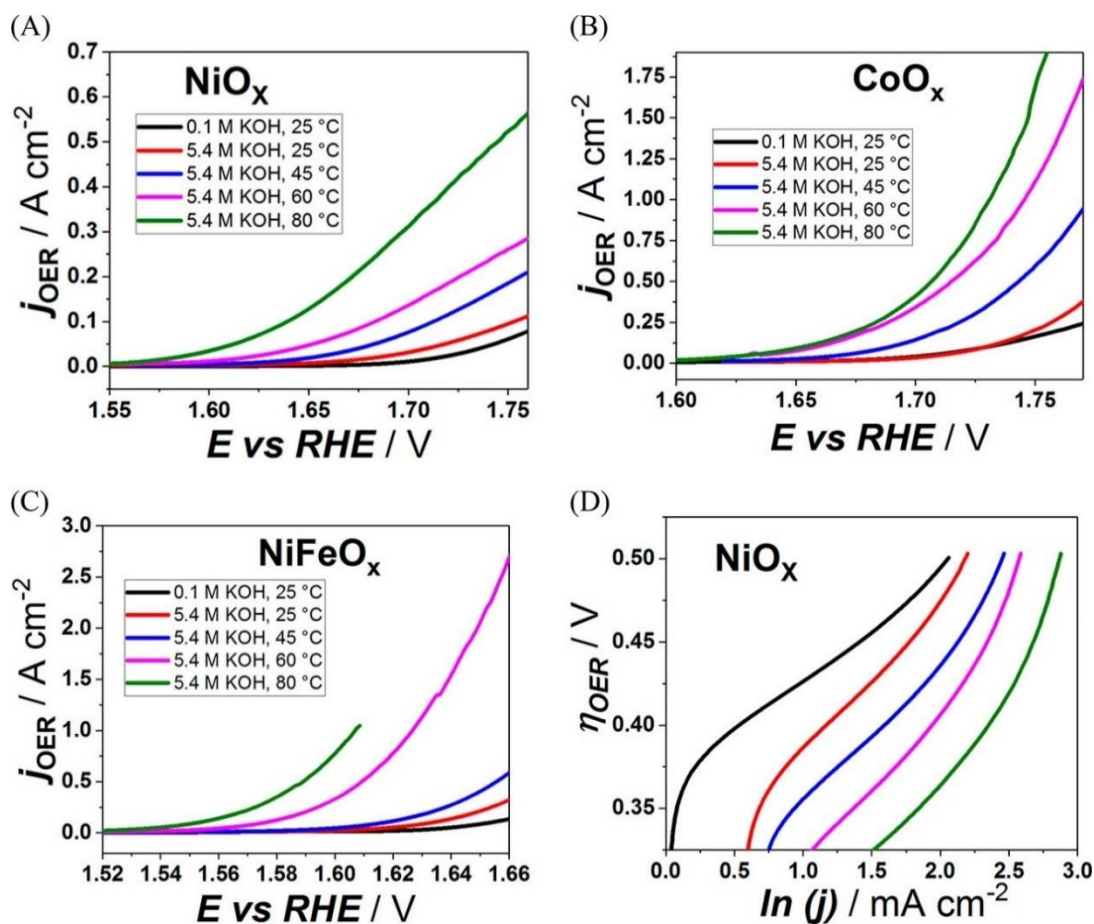


Figure 4.16. Anodic polarization curves of (A) NiO_x , (B) CoO_x , and (C) NiFeO_x , recorded in Ar-saturated alkaline electrolytes at different temperatures (scan rate 50 mV s^{-1}). Note that Pt microelectrodes served as the substrates for the catalyst thin films. Therefore, the curves are (almost) *iR*-free even without further compensation. All current densities are normalized to the ECSA of the corresponding catalyst, which was estimated through evaluation of the roughness factor. (D) Exemplary Tafel plots of the NiO_x thin film. Obviously, its slope changes over the whole potential range. The color code can be extracted from (A). Adapted with permission from ref. [144].

In accordance with the temperature dependence of the Butler-Volmer kinetics, an additional increase in the activity can be observed at elevated temperatures (see **Equation 28**). Moreover, an additional Nernst-shift of the equilibrium potential and an enhanced diffusion rate can be expected, which further improve the reaction speed. In absolute values, current densities of several A cm^{-2} can be reached, which even exceeds the requirement of state-of-the-art electrolyzers. As previously discussed, accurate benchmarking at these current densities is not possible with classical methods (*e.g.* using an RDE and macroscopic electrodes). This means, that in such cases, the values measured at low current densities need to be extrapolated in order to roughly estimate the catalyst performance at higher current densities. Herein, one can investigate the “Tafel behavior” of the catalysts, to evaluate the accuracy of such an extrapolation. Exemplary, **Figure 4.16 (D)** shows the Tafel representations for the NiO_x thin film at different electrolyte conditions. Obviously, none of the graphs shows a linear dependence. In fact, the graphs show varying slopes at almost every point, indicating, that an extrapolation would be inaccurate and highlights the necessity of benchmarking at higher current densities.

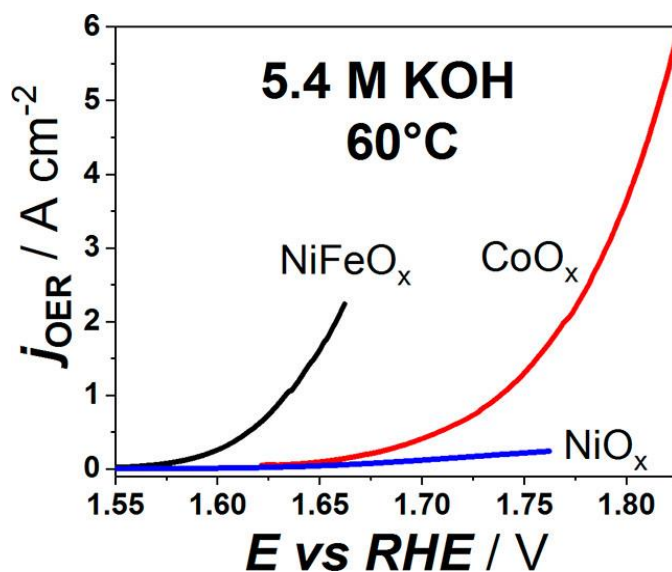


Figure 4.17. Anodic OER polarization curves of NiFeO_x , CoO_x and NiO_x , recorded in Ar-saturated 5.4 M KOH at a temperature of 60 °C. Scan rate: 50 mV s^{-1} . In terms of OER activity the following order can be observed: $\text{NiFeO}_x > \text{CoO}_x > \text{NiO}_x$. Adapted with permission from ref [144].

Table 4.3. Impact of temperature and electrolyte concentration on the OER activity of NiO_x, CoO_x and NiFeO_x. Here, * denotes measurements performed in 0.1 M Ar-saturated KOH, while all other measurements were performed in Ar-saturated 5.4 M KOH.

Catalyst	T / °C	E _{100 mA cm⁻²} / V	E _{500 mA cm⁻²} / V	I _{1.60 V} / mA cm ⁻²	I _{1.65 V} / mA cm ⁻²	I _{1.75 V} / mA cm ⁻²
NiO _x	25*	1.772±0.003	-	0.8±0.05	1.3±0.08	61±3.7
	25	1.753±0.008	-	3±0.4	7.5±0.9	95±12
	45	1.712±0.002	-	5±0.2	19±0.7	186±6.5
	60	1.683±0.001	-	11±0.3	48±1.2	262±6.6
	80	1.639±0.0005	1.745±0.001	34±0.4	128±1.4	523±5.7
CoO _x	25*	1.730±0.004	1.825±0.009	7.3±0.7	11.1±1.1	164±16
	25	1.729±0.002	1.779±0.002	8.6±0.5	11.1±0.7	205±13
	45	1.689±0.002	1.743±0.003	10.1±0.7	26.8±2.0	592±44
	60	1.658±0.004	1.715±0.005	14.3±1.7	76.7±9.5	1150±140
	80	1.623±0.003	1.707±0.003	20.0±1.5	92±6.9	1690±130
NiFeO _x	25*	1.654±0.001	-	16±0.9	90±5.4	-
	25	1.633±0.003	-	22±2.8	211±27	-
	45	1.615±0.002	1.656±0.002	45±3.7	402±33	-
	60	1.576±0.001	1.609±0.002	330±21	2054±133	-
	80	1.553±0.002	1.589±0.003	777±77	-	-

In **Figure 4.17**, the polarization curves of the aforementioned catalysts recorded at 60 °C in 5.4 M KOH are compared. Obviously, NiFeO_x shows by far the highest activity followed by CoO_x and NiO_x. Compared to NiFeO_x, the reaction onset of CoO_x is shifted by ~70-80 mV to more anodic potentials. Interestingly, the polarization curve of the NiO_x catalyst exhibits a less steep (quasi-)exponential increase, even at high potentials. This could indicate a lower density of active sites in comparison to NiFeO_x and CoO_x, when measured in 5.4 M KOH at 60 °C. To get an overview on the impact of temperature and electrolyte concentration on the OER activity, all recorded experimental values are summarized in **Table 4.3**.

As described before, microelectrodes can be used as a versatile tool to benchmark the activity of typical OER electrocatalysts used in alkaline electrolyzers. In turn, the question arises, if this procedure is also applicable to other reactions, such as the HER occurring at the cathode side of an electrolyzer. In this case, catalysts are typically compared to Pt. A way to further tune the HER activity of Pt, was proposed by Markovic in 2011¹⁴⁶. In detail, a ~7-times enhancement of the HER activity of Pt(111) in alkaline media was achieved through the decoration with Ni islands¹⁴⁶. Accordingly, three different electrodes were prepared and evaluated in concentrated electrolyte (5.4 M KOH) at 60 °C. One Pt microelectrode, denoted as “Ni_{UPD} on Pt”, was decorated using underpotential deposition of Ni, that was stopped before a monolayer was formed. A second electrode, denoted as “Ni_{OPD} on Pt”, was treated similarly. However, an additional short cathodic pulse was applied in order to galvanically deposit larger Ni islands. Cathodic potential scans (scan rate: 50 mV s⁻¹) of these three electrodes (“Pt”, “Ni_{UPD} on Pt”, and “Ni_{OPD} on Pt”) recorded in alkaline media at 60 °C are depicted in **Figure 4.18**. As expected, the Ni-modified surfaces outperform plain Pt (**Figure 4.18 (A)**). As visible in the figure, the electrodes with higher Ni loading showed the highest HER activity in the low current density region. Surprisingly, the predicted trend only holds true up to ~2 A cm⁻².

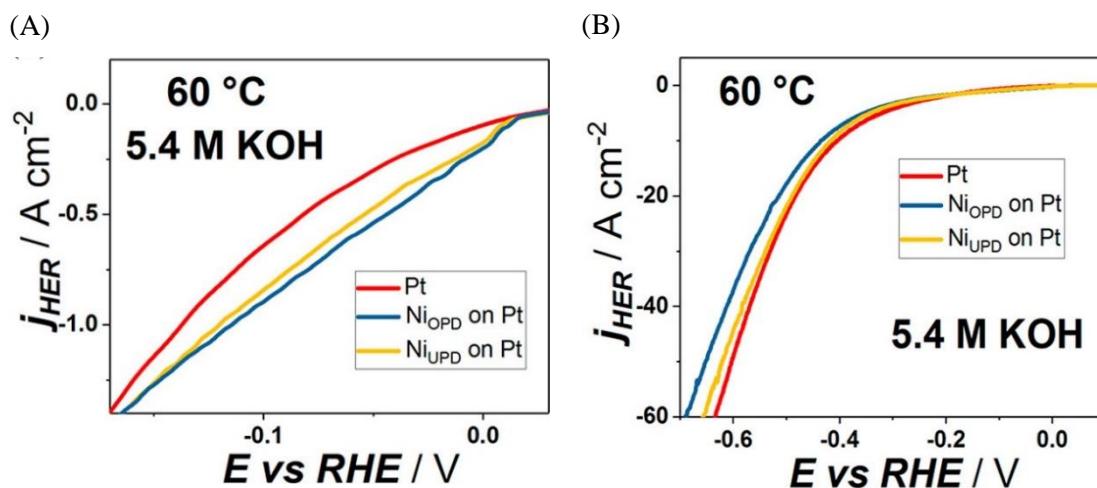


Figure 4.18. Cathodic polarization curves of different plain and Ni-decorated Pt microelectrodes, recorded in 5.4 M KOH at 60 °C in a (A) small and (B) large current density range. “Pt” corresponds to the untreated, clean Pt(pc) microelectrode. “Ni_{UPD} on Pt” and “Ni_{OPD} on Pt” corresponds to the microelectrodes decorated with Ni islands, as described in the main text. Adapted with permission from ref [144].

As shown in **Figure 4.18 (B)**, at larger current densities the trend is reversed, and the plain Pt electrode slightly outperforms the Ni decorated electrodes. One can only speculate about the reason of this unexpected transition: the key to the increased activity is the interplay between Ni, where the dissociation of water is promoted, and Pt, where the reaction intermediates are likely recombined into molecular H₂. At high current densities, the surface diffusion of adsorbed reaction intermediates from Ni to Pt might be limited and the effective blockage of Pt surface by Ni could outweigh the bifunctional effect, which results in a lower overall performance at high current densities. Regardless of the reason for this transition in the performance, this finding can be considered important for cathode material design: according to the electrode properties and reaction conditions (*e.g.* catalyst loading and applied current density), the specific material design can be tailored. However, regarding the methodology, one observes that current densities up to $\sim 100\ A\ cm^{-2}$ can be

easily achieved with low noise level, which shows the great potential for benchmarking at high currents^{vi}. The measured activities are summarized in **Table 4.4**

Table 4.4. Summary of activity data of Pt-based HER electrocatalysts, recorded at 60 °C in Ar-saturated 5.4 M KOH electrolyte.

Catalyst	$E_{0.5 \text{ A cm}^{-2}}$ / mV	$E_{2 \text{ A cm}^{-2}}$ / mV	$E_{5 \text{ A cm}^{-2}}$ / mV	$I_{100 \text{ mV}}$ / mA cm ⁻²	$I_{200 \text{ mV}}$ / mA cm ⁻²
Pt	-81.79±0.001	-209.03±0.003	321.11±0.002	-640±9	-1842±27
Ni _{OPD}	-43.82±0.003	-225.98±0.006	353.98±0.005	-896±35	-1719±69
Ni _{UPD}	-54.01±0.006	-219.10±0.011	343.93±0.010	-842±67	-1783±142

As mentioned in the beginning, it is important to ensure stability of the microelectrode under the harsh experimental conditions, especially concerning the above-mentioned glass corrosion. In particular, corrosion of the glass sheathing around the tip would have a big impact on the measurements. For instance, an ablation of just 6.25 μm (of glass) could cause a doubling of ECSA, as the side of the Pt gets partially exposed to the electrolyte. Therefore, following all benchmarking experiments, the tip of the microelectrode was investigated using an optical microscope, as depicted in **Figure 4.19**. No protruding of the tip was observed and no significant glass corrosion was visible even after the exposure to these harsh conditions. In contrast, other publications report relatively fast corrosion rates, which could be explained by the different type of glass used to produce the microelectrodes.

^{vi} Note, that **Figure 4.18 (B)** also just shows a section of the polarization curve and focuses on the relevant part.

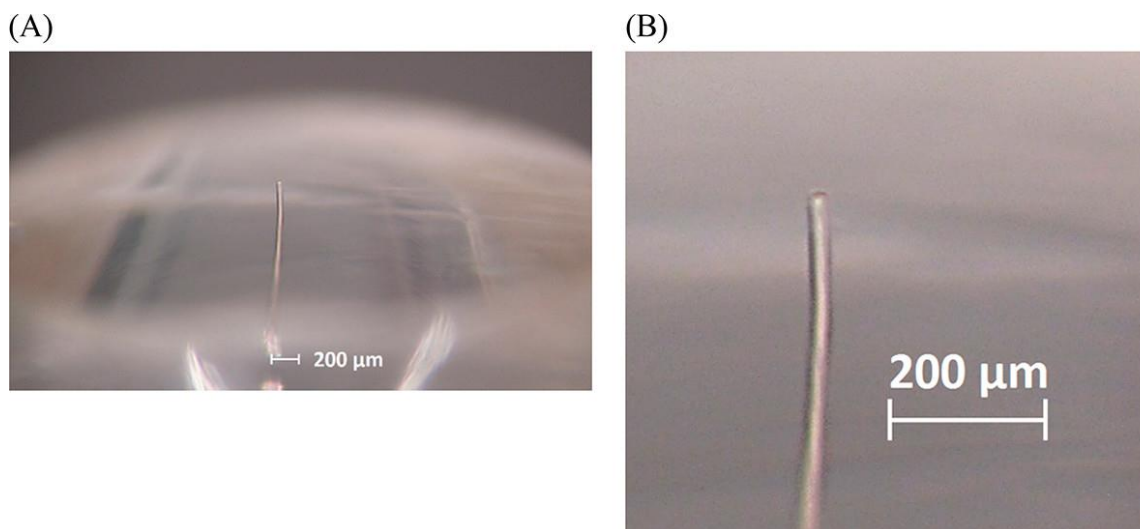


Figure 4.19. Optical microscopy images of the microelectrode tip after OER/ HER benchmarking in concentrated KOH at elevated temperatures. No protruding of the metallic tip out of the glass can be observed, indicating that glass corrosion does not affect the measurements. Adapted with permission from ref. [144].

Briefly, in this section we showed that the usage of microelectrodes is a powerful tool to benchmark the activity and stability of catalysts at industrially relevant conditions. In case of the OER, several A cm^{-2} and in case of HER up to 100 A cm^{-2} were reached without significant noise level. An unexpected non-trivial effect of electrolyte concentration and temperature was found, which justifies the importance to evaluate the catalysts under industrial relevant conditions. Further, evaluation of corresponding Tafel plots showed that extrapolation of the data obtained at low current densities is often inaccurate. Additionally, we observed that the superior HER kinetics of Ni-decorated Pt surfaces compared to pure Pt largely depends on operation conditions. Even though the literature reports indicate glass corrosion at high temperatures and in concentrated electrodes, we found that some Pt microelectrodes remain stable even under highly corrosive conditions, which justifies their application in the lab scale experiments.

4.2.2 Benchmarking the OER performance of novel MOF-based electrocatalysts

In the previous chapter, benchmarking of three state-of-the-art OER electrocatalysts under industrially relevant conditions was performed. These catalysts served as a reference for the next generation electrocatalysts. In the following, a novel and highly active OER electrocatalyst is benchmarked similarly. The catalyst was synthesized in the group of Prof. Roland Fischer (TUM) in cooperation with Dr. Weijin Li. This catalyst is derived from surface-mounted metal organic frameworks (SURMOFs), which were grown with a layer-by-layer technique using the electrode as the substrate. Immersion to an alkaline electrolyte resulted in leaching of the organic linkers and subsequent transformation of the film. The synthesis and characterization of this catalyst was recently published as a collaborative work between the “Chair of Inorganic and Metal-organic Chemistry” and the chair of “Physics of Energy Conversion and Storage (ECS)” (both TUM) in ” W. Li, S. Watzel, H.A. El-Sayed, Y. Liang, G. Kieslich, A.S. Bandarenka, K. Rodewald, B. Rieger, R.A. Fischer. Unprecedented high oxygen evolution activity of electrocatalysts derived from surface-mounted metal-organic frameworks. *J. American Chem. Soc.* 141 (2019) 5926–5933”. This section is based on this publication but focuses on the electrochemical part performed at ECS. In detail, this includes the activity and stability evaluation of the SURMOF thin films under industrially relevant conditions. However, the synthesis and characterization of this catalyst are presented briefly for better understanding.

4.2.2.1 Synthesis and Characterization

The synthesis was performed as described in **Chapter 3.1.3**. A relatively high level of crystallinity of the fresh SURMOF was evident through the x-ray diffraction (XRD) pattern, shown in **Figure 6.1** (see **Appendix**). Scanning electron microscopy (SEM) imaging and AFM revealed a sheet-like structure of the film, as shown in **Figure 4.20 (A)-(F)**. As one might expect, this structure is more pronounced when the amount of deposition cycles is increased from 10 to 50. However, after immersing the catalyst in alkaline solution (0.1 M KOH), a significant change was observed. As depicted in **Figure 4.20 (G)-(L)**, the

sheet-like structure is almost gone. This can be explained by leaching out the organic linker, which results in a collapse of the structure.

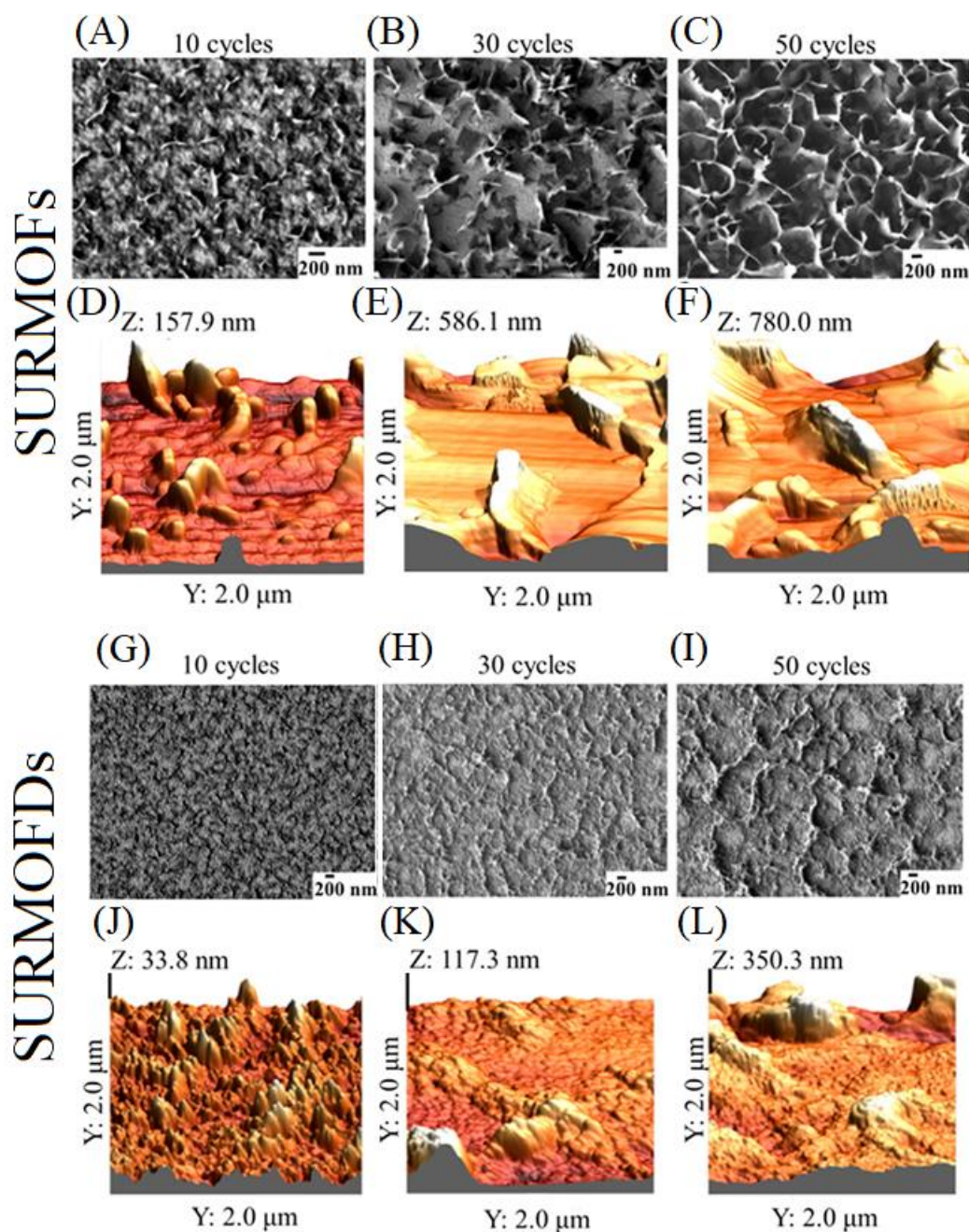


Figure 4.20. Investigation of the morphology of SURMOFs and SURMOFDs after different amount of deposition cycles. For each film, SEM and AFM pictures are shown before and after immersion in 0.1 M KOH. Each column presents one film. Row (A)-(C) and row (G)-(I) present SEM pictures of SURMOFs and SURMOFDs, respectively. Row (D)-(F) and row (J)-(K) are the corresponding AFM pictures. Adapted with permission from ref. [149].

XRD (**Figure 6.1**) showed that the film changed to a more amorphous structure, which supports this hypothesis. Additional measurements (attenuated total reflection spectroscopy and XPS) further confirms that the linkers partially leached out. For this work, it is mainly important to note, that an amorphous mixed metal hydroxide is formed, with a certain degree of BDC still being present in the structure.¹⁴⁹ These surface mounted metal organic derivatives are abbreviated as SURMOFDs, in the following.

4.2.2.2 Benchmarking Electrocatalytic Activity

For the activity evaluation, thin films of the SURMOFD-based electrocatalyst were prepared using Au-coated quartz crystal microbalance (QCM) chips as a substrate. These allowed to monitor the growth rate during film synthesis and the absolute mass deposited. These substrates, however, have a relatively large diameter (1 cm) and could not be rotated during electrochemical measurements. Herein, it has to be noted, that although the substrates were immersed vertically into the electrolyte, small oxygen bubbles might have partially blocked the electrode, which could lead to an underestimation of measured activities. The activity enhancement of the SURMOFD thin films was compared to the bare substrate and the activity of the substrate coated with the SAMs.

As depicted in **Figure 4.21 (A)**, the electrocatalytic activity of the substrate and the SAMs treated substrate were negligible compared to the activity of the SURMOFDs towards the OER. The two anodic peaks observed in the polarization curve of the SURMOFD can be attributed to the oxidation of Ni^{2+} to Ni^{3+} and Co^{2+} to Co^{3+} . Note that all the current densities are normalized to the geometric electrode area, not to the real ECSA, which is presumably much larger, due to the nanostructured nature of the SURMOFD film. Nevertheless, the determination of mass deposited on the substrate was very accurate, due to the usage of the quartz crystal microbalance.

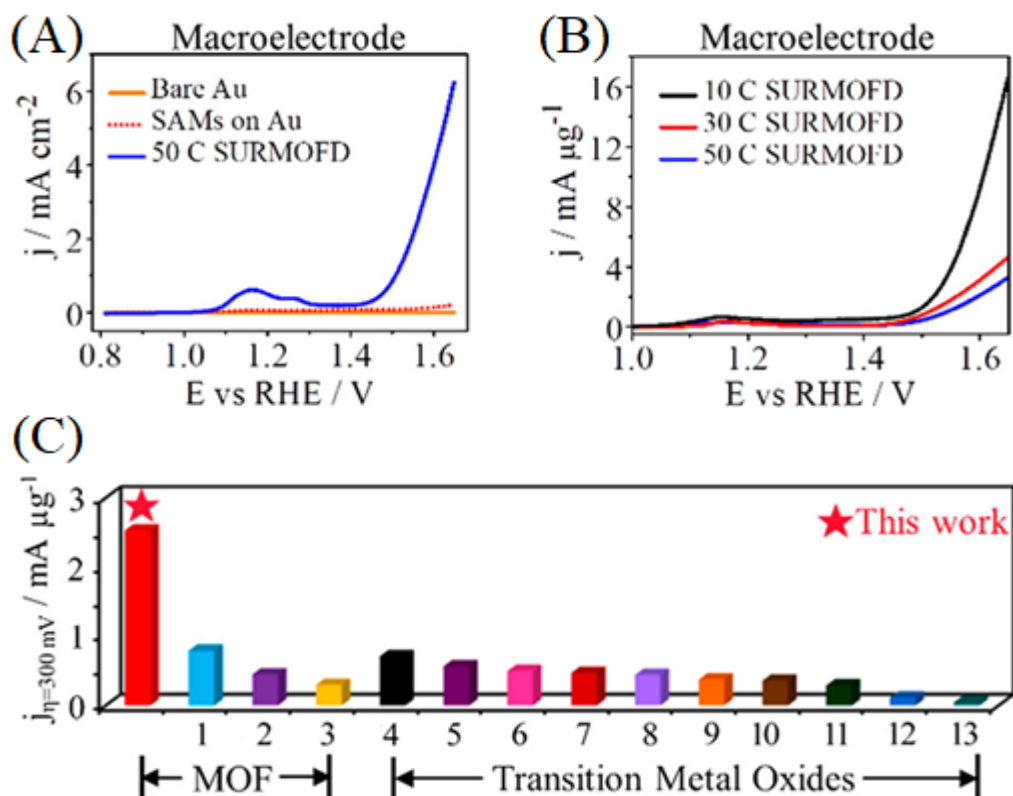


Figure 4.21. Benchmarking of the electrocatalytic activity towards the OER. (A) Polarization curves (normalized to geometric electrode area) of a 50 layered SURMOFD film, the Au(pc) substrate and SAMs, recorded in O_2 -saturated 0.1 M NaOH at 25 °C. The scan rate was 20 mV s^{-1} . Obviously, the OER activity does not originate from the substrate. (B) Comparison of polarization curves of SURMOFDs, which were produced with 10, 30, and 50 deposition cycles respectively. Note that these values are normalized to the catalyst's mass. (C) Comparison of the mass activity of a 10-layer SURMOFD film with the mass activity state-of-the-art OER catalysts reproduced from the literature. All activities are evaluated at an overpotential of 300 mV. (1-3) are MOFs and (4-13) are transition metal oxide hydroxide materials, all published recently and measured under similar conditions. “(1) $\text{Fe}_3\text{-Co}_2$ ²⁰⁷, (2) [M(BDC)] nanosheets (M = Ni^{2+} , Co^{2+})²⁰⁸, (3) M-MIL-53 (M = Co, Mn)²⁰⁹, (4) G-FeCoW²¹⁰, (5) $\acute{\alpha}$ -CoVO_x²¹¹, (6) Fe-Co-P²¹², (7) Ni-Fe-O mesoporous nanowire network²¹³, (8) $\text{CoFe}_2\text{O}_4/\text{C}$ ²¹⁴, (9) NiFe-LDH*²¹⁵, (10) $\text{Ba}_{0.5}\text{Sr}_{0.5}\text{Co}_{0.8}\text{Fe}_{0.2}\text{O}_{3-\delta}$ ²¹⁶, (11) IrO_2 ²¹⁷ (12) $\text{NaNi}_{0.9}\text{Fe}_{0.1}\text{O}_2$ ²¹⁸, (13) $\text{Co}_3\text{O}_4/\text{CoP}$ ²¹⁹ (asterisk (*) indicates experiments carried out under N_2 .”¹⁴⁹ Adapted with permission from ref. [149].

The influence of film thickness on the mass activity is presented in **Figure 4.21 (B)**. As expected, the mass activity of the thinnest (10 deposition cycles) SURMOFD film shows the best activity, followed by the films prepared with 30 and 50 deposition cycles, since the conductivity of SURMOFD films is typically limited by the functional groups^{220,221}. Moreover, we assume that the thinner SURMOFD films exhibit larger SSA. Compared to some of the best state-of-the-art OER catalysts, **Figure 4.21 (C)** points out the exceptionally high OER activity of the SURMOFD electrocatalyst. The origin of this enhanced activity, which is significantly higher than typical for NiCo oxyhydroxide films reported in literature⁹², still needs a more detailed investigation, for instance using DFT. Such calculations typically utilize model systems, which are not easy to elaborate considering partially amorphous SURMOFD structure. Nevertheless, we assume that strains induced by the remaining binders leads to optimal binding energies between certain surface sites and the reaction intermediates.

In order to confirm, that the measured currents really correspond to the OER and not to any side reaction, such as leaching of BDC, RRDE measurements were conducted. Therefore, the potential of the disk was cycled between 0.8 and 1.65 V, while the ring potential was fixed to 0.7 V. As shown in **Figure 4.22 (A)**, the redox peak can interfere with activity measurements, if too high scan rates (here 50 mV s⁻¹) are applied. Therefore, the following polarization curves were recorded at a scan rate of 2 mV s⁻¹. The exact OER onset potential was difficult to determine, but apparently at ~1.5 V oxygen reached the ring. However, it cannot be excluded that oxygen was already produced at slightly lower electrode potentials. To investigate the Faradaic efficiency of the catalyst, a constant current of 0.4 mA was applied to the disk, while the current at the ring ($E_{ring} = 0.7$ V) was monitored. As depicted in **Figure 4.22 (B)** an average current of ca 79.4 μ A was measured at the ring. This allowed to estimate the Faradaic efficiency FE , using $FE = I_{ring}/(I_{disk} \times N)$ and the factor $N \sim 0.2$, to be $\sim 99.4\%$ ²²². Herein we conclude, that the measured current indeed corresponds to the OER.

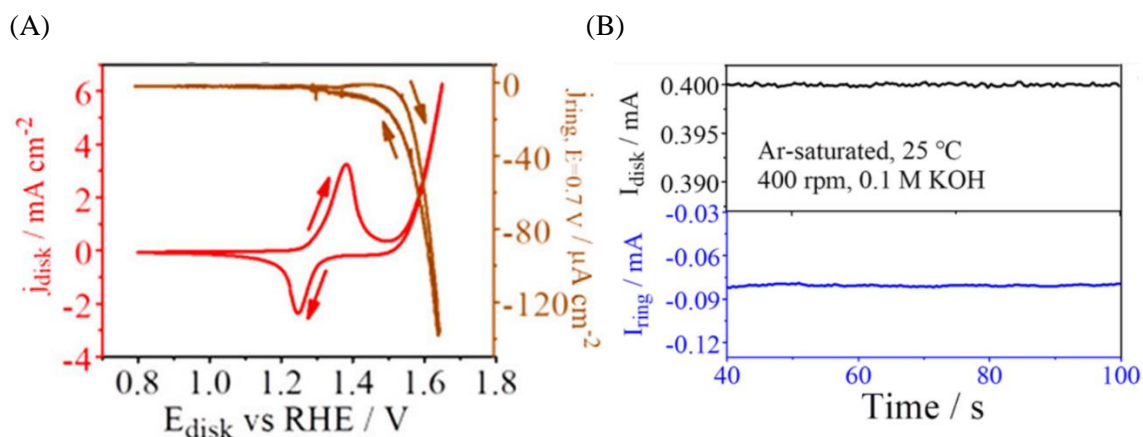


Figure 4.22. RRDE measurements in Ar-saturated 0.1 M KOH used to investigate the onset of the OER and the Faradaic efficiency. The SURMOFD film with 60 deposition layers was investigated. The potential of the ring was fixed to 0.7 V, while (A) the potential of the disk was cycled between ~0.8 and ~1.65 V vs RHE and rotated at 300 rpm and (B) a constant current of 0.4 mA was applied to the disk, during rotation at 400 rpm. Measuring the current of the ring allowed to estimate a Faradaic efficiency of ~99.4%. Adapted with permission from ref. [149].

For the benchmarking of the electrocatalytic activity at higher current densities, the previously described microelectrode-based technique was utilized (see **Chapter 4.2.1**). Initially, SURMOFDs were compared to NiO_x, CoO_x, and NiFeO_x measured under similar conditions (O₂ saturated 0.1 M KOH, 25 °C, 2 mV s⁻¹ scan rate). Independent of the film thickness, the SURMOFD films show significantly larger anodic current densities in comparison to the other catalysts. Even though there might be an overlap with the oxidation peak at ~1.3 V, its impact can be neglected due to the greatly reduced scan rate in comparison to the previous RRDE measurements. It is clearly visible, that the thicker film with 90 deposition cycles (90 C SURMOFD) shows the largest current (see **Figure 4.23 (A)**). This was expected based on SEM and AFM observations (**Figure 4.20**), which indicate a larger roughness factor for the thicker films. Thus, for further experiments, those were based on the thickest film (“90 C SURMOFD”). As expected, an increase in temperature (to 80 °C) resulted in a higher activity of all catalysts, as shown in **Figure 4.23 (B)**. Surprisingly, while the recorded current of the reference catalyst increased by a factor of ~10, the current of the SURMOFDs only increased by a factor of ~2. This might indicate a major weakness of such Ni-Co-based SURMOFDs, when it comes to the application under realistic electrolysis conditions: while their performance at low current densities is outstanding, they exhibit a drop of the activity at very high current densities. This is

probably caused by the low conductivity of these films coupled with limited diffusion in the pores. A possible solution to circumvent the high resistance of the SURMOFDs is to support the OER catalyst onto highly conductive, nanostructured materials. When it comes to application in real devices, another parameter is at least equally important as the activity of an electrocatalyst: its long-term stability. Hence, the durability of the SURMOFD films was investigated in 5.4 M KOH at ambient temperature (due to safety concerns) by applying a constant current density of 500 mA cm^{-2} . Similar experiment was already performed by Ganassin and co-workers, using a CoO_x thin film (200 nm thickness), which was deposited on a microelectrode⁹⁵. In this case, although a current density of only 400 mA cm^{-2} was applied, the catalyst completely degraded within only 9 minutes in 0.1 M KOH.⁹⁵ Conversely, as shown in **Figure 4.23 (C)**, the SURMOFD film proved to be stable over more than 100 hours under similar conditions. Interestingly, the voltage dropped by $\sim 50 \text{ mV}$ within the first 8 hours and continuously decreased further until the measurement was stopped after 100 hours. This is unexpected, as one would rather predict an increase of voltage, as catalyst surfaces can get blocked with bubbles or ECSA is lost due to leaching. Here, it seems that the catalyst further increased its activity. A reason could be that a higher fraction of the BDC binder was leached out over time. This could indirectly lead to an improvement of performance, as the resistance of the film decreases, or to a direct improvement, as the level of strain in the film changes. Although it is hard to prove the reason for the increase of activity over time, one should emphasize that the stability is remarkable when compared to other state-of-the-art catalysts such as CoO_x .

Herein, future work includes modifying the catalyst, *e.g.* by modulating strain through the nature of the organic linker or by exchanging Co cations with Fe cations. Their electrocatalytic activity should be also tested at industrial relevant conditions, combining high temperatures and using concentrated electrolytes.

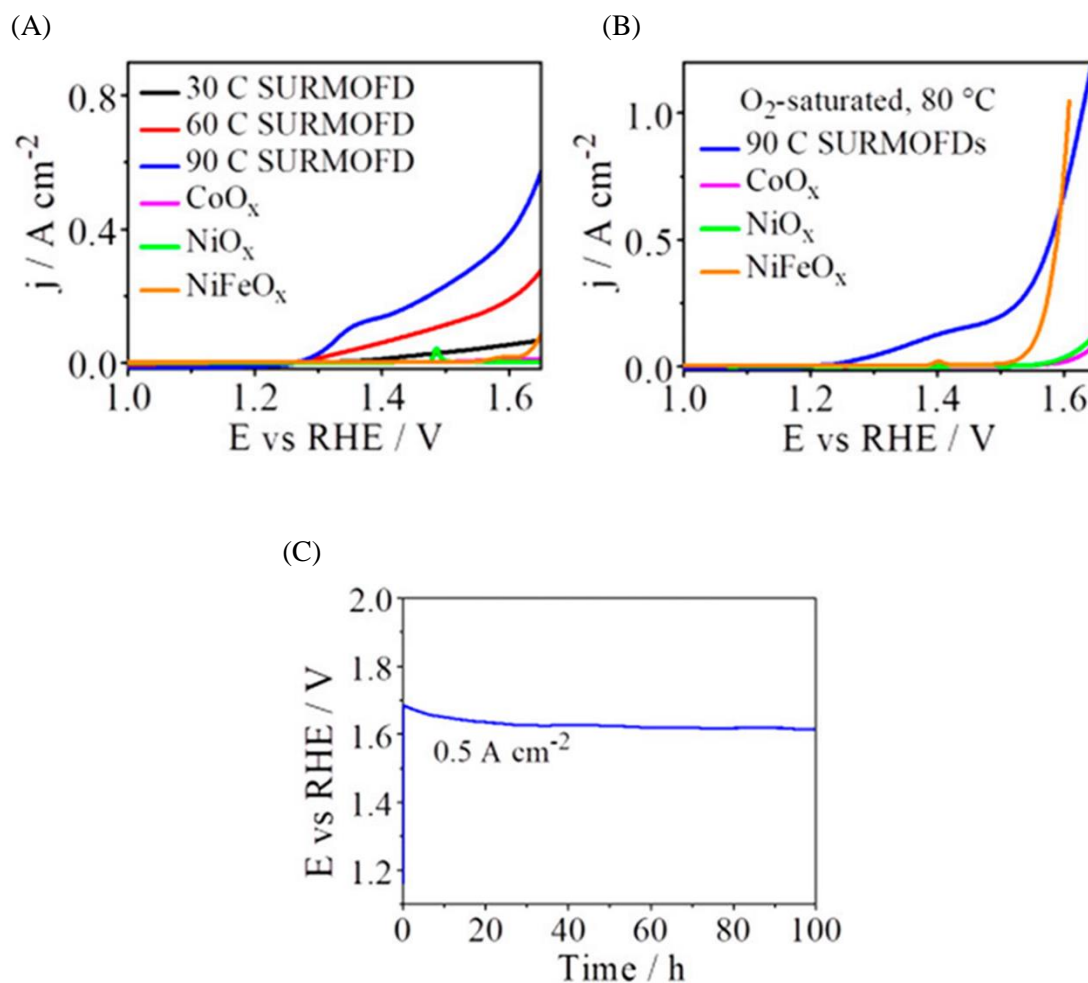


Figure 4.23. Comparison of the OER activities of the SURMOFDs with state-of-the-art OER electrocatalysts and a long-term stability measurement. All polarization curves were recorded using O_2 -saturated 0.1 M KOH. In all cases, the microelectrodes served as the substrates. SURMOFDs derived from SURMOFs grown with 30, 60 and 90 deposition cycles are denoted as “30 C SURMOFD”, “60 C SURMOFD”, and “90 C SURMOFD”, respectively. (A) Comparison of polarization of different SURMOFDs with CoO_x , NiO_x , and NiFeO_x electrocatalysts at 25 °C. (B) Comparison of anodic polarization curves of the “90 C SURMOFD” and state-of-the-art electrocatalysts recorded at 80 °C. (C) Galvanostatic long-term durability measurement of the “90 C SURMOFD” in 5.4 M KOH at room temperature. A current density of 500 mA cm^{-2} was applied for 100 hours. Adapted with permission from ref. [149].

4.3 On the dominating mechanism of the HER

The HER is an important reaction in various industrial systems *e.g.* in chlor-alkali industry and water electrolysis²²³. Although this relatively simple reaction is one of the most examined reactions in electrochemistry, there is still certain lack of understanding of its mechanistic steps^{224,225,226,227}. For instance, unexpected pH effects of the electrolytes and non-Tafel dependencies are observed for various catalysts^{228,229,230}. Reaction mechanisms are well-known, however their contribution to the overall reaction rate was never really quantified.

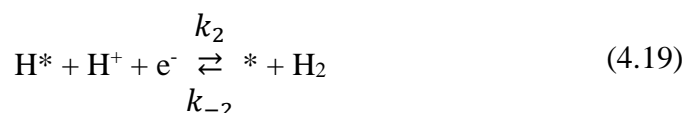
This chapter focuses on this aspect, investigating the dominating mechanism of the HER in acidic media and at different pH values. In this study, the microelectrodes were utilized in combination with EIS measurements. Firstly, Volmer-Heyrovsky (VH) and Volmer-Tafel (VT) mechanisms are briefly discussed and corresponding EECs for each reaction step are derived. Secondly, electrochemical measurements performed using the Pt(pc) microelectrodes in acidic media are presented. Then, the necessity of using the combination of both EECs for VH and VT is demonstrated by fitting the impedance data. Finally, the resulting values for the fitting parameters are presented and an evaluation of the dominating mechanism is made, based on this results. The results presented in this chapter were published: "S. Watzele, J. Fichtner, B. Garlyyev, J.N. Schwämmlein, A.S. Bandarenka. On the dominating mechanism of the hydrogen evolution reaction at polycrystalline Pt-electrodes in acidic media *ACS Catalysis* 8 (2018) 9456-9462"²³¹ (see **Chapter 6.3**).

4.3.1 HER mechanisms

The HER in acidic media involves an adsorption of protons at the electrode surface (H^*), which is called the **Volmer** mechanism.



The corresponding rate constants are k_1 and k_{-1} for the forward and backward reactions, respectively. Note that the asterisk (*) denotes a surface adsorption site. Following, there are two possibilities, either a second proton can adsorb at the adsorbed proton and hydrogen is formed by the so-called **Heyrovsky** mechanism with corresponding rate constants k_2 and k_{-2} :



or two adsorbed hydrogen atoms can recombine to form hydrogen (**Tafel** mechanism)



The corresponding rate constants are k_3 and k_{-3} . Other studies suggest different Tafel-slopes depending on the type of the mechanism taking place, for instance, slope of $\sim 30 \text{ mV dec}^{-1}$ is observed for a system rate determined by Tafel mechanism and $\sim 40 \text{ mV dec}^{-1}$ for Heyrovsky mechanism at low current densities. At higher current densities, the Tafel step is assumed to be limited by diffusion and the Tafel slope of Heyrovsky mechanism is increased to $\sim 120 \text{ mV dec}^{-1}$. As Pt(pc) electrodes in acidic media are reported to have a Tafel slope of $\sim 30 \text{ mV dec}^{-1}$, one could assume, that the Tafel step is rate determining under those conditions. Here, the analysis will not be performed based on the Tafel slopes but on the evaluation of EIS spectra recorded using microelectrodes.

The following derivations of the EECs are adopted from our recent publication²³¹ based on considerations in ref. [182]

For the following calculation, the initial assumption is made that VH and VT reaction are quasi-independent and occur simultaneously at different locations on the electrode surface. The total current i_{tot} consists of the sum of currents from Volmer-Heyrovsky, i_{VH} , and Volmer-Tafel, i_{VT} , reactions:

$$i_{\text{tot}} = i_{\text{VH}} + i_{\text{VT}} \quad (4.21)$$

Focusing first on the Volmer-Heyrovsky pathway, the reaction rates of the Volmer and Heyrovsky steps can be expressed, as shown in **Equation (4.22)** and **(4.23)**, respectively:

$$v_1 = N_{\text{VH}}(k_1(E)F_1(\theta) - k_{-1}(E)F_{-1}(\theta)) \quad (4.22)$$

$$v_2 = N_{\text{VH}}(k_2(E)F_2(\theta) - k_{-2}(E)F_{-2}(\theta)) \quad (4.23)$$

Here, N_{VH} is the ratio of adsorption sites that contributes to the VH reaction mechanism divided by the total amount of sites contributing to VH plus VT mechanism. The potential dependent rate constants $k_1(E)$ and $k_2(E)$ also account for the proton concentration. $F_1(\theta)$, $F_{-1}(\theta)$, $F_2(\theta)$, $F_{-2}(\theta)$ are functions that account for adsorbate-adsorbate interactions, they are also potential dependent. The total current *via* VH mechanism is therefore:¹⁸²

$$i_{\text{VH}} = F(v_1 + v_2) = Fr_0 \quad (4.24)$$

Here F is the Faraday constant and r_0 is the sum of both reaction rates.

The fractional coverage of the adsorbed H-species can be calculated from the difference of both reaction rates of the two-stage mechanism:¹⁸²

$$\frac{q_a}{F} \frac{d\theta}{dt} = v_1 - v_2 = r_1 \quad (4.25)$$

Here q_a is the charge resulting from a complete monolayer of H_{ads} and $\frac{d\theta}{dt}$ is the change of the coverage with time t .

During the EIS measurements, the potential $\Delta E = E_{\text{dc}} + \tilde{E}\exp(j\omega t)$ is applied, where E_{dc} is a constant bias and \tilde{E} is the complex E -amplitude (phasor), which is usually in the range of 10 mV. Further, j , ω , and t are the imaginary unit ($j^2 = -1$), the angular frequency ($\omega = 2\pi f$), and the time, respectively. This perturbation causes the current (i_{VH}) and the fractional coverage (θ) to oscillate around time averaged values $i_{\text{dc,VH}}$, θ_{dc} :

$$\Delta i_{VH} = i_{dc,VH} + \tilde{i}_{VH} \exp(j\omega t) \quad (4.26)$$

$$\Delta \theta = \theta_{dc} + \tilde{\theta} \exp(j\omega t) \quad (4.27)$$

Here, \tilde{i}_{VH} and $\tilde{\theta}$ are the corresponding complex amplitudes. For simplicity, the constants $i_{dc,VH}$ and θ_{dc} are excluded from further analysis, to keep the equations shorter.

Equations (4.24) and (4.25) can be linearized to¹⁸²:

$$\Delta i_{VH} = \left(\frac{\partial i_{VH}}{\partial E} \right)_{\theta} \Delta E + \left(\frac{\partial i_{VH}}{\partial \theta} \right)_{E} \Delta \theta = F \left[\left(\frac{\partial r_0}{\partial E} \right)_{\theta} \Delta E + \left(\frac{\partial r_0}{\partial \theta} \right)_{E} \Delta \theta \right] \quad (4.28)$$

$$\frac{q_a}{F} \frac{d\Delta \theta}{dt} = \left(\frac{\partial r_1}{\partial E} \right)_{\theta} \Delta E + \left(\frac{\partial r_1}{\partial \theta} \right)_{E} \Delta \theta \quad (4.29)$$

Equations (4.28) and (4.29) can be rewritten by using **Equations (4.26) and (4.27)**
182.

$$\frac{\tilde{i}_{VH}}{F} = \left(\frac{\partial r_0}{\partial E} \right)_{\theta} \tilde{E} + \left(\frac{\partial r_0}{\partial \theta} \right)_{E} \tilde{\theta} \quad (4.30)$$

$$\frac{q_a}{F} j\omega \tilde{\theta} = \left(\frac{\partial r_1}{\partial E} \right)_{\theta} \tilde{E} + \left(\frac{\partial r_1}{\partial \theta} \right)_{E} \tilde{\theta} \quad (4.31)$$

Equation (4.31) can be resolved for $\tilde{\theta}$ ¹⁸²:

$$\tilde{\theta} = \frac{\left(\frac{\partial r_1}{\partial E} \right)_{\theta} \tilde{E}}{\left(\frac{q_a}{F} j\omega - \left(\frac{\partial r_1}{\partial \theta} \right)_{E} \right)} \quad (4.32)$$

This allows to derive an equation for the complex admittance for the VH pathway:

From **Equation (4.30) and (4.31)**, one can write the following equation for the complex admittance for the Volmer-Heyrovsky pathway:

$$\begin{aligned}
\hat{Y}_{F,VH} &= -\frac{\tilde{i}_{VH}}{\tilde{E}} \stackrel{(4.30)}{=} -\frac{F}{\tilde{E}} \left(\left(\frac{\partial r_0}{\partial E} \right)_\theta \tilde{E} - \left(\frac{\partial r_0}{\partial \theta} \right)_E \tilde{\theta} \right) \stackrel{(4.32)}{=} & (4.33) \\
&= -F \left(\frac{\partial r_0}{\partial E} \right)_\theta - \frac{\frac{F}{\tilde{E}} \left(\frac{\partial r_0}{\partial \theta} \right)_E \left(\frac{\partial r_1}{\partial E} \right)_\theta \tilde{E}}{\left(\frac{q_a}{F} j\omega - \left(\frac{\partial r_1}{\partial \theta} \right)_E \right)} \\
&= -F \left(\frac{\partial r_0}{\partial E} \right)_\theta - \frac{\frac{F^2}{q_a} \left(\frac{\partial r_0}{\partial \theta} \right)_E \left(\frac{\partial r_1}{\partial E} \right)_\theta}{j\omega - \frac{F}{q_a} \left(\frac{\partial r_1}{\partial \theta} \right)_E} \\
&= A + \frac{B}{j\omega + C}
\end{aligned}$$

Here, the parameter A is defined as the inverse of the charge transfer resistance $R_{ct,1}^{-1}$ for the VH pathway. The complex impedance can be calculated as the inverse of the admittance¹⁸²:

$$\hat{Z}_{F,VH} = R_{ct,1} + \frac{1}{\frac{1}{R_a} + j\omega C_a} \quad (4.34)$$

$R_a = \frac{R_{ct,1}^2 |B|}{C - R_{ct,1} |B|}$ is the so-called ‘‘adsorption resistance’’ and $C_a = \frac{1}{R_{ct,1}^2 |B|}$ is the ‘‘adsorption capacitance’’. For a step by step calculation of $\hat{Z}_{F,VH}$, refer to the Supporting Information of the related recent publication ref. [231]. For the sake of clarity, it makes sense to represent **Equation (4.34)** by an EEC, consisting of a capacitance and two resistors, as displayed in **Figure 4.24 (A)**. Noteworthy, these circuit elements are not real capacitances and resistances, but solely describe the ‘‘AC-behavior’’ in an easier way.

Now, let us consider the VT pathway and its impedance response. Obviously, as **Equations 4.18-4.20** show, electrons are only transferred at each adsorption site during the Volmer step and not during the recombination step. The fact that the proton adsorption on the catalyst surface $H^+ + * + e^- = *H_{ads}$ is not slowed by the quick subsequent charge transfer

makes the calculations the VT kinetics relatively simple.²³² One can assume that this relatively fast reaction is diffusion limited at high current densities.

Therefore, the linearized current due to VT pathway originating from small perturbations can be expressed, as a function of the surface concentration of electroactive species (C^*) and the potential (E)¹⁸²:

$$\Delta i_{VT} = \left(\frac{\partial i_{VT}}{\partial E} \right)_{C^*} \Delta E + \left(\frac{\partial i_{VT}}{\partial C^*} \right)_E \Delta C^* \quad (4.35)$$

This allows to perform similar transformations and the Faradaic impedance of the VT pathway.

$$\hat{Z}_{F,VT} = R_{ct,2} + \hat{Z}_{Diff} \quad (4.36)$$

Here, $R_{ct,2}$ is the charge transfer resistance and \hat{Z}_{Diff} is the semi-infinite Warburg diffusion impedance, which originates from the last term in **Equation 4.35**. This impedance of the VT mechanism can be represented by the EEC shown in **Figure 4.24 (B)**.

So far, in the EEC the Faradaic processes, but not the non-Faradaic charging have been accounted. The impedance of the electrical double layer must be connected in parallel to the Faradaic impedances, according to the Dolin-Erschler-Randles approximation.^{233,234}

The impedance of the electrode double layer is typically approximated by a constant phase element:

$$Z_{DL} = Z_{CPE} = \frac{1}{C'_{DL}(j\omega)^n} \quad (4.37)$$

The exponent n accounts for the frequency dispersion of the double layer. For a value of $n=1$ the constant phase element could be replaced with a capacitor. C'_{DL} is in general proportional to the capacitance of the double layer but it cannot be considered as the true double layer capacitance, especially if n is significantly lower than 1. Though, due to convenience, in the following it will be simplified to $C'_{DL} \equiv C_{DL}$, irrespective of the values of n , as the focus of this chapter is on the reaction kinetics.

The complete EEC is shown in **Figure 4.24 (C)**, where the uncompensated resistance of the electrolyte R_U is also accounted.

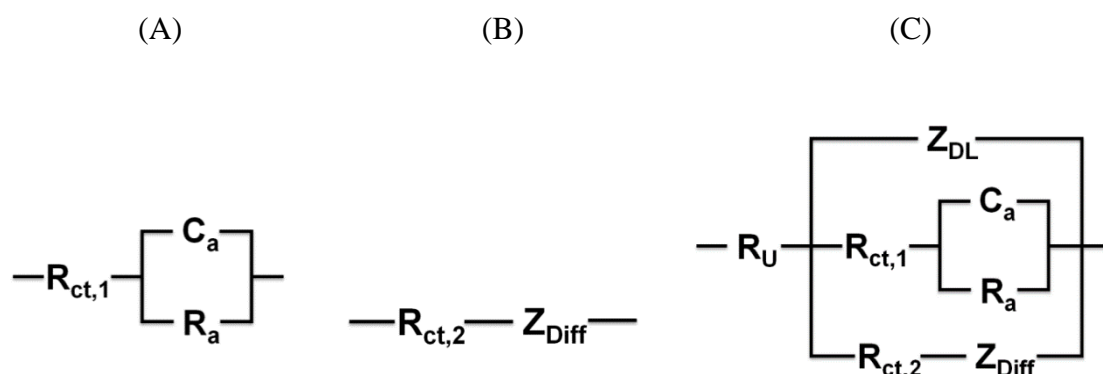


Figure 4.24. Equivalent electrical circuits (EECs) for the evaluation of EIS data recorded for the HER at Pt(pc) microelectrodes. The equivalent circuit for the Faradaic part of impedance splits into two parts: (A) an EEC for the Volmer-Heyrovsky and (B) an EEC for the Volmer-Tafel reaction. The complete EEC (C) includes also the impedance of the double layer Z_{dl} and the uncompensated resistance of the electrolyte R_u .

4.3.2 Analysis of polarization curves

Measurements were performed using Ar and H_2 saturated 0.01 M $HClO_4$, 0.1 M $HClO_4$, and 1 M $HClO_4$. **Figure 4.25 (A)** presents a typical CV recorded in 1 M $HClO_4$. It features H adsorption/desorption peaks, that can be attributed to Pt(100) and Pt(110) surfaces and it shows the expected shape for Pt(pc). Noteworthy, the onset of the HER in Ar saturated electrolyte was found to be at ~ 0.02 V. The polarization curves were recorded in the same potential range, where the EIS measurements were performed. **Figure 4.25 (B)** shows typical cathodic polarization curve, which was recorded at 50 mV s^{-1} in H_2 saturated electrolytes. Note, that these curves are corrected for the double layer capacitance, but not for the resistance of the electrolyte, as this is typically negligible for microelectrodes in such current range. At the overpotential of 100 mV, a current density of $\sim 1050 \text{ mA cm}^{-2}$, $\sim 440 \text{ mA cm}^{-2}$ and 80 mA cm^{-2} was recorded for the microelectrode in 1 M, 0.1 M and 0.01 M $HClO_4$, respectively. This demonstrates the advantage of utilizing microelectrodes when analyzing the reaction kinetics. Even at very high current densities, no significant noise

level was recorded allowing to perform EIS measurements quasi iR-free. The Tafel representation of these polarization curve is shown in **Figure 4.25 (C)**. Obviously, the curves recorded at different pH values are very similar in shape, but shifted. The Tafel slopes change over the whole potential range: at an overpotential of -15 mV it becomes $\sim 30 \text{ mV dec}^{-1}$ which would, according to classical analysis, be attributed to a rate determining Tafel step. However, it would be an arbitrary choice to evaluate exactly at -15 mV and the slope will differ at slightly lower and higher potentials. At high current densities the slope approaches $\sim 120 \text{ mV dec}^{-1}$, which would suggest Volmer-Heyrovsky mechanism to be rate determining.

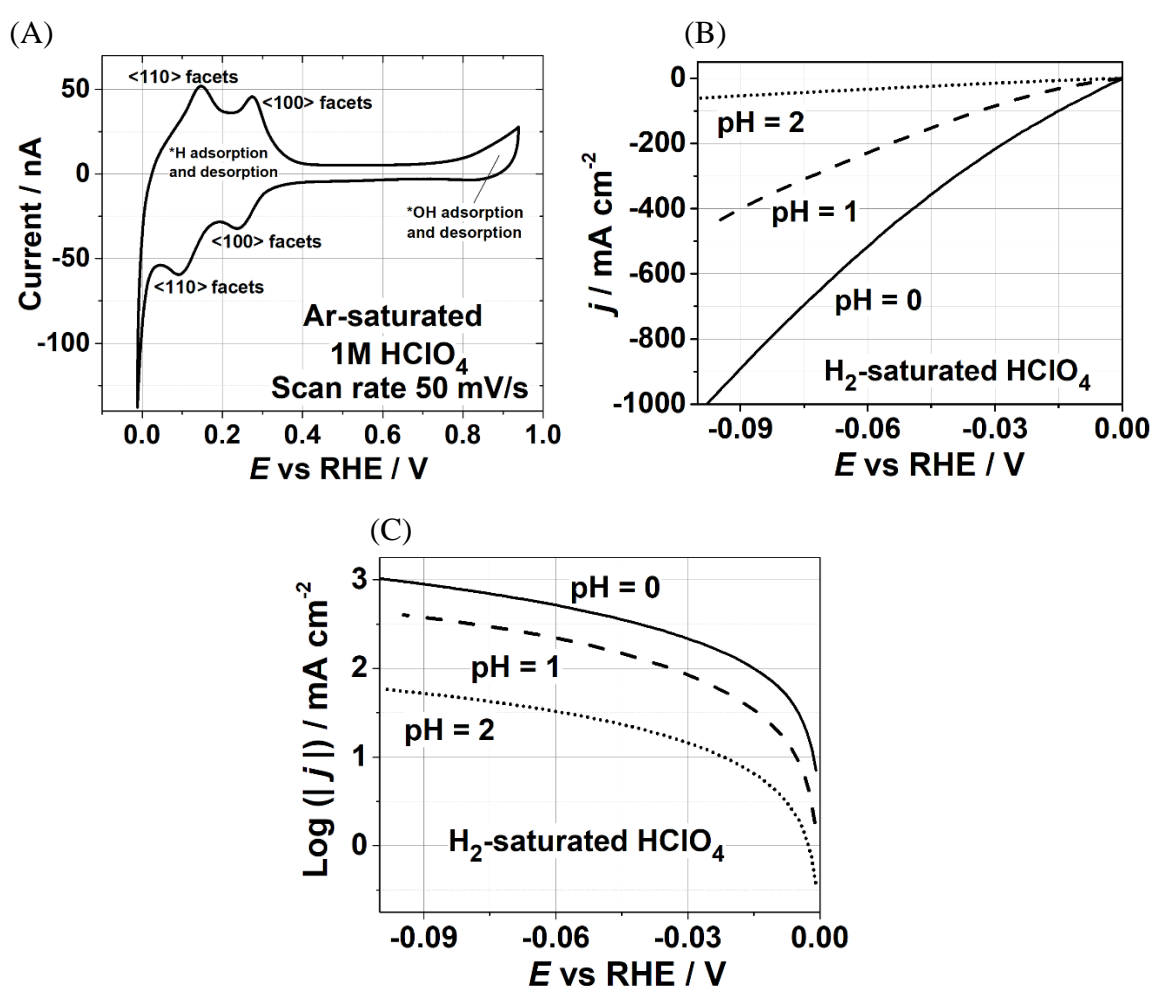


Figure 4.25. (A) A typical CV of the Pt(pc) microelectrode recorded in Ar saturated 1 M HClO₄ at a scan rate of 50 mV s⁻¹. It features characteristic adsorption peaks of Pt(100) and Pt(110) facets and indicates an onset of the HER at $\sim 0.02 \text{ V vs RHE}$. (B) Cathodic polarization curves of the Pt microelectrode recorded in H₂ saturated 1 M HClO₄, 0.1 M HClO₄ and 0.01 M HClO₄. (C) Corresponding Tafel-plots. Adapted with permission from ref. [231].

4.3.3 Analysis of the EIS spectra

The EIS data were recorded between -0.09 V and 0.03 V for Ar saturated and between -0.10 V and 0.00 V for H_2 saturated electrolytes. In **Chapter 4.3.1**, the EECs of VH and VT mechanisms as well as a combination of both was introduced. However, verification is required, *e.g.* that the EIS data cannot be fitted with just the EEC of the Faradaic current of a single reaction mechanism. Therefore, as an example, different EECs for the individual reaction mechanisms^{vii} are utilized to fit the experimental data recorded at -0.05 V.

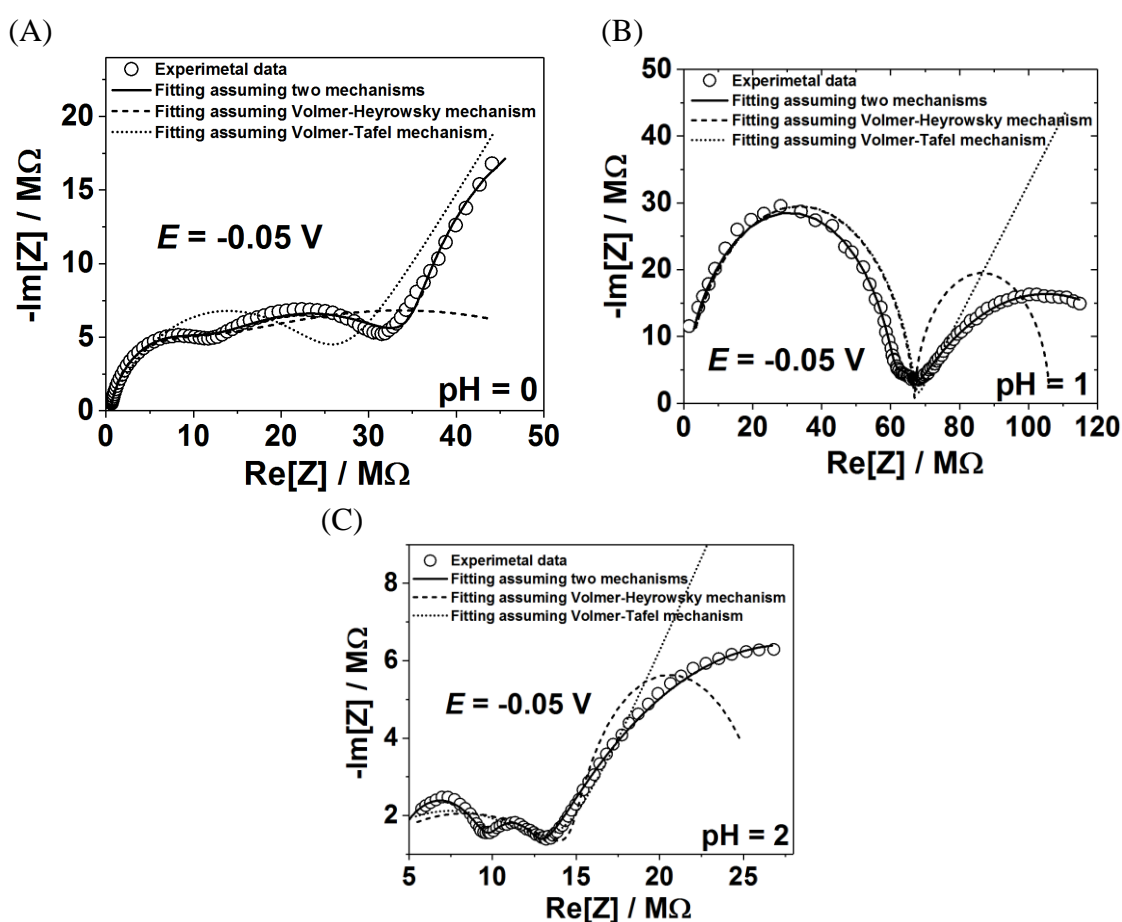


Figure 4.26. Typical EIS spectra (open symbols) of Pt(pc) microelectrode recorded at -0.05 V vs RHE in H_2 saturated acidic electrolytes. The spectra were taken in (A) 1 M $HClO_4$, (B) 0.1 M $HClO_4$, and (C) 0.01 M $HClO_4$ solutions. The dashed and dotted curves correspond to attempts to fit the spectra considering only VH and only VT mechanisms, respectively. A reasonable fitting can only be achieved by considering both mechanisms. Adapted with permission from ref. [231].

^{vii} Note, that the EECs shown for VH and VT are complemented with a parallel connected CPE and in series connected R_u , to account for double layer capacitance and electrolyte resistance.

As can be seen in **Figure 4.26**, a satisfactory fitting by only using the EEC for an individual mechanism (striped and dotted lines) is not possible; however, the utilization of the combination (solid line) allows good fitting for all shown cases. Hence, the next step was to apply this EEC for all recorded EIS data. **Figure 4.27** shows typical admittance data in Nyquist representation recorded at (A) pH 2, (B) pH 1, and (C) pH 0 for Ar saturated electrolytes with corresponding fitting curves. **Figure 4.27 (D)** plots the phase shift vs applied frequency evaluated at -0.09 V.

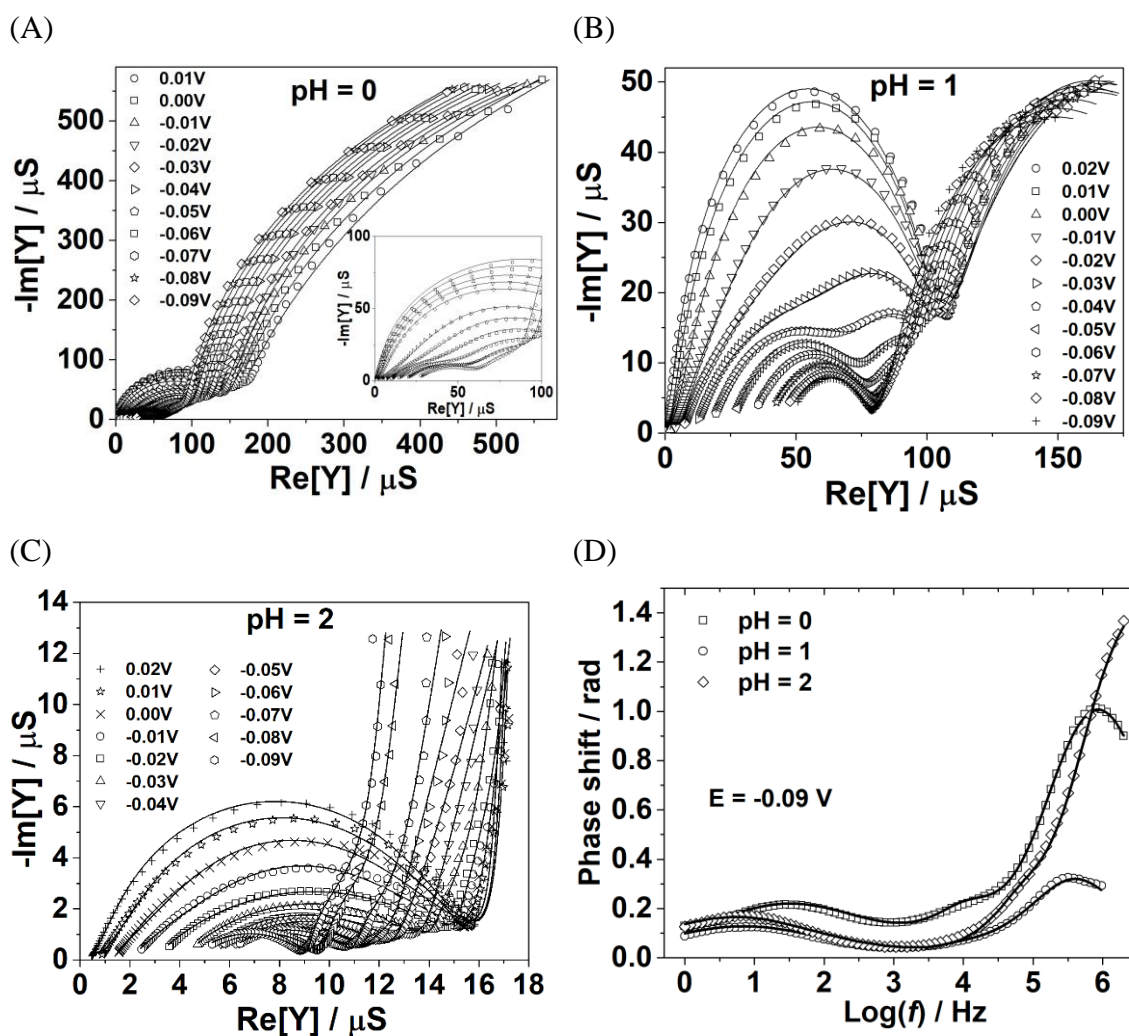


Figure 4.27. Typical admittance data (open symbols) in Nyquist representation of Pt(pc) microelectrodes, recorded in Ar saturated (A) 1 M HClO₄, (B) 0.1 M HClO₄, and (C) 0.01 M HClO₄. (D) Phase shift plots, as a function of applied probing frequency, recorded at -0.09 V vs RHE in Ar saturated acidic electrolytes (1 M, 0.1 M, and 0.01 M HClO₄). The EEC shown in **Figure 4.24 (C)** was utilized for the corresponding fitting, which are represented as solid lines. Adapted with permission from ref [231].

Figure 4.28 (A)-(D) presents corresponding data recorded in H_2 saturated electrolytes. As can be clearly seen, the model presented in **Figure 4.24 (C)** allows to accurately describe the impedance response in the whole potential range, with very low normalized root-mean-squared deviations of $< 2.5\%$.

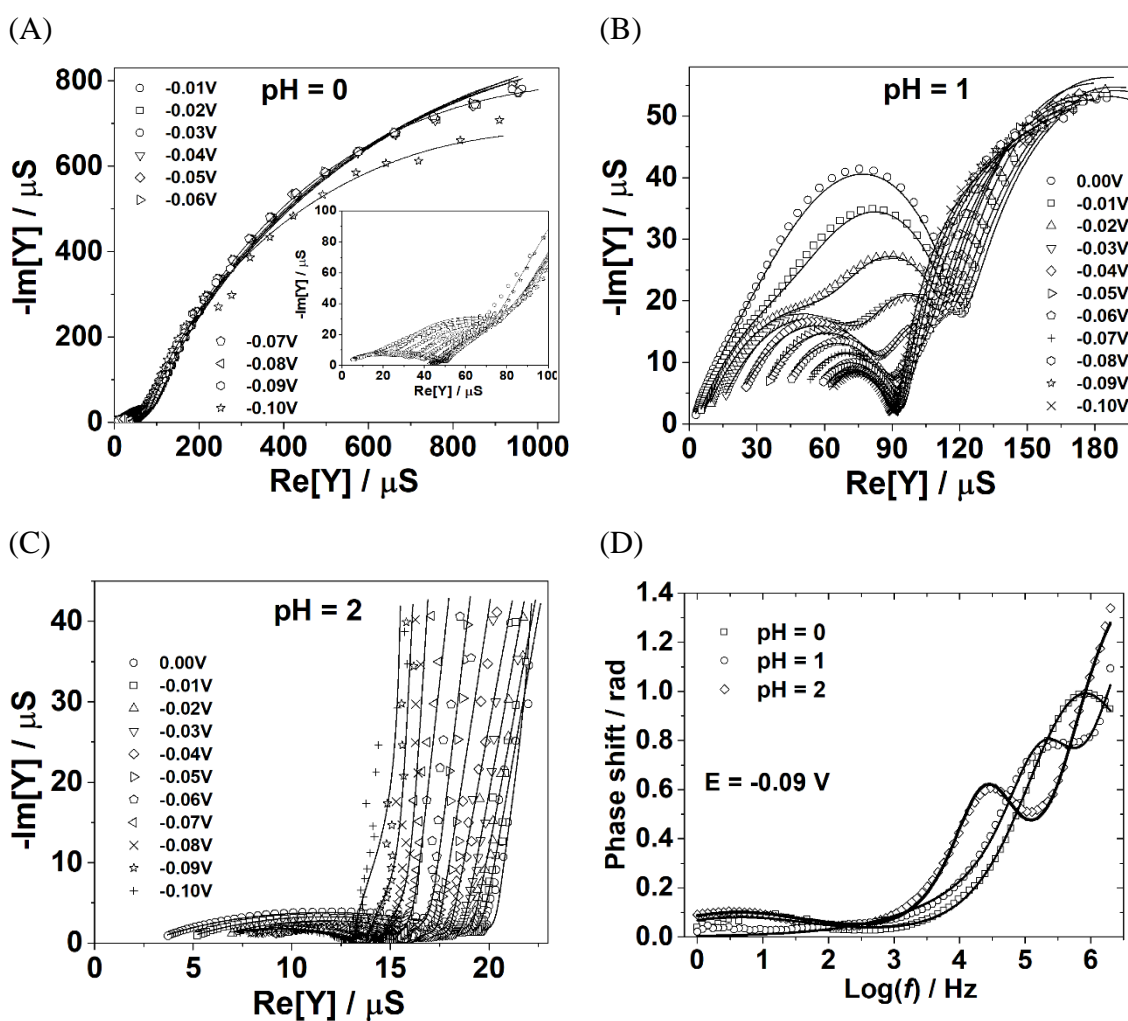


Figure 4.28. Typical admittance data (open symbols) in Nyquist representation of Pt(pc) microelectrodes recorded in H_2 saturated (A) 1 M $HClO_4$, (B) 0.1 M $HClO_4$, and (C) 0.01 M $HClO_4$. (D) Phase shift plots as a function of applied probing frequency, recorded at -0.09 V vs RHE in H_2 saturated acidic electrolytes (1 M, 0.1 M, and 0.01 M $HClO_4$). The EEC shown in **Figure 4.24 (C)** was utilized for the corresponding fitting, which are represented as solid lines. Adapted with permission from ref [231].

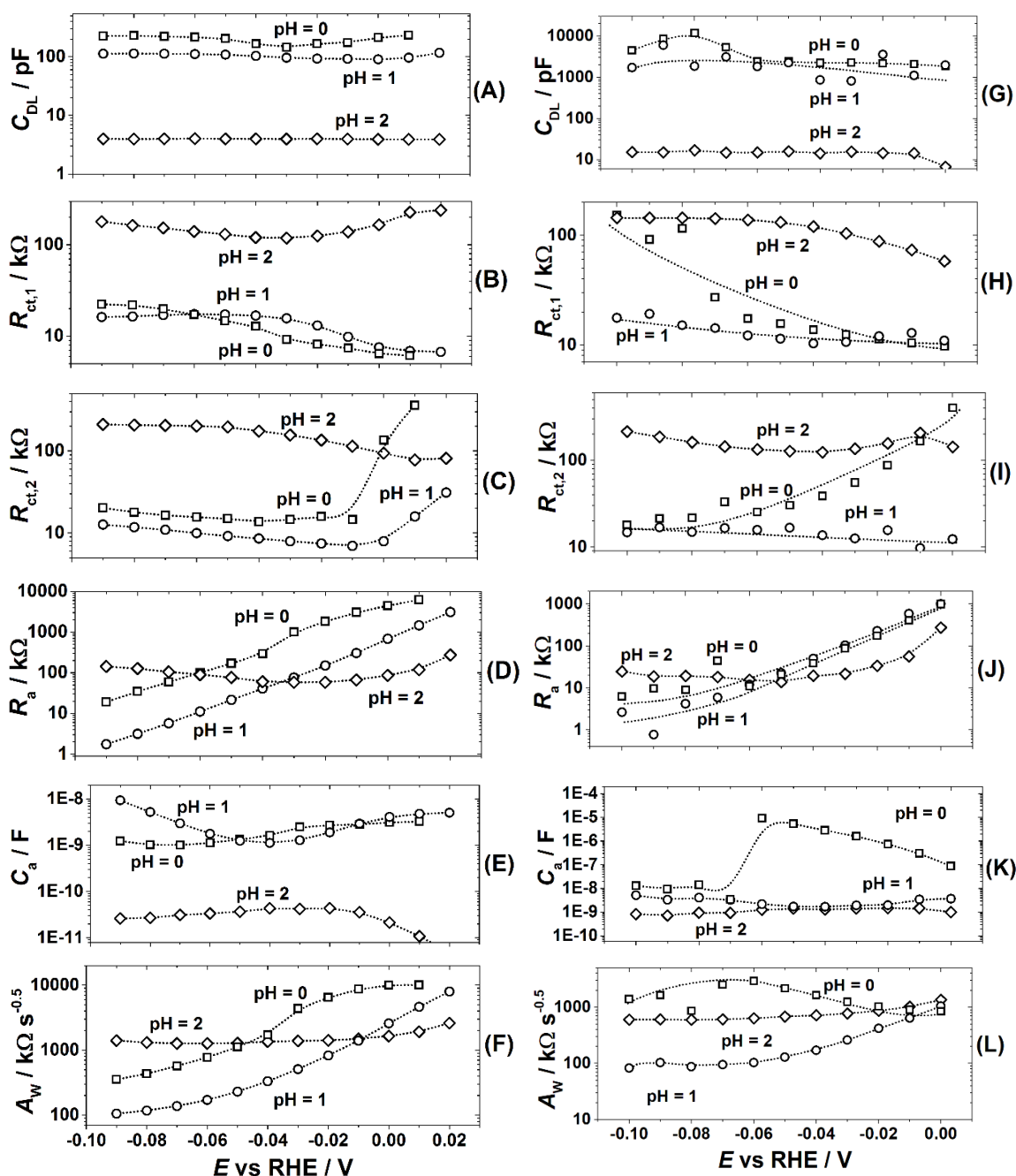


Figure 4.29. Main parameters of the EEC shown in **Figure 4.24 (C)** as a function of applied potential for the Pt(pc) microelectrodes in (A-F) Ar saturated and (G-L) H₂ saturated 1 M, 0.1 M, and 0.01 M HClO₄ electrolytes. The dotted lines connect the data points. Adapted with permission from ref. [231].

Furthermore, the individual EEC elements showed low relative errors of typically less than 10%, which verifies the choice of the EEC. The relatively low errors of the individual parameters implies the significant contribution of these parameters to the overall fitting. This was valid for all tested electrolyte concentrations, independent of the type of gas they

were saturated with. To further examine the physical meaning of the used fitting model and to investigate the reaction kinetics, it is important to take a look at the resulting fitting parameters. The potential dependencies of the relevant fitting parameters are displayed in **Figure 4.29**.

The left and right column present the results for the measurements performed in Ar and H₂ saturated electrolytes, respectively. The double layer capacitances^{viii} generally increased with decreasing pH, as expected. The considerable difference of C_{dl} measured in Ar (A)-(F) and H₂ (G)-(H) saturated electrolytes can be reasoned, by different values of *n*, which are likely caused by surface adsorbates, that interact with the double layer structure.^{235,236} Obviously, this surface adsorbate coverage should depend on the partial pressure of H₂. The situation for the charge transfer resistances of VH and VT steps (**Figure 4.29 (B, C, H, and I)**) is more complex. According to their definition, the inverse of these resistances is proportional to the local derivative of dc currents, associated to the corresponding reaction mechanism. In accordance, the values of R_{ct} in **Figure 4.25 (B)** and **(C)** decrease in higher electrolyte concentrations, with few exceptions. The other Faradaic impedance parameters such as *R_a* and *C_a* (for VH mechanism) correlate with each other, as expected from **Equation 4.34**. The Warburg parameter, *A_w*, indicates the existence of a diffusion limitation which is, however, not process limiting at the applied potentials. This observation is in accordance with the polarization curves shown in **Figure 4.25 (B)**²³¹. In order to identify the dominating mechanism of the HER, it is necessary to put R_{ct,1} with R_{ct,2} into a relation: R_{ct,1}/ R_{ct,2}. This ratio corresponds to the relative contribution of VT and VH pathways to the derivative of the total current related to HER:

$$\frac{R_{ct,1}}{R_{ct,2}} \propto \frac{N_{VT}}{N_{VH}} \cdot \frac{F(\theta)_{VT}}{F(\theta)_{VH}} \cdot \frac{C_{VT}^*}{C_{VH}^*} \quad (4.38)$$

Where *N_{VT}* and *N_{VH}* are the fraction of the adsorption sites, where the reaction proceeds according to VT and VH mechanisms, respectively. The functions describing adsorbate-adsorbate contributions *F(θ)_{VT}* and *F(θ)_{VH}* are assumed to be different for VT and VH, while transfer coefficients are assumed to be the same, and therefore cancel each other out.

^{viii} Note that for this study the constant phase elements are treated here as simple capacitors irrespective of their exponents *n* for sake of simplicity, as the main focus is on the reaction kinetics.

Further, C^*_{VH} and C^*_{VT} are effective surface concentrations of electroactive species at the site where VH and VT occur, respectively.²³¹

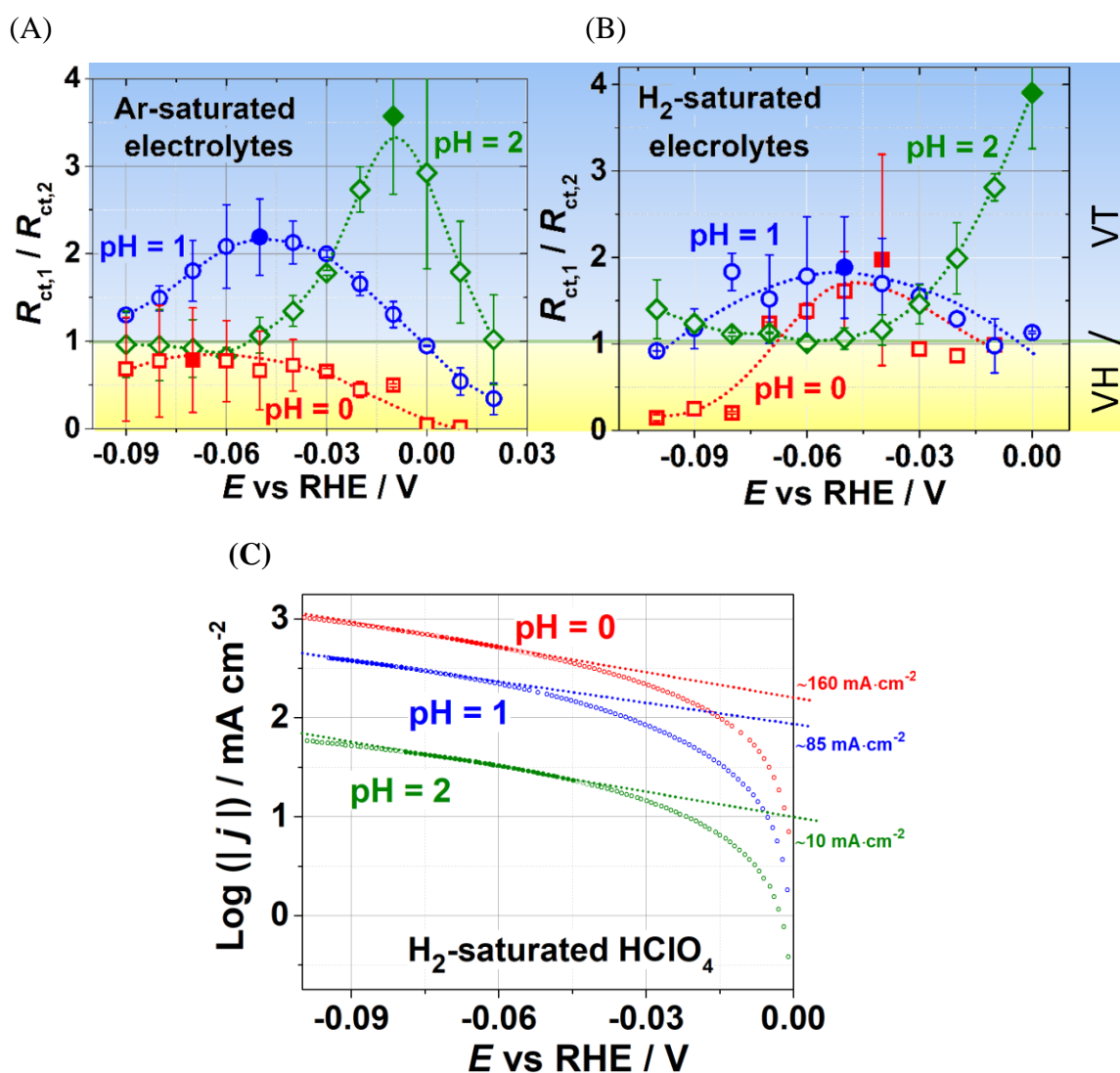


Figure 4.30. (A,B) The ratio $R_{\text{ct},1}/R_{\text{ct},2}$, illustrating the relative contribution of the Volmer-Heyrovsky and Volmer-Tafel pathways into the overall HER current at different pH values. The bold symbols designate extrema, where the relative contribution of the Volmer-Tafel pathway is maximal for the corresponding pH values. The data obtained in (A) Ar-saturated and (B) H₂-saturated electrolyte solutions. The error bars are from three independent measurements. Dotted lines are trend-lines. (C) Determination of the exchange current densities using “classical” approach, accounting for the situation, when $R_{\text{ct},1}/R_{\text{ct},2} \approx 1$ (bold symbols) at higher current densities for each pH. The error bars in (A) and (B) are from three independent measurements. Adapted and modified with permission from ref. [231].

Figure 4.30 (A) and (B) show the potential dependent ratio $R_{ct,1} / R_{ct,2}$ determined in Ar and H_2 saturated electrolytes, respectively. For the sake of clarity, the regimes, where certain mechanisms dominate, are highlighted with yellow and blue background. Remarkably, the trends of R_{ct} ratios at different pH values are comparable for different gas saturations. The main difference is observed for the 1 M $HClO_4$: especially at low overpotentials (<60 mV), the contribution of VT is significantly larger in H_2 saturated electrolytes. This could indicate a higher density of surface adsorbed protons in case of H_2 saturation, which could be explained with the Nernstian shift of the equilibrium potential for the Heyrovsky and Tafel step, while Volmer step is indirectly affected. At pH=2 and low overpotentials, the VT mechanism seems to slightly dominate over the VH mechanism, which seems to be due to the fact, that the proton concentration in the electrolyte is relatively low and as a result the VH mechanism might be impeded. However, in general, it is obvious, that at the measured potentials none of the reaction mechanisms absolutely dominates, contrary to classical interpretation of Tafel slopes. This study of course raises many fundamental and methodological questions, such as:

- 1.) It was shown that the Tafel slopes are strongly dependent on the electrode potential; but do they have a real physical meaning for the methodological challenge to differentiate and quantify the contributions from VH and VT mechanism to the reaction rate?
- 2.) Is it possible to determine the real HER/HOR exchange current density at 0.00 V vs RHE by using the common approach to extrapolate a “linear” part of the polarization curve shown in **Figure 4.24 (C)**?
- 3.) At which potential or current density should the DC curve be evaluated, and which reaction mechanism would be responsible for this exchange current density?

Figure 4.30 (C) indicates additional complications: aside from the issue, that the Tafel slope is potential dependent, it also changes in the case of low and high current density, even when the $R_{ct,1}/R_{ct,2}$ ratios are similar. This could be due to the difference in adsorbate-adsorbate interactions, which are complex and might not be adequately described by *e.g.* Langmuir, Temkin, or Frumkin isotherms^{237,238,239,240}. Hence, it is clear that the HER is more complex, than it is assumed to be. Moreover, as discussed in **Chapter 4.2**, in industrial applications the high current densities become more important. Therefore, it makes sense to focus on the quasilinear parts in **Figure 4.30 (C)** at high current densities,

where $R_{ct,1} \approx R_{ct,2}$. The slope approaches $\sim 120 \text{ mV dec}^{-1}$ and exchange current densities of ~ 160 , ~ 85 , and $\sim 10 \text{ mA cm}^{-2}$ were determined for $\text{pH} = 0, 1, \text{ and } 2$, respectively. The exchange current densities and the Tafel slopes are well comparable to literature values^{241,242}. One should again note, that these values were obtained (almost) without the influence of the ohmic drop in the electrolyte due to the use of microelectrodes.

5 Conclusions and an Outlook

This work presented several methodological approaches as indicated below.

(1) The development of a method was shown, which aims to solve the old and well-known problem of ECSA determination of oxide materials. The approach is based on the fact that OER reaction intermediates are reversibly and specifically adsorbed on electroactive catalyst surfaces. The resulting C_a can be measured *via* EIS and correlated to the ECSA. In fact, this means that this method redefines the ECSA of OER catalysts as the surface area that allows the reversible adsorption of reaction intermediates. This is very reasonable, as only these surfaces can contribute to the OER. To use this approach, reference values of C_a' are required. Therefore, a calibration step was initially executed to determine these values for the most common electrocatalysts. The applicability of this approach was demonstrated for several examples of supported and unsupported catalysts proving remarkable accuracy. Further, it was found that this method allows to quantify surface blockage (due to *e.g.* evolving gases) *in-situ*, which can, for instance, help to optimize catalyst surfaces, to be less prone for blockage, or catalyst layers with pores that are unsusceptible to clogging.

It is to be assumed, that this method with versatile applicability will impact future studies on OER electrocatalysts, as this affordable and non-destructive method allows a very quick *in-situ* analysis of the real ECSA, without the introduction of disturbing contaminations to the electrochemical cell. Developing this method resulted in two publications: the first introduced the principle using the example of NiO_x catalysts, the following one extended the calibration to CoO_x, NiCoO_x, CoFeO_x, IrO_x, and PtO_x and proved the applicability for supported nanoparticles. Additional expansion of the calibration might be meaningful for Mn-based electrocatalysts since, in the recent time, they attracted a lot of attention being recognized as *e.g.* ORR electrocatalysts.^{243,244} It is theoretically possible to apply the

method for *in-operando* characterization of electrolyzers. This, however, requires either the installation of a reference electrode or modification of the EEC to account for the cathode's response. An additional publication generated with a cooperation partner from industry regarding this topic is in preparation. Details of this work are still a subject of a secrecy agreement until publication or patent application. The discussed method was presented at various conferences: "CSCEC 2017 (Duisburg)", "69th Annual Meeting of the International Society of Electrochemistry (Bologna)", "GDCh Electrochemistry 2018 (Ulm)", "EFCF 2019 (Lucerne)", "SElectrochem (London)". This method was positively accepted by the audience, by university researcher as well as by representatives from industry.

(2) The problem was addressed, which deals with benchmarks of electrocatalysts performed in laboratory conditions are often not very significant for their performance in real devices, such as electrolyzers. Therefore, a novel method to benchmark electrocatalysts under industrially relevant conditions was developed. Microelectrodes served as the substrates for the catalyst thin films, which allowed to measure activities quasi iR -free and at the same time circumvent the formation of a gaseous phase originating from the reaction products at the electrode, even at high current densities. Additionally, the electrolyte concentration and the temperature were varied to investigate their impact on performance and to simulate conditions of electrolyzers. This was demonstrated on the state-of-the-art OER and HER electrocatalysts. Thereby, a non-trivial effect of temperature and electrolyte concentration was discovered. Further, it was shown that extrapolation of the activities measured at low current densities are incorrect, which justifies the importance of data evaluation under aforementioned conditions. Regarding the design of next-generation OER catalysts, such as Ni- Co- based SURMOFDs (shown in **Chapter 4.2.2**), particular relevance of the measurement conditions was verified: the catalyst showed uniquely high OER activity and stability at ambient temperature and at current densities below $\sim 500 \text{ mA cm}^{-2}$. However, when operated at $T \geq 80 \text{ }^\circ\text{C}$ and $j \geq 600 \text{ mA cm}^{-2}$, it loses activity in comparison to typical inorganic catalysts. We assume, that a possible solution to circumvent the limits at such high current densities is to decrease ohmic resistance, *e.g.* by utilizing a nanostructured substrate, and to decrease the film thickness.

This above-mentioned method can be useful to examine the catalysts activity at industrial relevant conditions before their implementation in membrane electrode assemblies or

electrolyzers. This can help to reduce costs and time to identify optimal catalysts as the method is significantly less prone to mispredictions in the regime of high current densities. Especially in combination with the previously discussed method for ECSA determination, intrinsic activities can be determined very accurately. Both parts of this work were published, and the discussed method was presented at the “8th Colloquium of the Munich School of Engineering, (Advances in Energy Transition)” and awarded with a presentation price.

(3) A more fundamental question was addressed: the relative contribution of the Volmer-Heyrovsky and Volmer-Tafel mechanism for the HER. Therefore, electrochemical impedance spectroscopy was utilized as a technique to differentiate both pathways of HER and quantify their relative contribution to the Faradaic current. This was done, as a function of potential for polycrystalline Pt microelectrodes in acidic electrolytes with different pH values (0, 1, and 2), which were saturated with either Ar or H₂. The usage of microelectrodes allowed to overcome difficulties, such as the potential drop in the electrolyte and enabled to perform the EIS measurements at relatively high current densities up to 1 A cm⁻². This indeed allowed to distinguish both reaction mechanisms for overpotentials up to 0.1 V. Interestingly, their contribution to the total Faradaic current is potential dependent and non-trivial. Further, none of them became predominant as the classical evaluation of Tafel slopes would suggest.

This questions the validity of current approaches to make statements on the rate determining reaction mechanism based on Tafel slopes. Moreover, recording EIS spectra on microelectrodes can be a generally promising approach to analyze reaction mechanisms, not restricted to the HER. The insights from this study can contribute to achieve a better understanding of non-Tafel behavior of the HER on Pt in acidic media. Moreover, applying this approach, additionally to model (Pt) surfaces could contribute to a better understanding of the actual origin of different activities and reported Tafel slopes of *e.g.* Pt(110) and Pt(100). This work was published, and presented at the “69th Annual Meeting of the International Society of Electrochemistry (Bologna)”

6 Appendix

6.1 Figures

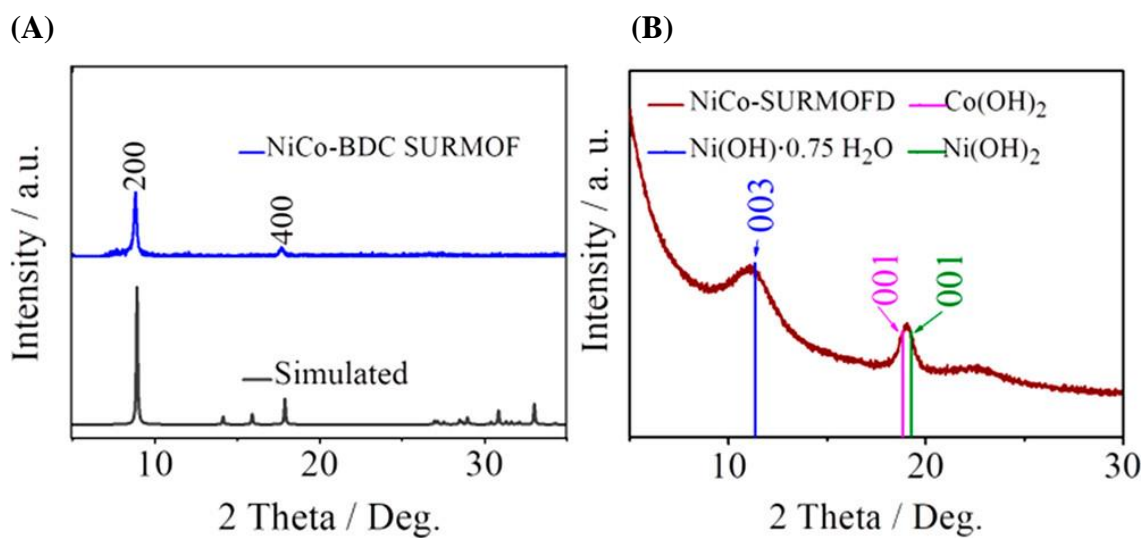


Figure 6.1. Grazing incidence X-ray diffraction patterns of (A) the SURMOF; (B) the SURMOFDs. Adapted with permission from ref. [149].

6.2 Symbols and abbreviations

a	activity
ac	alternating current
ACL	anode catalyst layer
AEM	anion exchange membrane
$A_{geometric}$	geometric surface area
AFM	atomic force microscopy
BET	Brunauer -Emmett -Teller theory
C	capacitance
C_a	adsorption capacitance
C_a'	(surface) specific adsorption capacitance
C_{dl}	double layer capacitance
C_{dl}'	(surface) specific double layer capacitance
c_0	concentration of the species [mol cm^{-3}]
CCL	cathode catalyst layer
CE	counter electrode
CPE	constant phase element
CV	cyclic voltammetry
D	diffusion coefficient
dc	direct current
DFT	density functional theory
e	elementary charge
E	potential
ECSA	electrochemical active surface area
EEC	equivalent electric circuit
E_{kin}	kinetic energy (of electrons)
EIS	electrochemical impedance spectroscopy
E_{red}^0	standard reduction potential
f	frequency
F	Faraday constant
FE	Faradaic efficiency
g	gas

G	Gibbs free energy
ΔG^\ddagger	activation energy
GDL	gas diffusion layer
H_{ads}	adsorbed hydrogen
HER	hydrogen evolution reaction
HOR	hydrogen oxidation reaction
HTE	high temperature electrolysis
H_{upd}	hydrogen underpotential deposition
I	electric current
$ImZ(f)$	imaginary part of the impedance
iR	ohmic drop
I-V	current-voltage
i_{VH}	current by VH mechanism
i_{VT}	current by VT mechanism
j	current density
j_0	exchange current density
j_{lim}	limiting current density
k	rate constant
KK	Kramer-Kronigs transform
l	liquid
MHDA	16-mercaptohexadecanoic acid
MMS	mercury/mercurous sulfate reference electrode
MOFs	metal organic frameworks
OER	oxygen evolution reaction
ORR	oxygen reduction reaction
pc	polycrystalline
PEM	polymer electrolyte membrane
PGMs	platinum group metals
Q	electric charge
q_a	charge resulting from an adsorbed monolayer
QCM	quartz -crystal microbalance
r	radius (electrode)
R	universal gas constant

R	resistance
R_a	adsorption resistance
R_{ct}	charge transfer resistance
RDE	rotating disk electrode
RE	reference electrode
$ReZ(f)$	real part of the complex impedance
RHE	reversible hydrogen electrode
rpm	revolutions per minute
R(R)DE	rotating (ring-)disk electrode
R_U	uncompensated resistance
SAMs	self-assembled organic monolayers
SEM	scanning electron microscope
SSC	silver/silver chloride electrode
STM	scanning tunneling microscopy
SURMOFDs	surface-mounted metal organic framework derivatives
SURMOFs	surface-mounted metal organic frameworks
t	time
T	temperature
TEM	transmission electron microscope
UPD	underpotential deposition
VH	Volmer-Heyrovsky
VT	Volmer-Tafel
WE	working electrode
XPS	X-ray photoelectron spectroscopy
XRD	X-ray diffraction
z	valence number
Z	impedance
Z_{dl}	impedance of the electrode double layer
Z_F	Faradaic impedance
\hat{Z}_{Diff}	impedance of semi-infinite Warburg diffusion
α	transfer coefficient
ε	gas phase fraction
κ	conductivity of the electrolyte

η	overpotential
ϕ_w	work function
ν^i	stoichiometric coefficient of species i
ν	kinetic viscosity // reaction rate
θ	(fractional) surface coverage
ω	angular frequency
$\Delta\varphi$	phase shift

6.3 Related publications

Reprinted with permission from ref. [90] Copyright (2019) American Chemical Society.


Determination of Electroactive Surface Area of Ni-, Co-, Fe-, and Ir-Based Oxide Electrocatalysts

Sebastian Watzel,^{†,||} Pascal Hauenstein,^{†,||} Yunchang Liang,[†] Song Xue,[†] Johannes Fichtner,[†] Batyr Garlyyev,[†] Daniel Scieszka,[†] Fabien Claudel,[§] Frédéric Maillard,[§] and Aliaksandr S. Bandarenka^{*,†,‡,§}

[†]Physics of Energy Conversion and Storage, Technical University of Munich, James-Frank-Strasse 1, 85748 Garching, Germany

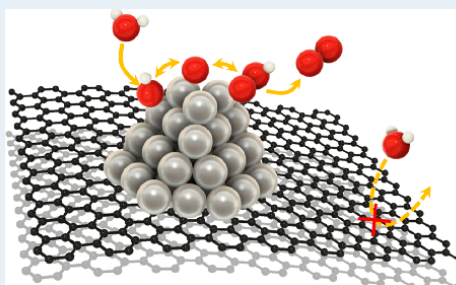
[‡]Catalysis Research Center TUM, Ernst-Otto-Fischer-Strasse 1, 85748 Garching, Germany

[§]University Grenoble Alpes, University Savoie Mont Blanc, CNRS, Grenoble INP, LEPMI, 38000 Grenoble, France

 Supporting Information

ABSTRACT: Metal oxides are important functional materials with a wide range of applications, especially in the field of electrocatalysis. However, quick and accurate assessment of their real electroactive surface area (ECSA), which is of paramount importance for the evaluation of their performance, remains a challenging task. Herein, we present a relatively simple strategy for an accurate *in situ* determination of the ECSA of commonly used metal oxide catalysts, namely Ni-, Co-, Fe-, Pt-, and Ir-based oxides. Similar to the well-established practice in electrocatalysis, the method is based on the phenomenon of specific adsorption. It uses the fact that at electrode potentials close to the onset of the oxygen evolution reaction, specifically adsorbed reaction intermediates manifest themselves through so called adsorption capacitance, which is unambiguously detectable using electrochemical impedance spectroscopy. We determined and calibrated these capacitances for common catalyst metal oxides using model thin films. Therefore, with simple impedance measurements, experimentalists can acquire the adsorption capacitance values and accurately estimate the real electroactive surface area of the above-mentioned oxide materials, including nanostructured electrocatalysts. Additionally, as illustrative examples, we demonstrate the application of the method for the determination of the ECSA of oxide catalyst nanoparticles.

KEYWORDS: electrocatalysis, electrode surface area, oxide catalysts, ECSA determination, electrochemical impedance spectroscopy, iridium oxide, oxygen evolution reaction



1. INTRODUCTION

Metal oxides constitute a class of materials with widespread applications, ranging from energy storage devices (e.g., supercapacitors¹ and batteries^{2–4}), to superconductors^{5–7} or various medical applications,^{8,9} to classical heterogeneous catalysts and electrocatalysts.^{10–16} Currently, the research focus has been mainly set on the development of supported nanostructures with optimized electrochemically active surface area (ECSA).^{17–21} However, the assessment of ECSA of oxide electrodes is nowadays often no more than a very rough estimation; or its reasonable determination is not possible at all. The lack of a widely accepted methodology for the above-mentioned problem practically impedes benchmarking of material properties and their further optimization. For instance, the commonly used Brunauer–Emmett–Teller (BET) method typically does not differentiate between the active and nonactive parts of the investigated material. In 2013, McCrory and co-workers²² utilized an approach to estimate the ECSA of metal oxides by measuring the parameter, which is proportional to the double layer capacitance of oxides in alkaline media using electro-

chemical impedance spectroscopy (EIS). However, one may argue that the reported method was rather qualitative as it encountered problems regarding the contribution of the bulk of the oxide material. Furthermore, it is not applicable to supported materials as it does not take the additional double layer contribution from the support into account.

In this work, we use a new procedure to address the challenge by measuring so-called adsorption capacitance (C_a), originating from the oxygen evolution reaction (OER) intermediates at low overpotentials (with respect to the standard OER potential), using EIS.²³ This adsorption capacitance, which is specific for each catalyst material, can be used to accurately determine the ECSA. We examine the applicability of this method using a common choice of electrocatalytically active oxide materials and provide a database of the material specific adsorption capacitance $C'_a = C_a/\text{ECSA}$ values. Finally, we show in detail

Received: May 15, 2019

Revised: August 29, 2019

Published: August 30, 2019

how to use the database and apply the method to determine the electroactive surface area of different nanoparticle-based catalysts supported on carbon.

2. EXPERIMENTAL SECTION

All experiments were conducted using a three-electrode configuration with a standard electrochemical glass cell, which was cleaned with a 3:1 ratio mixture of sulfuric acid and hydrogen peroxide (so-called "piranha solution") and afterward boiled three times with ultrapure water (Evoqua, 18.2 M Ω -cm, less than 5 ppb of total organic contamination) prior to use. A platinum mesh (Goodfellow, Germany) and a commercial Hg/Hg₂SO₄ (0.6 M K₂SO₄, Schott, Germany) electrode were used as counter (CE) and reference (RE) electrodes, respectively. A shunt capacitor (~4 μ F) connected between the reference electrode and counter electrodes was utilized to compensate potentiostat-caused artifacts at high frequencies.²⁴ The experiments were controlled using a VSP-300 potentiostat (Biologic, France). All potentials in this manuscript are reported relative to the reversible hydrogen electrode (RHE).

The measurements on supported nanoparticles were carried out using a slightly modified setup. A commercial HydroFlex hydrogen reference electrode (Gaskatel, Germany) was used, and experiments were controlled by an Autolab PGSTAT302N potentiostat (Metrohm, France).

All chemicals were high-purity reagents and used as received. NiSO₄·6H₂O (>99%), CoSO₄·7H₂O (>99%), anhydrous Na₂SO₄ (>99%), anhydrous NaOAc (>99%), FeSO₄·7H₂O (>99%), and anhydrous (NH₄)₂SO₄ (>99%) were purchased from Sigma-Aldrich (Germany). KOH (85%) and HClO₄ (Suprapur) were purchased from VWR and Merck (Germany), respectively. Experiments on carbon-supported oxide nanoparticles were performed using as-received 20 wt % Pt/C (TEC10 V20E, Tanaka Kikinzoku Kogyo, Japan) and 20 wt % Ir/C (Premetek, USA). For accuracy, the catalysts are denoted as PtO_x/C and IrO_x/C in the following, as their topmost layer typically oxidizes in OER conditions.

To exclude the theoretically possible influence of contaminations on the electrolyte due to corrosion of our glassware under alkaline conditions, we performed cyclic voltammetry (CV) of a single crystalline Pt(111) (Icryst, Jülich Germany, diameter: 10 mm) in 0.1 M Ar-saturated KOH, which is known to be highly sensitive to impurities.²⁵ As shown in Figure 1, the typical shape²⁶ of the CV of Pt(111) was observed, proving that our measurements are not significantly influenced by possible contaminations in the electrolyte due to glass corrosion. Further, it was previously proven that certain glassware is highly stable

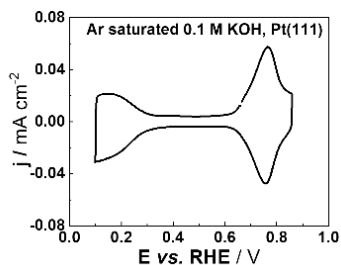


Figure 1. CV of Pt(111) recorded in 0.1 M Ar-saturated KOH at a scan rate of 50 mV s⁻¹ the same glass cell used in further experiments.

against glass corrosion, even under extreme conditions (concentrated KOH electrolyte, 80 °C).²⁷

Electrode Preparation. All oxy-hydroxide thin films were electrochemically deposited on a polycrystalline Pt electrode (Mateck, Germany, diameter: 5 mm) mounted on a rotating ring-disk electrode setup (Pine, USA). NiO_x and CoO_x films were prepared according to the procedure described by Tench et al.²⁸ The deposition procedures of NiCoO_x, NiFeO_x, and CoFeO_x films were adapted from McCrory et al.;²² however, in this work, NH₄ClO₄ was replaced with (NH₄)₂SO₄.

The IrO_x thin film was prepared by cycling an Ir(111) single crystal (Mateck, Germany, diameter: 5 mm) in 0.1 M HClO₄ solution (potential range: 0.7–1.575 V vs RHE) until a stable CV was obtained (see A. Ganasin et al.²⁹).

For the oxide nanoparticle catalysts, catalyst inks were mixed (composition is given in Table 1) and ultrasonicated (35 kHz, 40 W) for 10 min. Subsequently, the inks were drop-casted on a preheated glassy carbon electrode (~80 °C, diameter: 5 mm) and dried with a heat gun under rotation (~100 rpm).

Characterization of the Thin Films. X-ray photoelectron spectroscopy (XPS) of catalyst thin films deposited on Au(111) substrates (Arrandee, Germany) was used to investigate the catalyst composition. The XPS setup consisted of an XR 50 (Specs, Germany) X-ray source and a hemispherical energy analyzer (Specs, Germany) with 150 mm mean radius. The spectra were acquired using the Al K-alpha anode (1486.61 eV). The film morphology was investigated with atomic force microscopy (AFM), using a multimode EC-STM/AFM instrument (Veeco Instruments, Inc.) with a Nanoscope IIIID controller and the Nanoscope 5.31r1 software (AFM tips, Bruker RTESP-300).

Electrochemical Measurements. EIS and activity measurements were performed in Ar-saturated 0.1 M KOH at 400 rotations per minute (rpm). Due to their stability in acidic media, additional impedance data of IrO_x and PtO_x thin films were recorded in 0.1 M HClO₄.

EIS measurements were conducted using a standard measurement protocol. In order to activate the film, the electrode was cycled three times between 0.93 and 1.73 V vs RHE with a scan rate of 50 mV s⁻¹. Afterward, the electrode potential was slowly (1 mV/s⁻¹) shifted to the starting potential of the EIS measurement and kept for at least 10 s to reduce the "sample history" effects.²³ In a last step, the impedance measurements were performed in staircase mode (10 mV interval). For each potential, up to 198 frequencies between 30 kHz and 10 Hz were recorded using a probing signal amplitude of 10 mV. The impedance data were analyzed using EIS Data Analysis 1.3 software.^{30,31}

In the case of metallic platinum, a Pt(pc) crystal was first cycled in HClO₄ until a stable CV was obtained. The ECSA was determined by integration of the relevant features of the CV (H_{UPD} adsorption/desorption) and CO_{ads} stripping voltammogram. The composition of the oxide materials was verified using XPS (see SI Figure S2).

3. RESULTS AND DISCUSSION

Methodology. Although the exact OER pathways on different oxide materials are still under debate,³² the following simplified reaction pathway is widely accepted:

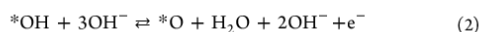
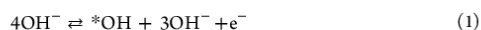
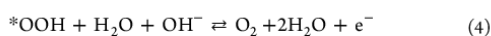


Table 1. Solution Compositions and Deposition Conditions for Different Catalyst Films

Catalyst	Solution composition	pH	Deposition Condition
NiO _x	0.13 M NiSO ₄ ·6H ₂ O	6.94	Anodic deposition, potential cycle between 0.97 and 1.83 V vs RHE at 50 mV s ⁻¹ , 400 rpm
	0.13 M NaOAc		
	0.10 M Na ₂ SO ₄		
CoO _x	0.10 M CoSO ₄ ·7H ₂ O	7.43	Anodic deposition, potential cycle between 1.30 and 1.70 V vs RHE at 50 mV s ⁻¹ , 400 rpm
	0.10 M NaOAc		
	0.10 M Na ₂ SO ₄		
NiFeO _x	9.0 mM NiSO ₄ ·6H ₂ O	2.32	Cathodic deposition, constant current of 50 mA cm ⁻² for 40 s, 1200 rpm
	9.0 mM FeSO ₄ ·7H ₂ O		
	7.3 mM (NH ₄) ₂ SO ₄		
CoFeO _x	0.4 mM CoSO ₄ ·7H ₂ O	5.4	Cathodic deposition, constant current of 125 mA cm ⁻² for 30 s, 1200 rpm
	0.36 mM FeSO ₄ ·7H ₂ O		
	1.35 mM (NH ₄) ₂ SO ₄		
NiCoO _x	10 mM NiSO ₄ ·6H ₂ O	4.72	Cathodic deposition, constant current of 50 mA cm ⁻² for 180 s, 400 rpm
	10 mM CoSO ₄ ·7H ₂ O		
	20 mM Na ₂ SO ₄		
	20 mM H ₃ BO ₃		
IrO _x	Ir (111) crystal 0.1 M HClO ₄	1.04	Potential cycling between 0.7 and 1.575 V vs RHE at 50 mV s ⁻¹ , 400 rpm
PtO _x /C	10 mg Pt/C (20 wt %), 54 μL Nafion solution (5 wt %), 1.446 mL isopropanol, 3.6 mL H ₂ O		10 μL of the ink drop-casted on a preheated glassy carbon electrode
	IrO _x /C	10 mg Ir/C (20 wt %), 54 μL Nafion solution (5 wt %), 1.446 mL isopropanol, 3.6 mL H ₂ O	10 μL of the ink drop-casted on a preheated glassy carbon electrode



It involves three specifically adsorbed reaction intermediates on the surface, namely *OH, *O, and *OOH (see Figure 2A). For convenience, we focus on the pathways in alkaline media. Nevertheless, similar argumentation is also valid in the case of acidic electrolytes, enabling utilization of the method under both conditions. As adsorption/desorption of these species involves interfacial charge transfer, and the coverage depends on the applied potential, one can define the differential adsorption capacitance as $C_a = q \frac{\partial \theta}{\partial E}$. This capacitance refers to the charge q associated with a complete adsorbate layer multiplied by the derivative of the fractional surface coverage, $\partial \theta$, with respect to

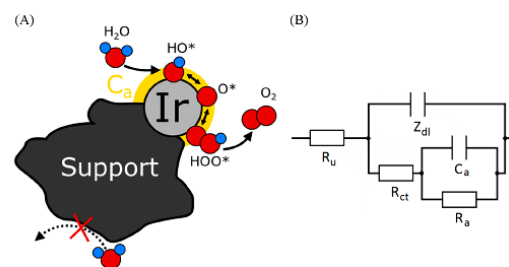


Figure 2. Origin of the adsorption capacitance. (A) Schematic representation of the oxygen evolution reaction mechanism at a nanoparticle surface on an inactive support. The reaction solely takes place on the active oxide particle; thus, only the ECSA contributes to C_a . (B) Equivalent electric circuit (physical model, for details see SI, section S1) for the OER at low overpotential. In parallel to the double layer impedance, Z_{dl} , which is in series with the uncompensated resistance, R_u , there are charge transfer resistance, R_{ct} , adsorption capacitance, C_a , and adsorption resistance, R_a . The adsorption capacitance and resistance account for the specific quasi-reversible adsorption of the reaction intermediates.

the applied probing potential, ∂E . As shown previously,²³ while C_a is in some cases a relatively small fraction of the total electrode capacitance, it can be accurately determined using EIS. The impedance measurements were performed at potentials close to the onset of the OER of the investigated sample to avoid complications arising from e.g., bubble formation. Fitting this data using the equivalent electric circuit (EEC) shown in Figure 2B (further details are given in the next sections and the Supporting Information (SI)) allows determination of C_a . As schematically depicted in Figure 2A, the OER occurs predominantly at the surface of the oxide material and not on the inactive support. Therefore, this support does not notably contribute to the adsorption capacitance. Thus, this method shares the main advantage of e.g., CO_{ads} stripping or H_{UPD} on Pt: it is sensitive to the active surface area, while masking surface area from nonactive materials such as carbon support. However, instead of integration of, e.g., the hydrogen adsorption/desorption peaks, we correlate the measured adsorption capacitance to the surface area. Typically, the procedure starts with the “calibration step”, where catalyst thin films with known electroactive surface area are investigated, and their adsorption capacitance is determined and normalized to the known surface area. This “calibration step” has to be performed once for each oxide material. Following the calibration, measuring the adsorption capacitance C_a [μF] and dividing it by the specific adsorption capacitance values $C'_a = C_a/ECSA$ [$\mu F/cm^2$] leads to the ECSA of the oxide materials of unknown morphology.

Thin Film Formation and Characterization. During the “calibration step”, it is crucial that the active surface area of the catalyst film is estimated accurately. Hence, the film morphology was investigated using AFM. In order to produce dense and nonporous catalyst films with low electrical resistance, we employed electrochemical deposition techniques. In detail, we aimed to form films as thin as possible, which enables minimization of electrical resistance and roughness; however, it had to be ensured that the activities of the films were comparable to their bulk analogues. Morphology analysis revealed roughness factors of 1.15 and 1.05 for NiO_x and CoO_x, respectively. NiFeO_x, CoFeO_x, and NiCoO_x showed higher roughness factors of 1.27, 2.25, and 1.45, respectively.

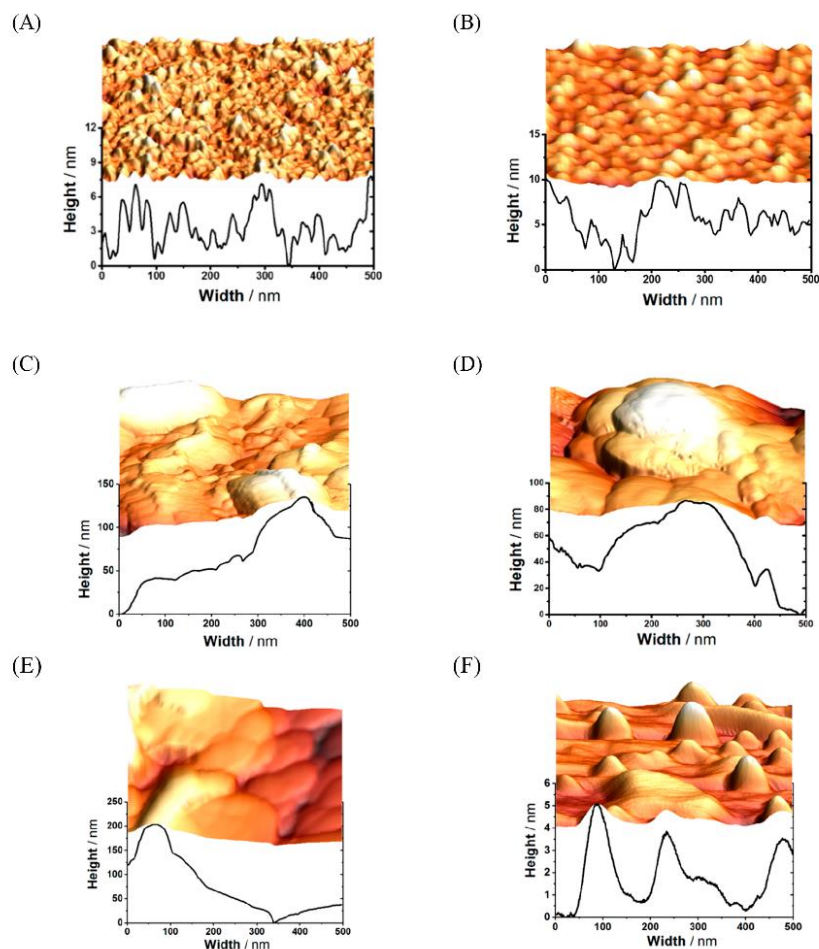


Figure 3. AFM images of (A) NiO_x , (B) CoO_x , (C) NiCoO_x , (D) NiFeO_x , (E) CoFeO_x , and (F) IrO_x thin films. In all cases, the y-axis is stretched compared to the x-axis for better visibility of the structure. (A), (B), and (D) are adapted with permission from ref 25, copyright 2019 American Chemical Society.

Cycling of the Ir(111) crystal resulted in a smooth IrO_x film with a roughness factor of 1.01. Corresponding AFM images are depicted in Figure 3A–F. It is noteworthy that metal dissolution coincides with the OER and can slightly reduce the catalysts ECSA. To increase accuracy for future studies, inductively coupled plasma mass spectrometry of dissolved species during OER can be one of the solutions to monitor and compensate the decrease of surface area.^{29,33}

Electrochemical Impedance Measurements Using Thin Films. As was mentioned above, the reaction intermediates (OH^* , $^*\text{OOH}$, and O^*) are in dynamic equilibrium and reversibly adsorbed on the entire active surface of the catalyst. As these intermediates are electrically charged, a fractional change of the catalyst surface coverage with those species ($\partial\theta$), induced by a perturbation of potential (∂E), results in an electric current. Thus, one can define the differential

adsorption capacitance ($C_a = q \frac{\partial\theta}{\partial E}$), where q is the charge of a complete monolayer (see S1, section S1). This capacitance can be distinguished from the double layer capacitance by fitting the EIS spectra (typical examples are shown in Figure S1) using the equivalent electric circuit shown in Figure 2B. This circuit, introduced by Conway et al.,³⁴ contains the constant phase element for the double layer response. However, the adsorption of the reaction intermediates is modeled with the corresponding adsorption capacitance and resistance. It is noteworthy that this is not just an arbitrary model to fit the impedance data; each component has a clear physical meaning. This is based on differential equations describing the Faradaic and non-Faradaic response to small perturbations in the electrode/electrolyte interface within the regime of the OER. Further explanation of this EEC is given in the SI.

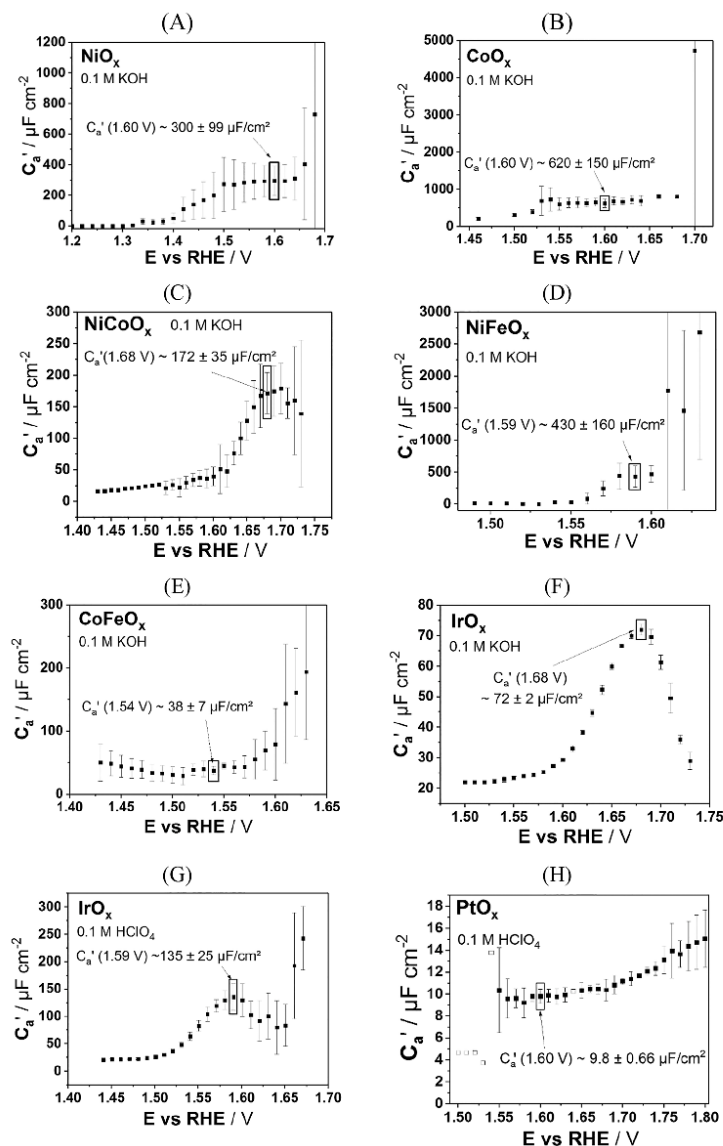


Figure 4. Specific adsorption capacitance as a function of potential for (A) NiO_x , (B) CoO_x , (C) NiCoO_x , (D) NiFeO_x , (E) CoFeO_x , (F) IrO_x in 0.1 M KOH, (G) IrO_x , and (H) PtO_x recorded in 0.1 M HClO_4 . Used electrolytes are denoted in the figure. The specific capacitances ($C_a' = C_a/\text{ECSA}$) are normalized to the ECSA of the corresponding thin films, determined by AFM or CO-stripping, respectively. Error bars are determined from at least five independent experiments.

As depicted in **Figure 4**, C_a' increases at the onset of OER. At slightly higher overpotentials, the majority of the sites become active and C_a' usually reaches a plateau. We benchmark C_a' in this region because it is locally independent of the applied potential. At higher voltages, the situation becomes less predictable, as produced oxygen bubbles stochastically block fractions of the electrode surface.

Figure S1 shows the Nyquist plots measured for each catalyst. Hollow rectangles represent the data points, while the solid line represents the fitting according to the EEC shown in **Figure 2B**. The impedance data were acquired in a broad range of potentials and measured over three decades in frequency for each metal oxide. As shown in **Figure S1**, utilizing the EEC results in good fitting with the low-mean-square deviations. At the plateau, each

individual C_a' value was estimated with an error of less than 4%. To further assess the accuracy of this method, for each catalyst at least five independent experiments were conducted. In general, at the plateau, between 5 and 52 individual measurements were considered for each catalyst. Figure 4 shows the corresponding C_a' values, normalized to their ECSA (estimated from AFM and CO_{ads} stripping voltammetry) vs the applied potential E . The error bars represent the standard deviation of the individual measurements.

Figure 4 shows that the specific adsorption capacitance is a function of applied potential and is both material- and electrolyte-dependent. Obviously, Pt shows the lowest C_a' . However, a tendency of more active materials toward higher adsorption capacitances cannot generally be reproduced, as exemplarily illustrated in the case of IrO_x , which shows a lower adsorption capacitance than the less active NiO_x (between 1.50 and 1.68 V vs RHE).

While most of the oxides are only stable in alkaline environment, the properties of Ir- and Pt-based films were additionally characterized in acidic media. Table 2 gives an overview of the different oxide materials and their specific adsorption capacitance C_a' at the plateau.

Table 2. Overview of the Specific Adsorption Capacitances $C_a' = C_a/\text{ECSA}$ of the Different Oxide Materials Measured in 0.1 M KOH (NiO_x , CoO_x , NiFeO_x , NiCoO_x , IrO_x), and 0.1 M HClO_4 (IrO_x and PtO_x)

Catalyst	Potential (V vs RHE)	$C_a' = C_a/\text{ECSA}$ ($\mu\text{F cm}^{-2}$)
NiO_x	1.60	300 ± 99
CoO_x	1.60	620 ± 150
NiFeO_x	1.59	430 ± 160
CoFeO_x	1.54	38 ± 7
NiCoO_x	1.68	172 ± 35
IrO_x	1.68	72 ± 2
IrO_x - in HClO_4	1.59	135 ± 25
PtO_x - in HClO_4	1.60	9.8 ± 0.66

Application of the Method to Carbon Supported Oxide Nanoparticles. In this section, formerly determined database values will be utilized to demonstrate the applicability of the method toward nanostructured electrocatalysts with unknown ECSA. In order to gain experimental evidence of the herein determined surface area, the results were verified by another well-established method. More precisely, both Pt and Ir nanoparticles, supported on Vulcan XC72 carbon (BET surface area: $250 \text{ m}^2/\text{g}$)³⁵ were examined as an illustrative example. We have chosen PtO_x/C due to two reasons; first, its small adsorption capacitance allows us to deduce the possible impact of the support material. Second, the ECSA of PtO_x/C can be accurately determined using CO_{ads} stripping voltammetry, being beneficial for a precise comparison.

For the surface area determination of PtO_x/C , the adsorption capacitance should be evaluated at 1.60 V vs RHE (Figure 4H). In order to decrease possible surface blocking by evolved oxygen bubbles, the electrode was rotated at 2500 rpm. Figure 5A shows the impedance data at 1.60 V in 0.1 M HClO_4 , including the fitting curve and the corresponding fitting parameters. At this potential, adsorption of $^*\text{OH}$ and $^*\text{O}$ happens spontaneously, but the energetically unfavorable formation of $^*\text{OOH}$ hinders the OER.³⁶ Nevertheless, the adsorption results in a capacitance, which was determined to be $\sim 31 \mu\text{F}$. Dividing this value by the specific adsorption capacitance of $C_a' = 9.8 \mu\text{F}/\text{cm}^2$ (taken from

Table 2) yields an ECSA of $\sim 3.2 \text{ cm}^2$. CO_{ads} stripping voltammetry of the same catalyst film (Figure 5B) exhibits an integrated charge of 1.32 mC, which corresponds to an ECSA of 3.14 cm^2 . With less than 2% deviation compared to CO_{ads} stripping voltammetry, the high accuracy of the method can be highlighted accordingly. Interestingly, this method shares also the second advantage: the carbon support which has a surface area of $\sim 40 \text{ cm}^2$ has no impact on the determination of ECSA, ensuring that only the surface area of active material contributes to the adsorption capacitance (carbon is inactive toward the OER at 1.6 V, see Figure S3). Comparing the specific adsorption capacitances (normalized to the ECSA determined through CO_{ads} stripping) of the bulk Pt(pc) disk and PtO_x/C , both curves show strong agreement in the potential range between ~ 1.575 and ~ 1.625 V vs RHE (as shown in Figure 5C). However, toward higher potentials (i.e., > 1.7 V vs RHE), the adsorption capacitance of PtO_x/C decreases, while the values of the bulk disk increase. We assume that evolved oxygen (being abundant at high potentials) traps more effectively at the nanostructured catalyst/support layer interface than on bulk Pt surface, causing increased surface blocking (and thus loss of ECSA).

In another example, we determined the ECSA of nanostructured IrO_x/C using the developed method. As shown before, the specific adsorption capacitance of the IrO_x/C was determined by fitting the corresponding impedance data, recorded at 1.59 V vs RHE, as shown in Figure 5D. Dividing the adsorption capacitance of $C_a = 623 \mu\text{F}$ by the specific adsorption capacitance $C_a' = 135 \mu\text{F}/\text{cm}^2$ yields a surface area of ca. 4.6 cm^2 . In order to enable a reliable verification of the technique, the ECSA was additionally estimated using transmission electron microscopy (TEM) images of the catalyst (Figure 5E and 5F). Other methods known to determine ECSA of Ir based catalyst are H_{UPD} and Hg_{UPD} (underpotential deposition of mercury)³⁷ as well as the granted flawed pseudocapacitance method.^{38,39} However, Durst et al.⁴⁰ showed that in the case of nanostructured Ir, there is no significant difference between the ECSA determined from H_{UPD} and TEM analysis. In detail, we derive the ECSA of IrO_x/C by comparison with the known ECSA of PtO_x/C , taking the different densities of Pt and Ir, as well as the difference in particle diameter into account. On average, the comparable Pt catalyst (with the same electrode loading) has a surface area of $A_{\text{PtO}_x/\text{C}} = 3.5 \text{ cm}^2$. Therefore, the surface area of the Ir catalyst $A_{\text{IrO}_x/\text{C}}$ (assuming spherical shape of the nanoparticles) can be approximated using the following relation:

$$\begin{aligned}
 A_{\text{IrO}_x/\text{C}} &\approx A_{\text{PtO}_x/\text{C}} \cdot \frac{\sqrt[3]{d_{\text{PtO}_x/\text{C}}^3} \cdot \rho_{\text{Pt}}}{\sqrt[3]{d_{\text{IrO}_x/\text{C}}^3} \cdot \rho_{\text{Ir}}} \cdot (1 - \alpha) \\
 &= 3.5 \text{ cm}^2 \cdot \frac{2.75 \text{ nm}}{1.796 \text{ nm}} \cdot \frac{21.45 \text{ g cm}^{-3}}{22.40 \text{ g cm}^{-3}} \cdot (1 - \alpha) \\
 &\approx 5.131 \text{ cm}^2 \cdot (1 - \alpha)
 \end{aligned}$$

Here $\sqrt[3]{d_{\text{PtO}_x/\text{C}}^3}$ and $\sqrt[3]{d_{\text{IrO}_x/\text{C}}^3}$ are the diameters of the nanoparticles (averaged over mass) and ρ_{Pt} and ρ_{Ir} are the densities of Pt and Ir (we assume that the bulk is not oxidized), respectively. Further, we introduced a parameter α to describe the reduction of the ECSA due to agglomeration of the Ir nanoparticles, as the corresponding Pt catalyst shows almost no agglomeration. Remarkably, even though the particles are

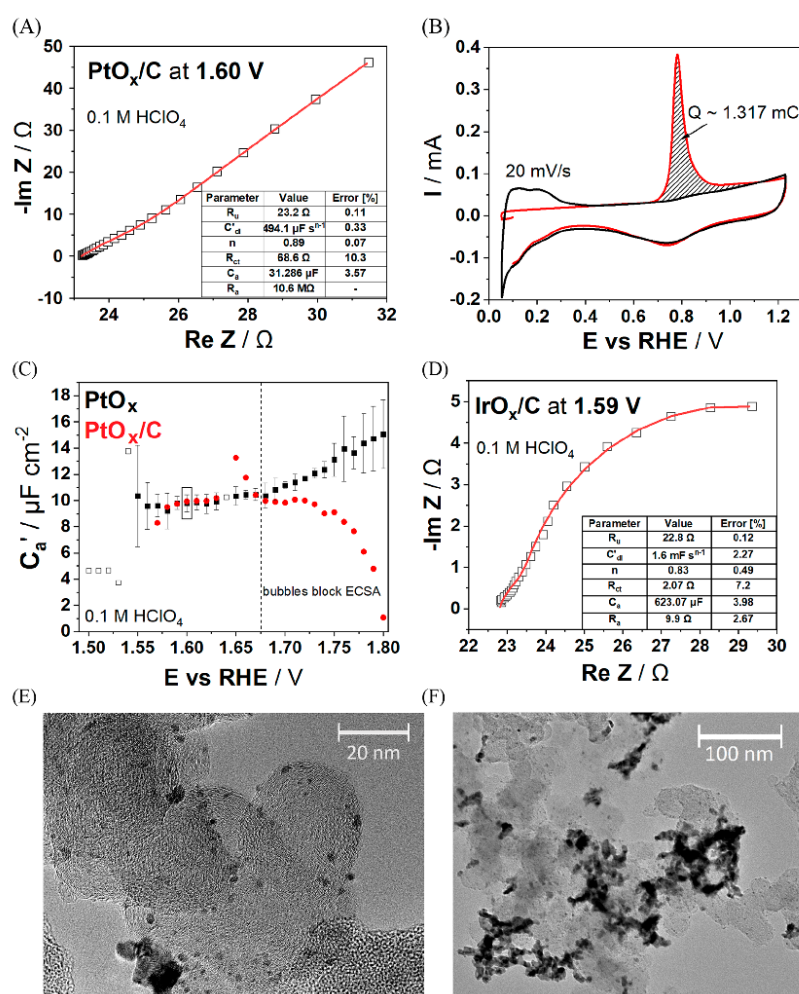


Figure 5. Surface area determination using the adsorption capacitance and control experiments. (A) EIS data (black squares) with fitting (red line) of a PtO_x/C coated glassy carbon electrode, recorded at 1.60 V vs RHE (2500 rpm). The fitting parameters are shown in the inset. (B) CO_{ads} stripping voltammogram of the PtO_x/C, recorded in 0.1 M HClO₄ with a sweep rate of 20 mV/s. Red curve: First cycle. Black curve: Second cycle. (C) Adsorption capacitance of PtO_x/C (red circles) and a bulk Pt(pc) disk (black rectangles) electrode (denoted as PtO_x) as a function of the potential, recorded in 0.1 M HClO₄. (D) EIS data of IrO_x/C (black curve) measured at 1.59 V vs RHE with fitting (red curve). The corresponding fitting parameters are shown in the inset. (E and F) TEM images of IrO_x/C at two different magnifications.

partially agglomerated, the ECSA determined via the adsorption capacitance is indeed close to the one estimated from the TEM images, only differing by about ~10% (~4.6 cm² vs ~5.1 cm²), which could be justified with the agglomeration of the IrO_x/C catalyst. Hence, for the first time with good accuracy, the (mass) specific surface area of the commercial IrO_x/C catalyst can be determined to be ~117.6 m²/g_(IrO_x). This again demonstrates the great advantage of our novel method, which enables the precise determination of the ECSA of various metal oxide

nanoparticles, contrary to any other state-of-the-art methodology.

4. CONCLUSION

In this work, we present a way to accurately determine the ECSA of common metal oxide catalysts. The method shares important advantages of other surface limited techniques (e.g., CO_{ads} stripping): the high accuracy and the independence of support materials. This technique takes advantage of reversibly adsorbed OER reaction intermediates, which manifest themselves

through so-called adsorption capacitance, C_{ad} . This capacitance is unambiguously detectable using impedance spectroscopy and can be correlated with the ECSA. For the first time, the specific adsorption capacitance was determined for NiO_x , CoO_x , NiCoO_x , NiFeO_x , CoFeO_x , IrO_x , and PtO_x/C , enabling the reader to utilize this method for a quick *in situ* ECSA determination of these materials. Moreover, we proved the applicability of the method even for the complex case of supported nanoparticles, where, to the best of our knowledge, other state-of-the-art methods fail. In fact, in the case of PtO_x/C , the determined ECSA was quasi identical with the one estimated by CO_{ads} stripping measurement. Likewise, investigations on IrO_x/C validate the accuracy even for different oxide materials and, for the first time, allowed us to accurately determine the ECSA of a commercial Ir/C catalyst. The wide-ranging applicability of this method in acidic and alkaline environments builds a fundament for the design and development of novel electrocatalysts, being crucial for future renewable energy provision.

■ ASSOCIATED CONTENT

Supporting Information

The Supporting Information is available free of charge on the ACS Publications website at DOI: 10.1021/acscatal.9b02006.

S1. Justification of the EEC. S2. X-ray photoelectron spectroscopy (XPS). S3. Description of electrochemical cell and measurement procedure. (PDF)

■ AUTHOR INFORMATION

Corresponding Author

*E-mail: bandarenka@ph.tum.de. Phone: +49 (0) 89 289 12531.

ORCID

Frédéric Maillard: 0000-0002-6470-8900

Aliaksandr S. Bandarenka: 0000-0002-5970-4315

Notes

The authors declare no competing financial interest.

[†]S.W. and P.H. contributed equally to this work.

■ ACKNOWLEDGMENTS

Financial support from Deutsche Forschungsgemeinschaft (DFG, German Research Foundation) under Germany's Excellence cluster "e-conversion" and TUM IGSSE cohort 11 (ActiveElectroCat, Project 11.01) is gratefully acknowledged.

■ REFERENCES

- (1) Nethravathi, C.; Rajamathi, C. R.; Rajamathi, M.; Wang, X.; Gautam, U. K.; Golberg, D.; Bando, Y. Cobalt hydroxide/oxide hexagonal ring–graphene hybrids through chemical etching of metal hydroxide platelets by graphene oxide: energy storage applications. *ACS Nano* **2014**, *8*, 2755–2765.
- (2) Armand, M.; Tarascon, J. M. Building better batteries. *Nature* **2008**, *451*, 652–657.
- (3) Li, R.; Lin, C.; Wang, N.; Luo, L.; Chen, Y.; Li, J.; Guo, Z. Advanced composites of complex Ti-based oxides as anode materials for lithium-ion batteries. *Adv. Compos. Hybrid Mater.* **2018**, *1*, 440–459.
- (4) Zhang, G.; Lou, X. W. General synthesis of multi-shelled mixed metal oxide hollow spheres with superior lithium storage properties. *Angew. Chem., Int. Ed.* **2014**, *53*, 9041–9044.
- (5) Pool, R. Superconductivity in a Nickel Oxide. *Science* **1989**, *243*, 741.
- (6) Comin, R.; Frano, A.; Yee, M. M.; Yoshida, Y.; Eisaki, H.; Schierle, E.; Weschke, R.; Sutarso, F.; He, Y. Charge order driven by Fermi-arc instability in $\text{Bi}_2\text{Sr}_{2-x}\text{La}_x\text{CuO}_{6+\delta}$. *Science* **2014**, *343*, 390–392.

- (7) da Silva Neto, E. H.; Aynajian, P.; Frano, A.; Comin, R.; Schierle, E.; Weschke, E.; Weschke, E.; Gyenis, A.; Wen, J.; Schneeloch, J.; Xu, Z.; Ono, S. Ubiquitous interplay between charge ordering and high-temperature superconductivity in cuprates. *Science* **2014**, *343*, 393–396.
- (8) Senpan, A.; Caruthers, S. D.; Rhee, I.; Mauro, N. A.; Pan, D.; Hu, G.; Scott, M. J.; Fuhrhop, R. W.; Gaffney, P. J.; Wickline, S. A.; Lanza, G. M. Conquering the dark side: colloidal iron oxide nanoparticles. *ACS Nano* **2009**, *3*, 3917–3926.
- (9) Nahrendorf, M. Detecting a Broken Heart. *Sci. Transl. Med.* **2012**, *4*, 135.
- (10) Eom, C. J.; Kuo, D. Y.; Adamo, C.; Moon, E. J.; May, S. J.; Crumlin, E. J.; Schlom, D. G.; Suntivich, J. Tailoring manganese oxide with atomic precision to increase surface site availability for oxygen reduction catalysis. *Nat. Commun.* **2018**, *9*, 4034.
- (11) Yeo, B. S.; Bell, A. T. Enhanced activity of gold-supported cobalt oxide for the electrochemical evolution of oxygen. *J. Am. Chem. Soc.* **2011**, *133*, 5587–5593.
- (12) Zhang, K.; Li, L.; Shaikhutdinov, S.; Freund, H. J. Carbon monoxide oxidation on metal-supported monolayer oxide films: establishing which interface is active. *Angew. Chem.* **2018**, *57*, 1275–1279.
- (13) Chen, Y.; Li, C. W.; Kanan, M. W. Aqueous CO_2 reduction at very low overpotential on oxide-derived Au nanoparticles. *J. Am. Chem. Soc.* **2012**, *134*, 19969–19972.
- (14) Lum, Y.; Ager, J. W. Stability of residual oxides in oxide-derived copper catalysts for electrochemical CO_2 reduction investigated with ^{18}O labeling. *Angew. Chem., Int. Ed.* **2018**, *57*, 551.
- (15) Biswas, S.; Khanna, H. S.; Nizami, Q. A.; Caldwell, D. R.; Cavanaugh, K. T.; Howell, A. R.; Raman, S.; Suib, L.; Nandi, P. Heterogeneous catalytic oxidation of amides to imides by manganese oxides. *Sci. Rep.* **2018**, *8*, 13649.
- (16) Zhao, A.; Masa, J.; Xia, W.; Maljusch, A.; Willinger, M. G.; Clavel, G.; Xie, K.; Schlögl, R.; Schuhmann, W.; Muhler, M. Spinel Mn–Co oxide in N-doped carbon nanotubes as a bifunctional electrocatalyst synthesized by oxidative cutting. *J. Am. Chem. Soc.* **2014**, *136*, 7551–7554.
- (17) George, C.; Dorfs, D.; Bertoni, G.; Falqui, A.; Genovese, A.; Pellegrino, T.; Roig, A.; Quarta, A.; Comparelli, R.; Curri, M. L.; Cingolani, R. A cast-mold approach to iron oxide and Pt/iron oxide nanocontainers and nanoparticles with a reactive concave surface. *J. Am. Chem. Soc.* **2011**, *133*, 2205–2217.
- (18) Choi, S. H.; Na, H. B.; Park, Y. I.; An, K.; Kwon, S. G.; Jang, Y.; Park, M.; Moon, J.; Son, J. S.; Song, I. C.; Moon, W. K.; Hyeon, T. Simple and generalized synthesis of oxide–metal heterostructured nanoparticles and their applications in multimodal biomedical probes. *J. Am. Chem. Soc.* **2008**, *130*, 15573–15580.
- (19) Bernicke, M.; Ortel, E.; Reier, T.; Bergmann, A.; Ferreira de Araujo, J.; Strasser, P.; Kraehnert, R. Iridium oxide coatings with templated porosity as highly active oxygen evolution catalysts: Structure-activity relationships. *ChemSusChem* **2015**, *8*, 1908–1915.
- (20) Kim, B. H.; Lee, N.; Kim, H.; An, K.; Park, Y. I.; Choi, Y.; Shin, K.; Lee, Y.; Kwon, S. G.; Na, H. B.; Park, J. G.; Ahn, T. Y.; Kim, Y. C.; Moon, W. K.; Hyeon, T. Large-scale synthesis of uniform and extremely small-sized iron oxide nanoparticles for high-resolution T₁ magnetic resonance imaging contrast agents. *J. Am. Chem. Soc.* **2011**, *133*, 12624–12631.
- (21) Hutchings, G. S.; Zhang, Y.; Li, J.; Yonemoto, B. T.; Zhou, X.; Zhu, K.; Jiao, F. In situ formation of cobalt oxide nanocubanes as efficient oxygen evolution catalysts. *J. Am. Chem. Soc.* **2015**, *137*, 4223–4229.
- (22) McCrory, C. C.; Jung, S.; Peters, J. C.; Jaramillo, T. F. Benchmarking heterogeneous electrocatalysts for the oxygen evolution reaction. *J. Am. Chem. Soc.* **2013**, *135*, 16977–16987.
- (23) Watzele, S.; Bandarenka, A. S. Quick determination of electroactive surface area of some oxide electrode materials. *Electroanalysis* **2016**, *28*, 2394–2399.

- (24) Colic, V.; Tymoczko, J.; Maljusch, A.; Ganassin, A.; Schuhmann, W.; Bandarenka, A. S. Experimental aspects in benchmarking of the electrocatalytic activity. *ChemElectroChem* **2015**, *2*, 143–149.
- (25) Strmcnik, D.; Kodama, K.; Van der Vliet, D.; Greeley, J.; Stamenkovic, V. R.; Marković, N. M. The role of non-covalent interactions in electrocatalytic fuel-cell reactions on platinum. *Nat. Chem.* **2009**, *1*, 466.
- (26) Subbaraman, R.; Tripkovic, D.; Chang, K. C.; Strmcnik, D.; Paulikas, A. P.; Hirunsit, P.; Chan, M.; Greeley, J.; Stamenkovic, V.; Markovic, N. M. Trends in activity for the water electrolyser reactions on 3d M (Ni, Co, Fe, Mn) hydr (oxy) oxide catalysts. *Nat. Mater.* **2012**, *11*, 550.
- (27) Watzel, S.; Liang, Y.; Bandarenka, A. S. Intrinsic activity of some oxygen and hydrogen evolution reaction electrocatalysts under industrially relevant conditions. *ACS Appl. Energy Mater.* **2018**, *1*, 4196–4202.
- (28) Tench, D.; Warren, L. F. Electrodeposition of conducting transition metal oxide/hydroxide films from aqueous solution. *J. Electrochem. Soc.* **1983**, *130*, 869–872.
- (29) Ganassin, A.; Colic, V.; Tymoczko, J.; Bandarenka, A. S.; Schuhmann, W. Non-covalent interactions in water electrolysis: influence on the activity of Pt (111) and iridium oxide catalysts in acidic media. *Phys. Chem. Chem. Phys.* **2015**, *17*, 8349–8355.
- (30) Bondarenko, A. S. Analysis of large experimental datasets in electrochemical impedance spectroscopy. *Anal. Chim. Acta* **2012**, *743*, 41–50.
- (31) Bandarenka, A. S. Development of hybrid algorithms for EIS data fitting, a book Chapter in *Lecture notes on impedance spectroscopy. Measurement, Modeling and Applications*, Vol. 4; Kanoun, O., Ed.; CRC Press, Taylor and Francis Group: London, 2013; pp 29–36.
- (32) Kasian, O.; Grote, J. P.; Geiger, S.; Cherevko, S.; Mayrhofer, K. J. The common intermediates of oxygen evolution and dissolution reactions during water electrolysis on iridium. *Angew. Chem., Int. Ed.* **2018**, *57*, 2488–2491.
- (33) Geiger, S.; Kasian, O.; Ledendecker, M.; Pizzutilo, E.; Mingers, A. M.; Fu, W. T.; Diaz-Morales, O.; Li, Z.; Oellers, T.; Fruchter, L.; Ludwig, A.; Mayrhofer, K. J.; Koper, M. T. M.; Cherevko, S. The stability number as a metric for electrocatalyst stability benchmarking. *Nat. Catal.* **2018**, *1*, 508.
- (34) Harrington, D. A.; Conway, B. E. AC Impedance of Faradaic reactions involving electroadsorbed intermediates—I. *Electrochim. Acta* **1987**, *32*, 1703–1712.
- (35) Lázaro, M. J.; Calvillo, L.; Celorrio, V.; Pardo, J. I.; Perathoner, S.; Moliner, R. Study and application of carbon black Vulcan XC-72R in polymeric electrolyte fuel cells. In *Carbon black: production, properties and uses*, 1st ed.; Sanders, I. J., Peeten, T. L., Eds.; Nova Science Publishers Inc.: Hauppauge, NY, 2011; p 41.
- (36) Rossmesl, J.; Logadottir, A.; Nørskov, J. K. Electrolysis of water on (oxidized) metal surfaces. *Chem. Phys.* **2005**, *319*, 178–184.
- (37) Alia, S. M.; Hurst, K. E.; Kocha, S. S.; Pivovar, B. S. Mercury underpotential deposition to determine iridium and iridium oxide electrochemical surface areas. *J. Electrochem. Soc.* **2016**, *163*, 3051–3056.
- (38) Zhao, S.; Yu, H.; Maric, R.; Danilovic, N.; Capuano, C. B.; Ayers, K. E.; Mustain, W. E. Calculating the electrochemically active surface area of iridium oxide in operating proton exchange membrane electrolyzers. *J. Electrochem. Soc.* **2015**, *162*, 1292–1298.
- (39) Trasatti, S.; Petrii, O. A. Real surface area measurements in electrochemistry. *Pure Appl. Chem.* **1991**, *63*, 711–734.
- (40) Durst, J.; Siebel, A.; Simon, C.; Hasché, F.; Herranz, J.; Gasteiger, H. A. New insights into the electrochemical hydrogen oxidation and evolution reaction mechanism. *Energy Environ. Sci.* **2014**, *7*, 2255–2260.

Quick Determination of Electroactive Surface Area of Some Oxide Electrode Materials

Sebastian Watzele^[a] and Aliaksandr S. Bandarenka^{*[a, b]}

Abstract: Quick and accurate determination of the real electroactive surface area of oxide electrodes remains one of the most challenging but at the same time important unsolved methodological tasks in the field of electroanalysis. For instance, the widely used Brunauer–Emmett–Teller (BET) method unfortunately provides no direct connection to it. On the other hand, its assessment through the double layer capacitance is complicated and not accurate enough, as the bulk oxide films themselves contribute to the measured capacitance, not mentioning the double layer frequency dispersion and other poorly understood factors. In this work, we propose a relatively simple methodology for a quick assessment of the electroactive surface area of some electron conducting oxide and perovskite materials. The methodology involves several steps. Initially, “calibration” experiments are performed aiming to form the thinnest (practically below ~100–200 nm) flat oxide films, which exhibit necessary functional properties (close to those expected for the bulk material) without significant side influence of the substrate. Then, AFM measurements are implemented to

estimate the surface roughness of the resulting samples. Finally, electrochemical impedance measurements are done at a small overpotential related to the oxygen evolution reaction (OER) aiming to extract not the double layer but the capacitance of adsorption C_a of the OER intermediates. The C_a values can then be used to evaluate the electroactive surface area of “real-world” high surface area oxide electrodes composed of the same material. Other words, similar to the hydrogen underpotential deposition or CO oxidation in the case of metals, we propose to use the oxygen evolution reaction as the probing reaction to evaluate the surface area of oxide electrocatalysts. However, instead of cyclic voltammetry, electrochemical impedance spectroscopy is used as the main probing technique. Due to relatively high reproducibility, clear physical meaning and exclusive connection to the electroactive area, the measurements of C_a can become a viable method in numerous electrochemical applications. An example using Ni-oxide electrodes is given to illustrate the methodology.

Keywords: Electrocatalysis • Oxide catalysts • Electrochemical impedance spectroscopy • Electrode surface area

1 Introduction

Oxides and perovskites are among the most important functional electrode materials [1–5]. This is true not only with respect to the energy conversion and storage applications. These materials are of particular significance in many industrial processes including the so-called chloralkali industry [6]. However, the level of current understanding of the origin of their functionality is often much lower compared to e.g. pure metals. For instance in electrocatalysis, elucidation of relations between the oxide surface structure and composition and the activity is very complicated, largely due to the fact that even determination of the real electroactive surface area of the electrode is extremely problematic. It has been demonstrated decades ago that the commonly used Brunauer–Emmett–Teller (BET) method is not reliable in this case, as there is no direct correlation between the BET-determined surface area and the electrochemically active surface area [7–9]. Measurements of the interfacial double layer capacitance in case of oxides are methodologically difficult due to the fact that some semiconducting and capacitive properties as well as the double layer frequency dispersion [10–16] contribute to it. There are no well-accepted

tabulated values for the double layer capacitances for the oxides, and those reported by different groups can lead to uncertainties of up to ~700% [17]. In contrast to metal surfaces, where the real electroactive area is often determined using surface limited adsorption reactions [18], no such reactions are used to apply them in the case of oxides. While some other approaches have been proposed (see e.g. [19]), they did not solve the key methodological issues mentioned above. On the other hand, for the so-called outer sphere reactions, no clear correlations between the voltammetric peak current and oxide surface roughness have been observed [20].

In this work, a relatively simple method for the determination of the electroactive surface area is proposed. It is based on the fact that the oxygen evolution reaction (OER) involves specifically adsorbed oxygenated species;

[a] S. Watzele, A. S. Bandarenka
Physik-Department ECS, Technische Universität München,
James-Franck-Straße 1, 85748 Garching, Germany
*e-mail: bandarenka@ph.tum.de

[b] A. S. Bandarenka
Nanosystems Initiative Munich (NIM), Schellingstraße 4,
80799 Munich, Germany

and if taken under conditions of low overpotentials it shows little complications associated with the gas bubble formation. The reversible specific adsorption of the OER intermediates manifests itself as an adsorption capacitance, C_a , during electrochemical impedance spectroscopy experiments and data analysis. The adsorption capacitance is directly proportional to the average (in time) amount of the intermediates located exactly at the surface and has a clear physical meaning ($C_a = -q_a(d\theta_a/dE)$, where θ_a is the effective adsorbate fractional coverage oscillating during the impedance probing at a given electrode potential; and q_a is the charge to form a saturated layer of the adsorbed species). Therefore, C_a can be used, similarly to the adsorption of hydrogen atoms or CO molecules in the case of metal electrodes, to quickly and accurately evaluate the electroactive surface area of electrochemically conducting oxide electrode materials. Model Ni-oxide electrocatalytic materials are used in this work to demonstrate the methodology.

2 Experimental

2.1 Electrochemical Experiments

Electrochemical experiments were performed using a VSP-300 (Bio-Logic, France) potentiostat in all experiments. All potentials in this work are referred to the RHE scale. A Hg/HgSO₄ electrode (Schott) and a Pt wire (Goodfellow) were used as the reference (RE) and counter electrodes (CE), respectively. Experiments were performed in an electrochemical cell described in detail elsewhere [21].

During the experiments, the working electrodes were rotated at 400 rpm using a rotating ring disk electrode (RRDE) equipment (Pine, USA). A polycrystalline Pt electrode (Mateck, Germany) with diameter of 5 mm was used as substrate for the NiO_x thin film deposition.

For the electrochemical impedance spectroscopy (EIS) experiments, a shunt capacitor of ~4 μF was connected between RE and CE to reduce possible errors caused by the potentiostat at high frequencies, as discussed in [22]. Before each individual impedance measurement, the electrode potential was held for 1 s; then *ac* probing signals were applied within the frequency range from 30 kHz to 5 Hz using 10 mV probing signal amplitude. A homemade software [23,24] was used to analyze the impedance data.

Ar-saturated (Ar 5.0, Air Liquide, Germany) 0.1 M KOH working electrolytes were prepared using KOH (≥ 85%, Grüssing, Germany). Electrolytes for the thin NiO_x film deposition [25] were prepared using NiSO₄ (99% Sigma Aldrich, Germany), Na₂SO₄ (99% Sigma Aldrich, Germany) and NaOAc·6H₂O (99% Sigma Aldrich, Germany).

Nickel oxy-hydroxide films (denoted in this work as NiO_x films; however, one cannot exclude the presence of e.g. active Fe-oxides in the film as a result of common contamination in the selected chemicals [26]) were anodically deposited onto the Pt electrode using cyclic voltam-

metry (CV) scans in the deposition solution (0.13 M NiSO₄, 0.13 M NaOAc·6H₂O and 0.1 M Na₂SO₄) as described in detail elsewhere [25]. For the deposition, the potential scan rate of 50 mV s⁻¹ and a potential window from 0.95 V to 1.86 V were used. The cyclic voltammogram (see inset in Fig. 1A) showed the growth of characteristic anodic and cathodic peaks, as typically reported for NiO_x deposition [21,27]. The OER current at the positive potential limit increased at each cycle, indicating the electrocatalytic behavior of the growing film. After film deposition, the electrodes were carefully rinsed with ultrapure water.

2.2 Thin Film Characterization

The surface of the obtained NiO_x electrodes was characterized using atomic force microscopy (AFM) in tapping mode at different spots to assess the film morphology, uniformity and surface roughness (see examples in Fig. 1B). The AFM utilized in this work was a multimode EC-STM/AFM instrument (Veeco VI) with a Nanoscope IIIID controller using the Nanoscope 5.31r1 software (AFM tips, Bruker RTESP-300).

AFM surface scans with 500×500 nm and 100×100 nm (see Fig. 1B) were conducted. The roughness factor of 1.15±0.15 and narrow height distribution reveal a smooth and nonporous surface.

X-ray photoelectron spectroscopy (XPS) of NiO_x thin films was performed using a XR 50 (Specs, Germany) X-ray source, and a hemispherical energy analyzer (Specs, Germany) with 150 mm mean radius. The characteristic X-ray emission line of Al was used. The spectra were acquired using the Al Kα anode (1486.61 eV).

The shape of the XPS spectra (see Fig. 1C) is similar to those reported earlier for NiOOH and Ni(OH)₂ [28,29]. The position of the Ni 2p_{3/2} peak (855.5 eV) is well in between the two peaks for NiOOH (855.8 eV) and Ni(OH)₂ (855.2 eV) reported in [28], indicating the presence of both phases.

3 Results and Discussion

As has been mentioned above, the proposed methodology requires a “calibration procedure”, which includes the following steps. Initially, it is important to form the thinnest oxide film, which exhibits the desired functional properties, e.g. the OER electrocatalytic activity without the influence of the substrate material, similar to [30]. In principle, a variety of the deposition techniques can be used to form thin non-porous films, for instance pulsed laser and chemical vapour deposition, cathodic or anodic deposition etc. In this work, anodic deposition of NiO_x thin films was selected.

Fig. 1A demonstrates how the OER activity at a given electrode potential, 1.83 V, changes with the nominal thickness of the NiO_x film. The latter can be assessed by the anodic charge, Q , obtained by integrating of the corresponding voltammetric peaks during the film deposition

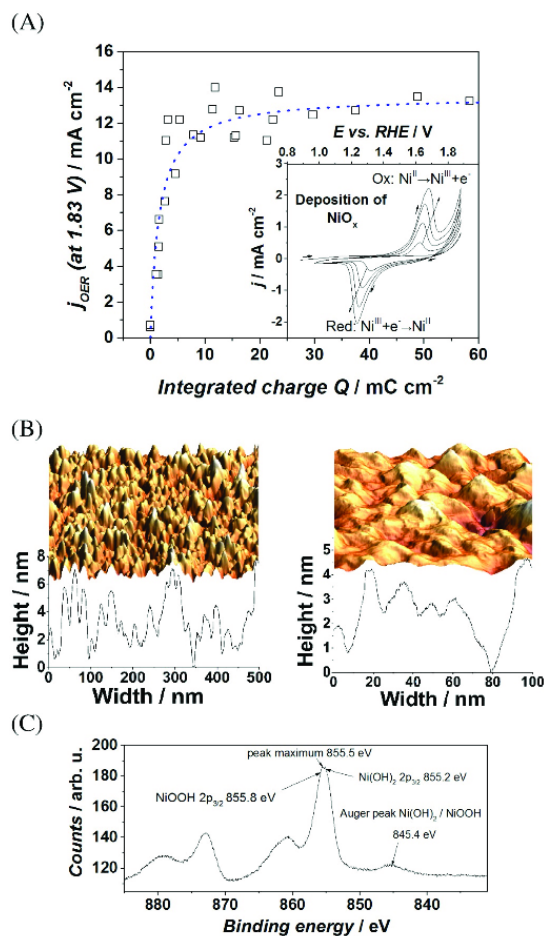


Fig. 1. (A) The dependence of the OER current in 0.1 M KOH at 1.83 V on the voltammetric anodic charge obtained during the NiO_x deposition which is used to assess the film thickness. The blue dotted line (A) is shown as a guide to the eye. The inset shows typical CVs obtained during the deposition of the oxide films. (B) Examples of AFM images of the resulting NiO_x sample surfaces: 500×500 nm (left) and 100×100 nm (right) scans. (C) A fragment of a typical XPS spectrum of the resulting NiO_x film.

(see inset in Fig. 1A). As can be seen in Fig. 1A, the current density due to the OER increases drastically with the increase of the amount of deposited NiO_x (corresponding to the Q values from 0 to ~ 10 mC cm^{-2}). Afterwards, the activity relatively slowly approaches a plateau (Fig. 1A). For further experiments, the net anodic charge $Q \approx 20$ mC cm^{-2} was chosen to form the target NiO_x films, which show the desired functional property (OER activity), without a significant substrate influence. According to [25] this corresponds to a nominal film thickness of ~ 170 nm.

In the second stage, it is important to select the electrode potential which is slightly more anodic than the onset of the OER. The overpotential for the oxygen evolution should be small enough to prevent the formation of the gas bubbles but suitable for the reproducible impedance measurements, with a strong contribution of the OER intermediates to the impedance response. Additionally, it is important to select a procedure which minimizes the “sample history” effect. In this work the following procedure has been applied. Immediately after the film formation, the electrode was cycled ($dE/dt = 50$ mV s^{-1} , 3 cycles as shown in Fig. 2) in Ar-saturated 0.1 M KOH. After the third cycle, a slower scan rate of 1 mV s^{-1} was set between 1.43 V and 1.53 V (Fig. 2). At the latter potential, the impedance measurements were performed in a staircase mode with the interval of 0.01 V between 1.53 V and 1.63 V. The impedance spectra obtained at $E = 1.6$ V were selected for the further analysis and fitting. Evaluation at this electrode potential is a compromise between being above the onset of the OER and complications associated with the gas bubble formation at higher overpotentials for this material. To find the potential where better reproducibility is observed, a total number of 51 independent measurements using 11 different NiO_x films have been performed.

In the following stage, the impedance measurements and data analysis are performed. The analysis of impedance data can be done using a well-accepted physical model describing the OER multistage mechanism, where at least one stage involving adsorbed intermediates is reversible (further theoretical details regarding this model and its connection to the OER can be found in refs [10, 22, 31, 32]). A simplified “visual” representation of

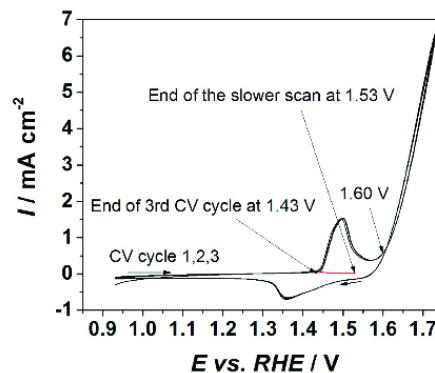


Fig. 2. Typical voltammograms of a freshly prepared NiO_x film. The electrode was cycled at the scan rate of 50 mV s^{-1} (black curves) to quickly ensure that the CVs are stable. After the third cycle the scan rate was reduced to 1 mV s^{-1} (red curve) to ensure that all the Faradaic processes inside the film were completed. At 1.53 V the slower scan was stopped and the impedance measurements were performed in a staircase mode with the interval of 0.01 V between 1.53 V and 1.63 V.

the physical model using the so-called equivalent electric circuit is given in Fig. 3A.

In the equivalent circuit shown in Fig. 3A, the R_u denotes the uncompensated resistance and R_{ct} is the charge transfer resistance. The response of the electric double layer is approximated by the constant phase element (CPE) [33] as $Z_{dl} = C_{dl}^{-1}(j\omega)^{-n}$, where C_{dl} is the parameter, which is proportional to the double layer capacitance, j is the imaginary unit, ω is the angular frequency, and n is the CPE-exponent, which is directly related to the so-called double layer frequency dispersion. R_a and C_a in Fig. 3A denote the resistance and the capacitance of adsorption of OER intermediates, respectively. Namely the latter parameter is proposed for the assessment of the electroactive surface area.

Fig. 3B schematically illustrates the origin of the adsorption capacitance related to the OER intermediates and explains predominant localization of these adsorbates at the surface of the metal oxide electrode.

Fig. 4A and B show a typical impedance spectrum of the NiO_x electrodes at the reference potential of 1.6 V vs RHE scale in 0.1 M KOH together with the fitting results obtained by using the model shown in Fig. 3A in Nyquist (Fig. 4A) and Bode (Fig. 4B) plots. As one can see from the figure, the physical model shown in Fig. 3A fits the data well, with normalized root-mean-square deviations

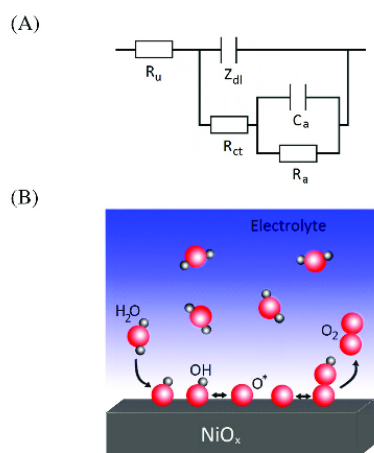


Fig. 3. (A) The equivalent electric circuit used to analyze the impedance data. Additionally to the uncompensated resistance (R_u), the charge-transfer resistance (R_{ct}) and the impedance of the double layer (Z_{dl}), this circuit contains the adsorption resistance (R_a) and capacitance (C_a) to describe the contribution of the reversibly adsorbed reaction intermediates to the impedance response. (B) A simplified sketch explaining the origin of the adsorption capacitance C_a . *OH, *O and *OOH denote OER intermediates where the redox transformations between them can be quasi-reversible with reproducible relevant physico-chemical parameters at a given electrode potential. As these transformations are surface limited, the adsorption capacitance is a parameter which is very sensitive to the electroactive surface area of the oxide electrodes.

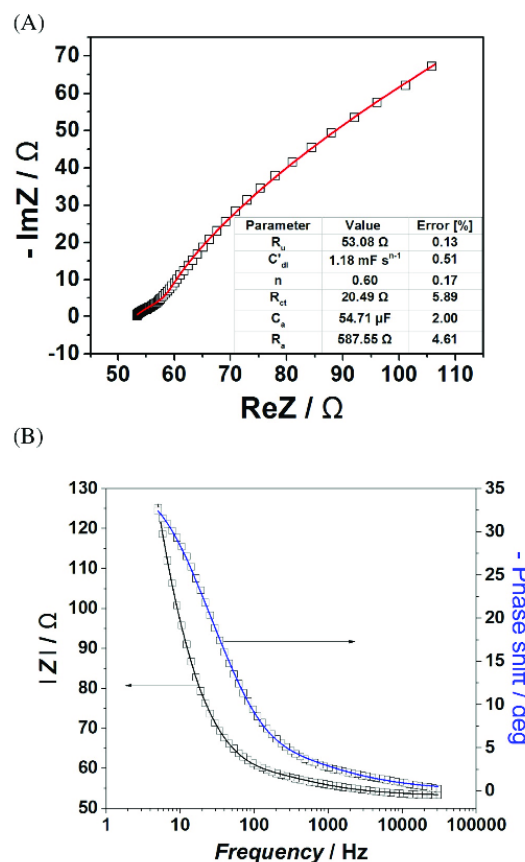


Fig. 4. A typical impedance spectrum of the NiO_x electrode in 0.1 M KOH at 1.6 V versus RHE scale in (A) Nyquist and (B) Bode plots. Open symbols represent the measured data; the lines show fitting results to the model shown in Fig. 3A. The inset in (A) shows the values of the corresponding fitting parameters.

of less than 2% and low estimated individual parameter uncertainties.

As it has been mentioned above, in total 51 independent measurements using 11 different films were done in order to ensure the reproducibility of the values for the adsorption capacitance, C_a , at the selected conditions. The following mean value and the standard deviation were obtained:

$$C_a \text{ (at 1.6 V RHE in 0.1 M KOH)} = 300 \pm 99 \text{ mF cm}^{-2}$$

We suggest that in the particular case of NiO_x films, this value can be used as the reference value to estimate the unknown electroactive area of "real-world" high surface area nickel oxy-hydroxide electrodes. Other conducting oxide materials can be benchmarked and assessed similarly.

Importantly, the estimated deviations from the mean values in the case of NiO_x films used in this work are in the range of $\sim 30\%$, approaching the best analogues in the case of metal surface area estimation. We hypothesize that the observed deviations in the case of the adsorption capacitance of NiO_x are mainly due to differences in the preferential surface structure and the exact surface and subsurface composition of the oxy-hydroxide films from deposition to deposition. Some similar structure-adsorption effects can be found in the case of Pt-electrodes, where for the polycrystalline samples the cumulative charge due to the adsorption of hydrogen atoms at 0.5 to 0.05 V vs RHE corresponds to $\sim 210 \mu\text{Ccm}^{-2}$, while for the Pt(111) it corresponds to $\sim 160 \mu\text{Ccm}^{-2}$, and for the e.g. Cu-Pt(111) near-surface alloys with just submonolayer amounts of Cu, which are located only in the subsurface region, can be as low as $\sim 80 \mu\text{Ccm}^{-2}$ [34]. Other words, the proposed methodology unfortunately shares common weaknesses with the ones typical for the classical methods of the electroactive surface area determination using surface limited adsorption reactions in case of metals: it is sensitive to the exact surface structure and small deviations in the surface/subsurface composition.

On the other hand, the proposed method is more accurate than determination of the electroactive area using BET (no direct connection, as explained above) and through the assessment of the double layer capacitance. One example comparing the proposed method with the one which uses the assessment of the double layer capacitance is given below. It is known that the parameter C'_{dl} extracted from the CPE is proportional to the true double layer capacitance. In some cases one can even estimate the real double layer capacitance [10]. However, as one can see from the example given in Fig. 5, this parameter deviates significantly (by up to $\sim 100\%$) from sample to sample without a clear (according to the up-to-

date) reason, while the values of the C_a for the same samples are very close to each other. This can probably be explained with the fact that C_a is more sensitive to the surface properties only, while the measured apparent “double layer capacitance” contains poorly predictable contributions from the bulk properties of the NiO_x films, double layer frequency dispersion, possible contributions from the space charge layers, non-separable from the double layer response fast Faradaic contributions etc.

In summary, the methodology for a quick determination of the electroactive surface area of some oxide electrodes is proposed. It is based on the fact that the OER adsorbates manifest themselves through the adsorption capacitance. The latter, being benchmarked at a low OER overpotential for a model system, can be used to assess the real electroactive surface area for the “real-world” functional electrodes.

Acknowledgements

We are thankful to Jonas Pfisterer (TUM) for AFM measurements. The Cluster of Excellence Nanosystems Initiative Munich (NIM) is acknowledged for the financial support.

References

- [1] M. Armand, J. M. Tarascon, *Nature* **2008**, *451*, 652–657.
- [2] J. Suntivich, K. J. May, H. A. Gasteiger, J. B. Goodenough, Y. Shao-Horn, *Science* **2011**, *334*, 1383.
- [3] O. Bicakova, P. Straka, *Int. J. Hydrogen Energy* **2012**, *37*, 11563.
- [4] A. R. Zeradjanin, E. Ventosa, A. S. Bondarenko, W. Schuhmann, *ChemSusChem* **2012**, *5*, 1905.
- [5] A. Maljusch, E. Ventosa, R. A. Rincón, A. S. Bandarenka, W. Schuhmann, *Electrochem. Commun.* **2014**, *38*, 142–145.
- [6] M. Grotheer, R. Alkire, R. Varjian, *Electrochem. Soc. Interface* **2006**, *15*, 52.
- [7] S. Trasatti, O. A. Petrii, *J. Electroanal. Chem.* **1992**, *327*, 353–376.
- [8] L. D. Burke, O. J. Murphy, *J. Electroanal. Chem.* **1980**, *112*, 39–50.
- [9] L. D. Burke, O. J. Murphy, *J. Electroanal. Chem.* **1979**, *96*, 19–27.
- [10] A. Lasia, *Electrochemical Impedance Spectroscopy and its Applications*, Springer-Verlag New York, **2014**, 367 p.
- [11] S. G. Ehrlich, P. J. Moran, *Corros. Sci.* **1989**, *45*, 689–696.
- [12] S. K. Roy, M. E. Orazem, *J. Electrochem. Soc.* **2009**, *156*, B203–B209.
- [13] Z. Kerner, T. Pajkossy, *Electrochim. Acta* **2000**, *46*, 207–211.
- [14] T. Pajkossy, *Solid State Ionics* **2005**, *176*, 1997–2003.
- [15] J. Tymoczko, V. Colic, A. S. Bandarenka, W. Schuhmann, *Surface Sci.* **2015**, *631*, 81–87.
- [16] J. Tymoczko, W. Schuhmann, A. S. Bandarenka, *Electrochem. Commun.* **2013**, *27*, 42–45.
- [17] C. C. L. McCrory, S. Jung, J. C. Peters, T. F. Jaramillo, *J. Am. Chem. Soc.* **2013**, *135*, 16977–16987.
- [18] S. Trasatti, O. A. Petrii, *J. Electroanal. Chem.* **1992**, *327*, 353–376.
- [19] L. Bai, L. Gao, B. E. Conway, *J. Chem. Soc. Faraday Transactions* **1993**, *89*, 243.

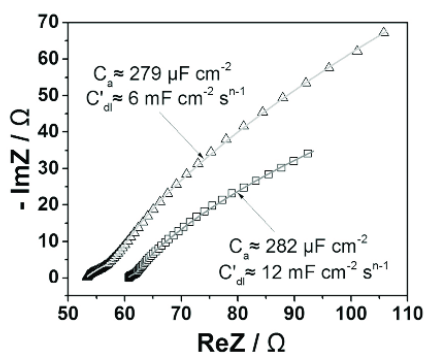


Fig. 5. Examples of impedance data for two different electrodes with almost the same amount of deposited NiO_x (5% deviation) and similar surface areas taken in 0.1 M KOH at 1.60 V. While the values of the C'_{dl} parameters of the constant phase element (CPE) are almost by a factor of two different, the adsorption capacitance C_a demonstrates only slight deviation. Solid lines represent the results of the fitting to the model shown in Fig. 3A.

- [20] M. J. Gira, K. P. Tkacz, J. R. Hampton, *Nano Convergence* **2016**, 3-6.
- [21] J. Tymoczko, W. Schuhmann, A. S. Bandarenka, *Phys. Chem. Chem. Phys.* **2013**, *15*, 12998.
- [22] V. Colic, J. Tymoczko, A. Maljusch, A. Ganassin, W. Schuhmann, A. S. Bandarenka, *ChemElectroChem* **2015**, *2*, 143–149.
- [23] A. S. Bondarenko, *Analyt. Chim. Acta* **2012**, *743*, 41–50.
- [24] A. S. Bondarenko, G. A. Ragoisha. "EIS spectrum analyser." <http://www.abc.chemistry.bsu.by/vi/analyser> (2008).
- [25] D. Tench, L. F. Warren, *J. Electrochem Soc.* **1983**, *130*, 869–872.
- [26] L. Trotochaud, S. L. Young, J. K. Ranney, S. W. Boettcher, *J. Am. Chem. Soc.* **2014**, *136*, 6744–6753.
- [27] M.-S. Wu, C.-H. Yang, M.-J. Wang, *Electrochim. Acta* **2008**, *54*, 155–161.
- [28] M. C. Biesinger, L. W. M. Lau, A. R. Gerson, R. St. C. Smart, *Phys. Chem. Chem. Phys.* **2012**, *14*, 2434–2442.
- [29] A. P. Grosvenor, M. C. Biesinger, R. St. C. Smart, N. S. McIntyre, *Surface Sci.* **2006**, *600*, 1771–1779.
- [30] A. Ganassin, A. Maljusch, V. Colic, L. Spanier, K. Brandl, W. Schuhmann, A. S. Bandarenka, *ACS Catal.* **2016**, *6*, 3017–3024.
- [31] R. L. Doyle, M. E. G. Lyons, *Phys. Chem. Chem. Phys.* **2013**, *15*, 5224–5237.
- [32] M. E. G. Lyons, M. P. Brandon, *Int. J. Electrochem. Sci.* **2008**, *3*, 1386–1424.
- [33] A. S. Bandarenka, *Analyst* **2013**, *138*, 5540–5554.
- [34] J. Tymoczko, F. Calle-Vallejo, W. Schuhmann, A. S. Bandarenka, *Nature Communications* **2016**, *7*, 10990.

Received: March 18, 2016

Accepted: May 2, 2016

Published online: June 1, 2016

Intrinsic Activity of Some Oxygen and Hydrogen Evolution Reaction Electrocatalysts under Industrially Relevant Conditions

Sebastian Watzele,^{†,‡} Yunchang Liang,[†] and Aliaksandr S. Bandarenka^{*,†,‡,§}

[†]Physik-Department ECS, Technische Universität München, James-Frank-Straße 1, 85748 Garching, Germany

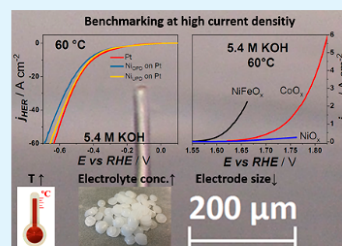
[‡]Nanosystems Initiative Munich (NIM), Schellingstraße 4, 80799 Munich, Germany

[§]Catalysis Research Center TUM, Ernst-Otto-Fischer-Straße 1, 85748 Garching, Germany

ABSTRACT: Water electrolysis to produce hydrogen fuel is one of the most important processes to optimize on the way to sustainable energy provision schemes. Its efficiency in both alkaline and acidic media is drastically limited by the sluggish kinetics of the oxygen evolution reaction (OER) taking place at the anode side of modern electrolyzers. Numerous electrocatalysts have been proposed recently to increase the activity of the anodes; most of them are transition metal oxides and perovskite materials. However, the activities reported in the literature for these electrodes are in the majority of cases measured at low overpotentials, low or moderate current densities (often 10–50 mA cm⁻²), relatively diluted electrolytes (e.g., 0.1 M KOH), and room temperatures. However, commercial electrolyzers operate at current densities that are at least 1 order of magnitude larger, elevated temperatures, and significantly higher pHs.

To enable new generation of electrocatalysts, it is important to evaluate their intrinsic activities under industrially relevant conditions. This is not a trivial task, neither in industry nor in research laboratories, particularly due to (i) formation of a nonconducting gas phase in the vicinity of the electrode under such conditions, (ii) limitations due to mass transfer and uncompensated resistances, and (iii) problems in determination of the real electroactive electrode surface area. In this work, with the use of microelectrodes, we evaluate intrinsic OER catalytic activities of several state-of-the-art nickel-, cobalt- and nickel/iron-oxide/hydroxide thin films at different temperatures (up to 80 °C), in 5.4 M KOH and at current densities up to several A cm⁻². Additionally, Ni-modified Pt electrocatalysts for the hydrogen evolution reaction were also tested under similar conditions and compared with pure Pt electrodes.

KEYWORDS: electrocatalysis, microelectrodes, oxygen evolution reaction, hydrogen evolution reaction, cobalt oxide, nickel oxide, nickel iron oxide, nickel



1. INTRODUCTION

The increasing demand for energy supplies from renewable sources requires efficient energy conversion and storage concepts. The oxygen evolution reaction (OER) is essential in many energy-related processes, for instance, in water splitting to produce H₂ fuel. The sluggish reaction kinetics of the OER can be improved by an appropriate choice of electrocatalysts. However, the research on finding the most active materials with optimum adsorption properties for OER intermediates is still ongoing. On the way to identification of ever better OER-electrocatalysts, the key verification procedure is accurate experimental benchmarking of electrocatalysts, which is often complicated.^{1–4} A nonconducting gas phase formed at the electrode leads to a periodic or stochastic blockage of the surface active sites complicating evaluation and comparison of intrinsic catalytic activities significantly. Additionally, it should be noted that common OER catalyst materials are metal oxides, and for them, the electroactive electrode surface area required to calculate the specific reaction current densities is difficult to determine.⁵ Further complications cause so-called uncompensated resistance, which depends on electrode size, cell geometry, current densities, and other

parameters. In particular, for the common electrode sizes at high current densities, the contribution of the potential drop makes evaluation of the intrinsic activities very problematic.^{6,7} All this makes evaluation of the intrinsic activity under industrially relevant conditions very rare in the literature. However, it is at least of 2-fold importance giving key information about not only activity but also stability under relevant temperature, electrolyte compositions, current densities, etc.⁸

In industrial alkaline electrolyzers, electrolytes of 10–30 wt %^{9,10} (approximately 1.8 to 5.4 M) KOH or NaOH are commonly used. These electrolyzers usually operate at elevated temperatures (40–90 °C)¹¹ at current densities close to 0.4 A cm⁻².¹² In research laboratories, in contrast, benchmarking for OER electrocatalysts is mostly conducted at room temperatures, diluted electrolytes and relatively low current densities close to 10 mA cm⁻².^{13,14} In this work, three state-of-the-art electrodeposited transition metal oxide-hydroxide electro-

Received: May 28, 2018

Accepted: July 9, 2018

Published: July 9, 2018

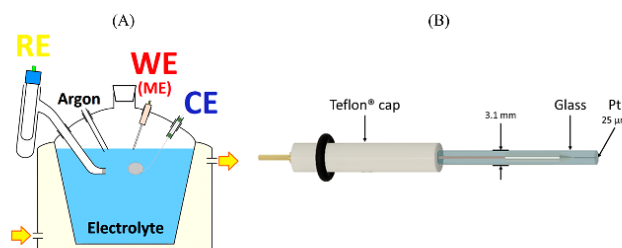


Figure 1. (A) Sketch of the electrochemical cell and (B) schematic representation of the microelectrodes used in this work.

catalysts, designated as NiO_x , CoO_x , and NiFeO_x were evaluated in 5.4 M KOH at different temperatures and current densities up to several A cm^{-2} . Moreover, hydrogen evolution reaction (HER) activity measurements of partially covered with nickel platinum electrodes, which has been recently reported to have superior HER activity in alkaline media,^{15,16} were conducted. For the measurements, we utilized a special type of Pt microelectrodes with a thick special glass coating releasing a $25 \mu\text{m}$ diameter working electrode surface. Smooth metal oxide films were electrochemically deposited on that surface. The small size of the electrode suppresses gas phase formation minimizing the surface active sites blockage and additionally eliminates the iR drop under high current densities.⁸

2. EXPERIMENTAL SECTION

A VSP-300 (Bio-Logic, France) potentiostat was utilized for all electrochemical measurements. A Hg/HgSO₄ electrode (Schott) and a Pt wire/mesh (Goodfellow) were used as the reference (RE) and counter electrodes (CE), respectively. However, all potentials are referred to the RHE scale. Experiments were performed in a double walled electrochemical cell, shown in Figure 1A, enabling thermal control during experiments using a thermostat (Julabo, Germany). Two polycrystalline Pt microelectrodes (Ch. Instruments, USA) with diameter of $25 \mu\text{m}$ (see Figure 1) were used as substrates for the thin film depositions. The OER activities showed only negligible differences when measuring the same electrocatalyst film deposited on different microelectrodes. Ar-saturated (Ar 5.0, Air Liquide, Germany) 0.1 and 5.4 M KOH working electrolytes were prepared using KOH ($\geq 85\%$, Grüssing, Germany).

Nickel (hydro)oxide and cobalt (hydro)oxide films (denoted as NiO_x and CoO_x) films were deposited as described by Tench et al.¹⁷ NiFeO_x deposition was performed as described by McCrory et al.,¹⁸ using $\text{NiSO}_4 \cdot 6\text{H}_2\text{O}$, $\text{CoSO}_4 \cdot 6\text{H}_2\text{O}$, Na_2SO_4 , $\text{NaOAc} \cdot 6\text{H}_2\text{O}$, $\text{FeSO}_4 \cdot 6\text{H}_2\text{O}$, and $(\text{NH}_4)_2\text{SO}_4$ (all 99%, Sigma-Aldrich, Germany). In brief, NiO_x and CoO_x films were anodically deposited onto the Pt-microelectrodes (Figure 1B) using cyclic voltammetry (CV) scans. For the deposition, the potential scan rate of 50 mVs^{-1} and a potential window from 0.95 to 1.86 V, and 0.95 to 1.76 V, for the nickel- and cobalt-oxhydroxide films, respectively, were used. The process can be roughly schematized (as described by D. Tench and F. Warren¹⁷) as

$$\text{Me}^{2+} \xrightarrow{-e^-} \text{Me}^{3+} \xrightarrow{\text{OH}^-} \text{MeO}(\text{OH}) \xrightarrow{-e^-} \text{Me}(\text{OH})_2$$

The deposition was stopped when a total anodic charge of $\sim 30 \text{ mC cm}^{-2}$ was reached.⁸

Nickel-iron oxy-hydroxide films (denoted as NiFeO_x) were deposited cathodically, applying a constant current of -250 mA cm^{-2} for 50s, whereas the microelectrode was immersed in the deposition solution (9 mM FeSO_4 , 9 mM NiSO_4 , and 7.3 mM $(\text{NH}_4)_2\text{SO}_4$). Table 1 summarizes the deposition procedure for all the three OER catalysts. After film deposition, the electrodes were carefully rinsed with ultrapure water.

Table 1. Catalyst Materials and Their Deposition Conditions

catalyst	deposition solution	deposition conditions
NiO_x	0.13 M NiSO_4 , 0.13 M NaOAc , and 0.1 M Na_2SO_4	anodic deposition, cycling (50 mV/s) between 0.95 and 1.86 V
CoO_x	0.1 M CoSO_4 , 0.1 M NaOAc , and 0.1 M Na_2SO_4	anodic deposition, cycling (50 mV/s) between 0.95 and 1.76 V
NiFeO_x	9 mM FeSO_4 , 9 mM NiSO_4 , and 7.3 mM $(\text{NH}_4)_2\text{SO}_4$	cathodic deposition, -250 mA cm^{-2}

The OER activities of the thin films deposited on the microelectrodes were measured in 0.1 M at 25°C and 5.4 M KOH at temperatures of 25, 45, 60, and 80°C . Subsequently the electrodes were cleaned by cycling them in 0.1 M HClO_4 (70% Suprapure, Merck, Germany) until a stable CV of polycrystalline Pt was achieved, before the next film was deposited.

For the HER experiments, the microelectrodes were initially cleaned by cycling them in 0.1 M HClO_4 . Nickel underpotential deposition (UPD) was utilized to achieve a partial Ni-coverage.^{19,20} The deposition was performed in a solution containing 0.1 M H_2SO_4 (96% Suprapure, Merck, Germany) and 2.5 mM NiSO_4 . A potential of 0.051 V was applied for 220 s. For the complete coverage with Ni, the potential was set to -0.031 V for 25 s (after the UPD).

The surfaces of similarly prepared macroscopic electrodes were characterized using atomic force microscopy (AFM) and X-ray photoelectron spectroscopy (XPS) (substrates: Pt(pc) $\varnothing = 5 \text{ mm}$ disc electrode for AFM and Au(111) Arrandee chip for XPS). AFM (AFM tips, Bruker RTESP-300) was performed in the tapping mode at different spots to assess the film morphology, uniformity, and surface roughness. A Multimode EC-STM/AFM instrument (Veeco Instruments Inc.) with a Nanoscope IIIID controller using the Nanoscope 5.31r1 software (AFM tips, Bruker RTESP-300) was utilized for this work. XPS of the thin films was performed using a XR 50 (Specs, Germany) X-ray source. The photoelectron energy was measured with a hemispherical energy analyzer (Specs, Germany). The spectra were taken using an Al $K\alpha$ anode (1486.61 eV). An optical microscope (Zeiss, Germany) was utilized for taking pictures of the microelectrode tips.

3. RESULTS AND DISCUSSION

3.1. AFM and XPS Characterization. Evaluation of electrocatalytic activity requires precise determination of the electrode surface area. The AFM images and the surface profile lines were used to evaluate the real surface area, which was assumed to be close to the electroactive surface area. The AFM images of the metal oxide thin films on polycrystalline Pt are shown in Figure 2A–C. The surface profiles display a narrow height distribution in the order of 10 nm for all three different films. Roughness analysis shows that the specific surface areas of the films are slightly larger than the cross-section of the electrode. All metal oxide films tested in the work had the

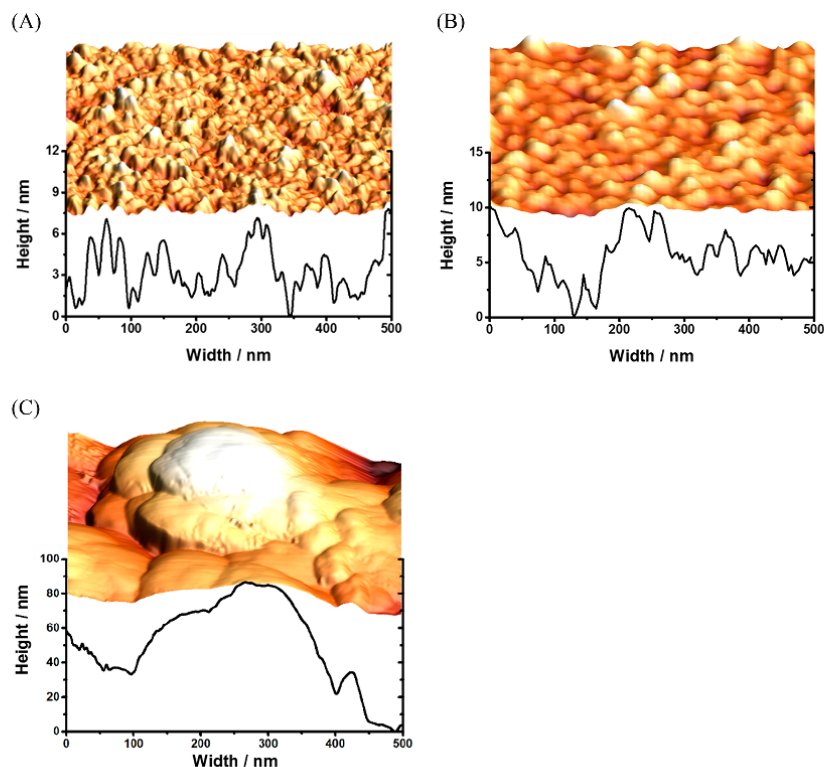


Figure 2. Examples of AFM images of the metal oxide electrocatalyst thin films: (A) NiO_x , (B) CoO_x , and (C) NiFeO_x .

following roughness factor, Θ , $\Theta_{\text{NiO}_x} \approx 1.25$, $\Theta_{\text{CoO}_x} \approx 1.05$, and $\Theta_{\text{NiFeO}_x} \approx 1.27$. All current densities reported in this work were normalized to the real surface area.

Figure 3 shows typical XPS patterns for the electrodeposited thin films of the OER electrocatalysts. The shape of the XPS spectra of the NiO_x thin film is shown in Figure 3A. It is well comparable to spectra of nickel oxy-hydroxide films reported by literature. The peak at the binding energy of 873.0 eV is close to the Ni $2p_{1/2}$ peak positions of NiOOH (873.1 eV),²¹ Ni(OH)_2 (873.7 eV),²² and NiO (873.8 eV).²³ Another peak at the binding energy of 855.4 eV fits to the Ni $2p_{3/2}$ peak positions of NiOOH (855.3 eV),²⁴ Ni(OH)_2 (855.0 eV),²⁵ and of NiO (855.5 eV).²⁶ In the regime of OER, the surface of the catalyst typically oxidizes to the Ni^{3+} phase.

XPS spectra of the CoO_x thin film (Figure 3B) indicate the presence of the Co(II) and the Co(III) phases. It features a pronounced double $p_{3/2}$ peak (780.4 and 782.8 eV) and a corresponding satellite at 787.8 eV. These values fit to those reported by other groups for Co(OH)_2 (~17%), CoOOH (~59%), and Co_3O_4 (~24%).²⁷

The XPS spectra of NiFeO_x film (Figure 3C) show Ni-peaks (873.6 eV for $2p_{1/2}$ and 855.7 eV for $2p_{3/2}$) in the vicinity of those of the NiO_x film. Additionally, a sharp peak at 852.7 eV indicates the presence of metallic Ni.²⁸ Two peaks of Fe can be found at around 724.9 eV, corresponding to the earlier reported $2p_{1/2}$ peaks of FeOOH and Fe_2O_3 .²⁹ A pronounced peak at 711.7 eV is the superposition of the $2p_{3/2}$ peaks of

FeOOH , Fe_2O_3 , and Fe_3O_4 .³⁰ The smaller peak at 707.0 eV indicates that a small amount of metallic Fe³¹ was deposited too. However, it can be assumed that the metallic Fe oxidizes under experimental conditions of OER. The ratio was determined as ~70% and ~30% for nickel and iron, respectively.

3.2. Electrocatalytic Activity Measurements. Figure 4A-C shows the anodic voltammetric scans characterizing the OER activities of the three metal-oxide-based electrocatalysts at various conditions. First, the electrocatalytic activity for the OER of all three metal oxide films was tested at standard laboratory conditions (0.1 M KOH and 25 °C). This is shown using the black lines in Figure 4. The current depends on the applied potential quasi-exponentially. This indicates that diffusion is not the limiting factor under the selected conditions. At ~1.75 V, the current densities of ~50 and ~120 mA cm^{-2} are reached for NiO_x (Figure 4A) and CoO_x (Figure 4B), respectively. The NiFeO_x film yields a current density of 150 mA cm^{-2} already at the potential of ~1.65 V (Figure 4C).

Afterward, these films were also tested in 5.4 M KOH at temperatures of 25 °C (red lines), 45 °C (blue lines), 60 °C (purple lines), and 80 °C (green lines). These conditions are close to those used in industrial applications. As expected, the current density increased with a higher concentration of the KOH and also with increasing the temperatures. This enhancement is caused by improved reaction kinetics, diffusion

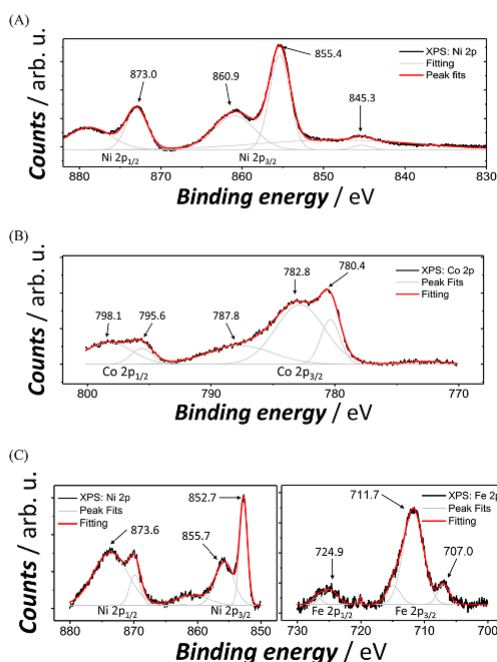


Figure 3. Typical XPS spectra of (A) NiO_x , (B) CoO_x , and (C) NiFeO_x thin film electrocatalysts.

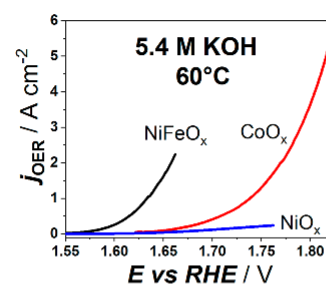


Figure 5. Comparison of the OER electrocatalytic activity of NiO_x , NiFeO_x , and CoO_x in 5.4 M KOH at 60 °C.

rates, and reduction of Gibbs free enthalpy required for water splitting reaction at higher temperatures.

Current densities of approximately 0.6 A cm^{-2} , in the case of NiO_x and several A cm^{-2} for CoO_x and NiFeO_x were reached without noticeable noise influence. Remarkably, the current does not reach a plateau in all the cases. That implies that the mass transfer is probably not the major limiting factor under these conditions. However, the Tafel-plot (inset of Figure 4D) shows nonlinearities at all the potentials, meaning that a simple extrapolation of data measured at lower current densities would deviate distinctly from the actual activities. Therefore, it is so important to perform the activity benchmarking also at current densities and other conditions of real application.

The bubble formation commonly, but not always,³² resulting in the current noise was suppressed and not detected at current densities smaller than 1 A cm^{-2} . Although in alkaline media, especially at high temperatures glass corrosion was reported

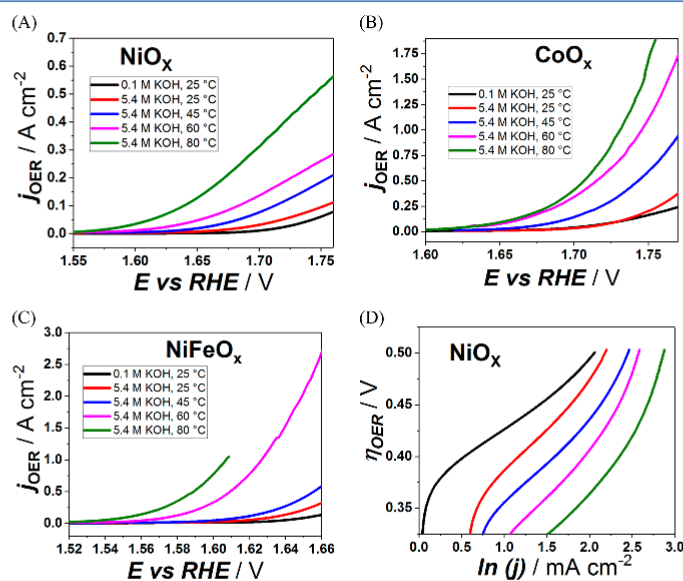


Figure 4. Benchmarking the catalytic activity of (A) NiO_x , (B) CoO_x , and (C) NiFeO_x in 0.1 and 5.4 M KOH electrolytes at different temperatures as indicated in the figure. (D) Tafel plots of the curves presented in A for NiO_x . All activities are normalized to the estimated surface area.

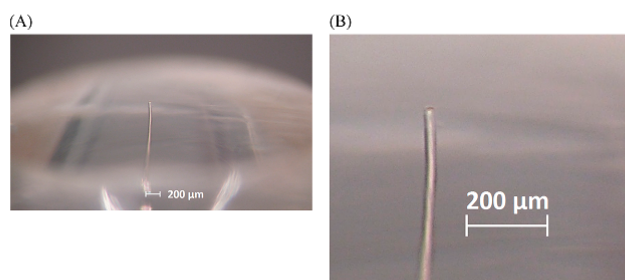


Figure 6. (A, B) Optical images of the microelectrodes after the OER experiments, where B shows an enlarged section of A. After the prolonged experiments in the 5.4 M KOH solutions at 80 °C, no obvious traces of corrosion are observed.

Table 2. OER Activity Data Measured at Different Temperatures and Current Densities in 5.4 M KOH

catalyst	T (°C)	$E_{100 \text{ mA cm}^{-2}}$ (V)	$E_{500 \text{ mA cm}^{-2}}$ (V)	$I_{1.60 \text{ V}}$ (mA cm ⁻²)	$I_{1.65 \text{ V}}$ (mA cm ⁻²)	$I_{1.75 \text{ V}}$ (mA cm ⁻²)
NiO _x	25 ^a	1.772 ± 0.003		0.8 ± 0.05	1.3 ± 0.08	61 ± 3.7
	25	1.753 ± 0.008		3 ± 0.4	7.5 ± 0.9	95 ± 12
	45	1.712 ± 0.002		5 ± 0.2	19 ± 0.7	186 ± 6.5
	60	1.683 ± 0.001		11 ± 0.3	48 ± 1.2	262 ± 6.6
	80	1.639 ± 0.0005	1.745 ± 0.001	34 ± 0.4	128 ± 1.4	523 ± 5.7
CoO _x	25 ^a	1.730 ± 0.004	1.825 ± 0.009	7.3 ± 0.7	11.1 ± 1.1	164 ± 16
	25	1.729 ± 0.002	1.779 ± 0.002	8.6 ± 0.5	11.1 ± 0.7	205 ± 13
	45	1.689 ± 0.002	1.743 ± 0.003	10.1 ± 0.7	26.8 ± 2.0	592 ± 44
	60	1.658 ± 0.004	1.715 ± 0.005	14.3 ± 1.7	76.7 ± 9.5	1150 ± 140
	80	1.623 ± 0.003	1.707 ± 0.003	20.0 ± 1.5	92 ± 6.9	1690 ± 130
NiFeO _x	25 ^a	1.654 ± 0.001		16 ± 0.9	90 ± 5.4	
	25	1.633 ± 0.003		22 ± 2.8	211 ± 27	
	45	1.615 ± 0.002	1.656 ± 0.002	45 ± 3.7	402 ± 33	
	60	1.576 ± 0.001	1.609 ± 0.002	330 ± 21	2054 ± 133	
	80	1.553 ± 0.002	1.589 ± 0.003	777 ± 77		

^a0.1 M KOH (all the other measurements were performed in 5.4 M KOH).

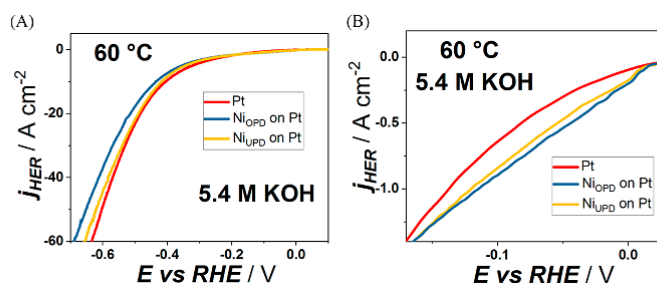


Figure 7. (A) Comparison of the electro catalytic activity toward the HER of Pt, overpotential-deposited (Ni_{OPD}) and underpotential-deposited Ni (Ni_{UPD}) on Pt in Ar-saturated 5.4 M KOH at 60 °C. (B) Magnified part of the curves shown in A and corresponding to the lower overpotentials.

Table 3. HER Activity Data Measured in 5.4 M KOH (Ar saturated) at 60 °C

catalyst	$E_{0.5 \text{ A cm}^{-2}}$ (mV)	$E_{2 \text{ A cm}^{-2}}$ (mV)	$E_{5 \text{ A cm}^{-2}}$ (mV)	$I_{-100 \text{ mV}}$ (mA cm ⁻²)	$I_{-200 \text{ mV}}$ (mA cm ⁻²)
Pt	-81.79 ± 0.001	-209.03 ± 0.003	321.11 ± 0.002	-640 ± 9	-1842 ± 27
Ni _{OPD}	-43.82 ± 0.003	-225.98 ± 0.006	353.98 ± 0.005	-896 ± 35	-1719 ± 69
Ni _{UPD}	-54.01 ± 0.006	-219.10 ± 0.011	343.93 ± 0.010	-842 ± 67	-1783 ± 142

and investigated by different groups,^{33,34} we could not observe any evidence for a significant contribution of such a corrosion process on our electrodes, as we were able to reproduce our measurements without noticeable deviations.

The activities of the different electrocatalyst films (at the equal conditions) follow the following trend: NiFeO_x > CoO_x > NiO_x, well in agreement with the literature data.³⁵ In further experiments, they are compared at the temperature of 60 °C (see Figure 5). For NiFeO_x the current at 60 °C can reach

$\sim 3.0 \text{ A cm}^{-2}$ at the potential $\sim 1.63 \text{ V}$. The microelectrode worked stably and reproducibly at all elevated temperatures. Additionally, also the micrographs of a used (Figure 6) microelectrode showed no evidence of significant glass corrosion. Table 2 summarizes the OER activity data measured in this work at different temperatures and current densities.

Additional to the OER experiments comparing Ni-, Co-, and NiFe-oxy-hydroxides, we performed hydrogen evolution experiments in the same electrolyte at 60°C for 3 different metal electrodes (see Figure 7). First, the clean polycrystalline platinum microelectrode (red line), then the same electrode, which was partially covered by underpotentially deposited Ni-atomic layer (yellow line) and finally the Pt electrode with higher coverage of Ni (blue line), which was achieved by overpotential deposition.

Figure 7A characterizes the Pt microelectrodes in the regime of the hydrogen evolution reaction at 60°C in 5.4 M KOH . At overpotentials less than 0.2 V , the Ni-covered electrodes seem to outperform the plain Pt electrode (Figure 7B). This finding is in agreement with the results from Markovic's group for Ni islands on Pt(111).³⁶ However, at higher overpotentials the trend seems to be inverse: at potentials below -0.2 V , Pt displays the highest activity followed by Pt covered with lower amount Ni (Ni_{UPD}) and, finally, by the one with higher amount of Ni (Ni_{OPD}).

At a current density of $j = 10 \text{ A cm}^{-2}$ the difference of the overpotential for nickel and Pt is $\Delta E_{10 \text{ A cm}^{-2}} = 0.03 \text{ V}$ and increases further for higher current densities. This transition at approximately -0.2 V demonstrates again that a deduction of activity trends at lower to higher current densities can be misleading. In this experiment, HER current densities up to 100 A cm^{-2} were reached without significant influence of mass transport limitations and without the impact of bubble formation, by the use of the microelectrodes. Table 3 summarizes the HER activity data measured in 5.4 M KOH (Ar saturated.) at 60°C .

SUMMARY AND CONCLUSIONS

The intrinsic activities of three different transition metal oxide catalysts toward OER at conditions relevant to industry were determined, especially at high ($>100 \text{ mA cm}^{-2}$) current densities. Therefore, microelectrodes were utilized to minimize several common experimental limits, such as mass transport limitations and gas bubble formation. Additional elevation of temperature and usage of high concentrated electrolytes (5.4 M KOH) allowed to test the intrinsic activity at current densities typical and even exceeding those of state-of-the-art alkaline electrolyzer anode catalysts. Nonlinearity in the Tafel slopes at every point was observed, indicating that a simple extrapolation of activities from lower to higher overpotentials is often faulty. This points out the importance of measurements for the determination of the real activity of the catalyst under industrially relevant conditions. Further, we examined the activity toward HER of electrochemically deposited Ni submonolayer on Pt(pc) and compared the activity of it with that of pure Pt(pc). Interestingly, at current densities lower than $\sim 1.5 \text{ A cm}^{-2}$, it follows the already reported trend³⁶ that the presence of Ni islands on Pt electrode enhances the overall activity. However, it turned out to be less active than bare Pt(pc) at current densities higher than $\sim 1.5 \text{ A cm}^{-2}$.

AUTHOR INFORMATION

Corresponding Author

*E-mail: bandarenka@ph.tum.de. Tel. +49 (0) 89 289 12531 (A.S.B.).

ORCID

Aliaksandr S. Bandarenka: 0000-0002-5970-4315

Author Contributions

The manuscript was written through contributions of all authors. All authors have given approval to the final version of the manuscript.

Notes

The authors declare no competing financial interest.

ACKNOWLEDGMENTS

We are thankful to Katia Rodewald for taking the optical micrograph images. Financial support from the cluster of excellence Nanosystems Initiative Munich (NIM) is gratefully acknowledged.

REFERENCES

- (1) Čolić, V.; Tymoczko, J.; Maljusch, A.; Ganassin, A.; Schuhmann, W.; Bandarenka, A. S. Experimental Aspects in Benchmarking of the Electrocatalytic Activity. *ChemElectroChem* **2015**, *2*, 143–149.
- (2) Jung, S.; McCrory, C. C. L.; Ferrer, I. M.; Peters, J. C.; Jaramillo, T. F. Benchmarking Nanoparticulate Metal Oxide Electrocatalysts for the Alkaline Water Oxidation Reaction. *J. Mater. Chem. A* **2016**, *4*, 3068–3076.
- (3) Zeradjanin, A. R.; Ventosa, E.; Bondarenko, A. S.; Schuhmann, W. Evaluation of Catalytic Performance of Gas Evolving Electrodes Using Local Electrochemical Noise Measurements. *ChemSusChem* **2012**, *5*, 1905–1911.
- (4) Chen, X.; Maljusch, A.; Rincón, R. A.; Battistel, A.; Bandarenka, A. S.; Schuhmann, W. Local Visualization of Catalytic Activity at Gas Evolving Electrodes Using Frequency-Dependent Scanning Electrochemical Microscopy. *Chem. Commun.* **2014**, *50*, 13250–13253.
- (5) Watzel, S.; Bandarenka, A. S. Quick Determination of Electroactive Surface Area of Some Oxide Electrode Materials. *Electroanalysis* **2016**, *28*, 2394.
- (6) Cooper, K. R.; Smith, M. Electrical Test Methods for On-Line Fuel Cell Ohmic Resistance Measurement. *J. Power Sources* **2006**, *160*, 1088.
- (7) Epelboin, I.; Keddam, M.; Takenouti, H. Use of Impedance Measurements for the Determination of the Instant Rate of Metal Corrosion. *J. Appl. Electrochem.* **1972**, *2*, 71.
- (8) Ganassin, A.; Maljusch, A.; Čolić, V.; Spanier, L.; Brandl, K.; Schuhmann, W.; Bandarenka, A. S. Benchmarking the Performance of Thin-Film Oxide Electrocatalysts for Gas Evolution Reactions at High Current Densities. *ACS Catal.* **2016**, *6*, 3017–3024.
- (9) Santos, D. M. F.; Sequeira, C. A. C.; Figueiredo, J. L. Hydrogen Production by Alkaline Water Electrolysis. *Quim. Nova* **2013**, *36*, 1176–1193.
- (10) Gutmann, F.; Murphy, O. J. *Modern Aspects of Electrochemistry*; Plenum Press: New York, 1983.
- (11) Kinoshita, K. *Electrochemical Oxygen Technology*, 1st ed.; John Wiley & Sons: New York, 1992.
- (12) Carmo, M.; Fritz, D.; Mergel, J.; Stolten, D. A Comprehensive Review on PEM Water Electrolysis. *Int. J. Hydrogen Energy* **2013**, *38*, 4901.
- (13) McCrory, C. C. L.; Jung, S.; Ferrer, I. M.; Chatman, S. M.; Peters, J. C.; Jaramillo, T. F. Benchmarking Hydrogen Evolving Reaction and Oxygen Evolving Reaction Electrocatalysts for Solar Water Splitting Devices. *J. Am. Chem. Soc.* **2015**, *137*, 4347–4357.
- (14) Monteverde Videla, A. H. A.; Stelmachowski, P.; Ercolino, G.; Specchia, S. Benchmark Comparison of Co_3O_4 Spinel-Structured Oxides with Different Morphologies for Oxygen Evolution Reaction Under Alkaline Conditions. *J. Appl. Electrochem.* **2017**, *47*, 295–304.

- (15) Ledezma-Yanez, I.; Wallace, W. D. Z.; Sebastian-Pascual, P.; Climent, V.; Feliu, J. M.; Koper, M. T. M. Interfacial Water Reorganization as a pH-Dependent Descriptor of the Hydrogen Evolution Rate on Platinum Electrodes. *Nature Energy* **2017**, *2*, 17031.
- (16) Strmcnik, D.; Uchimura, M.; Wang, C.; Subbaraman, R.; Danilovic, N.; van der Vliet, D.; Paulikas, A. P.; Stamenkovic, V. R.; Markovic, N. M. Improving the Hydrogen Oxidation Reaction Rate by Promotion of Hydroxyl Adsorption. *Nat. Chem.* **2013**, *5*, 300–306.
- (17) Tench, D.; Warren, L. F. Electrodeposition of Conducting Transition Metal Oxide/Hydroxide Films from Aqueous Solution. *J. Electrochem. Soc.* **1983**, *130*, 869–872.
- (18) McCrory, C. C. L.; Jung, S.; Peters, J. C.; Jaramillo, T. F. Benchmarking Heterogeneous Electrocatalysts for the Oxygen Evolution Reaction. *J. Am. Chem. Soc.* **2013**, *135*, 16977–16987.
- (19) El-Shafei, A. Study of Nickel UPD at a Polycrystalline Pt Electrode and its Influence on HCOOH Oxidation in Acidic and Nearly Neutral Media. *J. Electroanal. Chem.* **1998**, *447*, 81–89.
- (20) Chatenet, M.; Faure, R.; Soldo-Olivier, Y. Nickel-Underpotential Deposition on Pt(110) in Sulphate-Containing Media. *J. Electroanal. Chem.* **2005**, *580*, 275–283.
- (21) Mansour, A. N. Characterization of Electrochemically Prepared γ -NiOOH by XPS. *Surf. Sci. Spectra* **1994**, *3*, 271.
- (22) Mansour, A. N. Characterization of β -NiO by XPS. *Surf. Sci. Spectra* **1994**, *3*, 239.
- (23) Mansour, A. N. Characterization of NiO by XPS. *Surf. Sci. Spectra* **1994**, *3*, 231.
- (24) Shalvoy, R. B.; Reucroft, P. J.; Davis, B. H. Characterization of Co-Precipitated Nickel on Silica Methanation Catalysts by X-ray Photoelectron Spectroscopy. *J. Catal.* **1979**, *56*, 336–348.
- (25) Lian, K.; Thorpe, S. J.; Kirk, D. W. Electrochemical and Surface Characterization of Electrocatalytically Active Amorphous NiCo alloys. *Electrochim. Acta* **1992**, *37*, 2029–2041.
- (26) Ertl, G.; Hierl, R.; Knözinger, H.; Thiele, N.; Urbach, H. P. XPS Study of Copper Aluminate catalysts. *Appl. Surf. Sci.* **1980**, *5*, 49–64.
- (27) Casella, I. G.; Guascito, M. R. Anodic electrodeposition of Conducting Cobalt Oxyhydroxide Films on a Gold Surface. XPS Study and Electrochemical Behaviour in Neutral and Alkaline Solution. *J. Electroanal. Chem.* **1999**, *476*, 54–63.
- (28) Mansour, A. N. Copper Mg K α XPS Spectra from the Physical Electronics Model 5400 Spectrometer. *Surf. Sci. Spectra* **1994**, *3*, 202.
- (29) Tan, B. J.; Klabunde, K. J.; Sherwood, P. M. A. X-ray photoelectron Spectroscopy Studies of Solvated Metal Atom Dispersed Catalysts. Monometallic Iron and Bimetallic Iron-Cobalt Particles on Alumina. *Chem. Mater.* **1990**, *2*, 186–191.
- (30) Mills, P.; Sullivan, J. L. A Study of the Core Level Electrons in Iron and its Three Oxides by Means of X-Ray Photoelectron Spectroscopy. *J. Phys. D: Appl. Phys.* **1983**, *16*, 723.
- (31) Andersson, S.L. T.; Howe, R. F. An X-Ray Photoelectron Study of Metal Clusters in Zeolites. *J. Phys. Chem.* **1989**, *93*, 4913–4920.
- (32) Zeradjanin, A. R. Frequent Pitfalls in the Characterization of Electrodes Designed for Electrochemical Energy Conversion and Storage. *ChemSusChem* **2018**, *11*, 1278.
- (33) Gin, S.; Jollivet, P.; Fournier, M.; Berthon, C.; Wang, Z.; Mitroshkov, A.; Zhu, Z.; Ryan, J. V. The Fate of Silicon during Glass Corrosion under Alkaline Conditions: A Mechanistic and Kinetic Study with the International Simple Glass. *Geochim. Cosmochim. Acta* **2015**, *151*, 68–85.
- (34) Molchanov, V. S.; Prikhidko, N. E. Corrosion of Silicate Glasses by Alkaline Solutions. *Bull. Acad. Sci. USSR, Div. Chem. Sci.* **1958**, *6* (10), 1179–1184.
- (35) Diaz-Morales, O.; Ledezma-Yanez, I.; Koper, M. T. M.; Calle-Vallejo, F. Guidelines for the Rational Design of Ni-Based Double Hydroxide Electrocatalysts for the Oxygen Evolution Reaction. *ACS Catal.* **2015**, *5* (9), 5380–5387.
- (36) Subbaraman, R.; Tripkovic, D.; Chang, K.-C.; Strmcnik, D.; Paulikas, A. P.; Hirunsit, P.; Chan, M.; Greeley, J.; Stamenkovic, V.; Markovic, N. M. Trends in Activity for the Water Electrolyser Reactions on 3d M(Ni,Co,Fe,Mn) Hydr(oxy)oxide Catalysts. *Nat. Mater.* **2012**, *11*, 550–557.

Unprecedented High Oxygen Evolution Activity of Electrocatalysts Derived from Surface-Mounted Metal–Organic Frameworks

Weijin Li,[†] Sebastian Watzel,^{‡,§} Hany A. El-Sayed,^{||} Yunchang Liang,^{‡,§} Gregor Kieslich,[†] Aliaksandr S. Bandarenka,^{*,‡,§,||} Katia Rodewald,[⊥] Bernhard Rieger,^{⊥,||} and Roland A. Fischer^{*,†,||}

[†]Chair of Inorganic and Metal–organic Chemistry, Catalysis Research Center, Ernst-Otto-Fischer Straße 1 and Department of Chemistry, Technical University of Munich, Lichtenbergstraße 4, 85748 Garching b. München, Germany

[‡]Physics of Energy Conversion and Storage, Department of Physics, Technical University of Munich, James-Frank-Strasse 1, 85748 Garching b. München, Germany

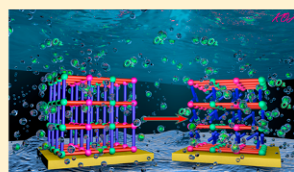
[§]Nanosystems Initiative Munich (NIM), Schellingstraße 4, 80799 Munich, Germany

^{||}Chair of Technical Electrochemistry, Catalysis Research Center, Ernst-Otto-Fischer Straße 1 and Department of Chemistry, Technical University of Munich, Lichtenbergstraße 4, 85747 Garching b. München, Germany

[⊥]Wacker-Chair of Macromolecular Chemistry, Catalysis Research Center, Ernst-Otto-Fischer Straße 1 and Department of Chemistry, Technical University of Munich, Lichtenbergstraße 4, 85747 Garching b. München, Germany

Supporting Information

ABSTRACT: The oxygen evolution reaction (OER) is a key process for renewable energy storage. However, developing non-noble metal OER electrocatalysts with high activity, long durability and scalability remains a major challenge. Herein, high OER activity and stability in alkaline solution were discovered for mixed nickel/cobalt hydroxide electrocatalysts, which were derived in one-step procedure from oriented surface-mounted metal–organic framework (SURMOF) thin films that had been directly grown layer-by-layer on macro- and microelectrode substrates. The obtained mass activity of $\sim 2.5 \text{ mA} \cdot \mu\text{g}^{-1}$ at the defined overpotential of 300 mV is 1 order of magnitude higher than that of the benchmarked IrO_2 electrocatalyst and at least 3.5 times higher than the mass activity of any state-of-the-art NiFe-, FeCoW-, or NiCo-based electrocatalysts reported in the literature. The excellent morphology of the SURMOF-derived ultrathin electrocatalyst coating led to a high exposure of the most active Ni- and Co-based sites.



INTRODUCTION

Highly efficient electrocatalysis for water splitting and fuel cells is one of the desired processes for sustainable and environmentally clean energy conversion.^{1–3} The oxygen evolution reaction (OER), a half-cell reaction involved in water splitting, is kinetically sluggish and typically requires high overpotentials.⁴ Earth-abundant transition metal oxide/hydroxide materials (e.g., NiFeO_x , Co_3O_4 , and Ni/Co/Fe layered double hydroxides) are considered some of the most viable electrocatalysts for the OER and offer a broad parameter range for optimization of their performance.^{5,6} Nevertheless, the poor compatibility between certain components in such materials impedes further improvement of their activity.^{7–9} New concepts for the scalable fabrication of high-performance transition metal oxide/hydroxide electrocatalysts are required; of these concepts, approaches inspired by structure–morphology–property relations show the most promise.

Metal–organic frameworks (MOFs) have evoked great interest due to their well-defined compositions, crystalline structures, tunable coordination space and attractive potential in manifold applications ranging from electronic devices, water-harnessing technologies and catalysis, to name only a few.^{10–14} Current literatures related to MOF-derived electro-

catalysts addresses synthesis schemes based on the controlled pyrolysis of MOFs and/or MOF-containing composites.^{15–18} Typically, such MOF-derived materials are obtained as bulk phase powders, which are then studied as multifunctional electrocatalysts. Despite some fascinating reports, approaches based on the pyrolysis of MOF powders challenge the precise control of the catalyst morphology and the coordination environment of the active metal centers. In contrast, the exfoliation of MOFs as nanosheets can lead to control of the morphology of the electrocatalyst and improve the OER performance.¹⁹ For example, a nanosheet-like MOF with the empirical formula $[\text{M}(\text{BDC})]$ (M = divalent cation, i.e., Ni^{2+} , Co^{2+} ; BDC = 1,4-benzenedicarboxylate, a divalent linker anion) has shown OER activity of $0.45 \text{ mA} \cdot \mu\text{g}^{-1}$ at an overpotential of 300 mV.²⁰ Nevertheless, such kinds of MOF nanosheets require additional binder-assisted film coating or casting procedures when the electrodes are fabricated; in turn, active sites may be buried and shielded in the catalyst bulk phase, by the binder agents for example, decreasing the mass activity.^{21,22}

Received: January 20, 2019

Published: March 19, 2019

A certain class of MOF thin films called surface-mounted MOFs (SURMOFs) are grown by a quasi-epitaxial, ideally self-terminated stepwise layer-by-layer (LBL) deposition method that allows for the controlled growth of MOF nanostructures with preferred crystallite orientations, precise film thickness and distinct morphologies.^{23,24} Inspired by the opportunities in controlling the spatial distribution of components at the molecular level through the fabrication of SURMOFs, we here compare a mixed-metal [M(BDC)] SURMOF (M = Ni²⁺, Co²⁺) to the related exfoliated [M(BDC)] nanosheets as electrocatalysts for OER. After preparation of the SURMOF by using the well-established LBL deposition directly at the electrode substrate, the electrocatalytically active coating is formed upon immersion of the initial SURMOF into alkaline electrolyte solution. Our SURMOF-derived materials, denoted SURMOFDs, exhibit an outstanding performance, with OER mass activity approximately 3.5 times higher than that of any state-of-the-art NiFe-, FeCoW-, or NiCo-based electrocatalyst, including the [M(BDC)] nanosheets. Their excellent durability at a current density of 500 mA·cm⁻² for at least 100 h and high faradaic efficiency (~99.4%) demonstrate the significance of these SURMOFDs for potential industrial applications. Our SURMOFDs demonstrate the importance of molecular control over the spatial distribution of active species and pave a new avenue for the fabrication of high-performance OER electrocatalysts.

EXPERIMENTAL SECTION

Chemicals. NiCl₂·6H₂O (99.3%, metal basis) was purchased from Alfa Aesar. CoCl₂·6H₂O (98%) was purchased from Gute Chemie-abr. Benzenedicarboxylic acid (H₂BDC), NiSO₄·6H₂O, CoSO₄·6H₂O, Na₂SO₄, NaOAc·6H₂O, FeSO₄·6H₂O, and (NH₄)₂SO₄ were purchased from Sigma-Aldrich. Ethanol absolute (99.8%) and triethylamine (TEA) were purchased from VWR and Acros, respectively. Sodium hydroxide (99.996%) was purchased from Alfa Aesar. Potassium hydroxide (KOH, ≥99% K⁺, Merck or 85% KOH Grüssing) was purchased from VWR (Germany). All chemicals were used as purchased. Ultrapure water (18.2 MΩ cm) was obtained from the Millipore System.

Liquid Phase Epitaxy Layer-by-Layer Preparation of [M(BDC)] SURMOFs. A gold electrode was initially modified with 16-mercaptohexadecanoic acid (MHDA) SAMs to facilitate nucleation and induce SURMOF growth toward a specific orientation. MHDA SAMs (denoted as carboxyl-terminated SAMs) were fabricated following standard procedures using commercially available quartz crystal microbalance (QCM) Au substrates (Biolin Scientific). Carboxyl-terminated SAMs were prepared by the immersion of these gold substrates into a 20 μM solution of MHDA in ethanol/acetic acid (5%). After incubation for 24 h, the substrates were washed with an ethanol/acetic acid solution (10%) and soaked in 2% triethylamine (Et₃N)/ethanol solution for 5 min before being used for the following deposition experiments. Then, metal (M = Ni²⁺, Co²⁺) and ligand (BDC) components were applied as diluted solutions in ethanol/water (v/v = 17:1). For example, a mixture of NiCl₂·6H₂O (0.5 mM) and CoCl₂·6H₂O (0.5 mM) was chosen as the metal source, while H₂BDC (0.2 mM) in 0.3 mL Et₃N was chosen as the linker source. SURMOFs were grown on an automated QCM instrument Q-Sense E4 Auto²⁵ at 60 °C with a flow rate of 100 μL·min⁻¹. Initially, the MHDA-treated substrates were exposed to the metal-ion-containing solution for 10 min, followed by a washing step with ethanol (for 2 min) to remove the unstable metal ions. Afterward, the electrode was exposed to the linker solution for 10 min, again followed by a washing step with ethanol to remove unstably attached linkers. For each additional cycle, both steps are repeated. [M(BDC)] SURMOFs made with different molar ratios of Ni²⁺:Co²⁺ were deposited according to the recipes compiled in Table S5. The SURMOFs on a microelectrode (Pt) and an RRDE (Pt) were

fabricated by automatic home-built, step-by-step deposition pump systems.^{25,26} The metal sources, ethanol, and organic linkers were soaked in pump system cells for 10, 2, and 10 min, respectively. For example, a 60 cycle SURMOF was deposited on an RRDE for further study. The Au and Pt microelectrodes used in this work can be easily modified with self-assembled organic monolayers (SAMs), which is beneficial for initiation of nucleation and oriented growth of SURMOFs. The Au coated quartz crystal electrodes allow the monitoring of the SURMOF growth process and, at the same time, allow the electrochemical characterization of the SURMOFDs. For practical applications, however, the described electrocatalyst fabrication concept will be limited not to these special substrates.

Preparation of NiOx, CoOx, and NiFeOx Reference Samples. The metal (hydro)oxide films were electrodeposited on the microelectrodes as described elsewhere.²⁷ For NiO_x, the electrode was cycled in a solution containing 0.13 M NiSO₄, 0.13 M NaOAc, and Na₂SO₄ between 0.95 and 1.86 V. The CoOx films were produced similarly by cycling the potential between 0.95 and 1.76 V in CoSO₄ 0.1 M NaOAc and 0.1 M Na₂SO₄. In both cases, the scan rate was 50 mV/s, and the deposition was stopped after reaching a total anodic charge of ~30 mC cm⁻². NiFeO_x films were deposited via cathodic deposition by applying 250 mAcm⁻² for 50 s while the electrode was immersed in the electrolyte containing 9 mM FeSO₄, 9 mM NiSO₄, and 7.3 mM (NH₄)₂SO₄.

Electrochemical Measurements. Electrochemical evaluation of the as-prepared catalysts was carried out using a typical three-electrode system. The as-prepared SURMOFs were directly used as working electrodes without further activation. However, as discussed in the paper, the as-prepared SURMOFs transform to the SURMOFDs upon immersion into the electrolyte. Pt wire (>99.99%, Goodfellow, Germany) was used as the counter electrode. Measurements with SURMOFDs on Au quartz were performed on Autolab potentiostats with a reversible hydrogen electrode (RHE) as the reference electrode and 0.1 M NaOH as the electrolyte. Measurements with SURMOFDs on Pt (pc, polycrystalline) microelectrodes (CH Instruments, USA) and a Pt (pc) (Mateck, Germany) RRDE (Pine, USA) were performed on a VSP-300 potentiostat (Bio-Logic, France) using Ag/AgCl (Schott, Germany) and a platinum wire (99.99%, Goodfellow, Germany) as reference and counter electrodes, respectively. In addition, 0.1 M KOH was used as the electrolyte and saturated with either argon (5.0, Air Liquide, Germany) or oxygen (4.7 Air Liquide, Germany). All potentials in this work were converted to the RHE scale. The mass of SURMOFDs on Au quartz substrates was directly measured by using BEL-QCM equipment (Table S2), and the currents were normalized to this catalyst mass (SURMOFD before the OER measurements). It was difficult to measure the mass of catalysts on the surface of microelectrodes. The currents in the case of microelectrode substrates were normalized to the electrode geometric surface area. All the experiments in this work were performed without IR ohmic drop compensation. The data were acquired after 20 electrochemical cycling on the catalysts. The electron transfer number (*n*) was determined according to the equation:^{28,29}

$$n = 4I_d / (I_d + I_r / N)$$

where *I_d* is the disk current, *I_r* is the ring current, and *N* is the current collection efficiency.

X-ray Diffraction Analysis. Grazing incidence X-ray diffraction (GIXRD) was carried out on an X'Pert PRO PANalytical instrument (Bragg–Brentano geometry with fixed divergence slits, position sensitive detector, continuous mode, room temperature, Cu Kα radiation, Ni filter, range 2θ = 5–35°, step size 0.01313°, accumulation time 160 s per step). The powder XRD (PXRD) data of powders were collected on a zero background silicon wafer.

Infrared Spectra, Scanning Electron Microscopy, and Atomic Force Microscope Image Analysis. Attenuated total reflectance infrared (ATR-IR) spectra of samples were collected on a PerkinElmer instrument with an ATR sampling accessory. The ATR cell was made of diamond crystal with an incidence angle of 45°. Scanning electron microscopy (SEM) images were collected using an

FE-SEM JSM 7500F JEOL instrument. Atomic force microscopy (AFM) images were obtained with a MultiMode STM/EC-AFM instrument (Veeco Instruments Inc.) with a Nanoscope IIIID controller using Nanoscope 5.31r1 software. AFM measurements utilized tapping mode (AFM tips, Bruker RTESP-300) at a scan rate of 0.5 Hz with a scan area of $2\ \mu\text{m} \times 2\ \mu\text{m}$.

X-ray Photoelectron Spectroscopy (XPS) Analysis. XPS was conducted with an Axis Supra system (Kratos, UK) using monochromatic Al K α radiation ($h\nu = 1486.6\ \text{eV}$) at a base pressure of $<3 \times 10^{-8}$ Torr, a pass energy of 20 eV, and a measured spot size of $800 \times 300\ \mu\text{m}^2$. Samples were mounted floating, and the instrument's charge neutralizer was applied. The obtained spectra were processed and fitted using Kratos ESCApe software (version 1.1). Binding energies were corrected based on the C–C/C–H peak of adventitious carbon at 284.8 eV in the C 1s spectrum. A mixture of 30% Lorentzian and 70% Gaussian functions was used for the least-squares curve fitting procedure utilizing a Shirley background subtraction.

RESULTS AND DISCUSSION

Preparation and Characterization of SURMOFs. The preparation of [M(BDC)] SURMOF (M = Ni²⁺, Co²⁺) is illustrated in Figure 1. Carboxylate-terminated SAM-modified

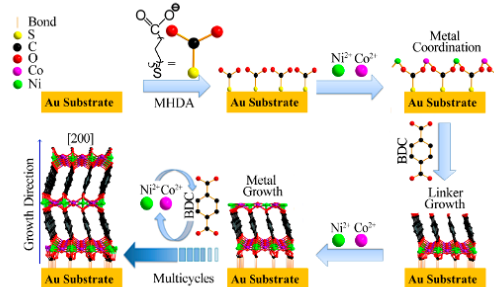


Figure 1. Approach used to synthesize the [M(BDC)] SURMOF directly at the electrode substrate. (M = Ni²⁺, Co²⁺; BDC, 1,4-benzenedicarboxylate; MHDA, 16-mercaptohexadecanoic acid.)

gold surfaces allow for an oriented growth of the SURMOFs.^{30–32} Typically, the parent SURMOF was deposited using the stepwise LBL method by first soaking the gold electrode (functionalized by SAMs of 16-mercaptohexadecanoic acid, MHDA) in a solution with both Ni²⁺ and Co²⁺ ions (e.g., a Ni/Co molar ratio of 1:1), then soaking it in ethanol wash solution and finally in H₂BDC solution, with repetition of the whole cycle as desired (Figure S1). Grazing incidence X-ray diffraction (GIXRD) confirmed [M(BDC)] that was a single phase and a preferred growth orientation along the [200] direction (Figure 2a). Attenuated total reflection infrared (ATR-IR) spectra of the films are in good agreement with the ATR-IR spectra reported for the parent bulk MOF (Figure S2). SEM images and AFM images revealed that the obtained [200]-oriented SURMOFs (10, 30, and 50 deposition cycles) exhibited a uniform morphology composed of vertically aligned ultrathin [M(BDC)] nanosheets (Figure 3).

The as-prepared SURMOFs were subsequently transformed into electrocatalyst coatings denoted as SURMOFDs by immersing them in KOH aqueous solution (0.1 mol·L⁻¹) at room temperature for different times (Figure 4). The characteristic GIXRD peaks of the SURMOFs already

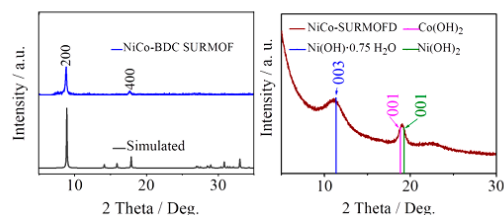


Figure 2. Grazing incidence X-ray diffraction patterns: (a) SURMOF; (b) SURMOF derived materials (SURMOFDs).

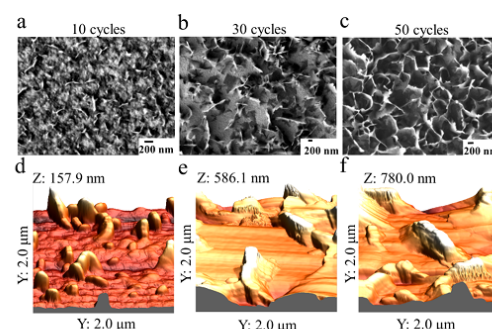


Figure 3. (a–c) SEM images and (d–f) AFM images of LBL deposited [M(BDC)] SURMOFs (M = Ni²⁺, Co²⁺, molar ratio of Ni:Co = 1:1) with variation of the number of deposition cycles: (a) 10 cycles; (b) 30 cycles; (c) 50 cycles. AFM: (d) 10 cycles; (e) 30 cycles; (f) 50 cycles. Note that z-axes in (d)–(f) are given in nm.

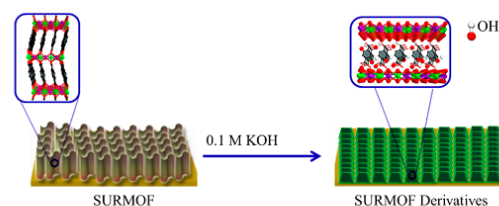


Figure 4. Transformation of the mixed metal ion [M(BDC)] SURMOF (M = Ni²⁺, Co²⁺) into SURMOF derivatives (SURMOFDs) upon immersing the films to the electrolyte (KOH).

disappeared when immersing them into KOH aqueous solution for a short period of 2 min. Only two broad features remained for the obtained SURMOFDs, suggesting the presence of Ni(OH)₂ and Co(OH)₂ and/or some mixed metal hydroxide phase when our pattern was compared with the literature data. However, an unambiguous assignment and structure determination was not possible (Figures 2b, S3, and S4).^{33–35} Prolonged immersion or variation of the KOH concentration did not give different results. Energy dispersive X-ray spectroscopy (EDS) spectra show that the SURMOFDs have a Ni/Co ratio similar to the Ni/Co feeding ratio during growth of the precursor SURMOF (Figure S5). EDS mapping indicates that Ni and Co were homogeneously distributed, and XPS revealed characteristic signals for Ni 2p_{3/2} at 856.2 eV and Co 2p_{3/2} at 780.9 eV which are similar (within the accuracy of the measurement of $\pm 0.2\ \text{eV}$) to the respective signals of

SURMOF and the [M(BDC)] nanosheets (Figure S6c,d and Table S1). ATR-IR and XPS revealed the presence of BDC and hydroxide in SURMOFDs. Peaks at 1581 and 1414 cm^{-1} (1581 and 1356 cm^{-1} in SURMOF) are attributed to the asymmetric and symmetric stretching vibration of the carboxylate group, respectively. Peaks at 3413 cm^{-1} attributed to the vibration of O–H. (Figure S7).^{36–38} XPS data show a shift in the O 1s binding energy from 531.7 to 531.3 eV (Figure S6a,b and Table S1), suggesting that the metal-carboxylate coordination bond has been slightly modified. Furthermore, the C 1s signal of the carboxylate O–C=O at 288.06 eV was still observed. The combined data of GIXRD, ATR-IR and XPS indicate the formation of a nanocrystalline to amorphous mixed metal hydroxide material with some BDC still present in the structure.^{39–41} This situation could be related to layered double hydroxides (LDHs, e.g., MgAl-LDHs and NiCo-LDHs), which can intercalate organic linkers and thus may contribute to the enhancement of the electron/ion/mass transport of the SURMOFD electrode.^{39,40}

Morphological and Compositional Study of SURMOFDs. The morphology of the SURMOFDs were investigated as a function of the number of deposition cycles in the LBL approach. Some representative SEM and AFM images are shown in Figure 5. Increasing the number of

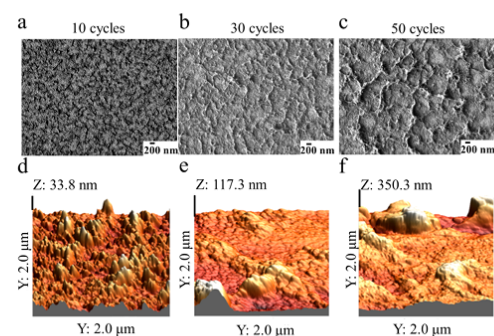


Figure 5. (a–c) SEM images and (d–f) corresponding AFM images of SURMOFD electrocatalysts derived from the mixed metal [M(BDC)] SURMOFs ($M = \text{Ni}^{2+}, \text{Co}^{2+}$, molar ratio Ni:Co = 1:1) created with various numbers of deposition cycles, as shown in Figure 3. SEM: (a) 10 cycles; (b) 30 cycles; (c) 50 cycles. AFM: (d) 10 cycles; (e) 30 cycles; (f) 50 cycles. Note that z-axes in (d)–(f) are given in nm.

deposition cycles makes the SURMOF dense and more uniform. (Figure 3) The number of SURMOF deposition cycles also correlates with the thickness (AFM data) of the SURMOFDs, which ranges from ~ 35 nm (10 cycles) to ~ 120 nm (30 cycles) and ~ 350 nm (50 cycles) (Figures 5d–f and S8). Therefore, by carefully adjusting the growth conditions of the SURMOFs, the surface coverage, morphology, and film thickness of the SURMOFDs can be controlled. For the electrocatalytic OER performance, a balance between coverage, thickness and access to catalytically active sites presumably plays the major role, and further optimization is possible by the outlined approach.

Electrocatalytic Activity of SURMOFDs toward the Oxygen Evolution Reaction (OER). The series of SURMOFDs based on different numbers of SURMOF

deposition cycles exhibits all the properties for high catalytic activity in the OER and has accordingly been tested. Initially, a conventional cell with a three-electrode configuration was used to test the OER activity in an alkaline electrolyte ($\text{pH} = 13$, O_2 saturated). SURMOFDs were deposited at electrochemically inactive electrodes (Au-based macroelectrode, Pt-based microelectrode). The linear polarization curves of SURMOFDs are shown in Figure 6a and reveal excellent OER activities. A

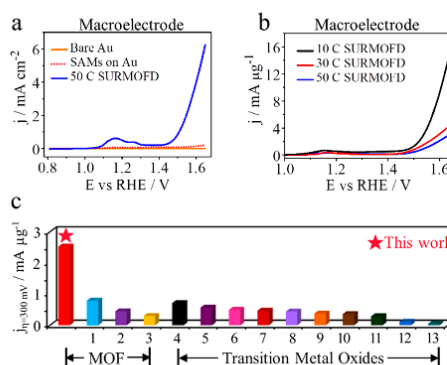


Figure 6. (a) Comparison of the anodic linear polarization scans of SURMOFD (50 cycles), SAMs on Au and the bare Au macroelectrode. (b) Comparison of mass activity-normalized anodic currents of SURMOFDs made with different numbers of deposition cycles on the SAM-modified Au macroelectrode. The linear polarization curves in (a) and (b) were recorded in 0.1 M O_2 -saturated NaOH with a scan rate of $20 \text{ mV}\cdot\text{s}^{-1}$ at 25°C . (c) Comparison of the OER mass activities of 10 cycles of SURMOFD (molar ratio Ni:Co = 1:1) with benchmarked data of MOFs (1–3) and transition metal oxide materials (4–13) published within the last two years (at an overpotential of 300 mV, 25°C , O_2 -saturated alkaline electrolytes): (1) $\text{Fe}_3\text{-Co}_2$,⁴⁷ (2) [M(BDC)] nanosheets ($M = \text{Ni}^{2+}, \text{Co}^{2+}$),²⁰ (3) M-MIL-53 ($M = \text{Co}, \text{Mn}$),⁴⁸ (4) G-FeCoW,⁹ (5) $\alpha\text{-CoVO}_4$,⁴⁹ (6) Fe–Co–P,⁵⁰ (7) Ni–Fe–O mesoporous nanowire network,⁵¹ (8) $\text{CoFe}_2\text{O}_4/\text{C}$,⁵² (9) NiFe-LDH*,⁵³ (10) $\text{Ba}_{0.5}\text{Sr}_{0.5}\text{Co}_{0.8}\text{Fe}_{0.2}\text{O}_{3-\delta}$,⁵⁴ (11) IrO_2 ,⁴⁵ (12) $\text{NaNi}_{10}\text{Fe}_{0.1}\text{O}_{20}$,⁵⁵ (13) $\text{Co}_3\text{O}_4/\text{CoP}^{14}$ (asterisk (*) indicates experiments carried out under N_2 ; for more details on the chemical nature of the catalysts, please refer to Table S3).

pronounced oxidation peak was observed between 1.1 V vs RHE and 1.3 vs RHE. This peak can be ascribed to the $\text{Co}^{2+}/\text{Co}^{3+}$ redox couple.^{42,43} As shown in Figure 6a, the 50 cycle SURMOFD had a mass activity of $\sim 0.8 \text{ mA}\cdot\mu\text{g}^{-1}$ (see the measured mass of deposited SURMOFDs in Table S2) at an overpotential of 300 mV (compared to the thermodynamic equilibrium potential of 1.23 V vs RHE). This mass activity is significantly higher than the mass activity benchmarked for all the other state-of-the-art transition metal and even noble metal catalysts. (Tables S3 and S4) Interestingly, the OER mass activity can be tuned and further improved by varying the thickness and morphology of the thin films via changing the number of deposition cycles together with the Ni/Co feeding ratios (Figures 6b and S9–S11). The reason is ascribed that Ni and Co species have an electronic coupling to each other and will synergistically affect the OER performance.⁴⁴ The mass activity increased from $\sim 0.8 \text{ mA}\cdot\mu\text{g}^{-1}$ to ~ 2.3 at overpotential of 300 mV when the number of deposition cycles is decreased to 30. For a deposition of only 10 cycles, the SURMOFD

exhibited a mass activity of $\sim 2.5 \text{ mA} \cdot \mu\text{g}^{-1}$. This value is ~ 9 times higher than that of the benchmarked IrO_2 electrocatalyst⁴⁵ and at least 3.5 times higher than any state-of-the-art NiFe_x , FeCoW_x , or NiCo -based electrocatalysts reported in the literature (Figure 6c and Tables S3 and S4). The increase in mass activity with the decrease in deposition cycles is due to the controlled decrease in the SURMOFD thickness, which enhances the electron/mass transport and increases the density of accessible active sites.⁴⁶

To reduce the effects of ohmic drop as well as the generation of nonconducting gas bubbles,⁵⁶ microelectrodes ($\varnothing = 25 \mu\text{m}$, Pt) were employed as a substrate to evaluate the OER activities of the SURMOFDs. At the same time, this approach allows studying the OER at high current densities (j), which is relevant for real-life applications ($j > 100 \text{ mA} \cdot \text{cm}^{-2}$). (Figures S12–S14).⁵⁶ The current densities of the SURMOFDs deposited on the microelectrode were normalized to the geometric surface area, as the exact determination of the mass deposited on the microelectrode was not possible. The determination of the electrochemical surface area (ECSA) with state-of-the-art methods is very inaccurate.^{29,57} As shown in Figure 7a, the SURMOFDs have a low onset potential of

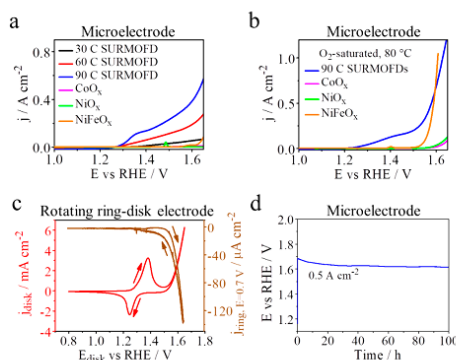


Figure 7. (a,b) Polarization curves of a series of SURMOFDs (molar ratio Ni:Co = 1:1) made with 30, 60, and 90 cycles (C) and deposited on Pt microelectrodes, in comparison with the corresponding curves from state-of-the-art CoO_x , NiO_x , and NiFeO_x catalysts fabricated on the same substrate. The experiments were performed in 0.1 M KOH (O_2 saturated) with a scan rate of 1 mV/s at (a) 25 °C and (b) at 80 °C. (c) Rotating ring-disk electrode (RRDE) measurement of SURMOFD (60 cycles) in 0.1 M KOH (Ar -saturated) at 25 °C and 300 rpm (arrows indicate the scan direction). (d) Galvanostatic experiment at 500 $\text{mA} \cdot \text{cm}^{-2}$ with 90 cycles SURMOFD on a Pt microelectrode in 5.4 M KOH (O_2 -saturated) at 25 °C. The samples exhibit good chemical stability during operation.

$\sim 1.47 \text{ V}$ vs RHE (90 cycles) and $\sim 1.61 \text{ V}$ vs RHE (60 cycles) at a current density of $200 \text{ mA} \cdot \text{cm}^{-2}$, thus outperforming state-of-the-art industrially relevant OER electrocatalysts, such as CoO_x , NiO_x , and NiFeO_x . When the temperature was increased from room temperature to 80 °C, the current densities of the SURMOFDs increased by a factor of 2 at a potential of 1.6 V vs RHE. These currents are significantly higher than those measured for the state-of-the-art OER catalysts at the same potential (Figure 7b).

The Tafel slope of $73 \text{ mV} \cdot \text{dec}^{-1}$ for 90 cycles SURMOFD, which is smaller than that of IrO_2/C ($97 \text{ mV} \cdot \text{dec}^{-1}$),⁴⁵

indicates that the second electron transfer is the rate-limiting step for the SURMOFD catalysts (eq S2, Figure S15). Generally, the OER involves four electron transfer steps with a Tafel slope value in the range of 30–120 $\text{mV} \cdot \text{dec}^{-1}$, which indicates that the first or the second step of electron transfer is the rate-determining step^{58,59} (eqs S2–S5). Thus, the SURMOFDs feature favorable kinetics toward the OER, which is attributed to their specific composition and morphology.

Investigations of SURMOFDs for the OER Using a Rotating Ring-Disk Electrode (RRDE). Oxygen produced at a disk electrode can be reduced and detected at the Pt ring electrode surrounding the disk (Figure S16). Therefore, the potential of the ring was fixed to 0.7 V vs RHE, and the electrolyte was saturated with argon while the potential of the SURMOFD-coated Pt(pc) electrode was cycled. As shown in Figure 7c, the OER current can be detected at the ring electrode as soon as the potential of the disk exceeds 1.48 V vs RHE. To prove that the recorded disk current originates from oxygen evolution at the catalyst site rather than from partially oxidized species, a constant potential of 0.2 V was applied to the Pt ring, allowing Pt to reduce possibly produced partially oxidized species, such as H_2O_2 (Figure S17). However, the Pt ring showed a negligible current before the potential of the disk reached 1.48 V vs RHE when a voltage of 0.2 V vs RHE was applied to it, suggesting that there are no side reactions, that no partially oxidized species contributed to the total current measured and that the great majority of the current is indeed caused by the OER. As shown in Figure S18, a negligible ring current can also be observed when a potential of 1.5 V vs RHE was applied to the Pt ring, and the potential of the disk was 0.9–1.685 V vs RHE in O_2 -saturated 0.1 M KOH. A high faradaic efficiency of $\sim 99.4\%$ was measured for SURMOFDs for the OER (Figure S19). These results demonstrate that the pathway for the OER was a desirable four-electron reaction (eq S1).

Catalyst lifetime is an important factor for electrocatalysis and its practical application in energy conversion and storage systems. A chronopotentiometry response experiment was carried out using SURMOFDs on microelectrodes to investigate the long-term stability of our catalyst thin film. We used microelectrodes because they can suppress gas bubble formation on the electrode surface and decrease the ohmic drop at high current densities. The potential of the SURMOFDs immersed in 5.4 M KOH remained almost unchanged over 100 h at a current density of $0.5 \text{ A} \cdot \text{cm}^{-2}$, which is relevant for their industrial application (Figures 7d and S20), outperforming the state-of-the-art oxide material electrocatalysts under similar harsh conditions, which are stable to just 540 s.⁵⁸ These results indicate that the SURMOFDs have excellent stability as OER catalysts during operation. The comparison of GIXRD patterns, ATR IR spectra, and SEM images of SURMOFDs before and after OER experiment show only small changes (Figures S21 and S22). These changes can be ascribed to leaching of BDC⁶⁰ and a slight loss of SURMOFDs from the electrodes (Table S2). These data suggest that overall composition and morphology of SURMOFDs are sustained after the long-term OER test.

CONCLUSIONS

In summary, we developed a versatile strategy as well as a facile and potentially scalable methodology to generate mixed metal hydroxide electrocatalysts with outstanding OER mass activity

and prominent durability compared to state-of-the-art and industrially relevant OER electrocatalysts, including IrO₂. The protocol for the fabrication of novel electrode materials is based on an alkaline derivation of prefabricated SURMOFs obtained by highly controlled liquid phase epitaxial layer-by-layer growth under ambient conditions. Our approach seems to maximize the density and accessibility of active sites, leading to the observed excellent electrocatalytic properties. Based on the analysis of SURMOFs by GIXRD, XPS, and ATR-IR, we attribute the performance of our SURMOFs to the mixed metal Ni and Co configuration of the double hydroxide sheets and its tuning via inclusion of the BDC linker. At this point, we highlight the fact that our mixed metal [M(BDC)] SURMOFs are structurally closely related to the [M(BDC)] nanosheets mentioned in the introduction. The electrocatalyst fabricated from the nanosheets was reported to be stable under alkaline conditions. In contrast, our [M(BDC)] SURMOF is not stable under alkaline conditions; however, the obtained SURMOF electrocatalyst coatings outperform the [M(BDC)] nanosheet based OER catalyst. The stability of the parent MOF material itself under OER conditions seems to be less important than its function as a precursor for the formation of ultrathin mixed metal hydroxide organic composites directly on the electrode substrate. Considering the striking performance of SURMOFs, with their high OER activity, the presented approach paves the way not only for producing next-generation highly active electrocatalysts but also for systematically studying the origin of these properties. This advancement specifically takes advantage of the well-controlled deposition of MOF films, which act as versatile platforms for the derivation of active electrocatalyst structures.

■ ASSOCIATED CONTENT

Supporting Information

The Supporting Information is available free of charge on the ACS Publications website at DOI: 10.1021/jacs.9b00549.

Layer-by-layer growth of thin film information monitored by Q-sense machine, IR data, PXRD patterns of bulk MOF and MOF derivatives, NMR analysis, EDS spectra, XPS data, cross section view of thin film, additional polarization curves, schemes; supporting equations and tables (PDF)

■ AUTHOR INFORMATION

Corresponding Authors

*roland.fischer@tum.de

*bandarenka@ph.tum.de

ORCID

Hany A. El-Sayed: 0000-0002-8769-8258

Gregor Kieslich: 0000-0003-2038-186X

Aliaksandr S. Bandarenka: 0000-0002-5970-4315

Bernhard Rieger: 0000-0002-0023-884X

Roland A. Fischer: 0000-0002-7532-5286

Notes

The authors declare no competing financial interest.

■ ACKNOWLEDGMENTS

W.J.L. is grateful for the support of an Alexander von Humboldt Fellowship for Postdoctoral Researchers. W.J.L. is particularly grateful to Prof. Dr. Hubert Gasteiger for offering the facilities in his laboratories (TUM-TEC). G.K. would like

to thank the Fond der Chemischen Industrie for financial support through the Liebig fellowship scheme. S.W., Y.L. and A.S.B. are grateful for the financial support from the DFG project BA 5795/3-1 and the cluster of excellence Nano-systems Initiative Munich (NIM). The authors appreciate Dr. Hans Beyer from TUM-TEC for the XPS measurement and discussion; Mr. Shujin Hou, Dr. Juan Liu, Mr. Werner Heinz, and Ms. Jasmin Haberl for joining in the discussion of this project.

■ REFERENCES

- (1) Chu, S.; Majumdar, A. Opportunities and challenges for a sustainable energy future. *Nature* **2012**, *488*, 294–303.
- (2) Fillol, J. L.; Codola, Z.; Garcia-Bosch, I.; Gómez, L.; Pla, J. J.; Costas, M. Efficient water oxidation catalysts based on readily available iron coordination complexes. *Nat. Chem.* **2011**, *3*, 807–813.
- (3) Fang, Y. X.; Ma, Y. W.; Zheng, M. F.; Yang, P. J.; Asiri, A. M.; Wang, X. C. Metal-organic frameworks for solar energy conversion by photoredox catalysis. *Coord. Chem. Rev.* **2018**, *373*, 83–115.
- (4) Oh, S. H.; Black, R.; Pomerantseva, E.; Lee, J.-H.; Nazar, L. F. Synthesis of a metallic mesoporous pyrochlore as a catalyst for lithium-O₂ batteries. *Nat. Chem.* **2012**, *4*, 1004–1010.
- (5) Subbaraman, R.; Tripkovic, D.; Chang, K.-C.; Strmcnik, D.; Paulikas, A. P.; Hirunsit, P.; Chan, M.; Greeley, J.; Stamenkovic, V.; Markovic, N. M. Trends in activity for the water electrolyser reactions on 3d M(Ni,Co,Fe,Mn) hydr(oxy)oxide catalysts. *Nat. Mater.* **2012**, *11*, 550–557.
- (6) Han, L.; Dong, S.; Wang, E. Transition-metal (Co, Ni, and Fe)-based electrocatalysts for the water oxidation reaction. *Adv. Mater.* **2016**, *28*, 9266–9291.
- (7) Xiao, X.; He, C.-T.; Zhao, S.; Li, J.; Lin, W.; Yuan, Z.; Zhang, Q.; Wang, S.; Dai, L.; Yu, D. A general approach to cobalt-based homobimetallic phosphide ultrathin nanosheets for highly efficient oxygen evolution in alkaline media. *Energy Environ. Sci.* **2017**, *10*, 893–899.
- (8) Wang, S.; Hou, Y.; Lin, S.; Wang, X. Water oxidation electrocatalysis by a zeolitic imidazolate framework. *Nanoscale* **2014**, *6*, 9930–9934.
- (9) Zhang, B.; Zheng, X.; Voznyy, O.; Comin, R.; Bajdich, M.; Garcia-Melchor, M.; Han, L.; Xu, J.; Liu, M.; Zheng, L.; Garcia de Arquer, F. P.; Dinh, C. T.; Fan, F.; Yuan, M.; Yassitepe, E.; Chen, N.; Regier, T.; Liu, P.; Li, Y.; De Luna, P.; Janmohamed, A.; Xin, H. L.; Yang, H.; Vojvodic, A.; Sargent, E. H. Homogeneously dispersed multimetal oxygen-evolving catalysts. *Science* **2016**, *352*, 333–337.
- (10) Sheberla, D.; Bachman, J. C.; Elias, J. S.; Sun, C.-J.; Yang, S.; Dincă, M. Conductive MOF electrodes for stable supercapacitors with high areal capacitance. *Nat. Mater.* **2017**, *16*, 220–224.
- (11) Miner, E. M.; Fukushima, T.; Sheberla, D.; Sun, L.; Surendranath, Y.; Dincă, M. Electrochemical oxygen reduction catalysed by Ni₃(hexaiminotriphenylene)₂. *Nat. Commun.* **2016**, *7*, 10942–10948.
- (12) Jiao, L.; Wang, Y.; Jiang, H.; Xu, Q. Metal-organic frameworks as platforms for catalytic applications. *Adv. Mater.* **2018**, *30*, 1703663–170385.
- (13) Majewski, M. B.; Peters, A. W.; Wasielewski, M. R.; Hupp, J. T.; Farha, O. K. Metal-organic frameworks as platform materials for solar fuels catalysis. *ACS Energy Lett.* **2018**, *3*, 598–611.
- (14) Wang, H.; Zhu, Q.-L.; Zou, R.; Xu, Q. Metal-organic frameworks for energy applications. *Chem.* **2017**, *2*, 52–80.
- (15) Aijaz, A.; Masa, J.; Rösler, C.; Xia, W.; Weide, P.; Botz, A. J. R.; Fischer, R. A.; Schuhmann, W.; Muhler, M. Co@Co₃O₄ encapsulated in carbon nanotube-grafted nitrogen-doped carbon polyhedral as an advanced bifunctional oxygen electrode. *Angew. Chem., Int. Ed.* **2016**, *55*, 4087–4091.
- (16) Zhou, J.; Dou, Y.; Zhou, A.; Guo, R.-M.; Zhao, M.-J.; Li, J.-R. MOF Template-directed fabrication of hierarchically structured electrocatalysts for efficient oxygen evolution reaction. *Adv. Energy Mater.* **2017**, *7*, 1602643–1602652.

- (17) Xia, B. Y.; Yan, Y.; Li, N.; Wu, H. B.; Lou, X. W.; Wang, X. A. metal-organic framework-derived bifunctional oxygen electrocatalyst. *Nat. Energy* **2016**, *1*, 15006–150013.
- (18) Cao, X.; Tan, C.; Sindoro, M.; Zhang, H. Hybrid micro-/nano-structures derived from metal-organic framework: preparation and applications in energy storage and conversion. *Chem. Soc. Rev.* **2017**, *46*, 2660–2677.
- (19) Jayaramulu, K.; Masa, J.; Morales, D. M.; Tomanec, O.; Ranc, V.; Petr, M.; Wilde, P.; Chen, Y. T.; Zboril, R.; Schuhmann, W.; Fischer, R. A. Ultrathin 2D cobalt zeolite-imidazole framework nanosheets for electrocatalytic oxygen evolution. *Adv. Sci.* **2018**, *5*, 1801029–1801038.
- (20) Zhao, S.; Wang, Y.; Dong, J.; He, C.-T.; Yin, H.; An, P.; Zhao, K.; Zhang, X.; Gao, C.; Zhang, L.; Lv, J.; Wang, J.; Zhang, J.; Khattak, A. M.; Khan, N. A.; Wei, Z.; Zhang, J.; Liu, S.; Zhao, H.; Tang, Z. Ultrathin metal-organic framework nanosheets for electrocatalytic oxygen evolution. *Nat. Energy* **2016**, *1*, 16184–16193.
- (21) Mahmood, N.; Yao, Y.; Zhang, J. W.; Pan, L.; Zhang, X.; Zou, J. J. Electrocatalysts for hydrogen evolution in alkaline electrolytes: mechanisms, challenges, and prospective solutions. *Adv. Sci.* **2018**, *5*, 1700464–1700486.
- (22) Grimaud, A.; Demortiere, A.; Saubanere, M.; Dachraoui, W.; Duchamp, M.; Doublet, M.-L.; Tarascon, J.-M. Activation of surface oxygen sites on an iridium-based model catalyst for the oxygen evolution reaction. *Nat. Energy* **2017**, *2*, 16189–16198.
- (23) Liu, J.; Woll, C. Surface-supported metal-organic framework thin films: fabrication methods, applications, and challenges. *Chem. Soc. Rev.* **2017**, *46*, 5730–5770.
- (24) Betard, A.; Fischer, R. A. Metal-organic framework thin films: from fundamentals to applications. *Chem. Rev.* **2012**, *112*, 1055–1083.
- (25) Bétard, A. Ph.D. Degree Thesis, Ruhr-Universität Bochum, October, 2011.
- (26) Tu, M.; Wannapaiboon, S.; Khaletskaia, K.; Fischer, R. A. Engineering zeolitic-imidazolate framework (ZIF) thin film devices for selective detection of volatile organic compounds. *Adv. Funct. Mater.* **2015**, *25*, 4470–4479.
- (27) Watzel, S.; Liang, Y.; Bandarenka, A. S. Intrinsic activity of some oxygen and hydrogen evolution reaction electrocatalysts under industrially relevant conditions. *ACS Appl. Energy Mater.* **2018**, *1*, 4196–4202.
- (28) Suntivich, J.; May, K. J.; Gasteiger, H. A.; Goodenough, J. B.; Yang, S. A perovskite oxide optimized for oxygen evolution catalysis from molecular orbital principles. *Science* **2011**, *334*, 1383–1385.
- (29) McCrory, C. C. L.; Jung, S.; Peters, J. C.; Jaramillo, T. F. Benchmarking heterogeneous electrocatalysts for the oxygen evolution reaction. *J. Am. Chem. Soc.* **2013**, *135*, 16977–16987.
- (30) Biemmi, E.; Scherb, C.; Bein, T. Oriented growth of the metal organic framework $\text{Cu}_3(\text{BTC})_2(\text{H}_2\text{O})_3 \cdot x\text{H}_2\text{O}$. *J. Am. Chem. Soc.* **2007**, *129*, 8054–8055.
- (31) Zacher, D.; Shekha, O.; Wöll, C.; Fischer, R. A. Thin film of metal-organic frameworks. *Chem. Soc. Rev.* **2009**, *38*, 1418–1429.
- (32) Huang, J.; Li, Y.; Huang, R. K.; He, C. T.; Gong, L.; Hu, Q.; Wang, L.; Xu, Y. T.; Tian, X. Y.; Liu, S. Y.; Ye, Z. M.; Wang, F. X.; Zhou, D. D.; Zhang, W. X.; Zhang, J. P. Electrochemical exfoliation of pillared-layer metal-organic framework to boost the oxygen evolution reaction. *Angew. Chem., Int. Ed.* **2018**, *57*, 4632–4636.
- (33) Huang, J. H.; Liu, Q. H.; Yao, T.; Pan, Z. Y.; Wei, S. Q. XAFS study on structure-activity correlations of $\alpha\text{-Co}(\text{OH})_2$ nanosheets water oxidation catalysts. *J. Phys.: Conf. Ser.* **2016**, *712*, 012128–012132.
- (34) Niu, S.; Jiang, W. J.; Tang, T.; Zhang, Y.; Li, J. H.; Hu, J. S. Facile and scalable synthesis of robust $\text{Ni}(\text{OH})_2$ Nanoplate arrays on NiAl Foil as hierarchical active scaffold for highly efficient overall water splitting. *Adv. Sci.* **2017**, *4*, 1700084–1700089.
- (35) Béléké, A. B.; Hosokawa, A.; Mizuhata, M.; Deki, S. Preparation of α -nickel hydroxide/carbon composite by the liquid phase deposition method. *J. Ceram. Soc. Jpn.* **2009**, *117*, 392–394.
- (36) Socrates, G. *Infrared and Raman Characteristic Group Frequencies, Tables and Charts*; John Wiley & Sons, Ltd.: London, 2004.
- (37) Valenzano, L.; Civalieri, B.; Chavan, S.; Bordiga, S.; Nilsen, M. H.; Jakobsen, S.; Lillerud, K. P.; Lamberti, C. Disclosing the complex structure of UiO-66 metal organic framework: A synergic combination of experiment and theory. *Chem. Mater.* **2011**, *23*, 1700–1718.
- (38) Scheinmann, F. *An Introduction to Spectroscopic Methods for the Identification of Organic Compounds*; Elsevier: England, 2013; p 308.
- (39) Kooli, F.; Chisem, I. C.; Vucelic, M.; Jones, W. Synthesis and properties of terephthalate and benzoate intercalates of Mg-Al layered double hydroxides possessing varying layer charge. *Chem. Mater.* **1996**, *8*, 1969–1977.
- (40) Song, F.; Hu, X. Exfoliation of layered double hydroxides for enhanced oxygen evolution catalysis. *Nat. Commun.* **2014**, *5*, 4477–4485.
- (41) Wang, Y.; Yan, D.; El Hankari, S.; Zou, Y.; Wang, S. Recent progress on layered double hydroxides and their derivatives for electrocatalytic water splitting. *Adv. Sci.* **2018**, *5*, 1800064–1800095.
- (42) Wasylenko, D. J.; Palmer, R. D.; Schott, E.; Berlinguette, C. P. Interrogation of electrocatalytic water oxidation mediated by a cobalt complex. *Chem. Commun.* **2012**, *48*, 2107–2109.
- (43) Wang, F.; Xiao, S.; Hou, Y.; Hu, C.; Liu, L.; Wu, Y. Electrode materials for aqueous asymmetric supercapacitors. *RSC Adv.* **2013**, *3*, 13059–13084.
- (44) Zheng, X. L.; Zhang, B.; De Luna, P.; Liang, Y. F.; Comin, R.; Voznyy, O.; Han, L.; Garcia de Arquer, F. P.; Liu, M.; Dinh, C. T.; Regier, T.; Dynes, J. J.; He, S.; Xin, H. L.; Peng, H. S.; Prendergast, D.; Du, X.; Sargent, E. H. Theory-driven design of high-valence metal sites for water oxidation confirmed using in situ soft X-ray absorption. *Nat. Chem.* **2018**, *10*, 149–154.
- (45) Ma, T. Y.; Dai, S.; Jaroniec, M.; Qiao, S. Z. Metal-organic framework derived hybrid Co_3O_4 -carbon porous nanowire arrays as reversible oxygen evolution electrodes. *J. Am. Chem. Soc.* **2014**, *136*, 13925–13931.
- (46) Chemelewski, W. D.; Lee, H. C.; Lin, J. F.; Bard, A. J.; Mullins, C. B. Amorphous FeOOH oxygen evolution reaction catalysts for photoelectrochemical water splitting. *J. Am. Chem. Soc.* **2014**, *136*, 2843–2850.
- (47) Shen, J.-Q.; Liao, P.-Q.; Zhou, D.-D.; He, C.-T.; Wu, J.-X.; Zhang, W.-X.; Zhang, J.-P.; Chen, X.-M. Modular and stepwise synthesis of a hybrid metal-organic framework for efficient electrocatalytic oxygen evolution. *J. Am. Chem. Soc.* **2017**, *139*, 1778–1781.
- (48) Li, F. L.; Shao, Q.; Huang, X.; Lang, J. P. Nanoscale trimetallic metal-organic frameworks enable efficient oxygen evolution electrocatalysis. *Angew. Chem., Int. Ed.* **2018**, *57*, 1888–1892.
- (49) Liardet, L.; Hu, X. Amorphous cobalt vanadium oxide as a highly active electrocatalyst for oxygen evolution. *ACS Catal.* **2018**, *8*, 644–650.
- (50) Liu, K.; Zhang, C.; Sun, Y.; Zhang, G.; Shen, X.; Zou, F.; Zhang, H.; Wu, Z.; Wegener, E. C.; Taubert, C. J.; Miller, J. T.; Peng, Z.; Zhu, Y. High-performance transition metal phosphide alloy catalyst for oxygen evolution reaction. *ACS Nano* **2018**, *12*, 158–167.
- (51) Dong, C.; Kou, T.; Gao, H.; Peng, Z.; Zhang, Z. Eutectic-derived mesoporous Ni-Fe-O nanowire network catalyzing oxygen evolution and overall water splitting. *Adv. Energy Mater.* **2018**, *8*, 1701347–1701356.
- (52) Lu, X. F.; Gu, L. F.; Wang, J. W.; Wu, J. X.; Liao, P. Q.; Li, G. R. Bimetal-organic framework derived $\text{CoFe}_2\text{O}_4/\text{C}$ porous hybrid nanorod arrays as high performance electrocatalysts for oxygen evolution reaction. *Adv. Mater.* **2017**, *29*, 1604437–160443.
- (53) Yu, L.; Yang, J. F.; Guan, B. Y.; Lu, Y.; Lou, X. W. D. Hierarchical hollow nanoprisms based on ultrathin Ni-Fe layered double hydroxide nanosheets with enhanced electrocatalytic activity towards oxygen evolution. *Angew. Chem., Int. Ed.* **2018**, *57*, 172–176.
- (54) Fabbri, E.; Nachttegaal, M.; Binner, T.; Cheng, X.; Kim, B.-J.; Durst, J.; Bozza, F.; Graule, T.; Schäublin, R.; Wiles, L.; Pertoso, M.; Danilovic, N.; Ayers, K. E.; Schmidt, T. J. Dynamic surface self-

reconstruction is the key of highly active perovskite nano-electrocatalysts for water splitting. *Nat. Mater.* **2017**, *16*, 925–931.

(55) Weng, B.; Xu, F.; Wang, C.; Meng, W.; Grice, C. R.; Yan, Y. A layer $\text{Na}_{1-x}\text{Ni}_x\text{Fe}_{1-y}\text{O}_2$ double oxide oxygen evolution reaction electrocatalyst for highly efficient water-splitting. *Energy Environ. Sci.* **2017**, *10*, 121–128.

(56) Ganassin, A.; Maljusch, A.; Colic, V.; Spanier, L.; Brandl, K.; Schuhmann, W.; Bandarenka, A. Benchmarking the performance of thin film oxide electrocatalysts for gas evolution reactions at high current densities. *ACS Catal.* **2016**, *6*, 3017–3024.

(57) Watzele, S.; Bandarenka, A. S. Quick determination of electroactive surface area of some oxide electrode materials. *Electroanalysis* **2016**, *28*, 2394–2399.

(58) Damjanovic, A.; Dey, A.; Bockris, J. O. M. Kinetics of oxygen evolution and dissolution on platinum electrodes. *Electrochim. Acta* **1966**, *11*, 791–814.

(59) Burke, M. S.; Kast, M. G.; Trotochaud, L.; Smith, A. M.; Boettcher, S. W. Cobalt-iron (oxy)hydroxide oxygen evolution electrocatalysts: the role of structure and composition on activity, stability, and mechanism. *J. Am. Chem. Soc.* **2015**, *137*, 3638–3648.

(60) Shi, Y.; Yu, Y.; Liang, Y.; Du, Y.; Zhang, B. In situ electrochemical conversion of an ultrathin tannin nickel iron complex film as an efficient oxygen evolution reaction electrocatalyst. *Angew. Chem., Int. Ed.* **2019**, *58*, 3769–3773.

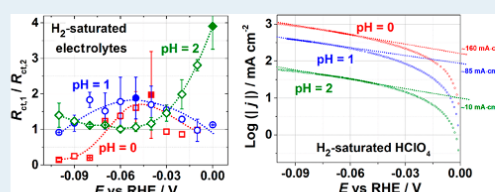
On the Dominating Mechanism of the Hydrogen Evolution Reaction at Polycrystalline Pt Electrodes in Acidic Media

Sebastian Watzel,^{†,‡} Johannes Fichtner,[†] Batyr Garlyyev,[†] Jan N. Schwämmlein,[§] and Aliaksandr S. Bandarenka^{*,†,‡,§}[†]Physik-Department ECS, Technische Universität München, James-Frank-Straße 1, 85748 Garching, Germany[‡]Nanosystems Initiative Munich (NIM), Schellingstraße 4, 80799 Munich, Germany[§]Technical Electrochemistry, Department of Chemistry, Technische Universität München, Lichtenbergstraße 4, 85748 Garching, Germany

Supporting Information

ABSTRACT: The hydrogen evolution reaction (HER) is of paramount importance for both fundamental and applied electrocatalysis. However, many issues related to understanding of this reaction remain unclear. These, for instance, include a surprising pH dependence of the electrode activities and non-Tafel dependency of the HER-associated current for various electrocatalysts. Even the dominating mechanism for this reaction at different potentials is often difficult to reveal. In this article, we use electrochemical impedance spectroscopy to estimate the relative contribution of the Volmer–Heyrovsky and Volmer–Tafel pathways to the overall hydrogen evolution process at polycrystalline Pt electrodes at pH = 0, 1, and 2 as a function of the electrode potential. Pt microelectrodes were used to facilitate impedance measurements at high current densities (up to $\sim 1 \text{ A}\cdot\text{cm}^{-2}$ in 1 M HClO_4) and to overcome common complications due to the fast kinetics of this reaction. Our results show that it is possible to distinguish different reaction pathways experimentally at each electrode potential using impedance measurements and demonstrate that the relative contributions of the Volmer–Heyrovsky and Volmer–Tafel pathways are in most cases comparable. Both mechanisms contribute differently to the total current at different electrode potentials, and none of them can be considered as absolutely dominating at a given complex Pt surface. These findings can be particularly used for elaboration of theoretical models and interpretation of non-Tafel behavior of polarization HER curves in acidic media.

KEYWORDS: electrocatalysis, microelectrodes, hydrogen evolution reaction mechanism, polycrystalline platinum, electrochemical impedance spectroscopy



1. INTRODUCTION

The hydrogen evolution reaction (HER) has attracted considerable attention due to its importance for the schemes of the provision of so-called renewable energy.^{1–5} At the same time, this reaction is an important model electrocatalytic process to gain better understanding of electrocatalysis itself, e.g., to find clearer links between the electrode structure/composition and the resulting activity.^{6,7} While it can also be recognized as the most studied electrocatalytic reaction, numerous important issues remain uncertain even for platinum-based electrodes, which demonstrate the highest activities toward the HER.⁸ Among those issues, one can mention an unusual pH dependence of the electrode activities,^{2,9} non-Tafel dependences of the polarization curves within wide potential ranges for various electrodes,¹⁰ uncertainties in the nature of the catalytic centers,¹¹ or adsorbate–adsorbate interactions, which complicate the overall reaction analysis.¹²

The origin of the above-mentioned issues is largely due to experimental and methodological difficulties in investigating the HER. While the mechanisms of this reaction were proposed at

the times of the “beginning of electrochemistry”, their experimental distinguishability is difficult. Recently, there were significant efforts to overcome the situation and provide a more comprehensive picture of the reaction both from theoretical and experimental points of view; see e.g., refs 13–15. Nevertheless, the choice of methods remains largely limited.

Electrochemical impedance spectroscopy is probably one of a few choices nowadays to provide in situ experimental data on the HER under various conditions. Initial successful attempts to apply this method to investigate mechanisms of hydrogen evolution in more detail were undertaken by Conway et al. more than 2 decades ago.^{16,17} However, the kinetics of this process as well as hydrogen underpotential adsorption/desorption¹⁸ enabled their detailed quantitative analysis only in some particular cases of high-index single crystals of platinum group metals^{19,20} and relatively high pH values.¹⁸

Received: August 22, 2018

Published: August 28, 2018

A powerful approach to further overcome experimental challenges associated with the HER kinetics and mechanisms is to use microelectrodes; among others, they offer an opportunity to minimize the influence of the nonconductive phase formation or effectively resolve constituents of fast electrode processes. The benefit of performing fundamental electrocatalytic measurements including microelectrodes related to the hydrogen-involved reactions was recognized decades ago (see e.g., ref. 21), and impedance measurements, particularly using microelectrodes, recently provided new insights into the electrochemical interface properties (see, e.g., refs 22–29 and references therein).

In this work, we aimed at answering the following fundamental and methodological electrocatalytic questions related to HER on Pt electrodes: (i) is it possible to resolve commonly accepted mechanisms of hydrogen evolution at Pt microelectrodes using electrochemical impedance spectroscopy at different electrode potentials in acidic media; (ii) if the latter is possible, what are the relative contributions of the Volmer–Heyrovsky and Volmer–Tafel pathways to the overall reaction kinetics at different potentials and pH values; (iii) at higher current densities, which are important for practical applications, does one of the mechanisms become dominating?

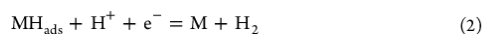
2. EXPERIMENTAL SECTION

A Hg/HgSO₄ electrode (Schott, Germany) and a Pt wire/mesh (99.9%, Goodfellow, Germany) were used as the reference (RE) and counter electrodes (CE), respectively. However, all of the potentials in this work are referenced to the reversible hydrogen electrode (RHE) scale. Polycrystalline Pt microelectrodes (Ch. Instruments, U.S.A.) with a diameter of 25 μm were used as working electrodes in all of the experiments. Ar-saturated (Ar 5.0, Air Liquide, Germany) and H₂-saturated (H₂ 5.0, Air Liquide, Germany) 1, 0.1, and 0.01 M HClO₄ electrolytes were prepared using HClO₄ (70% Suprapur, Merck, Germany) in ultraclean water (Evoqua, Germany). The microelectrodes were electrochemically cleaned by cycling them in 0.1 M HClO₄ solutions until stable characteristic voltammograms were obtained.

A VSP-300 (Bio-Logic, France) potentiostat was used in all experiments. Electrochemical impedance spectroscopy measurements were performed within the potential range between 0.02 and –0.1 V using AC-probing frequencies from 2 MHz to 1 Hz (10 mV amplitude). The impedance data were analyzed using the homemade software EIS Data Analysis 1.3.^{30,31}

3. RESULTS AND DISCUSSION

3.1. Theoretical Considerations. Consider that the HER on Pt in acidic media proceeds according to the Volmer–Heyrovsky mechanism (M refers to an adsorption site at the electrode surface)



or according to the Volmer–Tafel mechanism



For simplicity, assume that the processes take place at different parts of the electrode simultaneously and quasi-independently. The sum of the partial currents formally originating from the

Volmer–Heyrovsky, i_{VH} , and Volmer–Tafel, i_{VT} , reaction pathways gives the total Faradaic current, i_{tot}

$$i_{\text{tot}} = i_{\text{VH}} + i_{\text{VT}} \quad (4)$$

In order to obtain an equation for the impedance response due to the Volmer–Heyrovsky pathway, consider the equations for the corresponding reaction rates (in accordance with eqs 1 and 2)

$$\nu_1 = N_{\text{VH}}(k_1(E)F_1(\theta) - k_{-1}(E)F_{-1}(\theta)) \quad (5)$$

$$\nu_2 = N_{\text{VH}}(k_2(E)F_2(\theta) - k_{-2}(E)F_{-2}(\theta)) \quad (6)$$

The formal rate constants $k_1(E)$ and $k_2(E)$ contain the proton concentration and depend on the electrode potential, E . The potential-dependent functions $F_1(\theta)$, $F_{-1}(\theta)$, $F_2(\theta)$, and $F_{-2}(\theta)$ also depend on the H-adsorption isotherms, accounting for possible adsorbate–adsorbate interactions. N_{VH} is the fraction of adsorption sites where the reaction takes place according to the Volmer–Heyrovsky mechanism compared to the Volmer–Tafel mechanism.

The connection between the reaction rates ν_1 , ν_2 , and i_{VH} is

$$i_{\text{VH}} = F(\nu_1 + \nu_2) = Fr_0 \quad (7)$$

where F is the Faraday constant. As eqs 1 and 2 represent the two-stage mechanism with interfacial charge transfer at each stage, it is also necessary to take changes in the fractional coverage of the adsorbed H species into account³²

$$\frac{q_a}{F} \frac{d\theta}{dt} = \nu_1 - \nu_2 = r_1 \quad (8)$$

where q_a is the charge necessary to form a complete monolayer of H_{ads} and t is time.

For a small AC-probing amplitude, $\Delta E = E_{\text{dc}} + \tilde{E} \exp(j\omega t)$, where E_{dc} is an applied constant bias, \tilde{E} is the complex E amplitude (phasor), j is the imaginary unit, and ω is the angular frequency, the current, i_{VH} , and the fractional coverage, θ , will oscillate around some quasi-constant values, $i_{\text{dc,VH}}$, θ_{dc}

$$\Delta i_{\text{VH}} = i_{\text{dc,VH}} + \tilde{i}_{\text{VH}} \exp(j\omega t) \quad (9)$$

$$\Delta \theta = \theta_{\text{dc}} + \tilde{\theta} \exp(j\omega t) \quad (10)$$

where \tilde{i}_{VH} and $\tilde{\theta}$ are the corresponding complex amplitudes. In the following, $i_{\text{dc,VH}}$ and θ_{dc} are assumed to be constant and excluded from further analysis.

Linearization of eqs 7 and 8 gives

$$\begin{aligned} \Delta i_{\text{VH}} &= \left(\frac{\partial i_{\text{VH}}}{\partial E} \right)_{\theta} \Delta E + \left(\frac{\partial i_{\text{VH}}}{\partial \theta} \right)_{E} \Delta \theta \\ &= F \left[\left(\frac{\partial r_0}{\partial E} \right)_{\theta} \Delta E + \left(\frac{\partial r_0}{\partial \theta} \right)_{E} \Delta \theta \right] \end{aligned} \quad (11)$$

$$\frac{q_a}{F} \frac{d\Delta \theta}{dt} = \left(\frac{\partial r_1}{\partial E} \right)_{\theta} \Delta E + \left(\frac{\partial r_1}{\partial \theta} \right)_{E} \Delta \theta \quad (12)$$

Taking into account eqs 9 and 10, eqs 11 and 12 can be rewritten as follows

$$\frac{\tilde{i}_{\text{VH}}}{F} = \left(\frac{\partial r_0}{\partial E} \right)_{\theta} \tilde{E} + \left(\frac{\partial r_0}{\partial \theta} \right)_{E} \tilde{\theta} \quad (13)$$

$$\frac{q_a}{F} j\omega \bar{\theta} = \left(\frac{\partial r_1}{\partial E} \right)_\theta \bar{E} + \left(\frac{\partial r_1}{\partial \theta} \right)_E \bar{\theta} \quad (14)$$

From Equations 13 and 14, one can write the following equation for the complex admittance for the Volmer–Heyrovsky pathway

$$\hat{Y}_{F,VH} = -\frac{\bar{i}_{VH}}{\bar{E}} = -F \left(\frac{\partial r_0}{\partial E} \right)_\theta - \frac{F^2 \left(\frac{\partial r_0}{\partial \theta} \right)_E \left(\frac{\partial r_1}{\partial E} \right)_\theta}{j\omega - \frac{F}{q_a} \left(\frac{\partial r_1}{\partial \theta} \right)_E}$$

$$= A + \frac{B}{j\omega + C} \quad (15)$$

where A is equal to the inverse of the charge transfer resistance $R_{ct,1}^{-1}$ for the Volmer–Heyrovsky pathway. From eq 15, the complex impedance can be found as³²

$$\hat{Z}_{F,VH} = R_{ct,1} + \frac{1}{\frac{1}{R_a} + j\omega C_a} \quad (16)$$

where $R_a = \frac{R_{ct,1}^2 |B|}{C - R_{ct,1} |B|}$ and $C_a = \frac{1}{R_{ct,1}^2 |B|}$ can be called the “adsorption resistance” and “adsorption capacitance”, respectively. Equation 16 can be formally represented by an equivalent combination of the corresponding passive elements, the resistances, and the capacitance, as shown in Figure 1A.

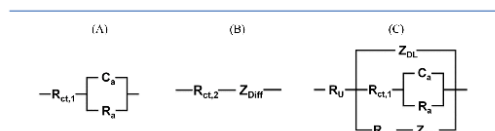


Figure 1. Models (EECs) for analysis of the impedance data expected for the HER at Pt microelectrodes. (A,B) Equivalent circuits for the Faradaic part of impedance associated with the (A) Volmer–Heyrovsky and (B) Volmer–Tafel pathways. (C) A complete EEC. See section 3.1 for the element explanation.

However, it should be emphasized that there are no real capacitances or resistances in the system. These elements just reflect the “AC behavior” of the kinetic equations in simpler terms.

The impedance response resulting from a Volmer–Tafel pathway can formally be taken into account comparatively easy. Equation 3 largely determines the model. In contrast to the Volmer–Heyrovsky pathway, only one electron transfer takes place at each adsorption site for a Volmer–Tafel mechanism. Additionally, the reaction $H^+ + M + e^- = MH_{ads}$ is not complicated by the fast subsequent charge transfer.¹⁵ Therefore, certain diffusion limitations are expected at high current densities (see the Supporting Information for details). The corresponding linear part of the AC response due to the Volmer–Tafel pathway can be written as

$$\Delta i_{VT} = \left(\frac{\partial i_{VT}}{\partial E} \right)_{C^*} \Delta E + \left(\frac{\partial i_{VT}}{\partial C^*} \right)_E \Delta C^* \quad (17)$$

where C^* is the surface concentration of the electroactive species. After similar transformations, the following equation for the complex Faradaic impedance resulting from the Volmer–Tafel pathway alone can be obtained

$$\hat{Z}_{F,VT} = R_{ct,2} + \hat{Z}_{Diff} \quad (18)$$

where \hat{Z}_{Diff} is the semi-infinite Warburg diffusion impedance originating from the term $\left(\frac{\partial i_{VT}}{\partial C^*} \right)$. Equation 18 can be formally represented by an equivalent combination of the corresponding passive elements connected in series, as shown in Figure 1B. According to the Dolin–Erschler–Randles approximation,^{33,34} the impedance of the electric double layer, Z_{DL} , is connected in parallel to the Faradaic impedances. In general, the response of the double layer can be approximated by the constant phase element, with the impedance, given as

$$Z_{DL} = Z_{CPE} = \frac{1}{C'_{DL} (j\omega)^n} \quad (19)$$

where the exponent n accounts for the frequency dispersion of the double layer and C'_{DL} is proportional but not equal to the true double-layer capacitance if n is significantly lower than 1. However, as the focus of this work is set to kinetic analysis, we assume here that $C_{DL} \equiv C'_{DL}$, irrespective of the values of n .

Together with the uncompensated resistance of the electrolyte, R_U , the complete equivalent electric circuit (EEC) can be constructed (Figure 1C). An explanation for the choice of each single-circuit element is given in the Supporting Information.

Taking into account the physical meaning of the charge transfer resistances

$$R_{ct,1} = -\frac{1}{\left(\frac{\partial i_{VH}}{\partial E} \right)} \quad (20)$$

$$R_{ct,2} = -\frac{1}{\left(\frac{\partial i_{VT}}{\partial E} \right)} \quad (21)$$

and the properties of the physicochemical equations (exponential functions) describing the corresponding kinetics, the ratio $R_{ct,1}/R_{ct,2}$ in the absence of significant diffusion limitations gives an estimate for the relative contribution of the Volmer–Tafel and the Volmer–Heyrovsky mechanisms to the total current.

It is now a key question if the analysis of experimental impedance data can confirm the hypothesis resulting from the theoretical considerations described here and if the use of microelectrodes facilitates resolution of the constituents of the fast electrocatalytic process.

3.2. Experimental Results. Figure 2A shows a characteristic cyclic voltammogram of the Pt microelectrode in Ar-saturated 1 M HClO₄. The voltammogram demonstrates features typical for polycrystalline Pt in acidic media, which are related to the adsorption and desorption of hydrogen (between ~0.03 and ~0.4 V) and hydroxyl (between ca. 0.7 and 0.9 V) species. The figure shows an approximate onset of ca. 20–30 mV of the HER in Ar-saturated electrolyte, which is slightly more positive (ca. 20–30 mV) compared to the thermodynamic equilibrium potential of the HOR/HER at standard conditions (0 V vs RHE). This is due to the absence of hydrogen in the electrolyte, causing a potential shift according to the Nernst equation. Therefore, impedance measurements in Ar-saturated electrolyte were performed at potentials ≤ 0.02 V vs RHE.

Figure 2B shows typical voltammograms characterizing the HER in the H₂-saturated HClO₄ electrolytes with three different pH values, i.e., 0, 1, and 2. As known, the activity (pH-corrected cases) of Pt electrodes toward this reaction depends on proton concentration in the solution, being the highest for the most acidic conditions. The origin of such a behavior is, however, still

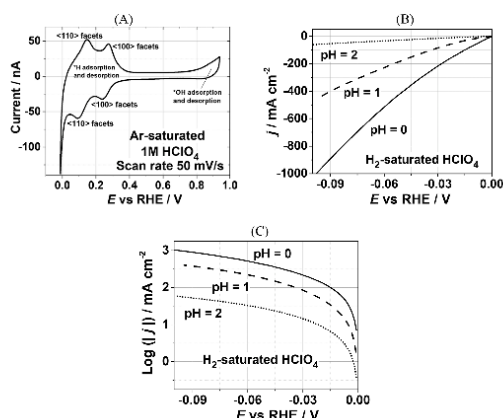


Figure 2. (A) Typical cyclic voltammogram of a Pt microelectrode in Ar-saturated 1 M HClO₄ at a scan rate of 50 mV/s. An approximate onset for the hydrogen evolution is ~ 0.02 V vs RHE. (B) Voltammograms of a Pt microelectrode in H₂-saturated 1 M HClO₄, 0.1 M HClO₄, and 0.01 M HClO₄ to indicate the HER activity. Microelectrodes enable practically iR -free measurements, revealing remarkably high intrinsic current densities. (C) Tafel plots for the dependences shown in (B).

under debate.^{2,9,35} It is also clear from Figure 2C that at a given electrode potential the quasi-Tafel slopes are dissimilar for the currents measured at different pH values, and in general, the nonlinear behavior of the current–potential dependency on the logarithmic scale is evident from Figure 2C.

Figure 3 shows examples of impedance spectra together with fitting results, which suggest that it is problematic to achieve good fitting assuming only one of the well-accepted mecha-

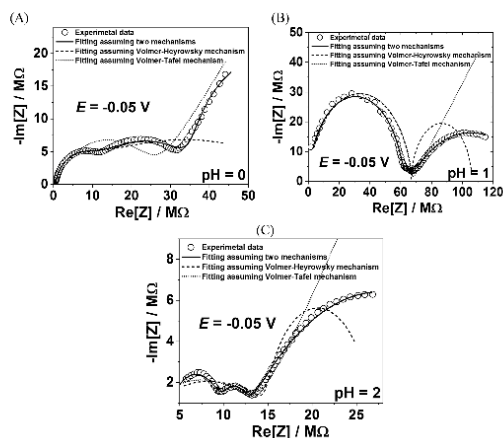


Figure 3. Typical impedance Nyquist plots (symbols) of the Pt microelectrode spectra taken at $E = -0.05$ V vs RHE in H₂-saturated (A) 1 M HClO₄, (B) 0.1 M HClO₄, and (C) 0.01 M HClO₄. The dashed/dotted lines represent attempts to fit the spectra assuming only Volmer–Heyrowsky and only Volmer–Tafel mechanisms, respectively. Only considering both mechanisms, satisfactory fitting can be achieved.

nisms. Typical electrochemical admittance spectra of the Pt microelectrodes recorded in 1, 0.1, and 0.01 M HClO₄ at different potentials are presented in Figure 4. As can also be seen

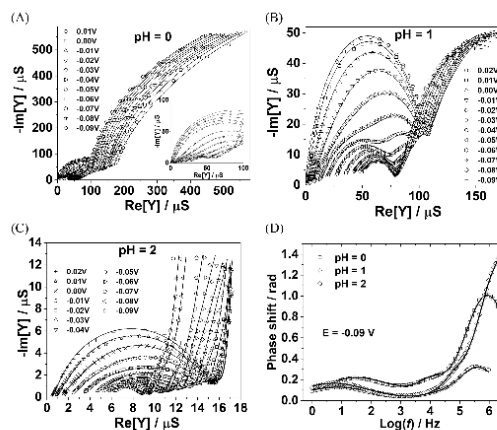


Figure 4. Typical admittance Nyquist plots (symbols) of the Pt microelectrode spectra taken at different potentials in Ar-saturated (A) 1 M HClO₄, (B) 0.1 M HClO₄, and (C) 0.01 M HClO₄. (D) Examples of the phase shifts plotted as a function of the AC probing frequency for Pt microelectrodes in Ar-saturated 1 M HClO₄, 0.1 M HClO₄, and 0.01 M HClO₄ at -0.09 V. Solid lines represent fitting to the equivalent circuit shown in Figure 1C.

from the figure, the model shown in Figure 1C is able to accurately describe the impedance response at all investigated potentials: the normalized root-mean-squared deviations were less than 2.5% in all cases. Moreover, the relative errors of the key individual EEC elements of this work were in the overwhelming majority of cases less than 10%, confirming the expectations outlined in section 3.1. In other words, these low values indicate the significance of the contributions of these elements to the overall fitting.

Figure 5 shows impedance spectra obtained in the H₂-saturated electrolytes. As can be seen from the figure, it is also possible to achieve good fitting with low root-mean-square deviations, further supporting the idea about a possibility to distinguish two HER mechanisms using impedance spectroscopy and Pt microelectrodes. Indeed, the spectra cannot be fitted using solely the model for the Volmer–Heyrowsky or the Volmer–Tafel mechanism, as demonstrated in Figure 3A–C. Fitting under the assumption of just one mechanism fails, and the combination of both mechanisms allows satisfactory fitting.

Figure 6 represents an example of the dependencies of the key EEC parameters of the equivalent circuit shown in Figure 1C. While the above-mentioned EEC parameters depend on complex factors, which are often difficult to predict (surface concentrations of H⁺ in the Ar-saturated solutions etc.), one can, e.g., observe the well-expected behavior of the double-layer “capacitance” being much higher in more concentrated electrolytes in both H₂-free and H₂-saturated electrolytes (Figure 6A,G). The differences in the “capacitance” values between the Ar-saturated and H₂-saturated electrolytes are caused by different exponents n (eq 19), and this difference is likely caused by different double-layer properties due to specific adsorption of reaction intermediates.^{36,37} However, further

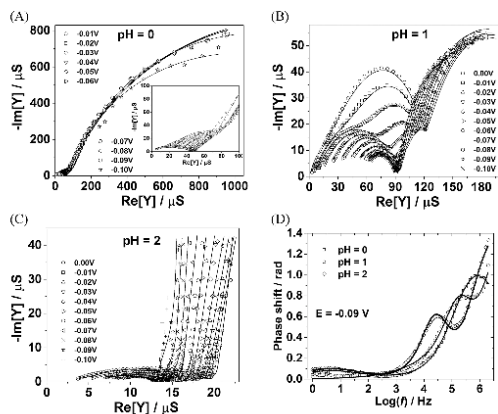


Figure 5. Typical admittance Nyquist plots (symbols) of the Pt microelectrode spectra taken at different potentials in H_2 -saturated (A) 1 M HClO_4 , (B) 0.1 M HClO_4 , and (C) 0.01 M HClO_4 . (D) Examples of the phase shifts plotted as a function of the AC probing frequency for Pt microelectrodes in H_2 -saturated 1 M HClO_4 , 0.1 M HClO_4 , and 0.01 M HClO_4 at -0.09 V. Solid lines represent fitting to the equivalent circuit shown in Figure 1C.

discussion regarding this is outside of the scope of this manuscript.

The charge transfer resistances related to the Volmer–Heyrovsky and Volmer–Tafel steps (Figure 6B,C,H,I) demonstrate complex dependencies associated with the fact that according to eqs 20 and 21 they are derivatives of the DC currents related to the corresponding mechanisms. However, even in this case, one can notice that the resistances are in general lower in more acidic media in accordance with the trends depicted in Figure 2B,C. The dependences of other constituents of the Faradaic impedance are R_a and C_a for the Volmer–Heyrovsky mechanism (Figures 6D,E,J,K, which according to eq 16 should in general correlate with each other, as observed) and the Warburg parameter, A_w , for the Volmer–Tafel mechanism. For the latter, it is clear from Figure 6F,L that the diffusion limitations exist, but they are not process-determining within the investigated potential range.

As stated earlier, further insight into the dominating mechanism of the hydrogen evolution in the investigated systems can be obtained from a simple ratio: $R_{ct,1}/R_{ct,2}$. Due to the physical meaning of these parameters (eqs 20 and 21) and the properties of the functions governing the current, this ratio illustrates a relative contribution of the Volmer–Heyrovsky and Volmer–Tafel pathways to the overall current due to the HER at different pH values

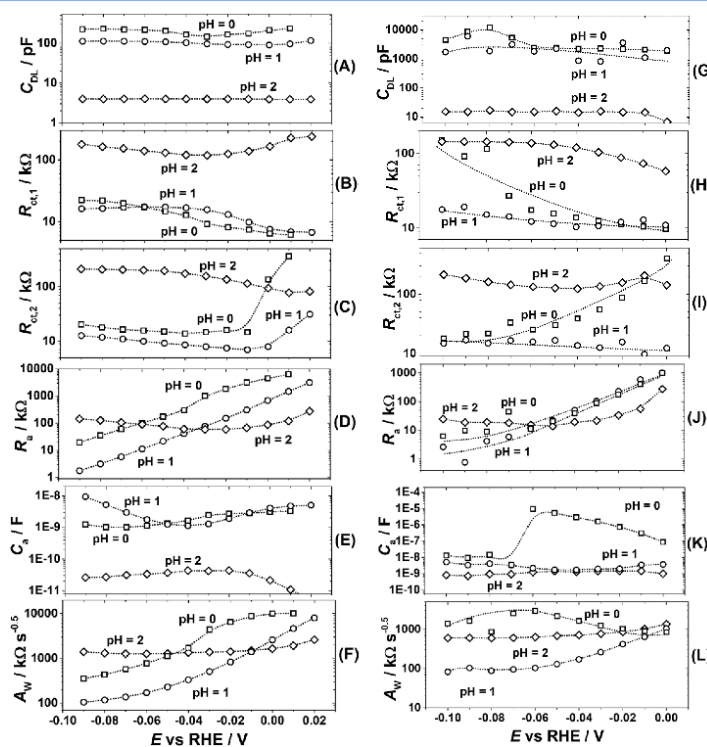


Figure 6. Dependences of the main parameters of the equivalent circuit shown in Figure 1C on the electrode potential for the Pt microelectrodes in (A–F) Ar-saturated and (G–L) H_2 -saturated 1 M HClO_4 , 0.1 M HClO_4 , and 0.01 M HClO_4 electrolytes. Dotted lines are the guides to the eyes.

$$\frac{R_{ct,1}}{R_{ct,2}} \propto \frac{N_{VT}}{N_{VH}} \cdot \frac{F(\theta)_{VT}}{F(\theta)_{VH}} \cdot \frac{C_{VT}^*}{C_{VH}^*} \quad (22)$$

where C_{VH}^* and C_{VT}^* are the effective surface concentrations of the electroactive species, which can be found at the sites where the Volmer–Heyrovsky and Volmer–Tafel pathways take place. For eq 22, we assume that the transfer coefficients for two mechanisms are equal to each other and the functions, which describe the adsorbate–adsorbate contributions, are dissimilar (new parameter, N_{VT} , is the fraction of the adsorption sites where the reaction takes place according to the Volmer–Tafel mechanism).

The ratios $R_{ct,1}/R_{ct,2}$ are plotted in Figure 7A as a function of the electrode potential for the Ar-saturated and in Figure 7B for

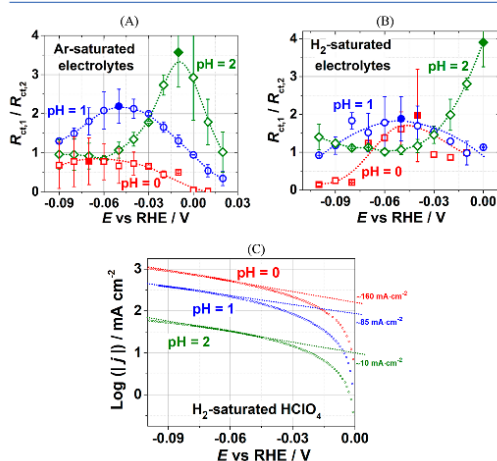


Figure 7. Ratio $R_{ct,1}/R_{ct,2}$, illustrating a relative contribution of the Volmer–Heyrovsky and Volmer–Tafel pathways into the overall current due to the HER at different pH values, as indicated in the figure. The bold symbols designate extrema where the relative contribution of the Volmer–Tafel pathway is maximal for the corresponding pH values. The data obtained in (A) Ar-saturated and (B) H_2 -saturated electrolyte solutions. The error bars account for only independent measurements. Dotted lines are guides to the eyes. (C) Determination of the exchange current densities using a “classical” approach accounting for the situation when $R_{ct,1}/R_{ct,2} \approx 1$ (bold symbols) at the higher current densities for each pH. The error bars in (A) and (B) refer to independent measurements.

the H_2 -saturated electrolytes. While there are noticeable differences between the H_2 -saturated and Ar-saturated solutions, one can see that the trends at each pH are similar, and the relative contributions of two mechanisms depend on the electrode potential. However, it is also clear that for the majority of the potentials in the investigated electrode potential range one cannot consider any of the mechanisms as absolutely dominating.

The dependences shown in Figure 7 pose several fundamental and methodological questions particularly related to nanostructured Pt electrocatalysts, where the surface structure is complex. At least three of them are listed below:

- (i) Would common extrapolation of any part of “linear” DC curves shown in Figure 2C indeed give the true HER/HOR exchange current density at 0.00 V vs RHE?

- (ii) If so, to which mechanism kinetics would it belong to?
- (iii) Do often reported arbitrary “Tafel slopes”, which change with the electrode potential, have some fundamental physical meaning in light of methodical challenges in distinguishing the two mechanisms and quantification of the kinetics of them?

Other complications arise when considering Figure 7C. Apart from the fact the Tafel slopes change with the electrode potential, it is clear that it is also different for the same ratio $R_{ct,1}/R_{ct,2}$ at higher and lower current densities. The most probable reason for this is different adsorbate–adsorbate interactions, which, unfortunately, cannot be described purely by, e.g., Langmuir, Temkin, or Frumkin isotherms. Therefore, one can note that consideration of HER as a “simple” reaction is only true from a historical point of view.

Taking into account that the higher current densities are more important for practical applications, one can consider quasi-linear parts in Figure 7C, which correspond to the ratio $R_{ct,1}/R_{ct,2} \approx 1$ at higher current densities. The values of ~ 160 , ~ 85 , and ~ 10 mA/cm² were obtained for pH = 0, 1, and 2, respectively. The former is in agreement with the values presented in ref 38. One should again notice that these values were obtained without the influence of the iR -factor due to the use of microelectrodes.

4. SUMMARY AND CONCLUSIONS

In this work, we used electrochemical impedance spectroscopy in an attempt to distinguish and estimate relative contributions of the Volmer–Heyrovsky and Volmer–Tafel pathways to the HER at polycrystalline Pt electrodes at pH = 0, 1, and 2 as a function of the electrode potential. Pt microelectrodes were used to facilitate EIS measurements at higher current densities and overcome complications due to the fast kinetics of this process. Our results show that it is possible to distinguish different reaction pathways experimentally up to 0.1 V vs RHE. However, they contribute differently to the total Faradaic current at different potentials, and at the same time, none of them can be considered as absolutely dominating. These findings can be used for elaboration of theoretical models and interpretation of non-Tafel behavior of HER polarization curves in acidic media.

■ ASSOCIATED CONTENT

Supporting Information

The Supporting Information is available free of charge on the ACS Publications website at DOI: 10.1021/acscatal.8b03365.

Description of the equivalent circuit elements and additional information on derivations of the equations (PDF)

■ AUTHOR INFORMATION

Corresponding Author

*E-mail: bandarenka@ph.tum.de. Tel. +49 (0) 89 289 12531.

ORCID

Aliaksandr S. Bandarenka: 0000-0002-5970-4315

Notes

The authors declare no competing financial interest.

■ ACKNOWLEDGMENTS

We are thankful to Prof. Dr. Hubert A. Gasteiger (Technical University Munich) for fruitful discussions regarding this manuscript. Financial support from the cluster of excellence Nanosystems Initiative Munich (NIM), the Deutsche For-

schungsgemeinschaft (DFG; Projects BA 5795/3-1 and BA 5795/4-1), and IGSE (Technische Universität München; Project 11.01) is gratefully acknowledged.

REFERENCES

- (1) Carmo, M.; Fritz, D. L.; Mergel, J.; Stolten, D. A comprehensive review on PEM water electrolysis. *Int. J. Hydrogen Energy* **2013**, *38*, 4901.
- (2) Sheng, W.; Zhuang, Z.; Gao, M.; Zheng, J.; Chen, J. G.; Yan, Y. Correlating hydrogen oxidation and evolution activity on platinum at different pH with measured hydrogen binding energy. *Nat. Commun.* **2015**, *6*, 5848.
- (3) Zeradjanin, A. R.; Grote, J.-P.; Polymeros, G.; Mayrhofer, K. J. J. A Critical Review on Hydrogen Evolution Electrocatalysis: Re-exploring the Volcano-relationship. *Electroanalysis* **2016**, *28*, 2256.
- (4) Tymoczko, J.; Calle-Vallejo, F.; Schuhmann, W.; Bandarenka, A. S. Making the hydrogen evolution reaction in polymer electrolyte membrane electrolyzers even faster. *Nat. Commun.* **2016**, *7*, 10990.
- (5) Sheng, W. C.; Gasteiger, H. A.; Shao-Horn, Y. Hydrogen oxidation and evolution reaction kinetics on platinum: acid vs alkaline electrolytes. *J. Electrochem. Soc.* **2010**, *157*, B1529.
- (6) Marković, N. M.; Grgur, B. N.; Ross, P. N. Temperature-dependent hydrogen electrochemistry on platinum low-index single-crystal surfaces in acid solutions. *J. Phys. Chem. B* **1997**, *101*, 5405.
- (7) Calle-Vallejo, F.; Koper, M. T. M.; Bandarenka, A. S. Tailoring the catalytic activity of electrodes with monolayer amounts of foreign metals. *Chem. Soc. Rev.* **2013**, *42*, S210.
- (8) Durst, J.; Siebel, A.; Simon, C.; Hasché, F.; Herranz, J.; Gasteiger, A. New insights into the electrochemical hydrogen oxidation and evolution reaction mechanism. *Energy Environ. Sci.* **2014**, *7*, 2255.
- (9) Rossmel, J.; Chan, K.; Skulason, E.; Björketun, M. E.; Tripkovic, V. On the pH dependence of electrochemical proton transfer barriers. *Catal. Today* **2016**, *262*, 36.
- (10) Quaino, P. M.; Gennero de Chialvo, M. R.; Chialvo, A. C. Hydrogen electrode reaction: A complete kinetic description. *Electrochim. Acta* **2007**, *52*, 7396.
- (11) Pohl, M. D.; Watzele, S.; Calle-Vallejo, F.; Bandarenka, A. S. Nature of Highly Active Electrocatalytic Sites for the Hydrogen Evolution Reaction at Pt Electrodes in Acidic Media. *ACS Omega* **2017**, *2*, 8141.
- (12) Skulason, E.; Tripkovic, V.; Björketun, M. E.; Gudmundsdottir, S.; Karlberg, G.; Rossmel, J.; Bligaard, T.; Jonsson, H.; Nørskov, J. K. Modeling the electrochemical hydrogen oxidation and evolution reactions on the basis of density functional theory calculations. *J. Phys. Chem. C* **2010**, *114*, 18182.
- (13) He, Z.-D.; Wei, J.; Chen, Y.-X.; Santos, E.; Schmickler, W. Hydrogen evolution at Pt(111) – activation energy, frequency factor and hydrogen repulsion. *Electrochim. Acta* **2017**, *255*, 391.
- (14) Zalizit, C. M.; Sharman, J.; Wright, E.; Kucernak, A. R. Properties of the hydrogen oxidation reaction on Pt/C catalysts at optimized high mass transport conditions and its relevance to the anode reaction in PEMFCs and cathode reactions in electrolyzers. *Electrochim. Acta* **2015**, *176*, 763.
- (15) Kucernak, A. R.; Zalizit, C. General Models for the Electrochemical Hydrogen Oxidation and Hydrogen Evolution Reactions: Theoretical Derivation and Experimental Results under Near Mass-Transport Free Conditions. *J. Phys. Chem. C* **2016**, *120*, 10721.
- (16) Harrington, D. A.; Conway, B. E. ac Impedance of Faradaic reactions involving electroadsorbed intermediates—I. Kinetic theory. *Electrochim. Acta* **1987**, *32*, 1703.
- (17) Barber, J.; Morin, S.; Conway, B. E. Specificity of the kinetics of H₂ evolution to the structure of single-crystal Pt surfaces, and the relation between opd and upd H. *J. Electroanal. Chem.* **1998**, *446*, 125.
- (18) Schouten, K. J. P.; van der Niet, M. J. T. C.; Koper, M. T. M. Impedance spectroscopy of H and OH adsorption on stepped single-crystal platinum electrodes in alkaline and acidic media. *Phys. Chem. Chem. Phys.* **2010**, *12*, 15217.
- (19) Lin, D.; Lasia, A. Electrochemical impedance study of the kinetics of hydrogen evolution at a rough palladium electrode in acidic solution. *J. Electroanal. Chem.* **2017**, *785*, 190.
- (20) Pohl, M. D.; Colic, V.; Scieszka, D.; Bandarenka, A. S. Elucidation of adsorption processes at the surface of Pt (331) model electrocatalysts in acidic aqueous media. *Phys. Chem. Chem. Phys.* **2016**, *18*, 10792.
- (21) Bagotzky, V. S.; Osetrova, N. V. Investigations of hydrogen ionization on platinum with the help of micro-electrodes. *J. Electroanal. Chem. Interfacial Electrochem.* **1973**, *43*, 233.
- (22) Pajkossy, T.; Jurczakowski, R. Electrochemical impedance spectroscopy in interfacial studies. *Current Opinion in Electrochemistry* **2017**, *1*, 53.
- (23) Ganassin, A.; Maljusch, A.; Colic, V.; Spanier, L.; Brandl, K.; Schuhmann, W.; Bandarenka, A. S. Benchmarking the Performance of Thin-Film Oxide Electrocatalysts for Gas Evolution Reactions at High Current Densities. *ACS Catal.* **2016**, *6*, 3017.
- (24) Bandarenka, A. S.; Eckhard, K.; Maljusch, A.; Schuhmann, W. Localized electrochemical impedance spectroscopy: Visualization of spatial distributions of the key parameters describing solid/liquid interfaces. *Anal. Chem.* **2013**, *85*, 2443.
- (25) Bandarenka, A. S.; Maljusch, A.; Kuznetsov, V.; Eckhard, K.; Schuhmann, W. Localized impedance measurements for electrochemical surface science. *J. Phys. Chem. C* **2014**, *118*, 8952.
- (26) Bandarenka, A. S. Exploring the interfaces between metal electrodes and aqueous electrolytes with electrochemical impedance spectroscopy. *Analyst* **2013**, *138*, 5540.
- (27) Colic, V.; Tymoczko, J.; Maljusch, A.; Ganassin, A.; Schuhmann, W.; Bandarenka, A. S. Experimental aspects in benchmarking of the electrocatalytic activity. *ChemElectroChem* **2015**, *2*, 143.
- (28) Morkvenaitė-Vilkonciene, I.; Genys, P.; Ramanaviciene, A.; Ramanavicius, A. Scanning electrochemical impedance microscopy for investigation of glucose oxidase catalyzed reaction. *Colloids Surf., B* **2015**, *126*, 598.
- (29) Shkirskiy, V.; Volovitch, P.; Vivier, V. Development of quantitative Local Electrochemical Impedance Mapping: an efficient tool for the evaluation of delamination kinetics. *Electrochim. Acta* **2017**, *235*, 442.
- (30) Bondarenko, A. S. Analysis of large experimental datasets in electrochemical impedance spectroscopy. *Anal. Chim. Acta* **2012**, *743*, 41.
- (31) Bandarenka, A. S. Development of hybrid algorithms for EIS data fitting. *Lecture Notes on Impedance Spectroscopy* **2013**, No. 4, 29.
- (32) Lasia, A. *Electrochemical Impedance Spectroscopy and Its Applications*; Springer-Verlag: New York, 2014; p 367.
- (33) Dolin, P. I.; Ershler, B. V. Kinetics of processes on the platinum electrode. The kinetics of the ionization of hydrogen adsorbed on a platinum electrode. *Acta Physicochem. U.R.S.S.* **1940**, *13*, 747.
- (34) Randles, J. E. B. Kinetics of rapid electrode reactions. *Discuss. Faraday Soc.* **1947**, *1*, 11.
- (35) Chen, X.; McCrum, I. T.; Schwarz, K. A.; Janik, M. J.; Koper, M. Co-adsorption of Cations as the Cause of the Apparent pH Dependence of Hydrogen Adsorption on a Stepped Platinum Single-Crystal Electrode. *Angew. Chem., Int. Ed.* **2017**, *56*, 15025.
- (36) Tymoczko, J.; Schuhmann, W.; Bandarenka, A. S. The constant phase element reveals 2D phase transitions in adsorbate layers at the electrode/electrolyte interfaces. *Electrochem. Commun.* **2013**, *27*, 42.
- (37) Tymoczko, J.; Colic, V.; Bandarenka, A. S.; Schuhmann, W. Detection of 2D phase transitions at the electrode/electrolyte interface using electrochemical impedance spectroscopy. *Surf. Sci.* **2015**, *631*, 81.
- (38) Durst, J.; Simon, C.; Hasché, F.; Gasteiger, H. A. Hydrogen oxidation and evolution reaction kinetics on carbon supported Pt, Ir, Rh, and Pd electrocatalysts in acidic media. *J. Electrochem. Soc.* **2015**, *162*, F190–F203.

6.4 Other publications

- S. Xue, R. W. Haid, R. M. Kluge, X. Ding, B. Garlyyev, J. Fichtner, S. Watzele, S. Hou, A. S. Bandarenka. Enhancing the hydrogen evolution reaction activity of platinum electrodes in alkaline media using Ni-Fe clusters. *Manuscript submitted for publication*.
- J. Fichtner,⁽¹⁾ S. Watzele,⁽¹⁾ B. Garlyyev, R. M. Kluge, F. Haimerl, H. A. El-Sayed, W. Li, F. Maillard, L. Dubau, R. Chattot, J. Michalička, J. Macak, W. Wang, D. Wang, T. Gigl, C. Hugenschmidt, A. S. Bandarenka. Tailoring the Oxygen Reduction Activity of Pt Nanoparticles through Surface Defects: A Simple Top-Down Approach. *Manuscript submitted for publication*.
- W. Li, S. Xue, S. Watzele, S. Hou, J. Fichtner, A. L. Semrau, L. Zhou, A. Welle, A. S. Bandarenka, R. A. Fischer. Advanced Bifunctional Oxygen Reduction and Evolution Electrocatalyst Derived from Surface-Mounted Metal-Organic Frameworks. *Angewandte Chemie International Edition* (2020) accepted, DOI: 10.1002/anie.201916507)
- J. Fichtner,⁽¹⁾ B. Garlyyev,⁽¹⁾ S. Watzele, H. A. El-Sayed, J. Schwaemmlein, W. Li, F. Maillard, L. Dubau, J. Michalicka, J. Macak, A.W. Holleitner, A.S. Bandarenka. Top-Down Synthesis of Nanostructured Platinum-Lanthanide Alloy Oxygen Reduction Reaction Catalysts: Pt_xPr/C as an Example *ACS Applied Materials and Interfaces*, 11 (2019)
- B. Garlyyev, Y. Liang, S. Xue, S. Watzele, J. Fichtner, W.J. Li, X. Ding, A.S. Bandarenka. Theoretical and experimental identification of active electrocatalytic surface sites *Current Opinion in Electrochemistry* 14 (2019)
- S. Xue, B. Garlyyev, S. Watzele, Y. Liang, J. Fichtner, M.D. Pohl, A.S. Bandarenka. Influence of alkali metal cations on the hydrogen evolution reaction activity of Pt, Ir, Au and Ag electrodes in alkaline electrolytes *ChemElectroChem* 5 (2018)

- B. Garlyyev, S. Xue, S. Watzele, D. Scieszka, A.S. Bandarenka. Influence of the nature of the alkali metal cations on the electrical double layer capacitance of model Pt(111) and Au(111) electrodes *The Journal of Physical Chemistry Letters* 9 (2018)
- S. Xue⁽¹⁾, S. Watzele⁽¹⁾, V. Čolić, K. Brandl, B. Garlyyev, A.S. Bandarenka. Reconsidering water electrolysis: producing H₂ at cathodes together with valuable chemicals at anodes. Selective anodic oxidation of n-butylamine to n-butyronitrile as an example (Cover Feature) *ChemSusChem* 10 (2017)
- M. D. Pohl, S. Watzele, F. Calle-Vallejo, A.S. Bandarenka. Nature of highly active electrocatalytic sites for the hydrogen evolution reaction at Pt electrodes in acidic media *ACS Omega* 2 (2017)

6.5 Conference presentations

- 1st IMPRS-RECHARGE Scientific Symposium 2017 “Catalysis for Sustainable Chemical Energy Conversion (CSCEC)”, Duisburg (oral presentation)
- 8th Colloquium of the Munich School of Engineering “Advances in Energy Transition” 2018, Munich (oral presentation), *awarded with a presentation price*
- GDCh, “Electrochemistry 2018”, Ulm (poster presentation)
- 69th Annual Meeting of the International Society of Electrochemistry, 2018 Bologna (oral and poster presentation)
- European Fuel Cell Forum 2019, Lucerne (poster presentation)
- SElectrochem, 2019, London (oral and poster presentation), *awarded with a presentation price*
- Toyota 2019 European Fuel Cell Research Workshop, Zaventem, Belgium (invited presentation)

6.6 References

1. Albritton, D. L., & Dokken, D. J. (2001). Climate change 2001: synthesis report. R. T. Watson (Ed.). Cambridge, UK: Cambridge University Press.
2. Thomas, C. D., Cameron, A., Green, R. E., Bakkenes, M., Beaumont, L. J., Collingham, Y. C., ... & Hughes, L. (2004). Extinction risk from climate change. *Nature*, *427*(6970), 145.
3. Höök, M., & Tang, X. (2013). Depletion of fossil fuels and anthropogenic climate change—A review. *Energy Policy*, *52*, 797-809.
4. Wuebbles, D. J., & Jain, A. K. (2001). Concerns about climate change and the role of fossil fuel use. *Fuel Processing Technology*, *71*(1-3), 99-119.
5. Global energy demand rose by 2.3% in 2018, its fastest pace in the last decade <https://www.iea.org/news/global-energy-demand-rose-by-23-in-2018-its-fastest-pace-in-the-last-decade> (accessed December 2019)
6. The shift project data portal “Breakdown of Electricity Generation by Energy Source” <http://www.tsp-data-portal.org/Breakdown-of-Electricity-Generation-by-Energy-Source#tspQvChart> (accessed December 2019)
7. Kiriya, E., & Suzuki, A. (2004). Use of real options in nuclear power plant valuation in the presence of uncertainty with CO2 emission credit. *Journal of Nuclear Science and Technology*, *41*(7), 756-764.
8. Eichholz, G. G. (1976). Environmental aspects of nuclear power. *Advances in Astronomy and Space Physics*.
9. Sailor, W. C., Bodansky, D., Braun, C., Fetter, S., & van der Zwaan, B. (2000). A nuclear solution to climate change?. *Science*, *288*(5469), 1177-1178.
10. REN21 “RENEWABLES 2018 GLOBAL STATUS REPORT” http://www.ren21.net/gsr-2018/chapters/chapter_01/chapter_01/ (accessed December 2019)
11. Dincer, I. (2000). Renewable energy and sustainable development: a crucial review. *Renewable and Sustainable Energy Reviews*, *4*(2), 157-175.
12. Ellabban, O., Abu-Rub, H., & Blaabjerg, F. (2014). Renewable energy resources: Current status, future prospects and their enabling technology. *Renewable and Sustainable Energy Reviews*, *39*, 748-764.
13. Boyle, G. (2004). Renewable energy. *Renewable Energy*, by Edited by Godfrey Boyle, pp. 456. Oxford University Press, May 2004. ISBN-10: 0199261784. ISBN-13: 9780199261789, 456.
14. Turner, J. A. (1999). A realizable renewable energy future. *Science*, *285*(5428), 687-689.
15. Lund, H. (2007). Renewable energy strategies for sustainable development. *Energy*, *32*(6), 912-919.
16. Zografakis, N., Sifaki, E., Pagalou, M., Nikitaki, G., Psarakis, V., & Tsagarakis, K. P. (2010). Assessment of public acceptance and willingness to pay for renewable energy sources in Crete. *Renewable and Sustainable Energy Reviews*, *14*(3), 1088-1095.

-
17. Peidong, Z., Yanli, Y., Yonghong, Z., Lisheng, W., & Xinrong, L. (2009). Opportunities and challenges for renewable energy policy in China. *Renewable and Sustainable Energy Reviews*, 13(2), 439-449.
18. Nelson, V. C., & Starcher, K. L. (2015). *Introduction to renewable energy*. 2nd edition. CRC press.
19. Brouwer, A. S., Van Den Broek, M., Seebregts, A., & Faaij, A. (2014). Impacts of large-scale Intermittent Renewable Energy Sources on electricity systems, and how these can be modeled. *Renewable and Sustainable Energy Reviews*, 33, 443-466.
20. Teleke, S., Baran, M. E., Bhattacharya, S., & Huang, A. Q. (2010). Rule-based control of battery energy storage for dispatching intermittent renewable sources. *IEEE Transactions on Sustainable Energy*, 1(3), 117-124.
21. Dallinger, D., & Wietschel, M. (2012). Grid integration of intermittent renewable energy sources using price-responsive plug-in electric vehicles. *Renewable and Sustainable Energy Reviews*, 16(5), 3370-3382.
22. Aamir, M., Poncela, J., Chowdhry, B. S., & Uqaili, M. A. (2012, March). Impact analysis of renewable energy in national grids for energy deficit countries. In *International Multi Topic Conference* (pp. 1-9). Springer, Berlin, Heidelberg.
23. Liserre, M., Sauter, T., & Hung, J. Y. (2010). Future energy systems: Integrating renewable energy sources into the smart power grid through industrial electronics. *IEEE industrial electronics magazine*, 4(1), 18-37.
24. Zhang, W. L., Qiu, M., & LAI, X. K. (2008). Application of energy storage technologies in power grids. *Power System Technology*, 7, 3-9.
25. Lindley, D. (2010). Smart grids: The energy storage problem. *Nature News*, 463(7277), 18-20.
26. Kroposki, B., Johnson, B., Zhang, Y., Gevorgian, V., Denholm, P., Hodge, B. M., & Hannegan, B. (2017). Achieving a 100% renewable grid: Operating electric power systems with extremely high levels of variable renewable energy. *IEEE Power and Energy Magazine*, 15(2), 61-73.
27. Abedini, A., & Nasiri, A. (2008, November). Applications of super capacitors for PMSG wind turbine power smoothing. In *2008 34th Annual Conference of IEEE Industrial Electronics* (pp. 3347-3351). IEEE.
28. Banerjee, S., Chatterjee, J. K., & Tripathy, S. C. (1990). Application of magnetic energy storage unit as load-frequency stabilizer. *IEEE Transactions on Energy Conversion*, 5(1), 46-51.
29. Molina, M. G. (2012, September). Distributed energy storage systems for applications in future smart grids. In *2012 Sixth IEEE/PES Transmission and Distribution: Latin America Conference and Exposition (T&D-LA)* (pp. 1-7). IEEE.
30. Li, X., Hu, C., Liu, C., & Xu, D. (2008, November). Modeling and control of aggregated super-capacitor energy storage system for wind power generation. In *2008 34th Annual Conference of IEEE Industrial Electronics* (pp. 3370-3375). IEEE.
31. Pinto, J., de Sousa, J., & Neves, M. V. (2011, May). The value of a pumping-hydro generator in a system with increasing integration of wind power. In *2011 8th International Conference on the European Energy Market (EEM)* (pp. 306-311). IEEE.
32. Letcher, T. M., Law, R., & Reay, D. (2016). *Storing Energy: with special reference to renewable energy sources* (Vol. 86). Oxford: Elsevier.
33. tagesschau.de-Archiv „Bis zu vier Millionen Chinesen sollen Wohnungen verlieren“ <https://tsarchive.wordpress.com/2007/10/12/china8/> (accessed December 2019)
34. Herrmann, U., Kelly, B., & Price, H. (2004). Two-tank molten salt storage for parabolic trough solar power plants. *Energy*, 29(5-6), 883-893.

-
35. Peng, Q., Yang, X., Ding, J., Wei, X., & Yang, J. (2013). Design of new molten salt thermal energy storage material for solar thermal power plant. *Applied Energy*, *112*, 682-689.
36. Liu, J., Zhang, J. G., Yang, Z., Lemmon, J. P., Imhoff, C., Graff, G. L., ... & Xia, G. (2013). Materials science and materials chemistry for large scale electrochemical energy storage: from transportation to electrical grid. *Advanced Functional Materials*, *23*(8), 929-946.
37. Yang, Z., Zhang, J., Kintner-Meyer, M. C., Lu, X., Choi, D., Lemmon, J. P., & Liu, J. (2011). Electrochemical energy storage for green grid. *Chemical Reviews*, *111*(5), 3577-3613.
38. Valøen, L. O., & Shoesmith, M. I. (2007, November). The effect of PHEV and HEV duty cycles on battery and battery pack performance. In *PHEV 2007 Conference* (pp. 4-5).
39. Hall, P. J., & Bain, E. J. (2008). Energy-storage technologies and electricity generation. *Energy Policy*, *36*(12), 4352-4355.
40. Grosjean, C., Miranda, P. H., Perrin, M., & Poggi, P. (2012). Assessment of world lithium resources and consequences of their geographic distribution on the expected development of the electric vehicle industry. *Renewable and Sustainable Energy Reviews*, *16*(3), 1735-1744.
41. Forbes: "China And The U.S. Heading For A Showdown In An Australian Lithium Mine" <https://www.forbes.com/sites/timtreadgold/2019/06/24/china-and-the-u-s-heading-for-a-showdown-in-an-australian-lithium-mine/#3e0e37811c04> (accessed December 2019)
42. CNN Business: "The rare earths industry can weather any Chinese trade battle" <https://edition.cnn.com/2019/07/23/perspectives/rare-earths-china-argentina-trade-war/index.html> (accessed December 2019)
43. Dorella, G., & Mansur, M. B. (2007). A study of the separation of cobalt from spent Li-ion battery residues. *Journal of Power Sources*, *170*(1), 210-215.
44. Financial Times: "Congo, child labour and your electric car" <https://www.ft.com/content/c6909812-9ce4-11e9-9c06-a4640c9feebb> (accessed December 2019)
45. Li, X., Zhang, H., Mai, Z., Zhang, H., & Vankelecom, I. (2011). Ion exchange membranes for vanadium redox flow battery (VRB) applications. *Energy & Environmental Science*, *4*(4), 1147-1160.
46. Parasuraman, A., Lim, T. M., Menictas, C., & Skyllas-Kazacos, M. (2013). Review of material research and development for vanadium redox flow battery applications. *Electrochimica Acta*, *101*, 27-40.
47. BloombergNEF: "A Behind the Scenes Take on Lithium-ion Battery Prices" <https://about.bnef.com/blog/behind-scenes-take-lithium-ion-battery-prices/> (accessed December 2019)
48. Zhang, M., Moore, M., Watson, J. S., Zawodzinski, T. A., & Counce, R. M. (2012). Capital cost sensitivity analysis of an all-vanadium redox-flow battery. *Journal of The Electrochemical Society*, *159*(8), A1183-A1188.
49. Turner, J. A. (2004). Sustainable hydrogen production. *Science*, *305*(5686), 972-974.
50. Steward, D., Saur, G., Penev, M., & Ramsden, T. (2009). *Lifecycle cost analysis of hydrogen versus other technologies for electrical energy storage* (No. NREL/TP-560-46719). National Renewable Energy Lab.(NREL), Golden, CO (United States).
51. Strategic Analysis Inc. "2019 DOE Hydrogen and Fuel Cells Program Review" https://www.hydrogen.energy.gov/pdfs/review19/st100_james_2019_o.pdf (accessed December 2019)
52. Nel Group "Nel ASA Q3 2017" <https://www.fch.europa.eu/sites/default/files/S2.3-J.A.L%C3%B6kke%2CNel.pdf> (accessed December 2019)

-
53. Ramachandran, R., & Menon, R. K. (1998). An overview of industrial uses of hydrogen. *International Journal of Hydrogen Energy*, 23(7), 593-598.
54. E&E Publishing. "Sinking Finances Throw Iceland's 'Hydrogen-Based Economy' Into the Freezer" <https://archive.nytimes.com/www.nytimes.com/cwire/2009/07/01/01climatewire-sinking-finances-throw-icelands-hydrogen-bas-47371.html?pagewanted=all> (accessed December 2019)
55. Árnason, B., & Sigfússon, T. I. (2000). Iceland—a future hydrogen economy. *International Journal of Hydrogen Energy*, 25(5), 389-394.
56. Grahame, A., & Aguey-Zinsou, K. F. (2018). Properties and Applications of Metal (M) dodecahydro-closo-dodecaborates (Mn= 1, 2B12H12) and Their Implications for Reversible Hydrogen Storage in the Borohydrides. *Inorganics*, 6(4), 106.
57. Stojić, D. L., Marčeta, M. P., Sovilj, S. P., & Miljanić, Š. S. (2003). Hydrogen generation from water electrolysis—possibilities of energy saving. *Journal of Power Sources*, 118(1-2), 315-319.
58. Collodi, G., & Wheeler, F. (2010). Hydrogen production via steam reforming with CO2 capture. *Chemical Engineering Transactions*, 19, 37-42.
59. Hug, W., Divisek, J., Mergel, J., Seeger, W., & Steeb, H. (1992). Highly efficient advanced alkaline electrolyzer for solar operation. *International Journal of Hydrogen Energy*, 17(9), 699-705.
60. Ulleberg, Ø. (2003). Modeling of advanced alkaline electrolyzers: a system simulation approach. *International Journal of Hydrogen Energy*, 28(1), 21-33.
61. Boudries, R. (2018). Techno-economic study of hydrogen production using CSP technology. *International Journal of Hydrogen Energy*, 43(6), 3406-3417.
62. Mohammadi, A., & Mehrpooya, M. (2019). Thermodynamic and economic analyses of hydrogen production system using high temperature solid oxide electrolyzer integrated with parabolic trough collector. *Journal of Cleaner Production*, 212, 713-726.
63. Siracusano, S., Di Blasi, A., Baglio, V., Brunaccini, G., Briguglio, N., Stassi, A., ... & Aricò, A. S. (2011). Optimization of components and assembling in a PEM electrolyzer stack. *International Journal of Hydrogen Energy*, 36(5), 3333-3339.
64. Millet, P., Ngameni, R., Grigoriev, S. A., Mbemba, N., Brisset, F., Ranjbari, A., & Etiévant, C. (2010). PEM water electrolyzers: from electrocatalysis to stack development. *International Journal of Hydrogen Energy*, 35(10), 5043-5052.
65. Ayers, K. E., Renner, J. N., Danilovic, N., Wang, J. X., Zhang, Y., Maric, R., & Yu, H. (2016). Pathways to ultra-low platinum group metal catalyst loading in proton exchange membrane electrolyzers. *Catalysis Today*, 262, 121-132.
66. Kokoh, K. B., Mayousse, E., Napporn, T. W., Servat, K., Guillet, N., Soyez, E., ... & Paul-Joseph, J. (2014). Efficient multi-metallic anode catalysts in a PEM water electrolyzer. *International Journal of Hydrogen Energy*, 39(5), 1924-1931.
67. Jinnouchi, R., & Asahi, R. (2017). Predicting catalytic activity of nanoparticles by a DFT-aided machine-learning algorithm. *The Journal of Physical Chemistry Letters*, 8(17), 4279-4283.
68. Vasić, D. D., Pašti, I. A., & Mentus, S. V. (2013). DFT study of platinum and palladium overlayers on tungsten carbide: Structure and electrocatalytic activity toward hydrogen oxidation/evolution reaction. *International Journal of Hydrogen Energy*, 38(12), 5009-5018.
69. Artrith, N., & Kolpak, A. M. (2014). Understanding the composition and activity of electrocatalytic nanoalloys in aqueous solvents: A combination of DFT and accurate neural network potentials. *Nano Letters*, 14(5), 2670-2676.

-
70. Shao, M., Liu, P., Zhang, J., & Adzic, R. (2007). Origin of enhanced activity in palladium alloy electrocatalysts for oxygen reduction reaction. *The Journal of Physical Chemistry B*, *111*(24), 6772-6775.
71. Sha, Y., Yu, T. H., Merinov, B. V., & Goddard III, W. A. (2014). DFT Prediction of oxygen reduction reaction on palladium–copper alloy surfaces. *ACS Catalysis*, *4*(4), 1189-1197.
72. Birss, V. I., & Damjanovic, A. (1983). A study of the anomalous pH dependence of the oxygen evolution reaction at platinum electrodes in acid solutions. *Journal of the Electrochemical Society*, *130*(8), 1694-1699.
73. Sheng, W., Gasteiger, H. A., & Shao-Horn, Y. (2010). Hydrogen oxidation and evolution reaction kinetics on platinum: acid vs alkaline electrolytes. *Journal of The Electrochemical Society*, *157*(11), B1529-B1536.
74. Xue, S., Garlyyev, B., Watzel, S., Liang, Y., Fichtner, J., Pohl, M. D., & Bandarenka, A. S. (2018). Influence of Alkali Metal Cations on the Hydrogen Evolution Reaction Activity of Pt, Ir, Au, and Ag Electrodes in Alkaline Electrolytes. *ChemElectroChem*, *5*(17), 2326-2329.
75. Skúlason, E., Tripkovic, V., Björketun, M. E., Gudmundsdottir, S., Karlberg, G., Rossmeisl, J., ... & Nørskov, J. K. (2010). Modeling the electrochemical hydrogen oxidation and evolution reactions on the basis of density functional theory calculations. *The Journal of Physical Chemistry C*, *114*(42), 18182-18197.
76. He, Z. D., Wei, J., Chen, Y. X., Santos, E., & Schmickler, W. (2017). Hydrogen evolution at Pt (111)–activation energy, frequency factor and hydrogen repulsion. *Electrochimica Acta*, *255*, 391-395.
77. Zalitis, C. M., Sharman, J., Wright, E., & Kucernak, A. R. (2015). Properties of the hydrogen oxidation reaction on Pt/C catalysts at optimised high mass transport conditions and its relevance to the anode reaction in PEFCs and cathode reactions in electrolyzers. *Electrochimica Acta*, *176*, 763-776.
78. Kucernak, A. R., & Zalitis, C. (2016). General models for the electrochemical hydrogen oxidation and hydrogen evolution reactions: theoretical derivation and experimental results under near mass-transport free conditions. *The Journal of Physical Chemistry C*, *120*(20), 10721-10745.
79. Halck, N. B., Petrykin, V., Krtil, P., & Rossmeisl, J. (2014). Beyond the volcano limitations in electrocatalysis–oxygen evolution reaction. *Physical Chemistry Chemical Physics*, *16*(27), 13682-13688.
80. Kimmel, Y. C., Yang, L., Kelly, T. G., Rykov, S. A., & Chen, J. G. (2014). Theoretical prediction and experimental verification of low loading of platinum on titanium carbide as low-cost and stable electrocatalysts. *Journal of Catalysis*, *312*, 216-220.
81. Janse van Rensburg, W., Steynberg, P. J., Meyer, W. H., Kirk, M. M., & Forman, G. S. (2004). DFT prediction and experimental observation of substrate-induced catalyst decomposition in ruthenium-catalyzed olefin metathesis. *Journal of the American Chemical Society*, *126*(44), 14332-14333.
82. Čolić, V., Tymoczko, J., Maljusch, A., Ganassin, A., Schuhmann, W., & Bandarenka, A. S. (2015). Experimental aspects in benchmarking of the electrocatalytic activity. *ChemElectroChem*, *2*(1), 143-149.
83. Wei, C., Rao, R. R., Peng, J., Huang, B., Stephens, I. E., Risch, M., ... & Shao-Horn, Y. (2019). Recommended Practices and Benchmark Activity for Hydrogen and Oxygen Electrocatalysis in Water Splitting and Fuel Cells. *Advanced Materials*, 1806296.
84. Jung, S., McCrory, C. C., Ferrer, I. M., Peters, J. C., & Jaramillo, T. F. (2016). Benchmarking nanoparticulate metal oxide electrocatalysts for the alkaline water oxidation reaction. *Journal of Materials Chemistry A*, *4*(8), 3068-3076.
85. Rudi, S., Cui, C., Gan, L., & Strasser, P. (2014). Comparative study of the electrocatalytically active surface areas (ECSAs) of Pt alloy nanoparticles evaluated by H upd and CO-stripping voltammetry. *Electrocatalysis*, *5*(4), 408-418.

-
86. Xu, H., Cao, J., Shan, C., Wang, B., Xi, P., Liu, W., & Tang, Y. (2018). MOF-Derived Hollow CoS Decorated with CeOx Nanoparticles for Boosting Oxygen Evolution Reaction Electrocatalysis. *Angewandte Chemie International Edition*, 57(28), 8654-8658.
87. Tao, Z., Wang, T., Wang, X., Zheng, J., & Li, X. (2016). MOF-derived noble metal free catalysts for electrochemical water splitting. *ACS Applied Materials & Interfaces*, 8(51), 35390-35397.
88. Binniger, T., Fabbri, E., Kötz, R., & Schmidt, T. J. (2014). Determination of the electrochemically active surface area of metal-oxide supported platinum catalyst. *Journal of The Electrochemical Society*, 161(3), H121-H128.
89. Watzele, S., & Bandarenka, A. S. (2016). Quick determination of electroactive surface area of some oxide electrode materials. *Electroanalysis*, 28(10), 2394-2399.
90. Watzele, S., Hauenstein, P., Liang, Y., Xue, S., Fichtner, J., Garlyyev, B., ... & Bandarenka, A. S. (2019). Determination of Electroactive Surface Area of Ni-, Co-, Fe-, and Ir-Based Oxide Electrocatalysts. *ACS Catalysis*, 9(10), 9222-9230.
91. Trasatti, S., & Petrii, O. A. (1991). Real surface area measurements in electrochemistry. *Pure and Applied Chemistry*, 63(5), 711-734.
92. McCrory, C. C.; Jung, S.; Peters, J. C.; Jaramillo, T. F. Benchmarking heterogeneous electrocatalysts for the oxygen evolution reaction. *Journal of the American Chemical Society*, 2013, 135, 16977-16987
93. Florida Solar Energy Center "Hydrogen Basics - Production" <http://www.fsec.ucf.edu/en/>. (accessed December 2019)
94. Hupp, J. T., Liu, H. Y., Farmer, J. K., Gennett, T., & Weaver, M. J. (1984). The prediction of electrochemical reactivities from contemporary theory: some comparisons with experiment. *Journal of Electroanalytical Chemistry and Interfacial Electrochemistry*, 168(1-2), 313-334.
95. Ganassin, A., Maljusch, A., Colic, V., Spanier, L., Brandl, K., Schuhmann, W., & Bandarenka, A. (2016). Benchmarking the performance of thin-film oxide electrocatalysts for gas evolution reactions at high current densities. *ACS Catalysis*, 6(5), 3017-3024.
96. Wiederhorn, S. M., & Johnson, H. (1973). Effect of electrolyte pH on crack propagation in glass. *Journal of the American Ceramic Society*, 56(4), 192-197.
97. Berzelius, J. J. (1836). Quelques Idées sur une nouvelle Force agissant dans les Combinaisons des Corps Organiques. *Annales de Chimie*, 61, 146-151.
98. Ostwald, W. (1902) Catalysis1, *Nature*, 65, 522
99. Chorkendorff, I., & Niemantsverdriet, J. W. (2017) Concepts of modern catalysis and kinetics. *John Wiley & Sons*.
100. Appleby, A. J. (1971). Electrocatalysis and fuel cells. *Catalysis Reviews*, 4(1), 221-244.
101. Sabatier, P. (1902). New synthesis of methane. *Comptes Rendus*, 134, 514-516.
102. Medford, A. J., Vojvodic, A., Hummelshøj, J. S., Voss, J., Abild-Pedersen, F., Studt, F., ... & Nørskov, J. K. (2015). From the Sabatier principle to a predictive theory of transition-metal heterogeneous catalysis. *Journal of Catalysis*, 328, 36-42.
103. Taylor, H. S. (1925). A theory of the catalytic surface. *Proceedings of the Royal Society of London. Series A, Containing Papers of a Mathematical and Physical Character*, 108(745), 105-111.
104. Balandin, A. A. (1969). Modern state of the multiplet theor of heterogeneous catalysis. In *Advances in catalysis* (Vol. 19, pp. 1-210). Academic Press.

-
105. Bligaard, T., Nørskov, J. K., Dahl, S., Matthiesen, J., Christensen, C. H., & Sehested, J. (2004). The Brønsted–Evans–Polanyi relation and the volcano curve in heterogeneous catalysis. *Journal of Catalysis*, 224(1), 206-217.
106. Trasatti, S. (1972). Work function, electronegativity, and electrochemical behaviour of metals: III. Electrolytic hydrogen evolution in acid solutions. *Journal of Electroanalytical Chemistry and Interfacial Electrochemistry*, 39(1), 163-184.
107. Koper, M. T. (2011). Thermodynamic theory of multi-electron transfer reactions: Implications for electrocatalysis. *Journal of Electroanalytical Chemistry*, 660(2), 254-260.
108. Abild-Pedersen, F., Greeley, J., Studt, F., Rossmeisl, J., Munter, T. R., Moses, P. G., ... & Nørskov, J. K. (2007). Scaling properties of adsorption energies for hydrogen-containing molecules on transition-metal surfaces. *Physical Review Letters*, 99(1), 016105.
109. Nørskov, J. K., Bligaard, T., Rossmeisl, J., & Christensen, C. H. (2009). Towards the computational design of solid catalysts. *Nature Chemistry*, 1(1), 37.
110. Khorshidi, A., Violet, J., Hashemi, J., & Peterson, A. A. (2018). How strain can break the scaling relations of catalysis. *Nature Catalysis*, 1(4), 263.
111. Calle-Vallejo, F., Krabbe, A., & García-Lastra, J. M. (2017). How covalence breaks adsorption-energy scaling relations and solvation restores them. *Chemical Science*, 8(1), 124-130.
112. Szécsényi, Á., Khramenkova, E., Chernyshov, I. Y., Li, G., Gascon, J., & Pidko, E. A. (2019). Breaking linear scaling relationships with secondary interactions in confined space: a case study of methane oxidation by Fe/ZSM-5 zeolite. *ACS Catalysis*, 9(10), 9276-9284.
113. Darby, M. T., Stamatakis, M., Michaelides, A., & Sykes, E. C. H. (2018). Lonely atoms with special gifts: Breaking linear scaling relationships in heterogeneous catalysis with single-atom alloys. *The Journal of Physical Chemistry Letters*, 9(18), 5636-5646.
114. Fernández, E. M., Moses, P. G., Toftelund, A., Hansen, H. A., Martínez, J. I., Abild-Pedersen, F., ... & Nørskov, J. K. (2008). Scaling relationships for adsorption energies on transition metal oxide, sulfide, and nitride surfaces. *Angewandte Chemie International Edition*, 47(25), 4683-4686.
115. Hamann, C. H., Hammett, A., & Vielstich, W., *Electrochemistry*, (2007). 2nd edition, Wiley-VCH, Weinheim
116. Davy, H. (1839). The Collected Works of Sir Humphry Davy (Vol. 1). *Smith, Elder.*, London
117. Voigt, J. H. (1800). *Magazin für den neuesten Zustand der Naturkunde mit Rücksicht auf die dazugehörigen Hilfswissenschaften.* Tafel V https://zs.thulb.uni-jena.de/receive/jportal_jpvolume_00079148
118. Heinrich Schellen (1884) Magneto-electric and Dynamo-electric Machines, 3rd Ed., Vol.1, D. Van Nostrand, New York, p.218, fig.124
119. Thomson, Sylvanus P. (1888), *Dynamo-electric machinery: a manual for students of electrotechnics.* London: E. & F.N. Spon. p. 140
120. Kreuter, W., & Hofmann, H. (1998). Electrolysis: the important energy transformer in a world of sustainable energy. *International Journal of Hydrogen Energy*, 23(8), 661-666.
121. Carmo, M., Fritz, D. L., Mergel, J., & Stolten, D. (2013). A comprehensive review on PEM water electrolysis. *International Journal of Hydrogen Energy*, 38(12), 4901-4934.
122. Medina, P., & Santarelli, M. (2010). Analysis of water transport in a high pressure PEM electrolyzer. *International Journal of Hydrogen Energy*, 35(11), 5173-5186.

-
123. Grigoriev, S. A., Porembsky, V. I., & Fateev, V. N. (2006). Pure hydrogen production by PEM electrolysis for hydrogen energy. *International Journal of Hydrogen Energy*, 31(2), 171-175.
124. Grigoriev, S. A., Millet, P., Dzhus, K. A., Middleton, H., Saetre, T. O., & Fateev, V. N. (2010). Design and characterization of bi-functional electrocatalytic layers for application in PEM unitized regenerative fuel cells. *International Journal of Hydrogen Energy*, 35(10), 5070-5076.
125. Selamet, Ö. F., Becerikli, F., Mat, M. D., & Kaplan, Y. (2011). Development and testing of a highly efficient proton exchange membrane (PEM) electrolyzer stack. *International Journal of Hydrogen Energy*, 36(17), 11480-11487.
126. Ito, H., Maeda, T., Nakano, A., & Takenaka, H. (2011). Properties of Nafion membranes under PEM water electrolysis conditions. *International Journal of Hydrogen Energy*, 36(17), 10527-10540.
127. Ito, H., Maeda, T., Nakano, A., Hwang, C. M., Ishida, M., Kato, A., & Yoshida, T. (2012). Experimental study on porous current collectors of PEM electrolyzers. *International Journal of Hydrogen Energy*, 37(9), 7418-7428.
128. Lettenmeier, P., Kolb, S., Burggraf, F., Gago, A. S., & Friedrich, K. A. (2016). Towards developing a backing layer for proton exchange membrane electrolyzers. *Journal of Power Sources*, 311, 153-158.
129. Buttler, A., & Spliethoff, H. (2018). Current status of water electrolysis for energy storage, grid balancing and sector coupling via power-to-gas and power-to-liquids: A review. *Renewable and Sustainable Energy Reviews*, 82, 2440-2454.
130. Schalenbach, M., Zeradjanin, A. R., Kasian, O., Cherevko, S., & Mayrhofer, K. J. (2018). A perspective on low-temperature water electrolysis—challenges in alkaline and acidic technology. *International Journal of Electrochemical Science*, 13, 1173-1226..
131. Marini, S., Salvi, P., Nelli, P., Pesenti, R., Villa, M., Berrettoni, M., ... & Kirov, Y. (2012). Advanced alkaline water electrolysis. *Electrochimica Acta*, 82, 384-391.
132. Manabe, A., Kashiwase, M., Hashimoto, T., Hayashida, T., Kato, A., Hirao, K., ... & Nagashima, I. (2013). Basic study of alkaline water electrolysis. *Electrochimica Acta*, 100, 249-256.
133. Marini, S., Salvi, P., Nelli, P., Pesenti, R., Villa, M., Berrettoni, M., ... & Kirov, Y. (2012). Advanced alkaline water electrolysis. *Electrochimica Acta*, 82, 384-391.
134. Brisse, A., Schefold, J., & Zahid, M. (2008). High temperature water electrolysis in solid oxide cells. *International Journal of Hydrogen Energy*, 33(20), 5375-5382.
135. Giraldo, M. R., François, J. L., & Martin-del-Campo, C. (2015). Life cycle assessment of hydrogen production from a high temperature electrolysis process coupled to a high temperature gas nuclear reactor. *International Journal of Hydrogen Energy*, 40(10), 4019-4033.
136. Hino, R., Haga, K., Aita, H., & Sekita, K. (2004). R&D on hydrogen production by high-temperature electrolysis of steam. *Nuclear Engineering and Design*, 233(1-3), 363-375.
137. Myland, J. C., & Oldham, K. B. (2000). Uncompensated resistance. 1. The effect of cell geometry. *Analytical Chemistry*, 72(17), 3972-3980.
138. Bruggeman, V. D. (1935). Berechnung verschiedener physikalischer Konstanten von heterogenen Substanzen. I. Dielektrizitätskonstanten und Leitfähigkeiten der Mischkörper aus isotropen Substanzen. *Annalen der Physik*, 416(7), 636-664.
139. Ward, C. A., Balakrishnan, A., & Hooper, F. C. (1970). On the thermodynamics of nucleation in weak gas-liquid solutions. *Journal of Basic Engineering*, 92(4), 695-701.

-
140. Westerheide, D. E., & Westwater, J. W. (1961). Isothermal growth of hydrogen bubbles during electrolysis. *AIChE Journal*, 7(3), 357-362.
141. Clark, H., Strenge, P. S., & Westwater, J. W. (1959). Active sites for nucleate boiling. *Chemical Engineering Progress*, 55.
142. Cole, R. (1974). Boiling nucleation. In *Advances in Heat Transfer*. Elsevier. 10, 85-166
143. Janssen, L. J. J., & Hoogland, J. G. (1973). The effect of electrolytically evolved gas bubbles on the thickness of the diffusion layer—II. *Electrochimica Acta*, 18(8), 543-550.
144. Watzele, S., Liang, Y., & Bandarenka, A. S. (2018). Intrinsic activity of some oxygen and hydrogen evolution reaction electrocatalysts under industrially relevant conditions. *ACS Applied Energy Materials*, 1(8), 4196-4202.
145. Tench, D., & Warren, L. F. (1983). Electrodeposition of conducting transition metal oxide/hydroxide films from aqueous solution. *Journal of The Electrochemical Society*, 130(4), 869-872
146. Subbaraman, R., Tripkovic, D., Strmcnik, D., Chang, K. C., Uchimura, M., Paulikas, A. P., ... & Markovic, N. M. (2011). Enhancing hydrogen evolution activity in water splitting by tailoring Li+-Ni (OH) 2-Pt interfaces. *Science*, 334(6060), 1256-1260.
147. El-Shafei, A. A. (1998). Study of nickel upd at a polycrystalline Pt electrode and its influence on HCOOH oxidation in acidic and nearly neutral media. *Journal of Electroanalytical Chemistry*, 447(1-2), 81-89.
148. Chatenet, M., Faure, R., & Soldo-Olivier, Y. (2005). Nickel-underpotential deposition on Pt (1 1 0) in sulphate-containing media. *Journal of Electroanalytical Chemistry*, 580(2), 275-283.
149. Li, W., Watzele, S., El-Sayed, H. A., Liang, Y., Kieslich, G., Bandarenka, A. S., ... & Fischer, R. A. (2019). Unprecedented High Oxygen Evolution Activity of Electrocatalysts Derived from Surface-Mounted Metal–Organic Frameworks. *Journal of the American Chemical Society*, 141(14), 5926-5933.
150. Bondarenko, A. S. (2012) Analysis of large experimental datasets in electrochemical impedance spectroscopy. *Analytica Chimica Acta*, 743(41)
- 151 Bandarenka, A. S. (2013) Development of hybrid algorithms for EIS data fitting. *Lecture Notes on Impedance Spectroscopy*, 4(29)
152. Kumsa, D. W., Bhadra, N., Hudak, E. M., Kelley, S. C., Untereker, D. F., & Mortimer, J. T. (2016). Electron transfer processes occurring on platinum neural stimulating electrodes: a tutorial on the $i(V_e)$ profile. *Journal of Neural Engineering*, 13(5), 052001.
153. Orazem, M. E., & Tribollet, B. (2017). *Electrochemical impedance spectroscopy*. John Wiley & Sons.
154. Siegbahn, K. (1982). Electron spectroscopy for atoms, molecules, and condensed matter. *Reviews of Modern Physics*, 54(3), 709.
155. Siegbahn, K., & Edvarson, K. (1956). β -Ray Spectroscopy in the Precision Range of 1: 105. *Nuclear Physics*, 1(3), 137-159.
156. Hüfner, S. (2013). *Photoelectron spectroscopy: principles and applications*. Springer Science & Business Media.
157. Binnig, G., Quate, C. F., & Gerber, C. (1986). Atomic force microscope. *Physical Review Letters*, 56(9), 930.

-
158. Wolter, O., Bayer, T., & Greschner, J. (1991). Micromachined silicon sensors for scanning force microscopy. *Journal of Vacuum Science & Technology B: Microelectronics and Nanometer Structures Processing, Measurement, and Phenomena*, 9(2), 1353-1357.
159. Marcus, R. B., Ravi, T. S., Gmitter, T., Chin, K., Liu, D., Orvis, W. J., ... & Trujillo, J. (1990). Formation of silicon tips with < 1 nm radius. *Applied Physics Letters*, 56(3), 236-238.
160. Maver, U., Maver, T., Peršin, Z., Mozetič, M., Vesel, A., Gaberšček, M., & Stana-Kleinschek, K. (2013). Polymer characterization with the atomic force microscope. *Polymer Science*, 4.
161. Haugstad, G. (2012). *Atomic force microscopy: understanding basic modes and advanced applications*. John Wiley & Sons.
162. Brunauer, S., Emmett, P. H., & Teller, E. (1938). Adsorption of gases in multimolecular layers. *Journal of the American Chemical Society*, 60(2), 309-319.
163. Adams, C. R., Benesi, H. A., Curtis, R. M., & Meisenheimer, R. G. (1962). Particle size determination of supported catalytic metals: Platinum on silica gel. *Journal of Catalysis*, 1(4), 336-344.
164. Lustenberger, P., Rohrer, H., Christoph, R., & Siegenthaler, H. (1988). Scanning tunneling microscopy at potential controlled electrode surfaces in electrolytic environment. *Journal of Electroanalytical Chemistry and Interfacial Electrochemistry*, 243(1), 225-235.
165. Parsons, R., & Zobel, F. R. (1965). The interphase between mercury and aqueous sodium dihydrogen phosphate. *Journal of Electroanalytical Chemistry (1959)*, 9(5-6), 333-348.
166. Breiter, M. W. (1977). Dissolution and adsorption of hydrogen at smooth Pd wires at potentials of the alpha phase in sulfuric acid solution. *Journal of Electroanalytical Chemistry and Interfacial Electrochemistry*, 81(2), 275-284.
167. Motoo, S., & Furuya, N. (1984). Hydrogen and oxygen adsorption on Ir (111),(100) and (110) planes. *Journal of Electroanalytical Chemistry and Interfacial Electrochemistry*, 167(1-2), 309-315.
168. Kita, H., Ye, S., Aramata, A., & Furuya, N. (1990). Adsorption of hydrogen on platinum single crystal electrodes in acid and alkali solutions. *Journal of Electroanalytical Chemistry and Interfacial Electrochemistry*, 295(1-2), 317-331.
169. Biegler, T., Rand, D. A. J., & Woods, R. (1971). Limiting oxygen coverage on platinized platinum; relevance to determination of real platinum area by hydrogen adsorption. *Journal of Electroanalytical Chemistry and Interfacial Electrochemistry*, 29(2), 269-277.
170. Bett, J., Kinoshita, K., Routsis, K., & Stonehart, P. (1973). A comparison of gas-phase and electrochemical measurements for chemisorbed carbon monoxide and hydrogen on platinum crystallites. *Journal of Catalysis*, 29(1), 160-168.
171. Gilman, S. (1967). Multipulse potentiodynamic studies of the adsorption of carbon monoxide and hydrogen on rhodium electrodes. II. Mixed adsorption of carbon monoxide and hydrogen. *The Journal of Physical Chemistry*, 71(13), 4339-4343.
172. Woods, R. (1974). Hydrogen adsorption on platinum, iridium and rhodium electrodes at reduced temperatures and the determination of real surface area. *Journal of Electroanalytical Chemistry and Interfacial Electrochemistry*, 49(2), 217-226.
173. Michri, A. A., Pshenichnikov, A. G., & Burshtein, R. K. (1972). Determination of the true surface of smooth au electrodes. *Elektrokhimiya*, 8(3), 364-366.
174. Angerstein-Kozłowska, H., Conway, B. E., Hamelin, A., & Stoicoviciu, L. (1986). Elementary steps of electrochemical oxidation of single-crystal planes of Au—I. Chemical basis of processes involving geometry of anions and the electrode surfaces. *Electrochimica Acta*, 31(8), 1051-1061.

-
175. Vashkylis, A., & Demontaite, O. (1978). Determination of the Value of the Surface Area of Silver by Electrochemical Precipitation of a Lead Monolayer. *Elektrokhimiya*, 14(8), 1213-1215.
176. Siegenthaler, H., & Jüttner, K. (1984). Voltammetric investigation of lead adsorption on Cu (111) single crystal substrates. *Journal of electroanalytical chemistry and interfacial electrochemistry*, 163(1-2), 327-343.
177. Quiroz, M. A., Meas, Y., Lamy-Pitara, E., & Barbier, J. (1983). Characterization of a ruthenium electrode by underpotential deposition of copper. *Journal of Electroanalytical Chemistry and Interfacial Electrochemistry*, 157(1), 165-174.
178. Alia, S. M., Hurst, K. E., Kocha, S. S., & Pivovar, B. S. (2016). Mercury underpotential deposition to determine iridium and iridium oxide electrochemical surface areas. *Journal of the Electrochemical Society*, 163(11), F3051-F3056.
179. Bett, J., Kinoshita, K., Routsis, K., & Stonehart, P. (1973). A comparison of gas-phase and electrochemical measurements for chemisorbed carbon monoxide and hydrogen on platinum crystallites. *Journal of Catalysis*, 29(1), 160-168.
180. Rodriguez, J. F., Mebrahtu, T., & Soriaga, M. P. (1987). Determination of the surface area of gold electrodes by iodine chemisorption. *Journal of Electroanalytical Chemistry and Interfacial Electrochemistry*, 233(1-2), 283-289.
181. Kasian, O., Grote, J. P., Geiger, S., Cherevko, S., & Mayrhofer, K. J. (2018). The common intermediates of oxygen evolution and dissolution reactions during water electrolysis on iridium. *Angewandte Chemie International Edition*, 57(9), 2488-2491.
182. Lasia, A. (2014). Semiconductors and Mott-Schottky Plots. In *Electrochemical Impedance Spectroscopy and its Applications* (pp. 251-255). Springer, New York, NY.
183. Harrington, D. A., & Conway, B. E. (1987). ac Impedance of Faradaic reactions involving electrosorbed intermediates—I. Kinetic theory. *Electrochimica Acta*, 32(12), 1703-1712.
184. Biesinger, M. C., Lau, L. W., Gerson, A. R., & Smart, R. S. C. (2012). The role of the Auger parameter in XPS studies of nickel metal, halides and oxides. *Physical Chemistry Chemical Physics*, 14(7), 2434-2442.
185. Casella, I. G., & Guascito, M. R. (1999). Anodic electrodeposition of conducting cobalt oxyhydroxide films on a gold surface. XPS study and electrochemical behaviour in neutral and alkaline solution. *Journal of Electroanalytical Chemistry*, 476(1), 54-63.
186. Mansour, A. N., & Brizzolara, R. A. (1996). Iron XPS Spectra from the Physical Electronics Model 5400 Spectrometer. *Surface Science Spectra*, 4(2), 175-179.
187. Tan, B. J., Klabunde, K. J., & Sherwood, P. M. (1990). X-ray photoelectron spectroscopy studies of solvated metal atom dispersed catalysts. Monometallic iron and bimetallic iron-cobalt particles on alumina. *Chemistry of Materials*, 2(2), 186-191.
188. Mills, P., & Sullivan, J. L. (1983). A study of the core level electrons in iron and its three oxides by means of X-ray photoelectron spectroscopy. *Journal of Physics D: Applied Physics*, 16(5), 723.
189. Andersson, S. L. T., & Howe, R. F. (1989). An X-ray photoelectron study of metal clusters in zeolites. *The Journal of Physical Chemistry*, 93(12), 4913-4920.
190. Friebel, D., Louie, M. W., Bajdich, M., Sanwald, K. E., Cai, Y., Wise, A. M., ... & Davis, R. C. (2015). Identification of highly active Fe sites in (Ni, Fe) OOH for electrocatalytic water splitting. *Journal of the American Chemical Society*, 137(3), 1305-1313.
191. Dionigi, F., & Strasser, P. (2016). NiFe-Based (Oxy) hydroxide Catalysts for Oxygen Evolution Reaction in Non-Acidic Electrolytes. *Advanced Energy Materials*, 6(23), 1600621.

-
192. Freakley, S. J., Ruiz-Esquius, J., & Morgan, D. J. (2017). The X-ray photoelectron spectra of Ir, IrO₂ and IrCl₃ revisited. *Surface and Interface Analysis*, 49(8), 794-799.
193. Pfeifer, V., Jones, T. E., Velasco Vélez, J. J., Massué, C., Arrigo, R., Teschner, D., ... & Hashagen, M. (2016). The electronic structure of iridium and its oxides. *Surface and Interface Analysis*, 48(5), 261-273.
194. Moreau, M., Valentin, P., Vidal-Madjar, C., Lin, B. C., & Guiochon, G. (1991). Adsorption isotherm model for multicomponent adsorbate—adsorbate interactions. *Journal of Colloid and Interface Science*, 141(1), 127-136.
195. El-Sayed, H. A., Weiß, A., Olbrich, L. F., Putro, G. P., & Gasteiger, H. A. (2019). OER Catalyst Stability Investigation Using RDE Technique: A Stability Measure or an Artifact?. *Journal of the Electrochemical Society*, 166(8), F458-F464.
196. Lázaro, M. J., Calvillo, L., Celorrio, V., Pardo, J. I., Perathoner, S., & Moliner, R. (2011). Study and application of carbon black Vulcan XC-72R in polymeric electrolyte fuel cells. *Carbon black: production, properties and uses*, 41.
197. Rossmeisl, J., Logadottir, A., & Nørskov, J. K. (2005). Electrolysis of water on (oxidized) metal surfaces. *Chemical Physics*, 319(1-3), 178-184.
198. Zhao, S., Yu, H., Maric, R., Danilovic, N., Capuano, C. B., Ayers, K. E., & Mustain, W. E. (2015). Calculating the electrochemically active surface area of iridium oxide in operating proton exchange membrane electrolyzers. *Journal of the Electrochemical Society*, 162(12), F1292-F1298.
199. Durst, J., Siebel, A., Simon, C., Hasche, F., Herranz, J., & Gasteiger, H. A. (2014). New insights into the electrochemical hydrogen oxidation and evolution reaction mechanism. *Energy & Environmental Science*, 7(7), 2255-2260.
200. Thomas RECORDING “Electrochemical Microelectrodes”
<https://www.thomasrecording.com/products/electrochemical-products/electrochemical-microelectrodes.html>
201. Gin, S., Jollivet, P., Fournier, M., Berthon, C., Wang, Z., Mitroshkov, A., ... & Ryan, J. V. (2015). The fate of silicon during glass corrosion under alkaline conditions: a mechanistic and kinetic study with the international simple glass. *Geochimica et Cosmochimica Acta*, 151, 68-85..
202. Molchanov, V. S., & Prikhidko, N. E. (1957). Corrosion of silicate glasses by alkaline solutions. *Russian Chemical Bulletin*, 6(10), 1179-1184.
203. Etienne, M., Moulin, J. P., & Gourhand, S. (2013). Accurate control of the electrode shape for high resolution shearforce regulated SECM. *Electrochimica Acta*, 110, 16-21.
204. Etienne, M., Dossot, M., Grausem, J., & Herzog, G. (2014). Combined Raman microspectrometer and shearforce regulated SECM for corrosion and self-healing analysis. *Analytical Chemistry*, 86(22), 11203-11210.
205. Garlyyev, B., Xue, S., Pohl, M. D., Reinisch, D., & Bandarenka, A. S. (2018). Oxygen Electroreduction at High-Index Pt Electrodes in Alkaline Electrolytes: A Decisive Role of the Alkali Metal Cations. *ACS Omega*, 3(11), 15325-15331.
206. Garcia, A. C., Touzalin, T., Nieuwland, C., Perini, N., & Koper, M. T. (2019). Enhancement of Oxygen Evolution Activity of Nickel Oxyhydroxide by Electrolyte Alkali Cations. *Angewandte Chemie International Edition*, 58(37), 12999-13003.
207. Shen, J. Q., Liao, P. Q., Zhou, D. D., He, C. T., Wu, J. X., Zhang, W. X., ... & Chen, X. M. (2017). Modular and stepwise synthesis of a hybrid metal–organic framework for efficient electrocatalytic oxygen evolution. *Journal of the American Chemical Society*, 139(5), 1778-1781.

-
208. Zhao, S., Wang, Y., Dong, J., He, C. T., Yin, H., An, P., ... & Lv, J. (2016). Ultrathin metal–organic framework nanosheets for electrocatalytic oxygen evolution. *Nature Energy*, *1*(12), 16184.
209. Li, F. L., Shao, Q., Huang, X., & Lang, J. P. (2018). Nanoscale trimetallic metal–organic frameworks enable efficient oxygen evolution electrocatalysis. *Angewandte Chemie International Edition*, *57*(7), 1888-1892.
210. Zhang, B., Zheng, X., Voznyy, O., Comin, R., Bajdich, M., García-Melchor, M., ... & de Arquer, F. P. G. (2016). Homogeneously dispersed multimetal oxygen-evolving catalysts. *Science*, *352*(6283), 333-337.
211. Liardet, L., & Hu, X. (2017). Amorphous cobalt vanadium oxide as a highly active electrocatalyst for oxygen evolution. *ACS Catalysis*, *8*(1), 644-650.
212. Liu, K., Zhang, C., Sun, Y., Zhang, G., Shen, X., Zou, F., ... & Miller, J. T. (2017). High-performance transition metal phosphide alloy catalyst for oxygen evolution reaction. *ACS Nano*, *12*(1), 158-167.
213. Dong, C., Kou, T., Gao, H., Peng, Z., & Zhang, Z. (2018). Eutectic-Derived Mesoporous Ni-Fe-O Nanowire Network Catalyzing Oxygen Evolution and Overall Water Splitting. *Advanced Energy Materials*, *8*(5), 1701347.
214. Lu, X. F., Gu, L. F., Wang, J. W., Wu, J. X., Liao, P. Q., & Li, G. R. (2017). Bimetal-organic framework derived CoFe₂O₄/C porous hybrid nanorod arrays as high-performance electrocatalysts for oxygen evolution reaction. *Advanced Materials*, *29*(3), 1604437.
215. Yu, L., Yang, J. F., Guan, B. Y., Lu, Y., & Lou, X. W. (2018). Hierarchical Hollow Nanoprisms Based on Ultrathin Ni-Fe Layered Double Hydroxide Nanosheets with Enhanced Electrocatalytic Activity towards Oxygen Evolution. *Angewandte Chemie International Edition*, *57*(1), 172-176.
216. Fabbri, E., Nachtegaal, M., Binninger, T., Cheng, X., Kim, B. J., Durst, J., ... & Pertoso, M. (2017). Dynamic surface self-reconstruction is the key of highly active perovskite nano-electrocatalysts for water splitting. *Nature Materials*, *16*(9), 925.
217. Ma, T. Y., Dai, S., Jaroniec, M., & Qiao, S. Z. (2014). Metal–organic framework derived hybrid Co₃O₄-carbon porous nanowire arrays as reversible oxygen evolution electrodes. *Journal of the American Chemical Society*, *136*(39), 13925-13931.
218. Weng, B., Xu, F., Wang, C., Meng, W., Grice, C. R., & Yan, Y. (2017). A layered Na_{1-x}Ni_yFe_{1-y}O₂ double oxide oxygen evolution reaction electrocatalyst for highly efficient water-splitting. *Energy & Environmental Science*, *10*(1), 121-128.
219. Wang, H., Zhu, Q. L., Zou, R., & Xu, Q. (2017). Metal-organic frameworks for energy applications. *Chem*, *2*(1), 52-80.
220. Sheberla, D., Bachman, J. C., Elias, J. S., Sun, C. J., Shao-Horn, Y., & Dincă, M. (2017). Conductive MOF electrodes for stable supercapacitors with high areal capacitance. *Nature Materials*, *16*(2), 220.
221. Talin, A. A., Centrone, A., Ford, A. C., Foster, M. E., Stavila, V., Haney, P., ... & Léonard, F. (2014). Tunable electrical conductivity in metal-organic framework thin-film devices. *Science*, *343*(6166), 66-69.
222. Ma, T. Y., Dai, S., Jaroniec, M., & Qiao, S. Z. (2014). Metal–organic framework derived hybrid Co₃O₄-carbon porous nanowire arrays as reversible oxygen evolution electrodes. *Journal of the American Chemical Society*, *136*(39), 13925-13931.
223. Iwakura, C., Tanaka, M., Nakamatsu, S., Inoue, H., Matsuoka, M., & Furukawa, N. (1995). Electrochemical properties of Ni (Ni+ RuO₂) active cathodes for hydrogen evolution in chlor-alkali electrolysis. *Electrochimica Acta*, *40*(8), 977-982.
224. Bockris, J. M., & Potter, E. C. (1952). The mechanism of the cathodic hydrogen evolution reaction. *Journal of the Electrochemical Society*, *99*(4), 169-186.

-
225. Bockris, J. O. M., Ammar, I. A., & Huq, A. K. M. S. (1957). The mechanism of the hydrogen evolution reaction on platinum, silver and tungsten surfaces in acid solutions. *The Journal of Physical Chemistry*, *61*(7), 879-886.
226. Conway, B. E., & Salomon, M. (1964). Electrochemical reaction orders: Applications to the hydrogen- and oxygen-evolution reactions. *Electrochimica Acta*, *9*(12), 1599-1615.
227. Gao, L., & Conway, B. E. (1994). Absorption and adsorption of H in the H₂ evolution reaction and the effects of co-adsorbed poisons. *Electrochimica Acta*, *39*(11-12), 1681-1693.
228. Sheng, W., Zhuang, Z., Gao, M., Zheng, J., Chen, J. G., & Yan, Y. (2015). Correlating hydrogen oxidation and evolution activity on platinum at different pH with measured hydrogen binding energy. *Nature Communications*, *6*, 5848.
229. Schmidt, T. J., Ross Jr, P. N., & Markovic, N. M. (2002). Temperature dependent surface electrochemistry on Pt single crystals in alkaline electrolytes: Part 2. The hydrogen evolution/oxidation reaction. *Journal of Electroanalytical Chemistry*, *524*, 252-260.
230. Sheng, W., Zhuang, Z., Gao, M., Zheng, J., Chen, J. G., & Yan, Y. (2015). Correlating hydrogen oxidation and evolution activity on platinum at different pH with measured hydrogen binding energy. *Nature Communications*, *6*, 5848.
231. Watzele, S., Fichtner, J., Garlyyev, B., Schwämmlein, J. N., & Bandarenka, A. S. (2018). On the Dominating Mechanism of the Hydrogen Evolution Reaction at Polycrystalline Pt Electrodes in Acidic Media. *ACS Catalysis*, *8*(10), 9456-9462.
232. Kucernak, A. R., & Zalitis, C. (2016). General models for the electrochemical hydrogen oxidation and hydrogen evolution reactions: theoretical derivation and experimental results under near mass-transport free conditions. *The Journal of Physical Chemistry C*, *120*(20), 10721-10745.
233. Dolin, P., & Ershler, B. (1940). The kinetics of discharge and ionization of hydrogen adsorbed at Pt-electrode. *Acta physicochimica. URSS*, *13*, 747.
234. Randles, J. E. B. (1947). Kinetics of rapid electrode reactions. *Discussions of the Faraday Society*, *1*, 11-19.
235. Tymoczko, J., Schuhmann, W., & Bandarenka, A. S. (2013). The constant phase element reveals 2D phase transitions in adsorbate layers at the electrode/electrolyte interfaces. *Electrochemistry Communications*, *27*, 42-45.
236. Tymoczko, J., Colic, V., Bandarenka, A. S., & Schuhmann, W. (2015). Detection of 2D phase transitions at the electrode/electrolyte interface using electrochemical impedance spectroscopy. *Surface Science*, *631*, 81-87.
237. Lang, N. D., Holloway, S., & Nørskov, J. K. (1985). Electrostatic adsorbate-adsorbate interactions: The poisoning and promotion of the molecular adsorption reaction. *Surface Science*, *150*(1), 24-38.
238. Azizian, S., & Volkov, A. G. (2008). A new isotherm for nondissociative gas adsorption with two different states of an adsorbate. *Chemical Physics Letters*, *454*(4-6), 409-414.
239. Laviron, E. (1979). AC polarography and faradaic impedance of strongly adsorbed electroactive species: Part II. Theoretical study of a quasi-reversible reaction in the case of a Frumkin isotherm. *Journal of Electroanalytical Chemistry and Interfacial Electrochemistry*, *105*(1), 25-34.
240. Yang, C. (1993). Statistical mechanical aspects of adsorption systems obeying the Temkin isotherm. *The Journal of Physical Chemistry*, *97*(27), 7097-7101.

-
241. Durst, J., Simon, C., Hasché, F., & Gasteiger, H. A. (2015). Hydrogen oxidation and evolution reaction kinetics on carbon supported Pt, Ir, Rh, and Pd electrocatalysts in acidic media. *Journal of the Electrochemical Society*, 162(1), F190-F203..
242. Zhou, J., Zu, Y., & Bard, A. J. (2000). Scanning electrochemical microscopy: Part 39. The proton/hydrogen mediator system and its application to the study of the electrocatalysis of hydrogen oxidation. *Journal of Electroanalytical Chemistry*, 491(1-2), 22-29..
243. Liang, Y., Wang, H., Zhou, J., Li, Y., Wang, J., Regier, T., & Dai, H. (2012). Covalent hybrid of spinel manganese–cobalt oxide and graphene as advanced oxygen reduction electrocatalysts. *Journal of the American Chemical Society*, 134(7), 3517-3523..
244. Mao, L., Zhang, D., Sotomura, T., Nakatsu, K., Koshihara, N., & Ohsaka, T. (2003). Mechanistic study of the reduction of oxygen in air electrode with manganese oxides as electrocatalysts. *Electrochimica Acta*, 48(8), 1015-1021.